



**MONASH**  
University

---

**Dynamic X-ray imaging of mice *in vivo* to  
investigate lung function and structure in  
ventilator-induced lung injury**

---

Melissa Helene Preissner

A thesis submitted for the degree of Doctor of Philosophy  
at Monash University

2020

Department of Mechanical and Aerospace Engineering



# Copyright notice

© Melissa Helene Preissner 2020.

I certify that I have made all reasonable efforts to secure copyright permissions for third-party content included in this thesis and have not knowingly added copyright content to my work without the owner's permission.



# Abstract

Ventilator-induced lung injury (VILI) is defined as lung injury associated with mechanical ventilation. The risk of VILI is highest in mechanically-ventilated patients with an initial lung injury, such as acute respiratory distress syndrome (ARDS), where hospital mortality remains high at 40%. CT imaging has shown that when mechanical ventilation is applied to injured, non-homogeneous lungs in ARDS it can lead to further injury, despite lung-protective strategies.

Therefore, a deeper understanding of the regional distribution of the volume of air throughout the ARDS lung during mechanical ventilation can provide insights into the mechanisms of VILI. Furthermore, little is known about the effects of mechanical ventilation on the delicate structures in the lung, such as the airways and the pulmonary vasculature. However, in order to capture functional changes in the lung associated with VILI, a specialised system capable of both high resolution and high speed CT imaging is required.

In this research, a liquid-metal jet X-ray laboratory imaging system was used, demonstrating both superior resolution and high speed CT imaging. The system provides a unique capability of regional functional imaging of mechanically-ventilated mouse lungs *in vivo*, previously only possible on synchrotron facilities.

First, the imaging capabilities of the laboratory X-ray system were investigated and shown to provide high resolution and high speed imaging (i.e., 50  $\mu\text{m}$  features at 30 Hz), critical for dynamic imaging of mouse lungs *in vivo*. The system also demonstrated the ability to distinguish between materials of low contrast, crucial for contrast in soft tissues, such as the lungs.

In a study of mouse models of VILI with images from the laboratory system, combined with customised image analysis developed in this thesis, lung volumes for ten regions in the lung were obtained. This enabled a novel method of matching regional tissue injury with regional lung volume, elucidating a link between high

regional lung volumes and regional injury in one-hit VILI, and a link between low regional lung volumes and regional injury in two-hit VILI.

In complimentary studies, *in vivo* imaging was conducted on the laboratory system to investigate the effects of mechanical ventilation on the airways and the vascular tree. The airway tree was segmented from the images, and it was found that anatomic dead space fraction significantly increased during mechanical ventilation, despite prior lung injury. In a separate group of mice, the vascular tree was segmented from the images, allowing measurements such as vessel count and total pulmonary blood volume to be obtained.

In this thesis, a unique high resolution and high speed imaging system is used for the first time to capture dynamic images of mouse lungs during mechanical ventilation in the laboratory. Customised image analysis was developed in order to investigate links between regional tissue injury and regional lung volume, giving insights into the mechanisms of VILI. In addition, the effect of mechanical ventilation on the airways and the pulmonary vasculature was investigated. These insights provide a greater understanding of how the ventilator affects the lungs in a pre-clinical model of VILI and adds to the knowledge required to advance the development of safe mechanical ventilation.

# Publications

The following journal articles were published during candidature. Journal article 1 is included in Chapter 3. Journal articles 2 and 3 are included in Chapter 5. Journal articles 4 and 5 were published from the studies in Chapter 4, with the full journal articles included in Appendix A. Authors indicated with an asterisk (\*) contributed equally to the work.

## Constituent journal articles of the thesis

1. **Preissner, M.**, Murrie, R. P., Pinar, I., Werdiger, F., Carnibella, R. P., Zosky, G. R., Fouras, A. & Dubsky, S. High resolution propagation-based imaging system for in vivo dynamic computed tomography of lungs in small animals. *Physics in Medicine and Biology* **63** 08NT03 (2018)
2. Kim, E. H.\*, **Preissner, M.\***, Carnibella, R. P., Samarage, C. R., Bennett, E., Fouras, A., Zosky, G. R. & Jones, H. D. Novel analysis of 4DCT imaging quantifies progressive increases in anatomic dead space during mechanical ventilation in mice. *Journal of Applied Physiology* **123** 578–584 (2016)
3. **Preissner, M.**, Bresee, C., Carnibella, R., Fouras, A., Weir, E. K., Dubsky, S., Pinar, I. P. & Jones, H. D. Application of a novel in vivo imaging approach to measure pulmonary vascular responses in mice. *Physiological Reports* **6** e13875 (2018)

## Additional journal articles published during the PhD

4. Yen, S.\*, **Preissner, M.\***, Bennett, E., Dubsky, S., Carnibella, R., OToole, R., Roddam, L., Jones, H. D., Dargaville, P. A., Fouras, A. & Zosky, G. R. The link between regional tidal stretch and lung injury during mechanical ventilation. *American Journal of Respiratory Cell and Molecular Biology* **60** 569–577 (2019)
5. Yen, S.\*, **Preissner, M.\***, Bennett, E., Dubsky, S., Carnibella, R., Murrie, R., Fouras, A., Dargaville, P. A. & Zosky, G. R. Interaction between regional lung volumes and ventilator induced lung injury in the normal and endotoxaemic lung. *American Journal of Physiology - Lung Cellular and Molecular Physiology* **318** L494–L499 (2020)
6. Samarage, C. R., Carnibella, R., **Preissner, M.**, Jones, H. D., Pearson, J. T., Fouras, A. & Dubsky, S. Technical Note: Contrast free angiography of the pulmonary vasculature in live mice using a laboratory X-ray source. *Medical Physics* **43** 6017–6023 (2016)
7. Murrie, R. P., Werdiger, F., Donnelley, M., Lin, Y.-W., Carnibella, R. P., Samarage, C. R., Pinar, I., **Preissner, M.**, Wang, J., Li, J., Morgan, K. S., Parsons, D. W., Dubsky, S. & Fouras, A. Real-time in vivo imaging of regional lung function in a mouse model of cystic fibrosis on a laboratory X-ray source. *Scientific Reports* **10** 447 (2020)



# Declaration for a thesis including published works

I hereby declare that this thesis contains no material which has been accepted for the award of any other degree or diploma at any university or equivalent institution and that, to the best of my knowledge and belief, this thesis contains no material previously published or written by another person, except where due reference is made in the text of the thesis.

This thesis includes three original papers published in peer reviewed journals. The core theme of the thesis is pre-clinical dynamic lung imaging. The ideas, development and writing up of all the papers in the thesis were the principal responsibility of myself, the student, working within the Department of Mechanical and Aerospace Engineering, under the supervision of Dr Stephen Dubsy.

The inclusion of co-authors reflects the fact that the work came from active collaboration between researchers and acknowledges input into team-based research.

In the case of Chapters 3 and 5 my contribution to the work involved the following:

Thesis chapter	Publication title	Status	Nature and percent contribution	Co-author names and contribution	Co-authors Monash student
3	High resolution propagation based imaging system for in vivo dynamic computed tomography of lungs in small animals	Published	85%. Planned the paper, surveyed the literature, designed experiments, collection of experimental data, processing and analysis of all the data, writing and editing the manuscript with figures, responding to reviewers with revisions.	10% SD, 5% others	No
5	Novel analysis of 4DCT imaging quantifies progressive increases in anatomic dead space during mechanical ventilation in mice	Published	50%. Performed imaging experiments, completion of all the 4DCT imaging analysis, data analysis, writing the imaging sections, manuscript revision.	40% EK, 5% HJ, 5% others	No
5	Application of a novel in vivo imaging approach to measure pulmonary vascular responses in mice	Published	80%. Performed imaging experiments, completion of all the imaging analysis, data analysis, writing the imaging sections, manuscript revisions.	10% HJ, 10% others	No

Animal handling and lung tissue analysis for the *in vivo* studies was performed by collaborators Dr Heather Jones (Chapter 5), Prof Graeme Zosky (Chapter 3), Dr Ellen Bennett (Chapter 4) and Dr Seiha Yen (Chapter 4).

I have not renumbered sections of submitted or published papers in order to generate a consistent presentation within the thesis.

**Student signature:**

(Signature removed from final thesis)

**Date:** 12 February 2020

The undersigned hereby certify that the above declaration correctly reflects the nature and extent of the student's and co-authors' contributions to this work. In instances where I am not the responsible author I have consulted with the responsible author to agree on the respective contributions of the authors.

**Main supervisor signature:**

(Signature removed from final thesis)

**Date:** 12 February 2020

# Acknowledgements

It has been an immense privilege to undertake this PhD. I have enjoyed every moment, relishing in both the challenges and the opportunities.

I would firstly like to thank my doctoral supervisors: Dr Stephen Dubsky, Prof Kerry Hourigan and Prof Andreas Fouras. Steve - for providing guidance and professionalism in PhD supervision; you encouraged independent research whilst providing excellent support and the much-needed flexibility required when undertaking a PhD with a young family. Kerry - for your wealth of experience and sound advice in navigating a PhD. Andreas - for providing me with the initial opportunity and resolute support throughout. With that combination, I think I have had one of the best supervisory teams I could have hoped for.

To all my fellow lab members, especially those who provided support and collegiality in the early phase of my PhD, especially Dr Richard Carnibella and Dr Rajeev Samarage - thank you, it made all the difference.

This work is very much a result of an ongoing, fruitful collaboration between engineers, X-ray imaging physicists, biomedical scientists and clinicians. Thank you to our collaborators for providing excellent research opportunities and collegiality throughout this PhD: Prof Graeme Zosky, Dr Seiha Yen and Dr Ellen Bennett at the University of Tasmania, and Dr Heather Jones in Los Angeles.

I am also honoured to have been able to contribute to Monash University more broadly during my PhD, in my membership as a postgraduate student on the University's Diversity and Inclusion Committee, Athena SWAN and the Ally Network. I have sincerely enjoyed being a part of the diverse and inclusive Monash University community again.

I began this PhD with three children under four years of age. Without affordable childcare and flexibility, it would not have been possible to do this. And of course, underpinning it all is a supportive and progressive partner; none of this would have been possible without a lot of support at home. Aran - thank you.



# Contents

<b>Abstract</b>	<b>v</b>
<b>Publications</b>	<b>vii</b>
<b>Declaration for a thesis including published works</b>	<b>ix</b>
<b>Acknowledgements</b>	<b>xi</b>
<b>1 Introduction</b>	<b>1</b>
<b>2 Literature review</b>	<b>7</b>
2.1 Introduction . . . . .	7
2.2 Lung mechanics and lung volumes . . . . .	7
2.3 Pulmonary function testing . . . . .	11
2.4 Mechanical ventilation . . . . .	13
2.5 Acute respiratory distress syndrome (ARDS) . . . . .	15
2.6 Ventilator-induced lung injury (VILI) . . . . .	17
2.7 Safe mechanical ventilation in ARDS . . . . .	23
2.8 Airways and the pulmonary vasculature in ARDS and VILI . . . . .	30
2.9 Mouse models of ARDS and VILI . . . . .	31
2.10 <i>In vivo</i> X-ray imaging of mice for ARDS and VILI . . . . .	35
2.11 Summary . . . . .	42
2.12 Research Aims . . . . .	42
<b>3 Characterising the X-ray system for dynamic <i>in vivo</i> lung imaging</b>	<b>45</b>
3.1 High resolution propagation-based imaging system for <i>in vivo</i> dynamic computed tomography of lungs in small animals . . . . .	45
<b>4 Dynamic <i>in vivo</i> imaging for regional lung function in VILI</b>	<b>55</b>
4.1 Introduction and aims . . . . .	55
4.2 Mouse models and study design . . . . .	56
4.3 Dynamic <i>in vivo</i> 4DCT imaging . . . . .	61
4.4 Post processing of imaging data . . . . .	63
4.5 Data analysis . . . . .	71
4.6 Results and Discussion . . . . .	72
4.7 Conclusions . . . . .	80
<b>5 Dynamic <i>in vivo</i> imaging of structures in the lung</b>	<b>83</b>
5.1 Novel analysis of 4DCT imaging quantifies progressive increases in anatomic dead space during mechanical ventilation . . . . .	83
5.2 Application of a novel <i>in vivo</i> imaging approach to measure pulmonary vascular responses in mice . . . . .	92
<b>6 Conclusions and recommendations for future work</b>	<b>105</b>

<b>A</b>	<b>Journal articles published from the studies in Chapter 4</b>	<b>111</b>
A.1	The link between regional tidal stretch and lung injury during mechanical ventilation . . . . .	111
A.2	Interaction between regional lung volumes and ventilator induced lung injury in the normal and endotoxaemic lung . . . . .	121
<b>B</b>	<b>Related journal articles published during the PhD</b>	<b>129</b>
B.1	Technical Note: Contrast free angiography of the pulmonary vasculature in live mice using a laboratory X-ray source . . . . .	129
B.2	Real-time in vivo imaging of regional lung function in a mouse model of cystic fibrosis on a laboratory X-ray source . . . . .	137
<b>C</b>	<b>Substitution of figures in Chapter 2</b>	<b>147</b>
	<b>Bibliography</b>	<b>149</b>

*To my beautiful boys*



# 1 Introduction

The lungs are one of the most important organs in the body. When the lungs begin to fail, mechanical ventilation is a life-saving intervention. However, it is not just a case of getting air into the lungs for improving gas exchange, but of also safely ventilating the lungs in order to avoid further damage to the lung. The damage that may occur as a result of mechanical ventilation is known as ventilator-induced lung injury (VILI) (Slutsky & Ranieri, 2013).

A common reason for mechanical ventilation in the intensive care unit (ICU) is respiratory failure due to acute respiratory distress syndrome (ARDS). ARDS accounts for almost one in four patients requiring mechanical ventilation in the ICU. Despite advances in clinical care, hospital mortality for mechanically ventilated patients with severe ARDS is unacceptably high at 46.1%, with the average mortality at 40% for patients ranging from mild to severe ARDS (Bellani *et al.*, 2016).

ARDS is characterised by the sudden onset of hypoxic respiratory failure following a direct or an indirect insult to the lungs. In severe cases of ARDS, invasive mechanical ventilation (such as with endotracheal intubation) is required.

VILI can occur from either the ventilation alone, known as one-hit VILI, or as a secondary injury in the context of mechanically ventilated patients with initial lung injury, known as two-hit VILI (Altemeier *et al.*, 2004). ARDS patients' lung mechanics often worsen during mechanical ventilation and it is currently not completely understood what role mechanical ventilation plays in this progression (Henderson *et al.*, 2017).

The implementation of lung-protective strategies, such as positive end-expiratory pressure (Webb & Tierney, 1974) and lower tidal volumes (Brower *et al.*, 2000), resulted in decreases in mortality. However, despite ongoing efforts at safe mechanical ventilation, there has been little further improvement in mortality (Bellani *et al.*, 2016; Phua *et al.*, 2009). The current high mortality rate indicates that there is a proportion

of mechanically ventilated ARDS patients that are unresponsive to the current lung-protective ventilation strategies.

In addition to lung tissue (alveolar) injury, other delicate structures in the lungs, such as the airways and the blood vessels, may be adversely affected by mechanical ventilation (Beitler *et al.*, 2016). Distension of the proximal airways can lead to an increase in anatomic dead space, leading to worsening hypoxaemia (Nickles *et al.*, 2014), whereas closure of the distal airways can cause air trapping in the case of low positive end-expiratory pressure, which may lead to increased airway resistance and ventilation-perfusion mismatch (Jain & Sznajder, 2007). Mechanical ventilation may also alter haemodynamics (Broccard *et al.*, 1998), or cause damage to the capillary-alveolar interface, adversely affecting the pulmonary surfactant, leading to an increase in alveolar stress (Hamlington *et al.*, 2018).

VILI is thought to occur via volutrauma and atelectrauma, leading to biotrauma (Tremblay & Slutsky, 1998). Volutrauma is damage caused by high lung volumes, and atelectrauma is damage caused by low lung volumes, specifically due to the cyclical opening and closing of initially collapsed or oedematous, but recruitable, alveoli. Biotrauma begins as damage to the alveoli, and, in a downward spiral, can lead to systemic injury and multi-organ failure (Slutsky & Ranieri, 2013).

Moreover, VILI manifests in a regional manner in ARDS. Clinical computed tomography (CT) imaging has shown that both over-distended (high volume) areas and under-distended (low volume) areas are distributed heterogeneously throughout the mechanically ventilated ARDS lung (Gattinoni *et al.*, 1987; Maunder *et al.*, 1986; Motta-Ribeiro *et al.*, 2018). Therefore, an understanding of how the ventilator settings relate to the regional distribution of air in the lungs of mechanically ventilated ARDS patients is required to prevent VILI.

The distending pressure across the alveolar wall, i.e., the transpulmonary pressure, is the critical pressure in the lungs for alveolar injury (Beitler *et al.*, 2016). The transpulmonary pressure is determined by subtracting the local intrapleural pressure from the alveolar pressure (Slutsky & Ranieri, 2013). Whilst measurement of the alveolar pressure is possible, it is not possible to obtain the local intrapleural pressure (Marino, 2014; West, 2012). Consequently, it is not possible to obtain a regional distribution of the transpulmonary pressure - or the regional compliance -

throughout the lung.

In contrast, it is possible to assess lung regions for volutrauma and atelectrauma by measuring the volume of air in the region (Gattinoni *et al.*, 2001). One way to do this is with X-ray CT imaging, which provides the regional distribution of the volume of air throughout the lungs (Motta-Ribeiro *et al.*, 2018). Furthermore, CT images provide structural information on the airways and the pulmonary vasculature, revealing important information about airway blockage or collapse (Jain & Sznajder, 2007; Verbanck, 2020), pulmonary embolism and hypertension (Vieillard-Baron *et al.*, 2016).

Animal models are ideal for investigating VILI, due to the availability of reductionist models combined with potentially injurious ventilation protocols and novel interventions (Matute-Bello *et al.*, 2008). Pre-clinical CT imaging is a valuable research tool for animal models of VILI and, depending on the model, can be used at a synchrotron X-ray source (Dubsky *et al.*, 2017; Dubsky *et al.*, 2018), on clinical equipment (Cereda *et al.*, 2017), or in a laboratory as micro-CT (Xin *et al.*, 2018). The advantage of obtaining high quality CT images of small animals in a laboratory environment enables novel or pilot experiments to be conducted at a high throughput, within a readily-accessible facility. This is often not feasible or too costly for synchrotron imaging.

Pre-clinical CT imaging provides information on the distribution of the volume of air throughout the lung, depending on where in the breath cycle the image is taken (Motta-Ribeiro *et al.*, 2018). A breath-hold is required for static image acquisition. However, when acquired dynamically, as a series of CT images, i.e., four-dimensional CT (4DCT), the distribution of air is captured throughout the breath cycle, without the need for a breath-hold (Yamamoto *et al.*, 2009). From this dynamic data, four-dimensional X-ray velocimetry (4DXV) can be applied in order to obtain the regional distribution of the tidal volume throughout the lung (Dubsky *et al.*, 2012).

Furthermore, the ability to image detailed structures in the lung without the administration of contrast agents opens up avenues for investigation into repeated interventions requiring recovery or for longitudinal studies. This is possible for the pulmonary vasculature with the contrast-free angiography technique described in

Samarage *et al.* (2016) in Appendix B.

However, dynamic imaging requires short exposure times in order to avoid motion blur. Therefore, a system capable of high speed imaging is required. The X-ray CT system in the New Horizons biomedical engineering research laboratory at Monash University was designed for this purpose.

The **overall aim** of this research project is to use a laboratory-based imaging system, with the unique capability of both high resolution and high speed *in vivo* imaging, to obtain dynamic 4DCT images of the mechanically-ventilated lung, in order to investigate the mechanisms of volutrauma and atelectrauma from regional lung volumes, as well as to obtain quantitative measurements of the airways and the pulmonary vasculature in mouse models of VILI.

The **first aim** of the research presented in this thesis is to characterise the laboratory X-ray imaging system for resolution, speed and contrast - the parameters pertinent to high quality dynamic (4DCT) *in vivo* lung imaging.

The **second aim** is to obtain regional lung volumes (i.e., the tidal volume and the end-expiratory volume) from dynamic 4DCT images acquired with the laboratory system and to map these to regional biomarkers of lung tissue injury. The linking of lung volumes with biomarkers for the same lung regions is crucial for understanding the effects of mechanical ventilation on regional lung injury.

The **third aim** is to use dynamic 4DCT images from the laboratory system to measure the volume of air in the airways and the volume of the pulmonary vasculature in the mouse lung, in order to observe changes in these structures occurring as a result of mechanical ventilation.

This thesis reports the research undertaken to achieve these three aims. An extensive review of the literature is provided in Chapter 2. Chapter 3 contains a published journal article characterising the laboratory X-ray system for its high resolution, high speed and low contrast *in vivo* imaging capabilities. Chapter 4 uses mouse models of VILI with the laboratory X-ray system to obtain regional lung volumes for ten regions in the lung and investigates the link between these regional volumes and regional tissue injury. Chapter 5 contains two published journal articles using images of mechanically ventilated mice from the laboratory X-ray system to investigate lung

structures, specifically, the anatomical deadspace of the airways, and the effects of mechanical ventilation on the pulmonary vasculature.



## 2 Literature review

### 2.1 Introduction

Mechanical ventilation is a life-saving intervention for respiratory failure. However, paradoxically, mechanical ventilation can also damage the delicate structures in the lung. This is known as ventilator-induced lung injury (VILI). VILI is a heightened risk when the lungs are in a pathological state, such as with acute respiratory distress syndrome (ARDS), where it can lead to multi-organ dysfunction (Slutsky & Ranieri, 2013).

In order to investigate the pathophysiology of lung mechanics in VILI, it is important to first understand how the healthy lung functions. The first part of this literature review contains an overview of lung mechanics and mechanical ventilation. Following on from the fundamental concepts, a detailed description of the current literature on acute respiratory distress syndrome, ventilator-induced lung injury and approaches for determining safe mechanical ventilation in ARDS is provided. A discussion of mouse models of VILI and ARDS, and current techniques for *in vivo* X-ray imaging in small animals, with a specific focus on the imaging techniques pertinent to VILI, is provided in the final sections of this chapter.

### 2.2 Lung mechanics and lung volumes

The basic structure of the human lung with the major anatomy is shown in Figure 2.1. The following are required for adequate gas exchange (West, 2012): 1. ventilation: the movement of gas from the mouth into and out of the alveoli; 2. diffusion: the movement of gas across the thin alveolar wall (blood-air barrier); and 3. perfusion: blood flow to and from the alveoli. A further requirement for adequate gas exchange is the regional matching of ventilation and perfusion, which the body is able to regulate with the vasoconstriction and dilation of the pulmonary arterioles.

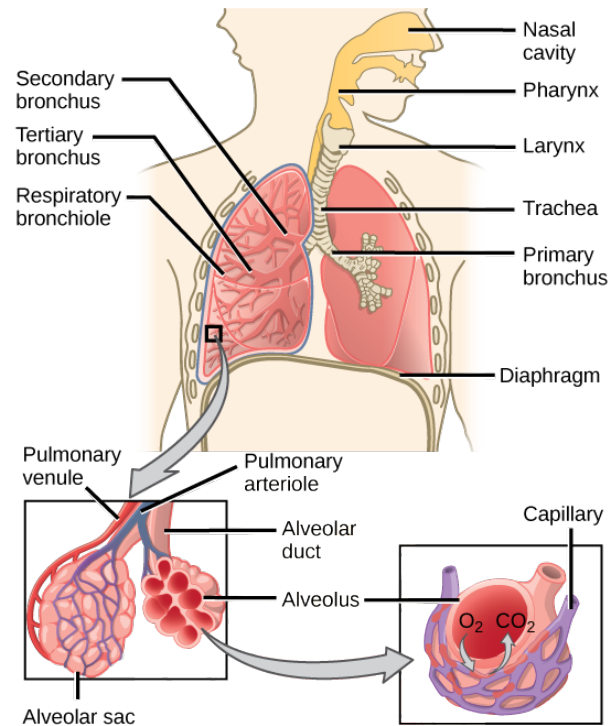


FIGURE 2.1: Human lungs with major anatomy, alveoli and gas exchange shown (Fowler *et al.*, 2013).

During spontaneous breathing, inflation of the lungs is achieved by generating a slightly sub-atmospheric pressure in the lungs, allowing the air (at atmospheric pressure) to flow in. This is achieved by contraction of the respiratory muscles, which creates a sub-atmospheric pressure in the thin, fluid-filled pleural space, due to the opposing forces of lung recoil and chest expansion. In order for the lung to inflate to the required volume, the forces that need to be overcome are: the resistance to flow in the airways; the elastic recoil of the lung, which includes the tissue fibre elasticity plus the surface tension in the alveoli; and the elastic recoil of the chest wall (Bates, 2009; von Neergaard, 1929). In healthy lungs during normal breathing, the alveoli do not collapse entirely at end-expiration, due to the opposing forces of surface tension in the alveoli and the expanding chest wall (West, 2012). Thus, a volume of air remains in the lungs at the end of a normal exhalation, called the functional residual capacity (FRC).

The transpulmonary pressure ( $P_{tp}$ ) describes the pressure that is required to inflate the lungs. The transpulmonary pressure is the pressure difference between the alveolar compartment ( $P_{alv}$ ) and the intrapleural pressure ( $P_{pl}$ ), given by

$$P_{tp} = P_{alv} - P_{pl}. \quad (2.1)$$

Transpulmonary pressure is an important physiological variable in mechanical ventilation, since it relates to the distension, or stretch, of the alveoli (Slutsky & Ranieri, 2013). High transpulmonary pressure can lead to over-distension or rupture of the alveoli (volutrauma).

Deflation of the lung is achieved passively by elastic recoil, mainly due to the surface tension in the alveoli, as well as the elastin fibres in the lung tissue (von Neergaard, 1929). Elastic recoil is an important function that can be disrupted through disease, such as emphysema, where it is decreased, making it difficult to breathe out, or in pulmonary fibrosis, where it is increased, making it difficult to breathe in. In reality, the lungs do not behave in an entirely elastic manner, rather, they are viscoelastic (Bachofen, 1968). The viscoelastic behaviour is attributed, in part, to the complex microstructure of lung tissue fibres which are composed of both elastin and collagen, whereby the elastin exhibits elastic behaviour, and the collagen provides tensile strength, which is of increasing stiffness at high volumes, providing protection from over-distension (Suki & Bates, 2011; Suki *et al.*, 2011).

The elasticity of the lungs is reported in the clinic as the pulmonary compliance, i.e., the inverse of elasticity. The total respiratory system compliance is a sum of the pulmonary compliance plus the chest wall compliance. In order to measure the pulmonary compliance without the chest wall compliance included, the respiratory muscles need to be inactivated by sedation and muscle paralysis (Lu & Rouby, 2000). The pulmonary compliance is a measure of the distensibility of the lung tissue and is a critical concept for lung mechanics. Low pulmonary compliance indicates stiff lungs, whereas high pulmonary compliance refers to floppy lungs. The static pulmonary compliance,  $C_{stat}$ , is given by

$$C_{stat} = \frac{\Delta V}{\Delta P_{tp}}, \quad (2.2)$$

where  $\Delta V$  is the change in lung volume for a given change in transpulmonary pressure,  $\Delta P_{tp}$ , calculated from measurements at zero flow conditions.

For Equation 2.2, the transpulmonary pressure can be calculated by subtracting

the oesophageal pressure from the airway pressure (Galetke *et al.*, 2007). The airway pressure at zero airflow provides a measure of the alveolar pressure ( $P_{alv}$ ) under static conditions, and the oesophageal pressure provides a global estimate of the intrapleural pressure ( $P_{pl}$ ) in the lung, allowing the transpulmonary pressure to be calculated as per Equation 2.1.

However, the pulmonary compliance of the lungs changes across the breath cycle, due to the fluctuating volumes and pressures in the lungs during normal breathing or during mechanical ventilation (Harris, 2005). This is called dynamic (pulmonary) compliance. In the context of this thesis, the definition of dynamic compliance,  $C_{dyn}$ , is given by

$$C_{dyn} = \frac{dV}{dP_{tp}}, \quad (2.3)$$

where  $\frac{dV}{dP_{tp}}$  is the gradient of the pressure-volume curve.

This definition of dynamic pulmonary compliance takes into account the mechanical behaviour that the lung experiences during normal breathing or mechanical ventilation. These measurements are currently difficult to obtain in the clinic (Harris, 2005). Regional volumes under normal flow conditions during mechanical ventilation can be captured with dynamic four-dimensional CT (4DCT) imaging (Dubsky *et al.*, 2012).

Moreover, compliance is distributed regionally throughout the lung, since the volume of air and the transpulmonary pressures vary regionally throughout the lung, due to the regional distribution of the intrapleural pressure (Agostoni, 1972).

For normal function, the lungs must be compliant upon inspiration, but be less compliant upon expiration, in order for the lungs to contract (recoil) for the next breath. This is moderated in healthy lungs, in part, by the changing surface tension in the alveoli (von Neergaard, 1929; West, 2012). Pulmonary compliance is a physical property of the lungs, and similar to the spring constant in engineering, the value depends on the size of the lung. In ARDS patients, the pulmonary compliance is decreased due to the reduced aeratable lung volume available for ventilation, as well as due to disruption to the normal functioning of surface tension in the alveoli.

Figure 2.2 illustrates the definition of lung volumes and capacities. The two volumes that are relevant to this thesis are: functional residual capacity (FRC); the volume of air left in the lungs after expiration during quiet breathing, and tidal volume ( $V_T$ ); the volume of air that moves in and out of the lungs during quiet breathing. When referring to mechanically-ventilated lungs, the term end-expiratory lung volume (EELV), or end-expiratory volume (EEV), is used instead of FRC. A spirometer can be used to measure the tidal volume and the vital capacity. In the clinic, the FRC and the residual volume can be measured with a gas dilution technique or a body plethysmograph. The FRC (or EELV) and the tidal volume can also be measured from end-expiratory and end-inspiratory CT images (Fuld *et al.*, 2008).

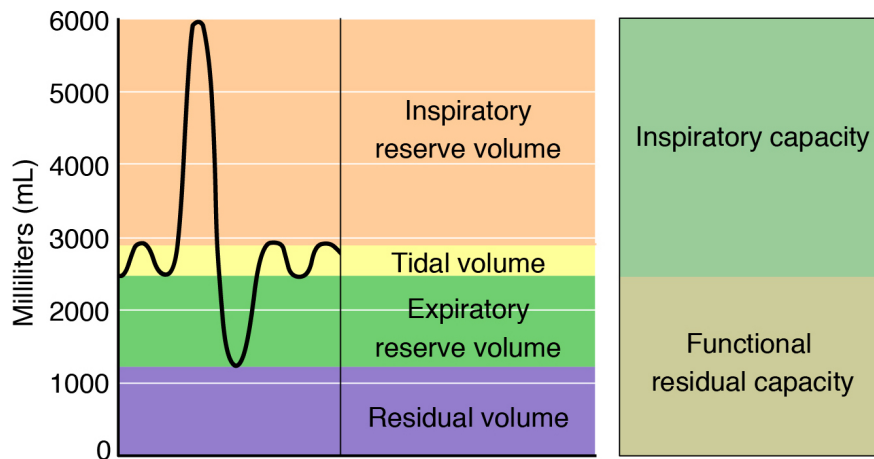


FIGURE 2.2: Typical lung volumes and capacities. The spirometer only measures the tidal volume and the vital capacity. The functional residual capacity and the residual volume can be measured with a gas dilution technique or a body plethysmograph (Betts *et al.*, 2013).

## 2.3 Pulmonary function testing

Clinical pulmonary function testing provides information on lung function by measuring global lung volumes. It is usually performed for clinical diagnosis when a patient complains of breathlessness, or for disease monitoring, such as in asthma or in chronic obstructive pulmonary disease (COPD), in order to adjust medication. Most of the tests, such as spirometry, require active participation from the patient.

However, passive tests can be performed, for example, with the forced oscillation technique (Evans *et al.*, 2019).

For mechanically ventilated patients, the ventilator can monitor pressures, volume and flow (Marino, 2014). It can perform lung function tests without active participation of the patient. These tests give vital information to the clinician, such as respiratory compliance or whether there is a blockage in the endotracheal tube. In the context of VILI and ARDS, monitoring pulmonary compliance via the pressure-volume curves from the ventilator provides information on lung function (Harris, 2005). A decrease in lung tissue compliance indicates a loss of aeratable lung volume due to oedema and inflammation (Gattinoni & Pesenti, 2005; Henderson *et al.*, 2017). The role of pressure-volume curves in mechanical ventilation are described in more detail in Section 2.7.4.

Spirometry requires active participation from the patient and provides measures of pulmonary function that include the forced expiratory volume exhaled in one second (FEV1) and flow-volume loops, which can indicate increased airway resistance (via decreased flow), due to bronchoconstriction, such as observed in asthma (West, 2013).

Pulmonary function testing that does not require active participation from the patient includes the multiple breath washout technique (Horsley, 2009) and the forced oscillation technique (Milne *et al.*, 2019; Nilsen *et al.*, 2019). There is ongoing interest in the forced oscillation technique for paediatric lung function testing, due to the non-invasive and passive nature of this test (Evans *et al.*, 2019).

Despite these advantages, these pulmonary function tests remain a global measure of overall lung function and do not provide data on the regional distribution of lung function.

Deviation from normal or healthy values of lung function from clinical pulmonary function tests gives an insight into abnormal or diseased states and can provide information about the underlying disease. Severe disruption of the normal processes of breathing can lead to respiratory failure requiring mechanical ventilation, which will be discussed in the next section.

## 2.4 Mechanical ventilation

Mechanical ventilation is a crucial life-saving clinical intervention in an intensive care setting. Critically ill patients may require mechanical assistance with breathing, either because they are unconscious, or because there is a problem with the lungs that prevents them from breathing adequately unassisted.

From the point of view of clinical management, there are five broad categories of respiratory failure that may lead to mechanical ventilation (West, 2012):

1. **Acute overwhelming lung disease**, e.g., bacterial pneumonia. In severe cases, this can also deteriorate to ARDS, requiring mechanical ventilation.
2. **Neuromuscular disorder**, e.g., poliomyelitis or barbiturate poisoning.
3. **Acute on chronic lung disease**, e.g., an exacerbation due to asthma or cystic fibrosis.
4. **Acute respiratory distress syndrome (ARDS)**.
5. **Infant respiratory distress syndrome**, previously known as hyaline membrane disease.

The two broad modes of positive pressure mechanical ventilation in the clinic are (Campbell & Davis, 2002):

1. **Pressure-control ventilation**, whereby an inflation pressure is set over a duration of time.
2. **Volume-control ventilation**, whereby a set tidal volume is delivered within allowable pressure limits.

The aim in the clinic is to conform to a lung protective ventilation strategy (Needham *et al.*, 2012). If this cannot be achieved whilst simultaneously providing adequate ventilation to the patient, for example, by increasing PEEP to the maximum allowable limit, then extracorporeal membrane oxygenation (ECMO) may be initiated in order to reduce the load on the lungs for a duration of time to facilitate recovery (Abrams *et al.*, 2019). However, ECMO is also highly invasive and fraught with its own risks (Peek *et al.*, 2009).

During mechanical ventilation, inflation is achieved by generating a positive pressure (relative to atmospheric pressure) in the airway, whereby the pressure has to be large enough to overcome the resistive and elastic forces of the lung. The ventilator has to inflate the lung sufficiently for adequate gas exchange. In the case of the ARDS, this may require pressures that are higher than those required to adequately ventilate the healthy lung, due to the increased stiffness (decreased compliance) of the ARDS lung (Ashbaugh *et al.*, 1967; Henderson *et al.*, 2017). In the case of ARDS, areas of alveolar collapse (atelectasis) need to be re-opened (recruited) in order to increase the size of the lung available for ventilation (gas exchange) and to prevent cyclical injury (atelectrauma) to the lung tissue (West, 2012).

Figure 2.3 <sup>1</sup> illustrates the pressures that are monitored during volume-control ventilation, whereby the plateau pressure (airway pressure at zero flow, during an inflation hold) is the pressure in the alveoli, i.e., at equilibrium (Marino, 2014). The plateau pressure is used to determine whether the set pressure is within clinical lung-protective guidelines. The difference in magnitude between the peak pressure and the plateau pressure determines the component of pressure loss due to airway resistance, which is usually small, but if found to be large, prompts the clinician to investigate tube blockages or other causes of the increase in airway resistance.

At this point, the question may arise as to whether the adverse effects of positive-pressure ventilation could be avoided by applying negative pressure ventilation to the patient. The primary aim of mechanical ventilation is to achieve a pressure difference across the lung to allow air to flow into the lungs. In theory, this can be achieved either via a positive pressure in the airway (trachea) or via a negative (sub-atmospheric) pressure inside the lungs. Negative pressure ventilation achieves a pressure difference by applying a sub-atmospheric pressure to the thorax (and the intrapleural space), thus mimicking spontaneous breathing more closely. Early ventilator designs operated under negative pressure; patients were fully enclosed in a large tank, known as the iron lung (Drinker & Shaw, 1932). Despite the effectiveness

<sup>1</sup>From the MSD Manual Professional Version (known as the Merck Manual in the US and Canada and the MSD Manual in the rest of the world), edited by Robert Porter. Copyright 2020 by Merck Sharp & Dohme Corp., a subsidiary of Merck & Co., Inc., Kenilworth, NJ. Available at <http://www.msdmanuals.com/professional>. Accessed 16 May 2020.

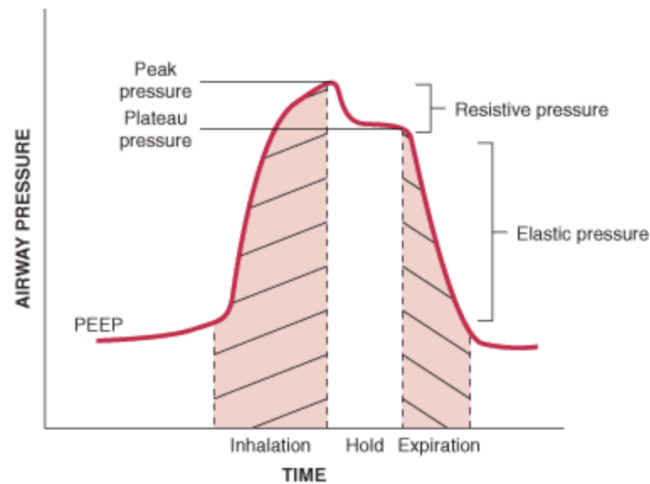


FIGURE 2.3: Airway pressure versus time during constant flow, volume-control mechanical ventilation. The inflation-hold manoeuvre (typically 1 second) enables the plateau (alveolar) pressure to be measured. The resistive pressure is the pressure required to overcome airway resistance. Elastic pressure is the pressure required to overcome the elastic recoil of the lungs and chest wall (Porter, 2020).

of this mode of ventilation in poliomyelitis, it was shown to be less effective for injured lungs, such as in ARDS (Lassen, 1953). A review by Corrado & Gorini (2002) cites additional reasons such as: lack of upper airway protection (that the endotracheal tube provides in positive pressure ventilation), practical difficulty of access to patients for observation by clinicians and nurses, and discomfort for the patient due to motion restriction. Consequently, negative pressure ventilation is no longer routinely used in the clinic.

This section has provided an overview of the fundamental concepts in lung anatomy, lung mechanics and mechanical ventilation. The next sections provide a discussion of the current literature in ARDS and VILI, the challenges of providing safe mechanical ventilation in ARDS, and pre-clinical *in vivo* studies using small animals, with a specific focus on X-ray imaging in Section 2.10.

## 2.5 Acute respiratory distress syndrome (ARDS)

ARDS is one of the five types of respiratory failure described by West (2013). ARDS patients' lung mechanics often worsen during ventilation, and, in severe cases, they can develop multiple-organ failure leading to death (Bellani *et al.*, 2016).

The current clinical definition of ARDS, known as the Berlin Definition, is based on a set of criteria, including timing, chest imaging and origin of edema, shown in Figure 2.4 (The ARDS Definition Task Force: Ranieri *et al.*, 2012). This consensus definition uses oxygenation values to classify the severity of ARDS as either mild, medium or severe.

**Table 3.** The Berlin Definition of Acute Respiratory Distress Syndrome

Acute Respiratory Distress Syndrome	
Timing	Within 1 week of a known clinical insult or new or worsening respiratory symptoms
Chest imaging <sup>a</sup>	Bilateral opacities—not fully explained by effusions, lobar/lung collapse, or nodules
Origin of edema	Respiratory failure not fully explained by cardiac failure or fluid overload Need objective assessment (eg, echocardiography) to exclude hydrostatic edema if no risk factor present
Oxygenation <sup>b</sup>	
Mild	200 mm Hg < PaO <sub>2</sub> /FIO <sub>2</sub> ≤ 300 mm Hg with PEEP or CPAP ≥5 cm H <sub>2</sub> O <sup>c</sup>
Moderate	100 mm Hg < PaO <sub>2</sub> /FIO <sub>2</sub> ≤ 200 mm Hg with PEEP ≥5 cm H <sub>2</sub> O
Severe	PaO <sub>2</sub> /FIO <sub>2</sub> ≤ 100 mm Hg with PEEP ≥5 cm H <sub>2</sub> O

Abbreviations: CPAP, continuous positive airway pressure; FIO<sub>2</sub>, fraction of inspired oxygen; PaO<sub>2</sub>, partial pressure of arterial oxygen; PEEP, positive end-expiratory pressure.

<sup>a</sup>Chest radiograph or computed tomography scan.

<sup>b</sup>If altitude is higher than 1000 m, the correction factor should be calculated as follows: [PaO<sub>2</sub>/FIO<sub>2</sub> × (barometric pressure/760)].

<sup>c</sup>This may be delivered noninvasively in the mild acute respiratory distress syndrome group.

FIGURE 2.4: Table from The ARDS Definition Task Force: Ranieri *et al.* (2012) showing the criteria for mild, moderate and severe ARDS, based on the Berlin Definition.

ARDS can be caused by either a direct or an indirect injury or insult to the lungs. Direct, or pulmonary, ARDS, includes pneumonia or acid aspiration, whereas indirect, or extrapulmonary, ARDS can be due to major trauma or sepsis (Pelosi *et al.*, 2001; The ARDS Definition Task Force: Ranieri *et al.*, 2012). The differences between pulmonary and extrapulmonary ARDS are outlined in a review by Pelosi *et al.* (2003), which includes differences in patterns on clinical CT images as well as differences in biological markers.

ARDS of any severity requires ventilation support. In milder cases, this may begin with non-invasive methods, such as with a face mask or nasal prongs (Liu *et al.*, 2016). As ARDS worsens, intubation and mechanical ventilation is required. The clinical decision of when to provide invasive ventilatory support to a patient is based on the patient's condition (i.e., hypoxaemic or hypercarbic respiratory failure),

whereby the risk of VILI influences the management of lung protective ventilation (Neudoerffer Kangelaris *et al.*, 2016).

ARDS and VILI are inextricably linked. The respiratory distress and hypoxaemia associated with ARDS leads to the requirement to mechanically ventilate the patient, which can lead to VILI.

## 2.6 Ventilator-induced lung injury (VILI)

Ventilator-induced lung injury is defined as lung injury associated with either mechanical ventilation alone, called one-hit VILI, or, more commonly, in combination with an initial lung injury, called two-hit VILI. In the case of two-hit VILI, an initial lung injury leads to the sudden onset of respiratory failure, such as ARDS, requiring mechanical ventilation (Slutsky & Ranieri, 2013).

Two-hit VILI is a combination of the initial lung injury from ARDS plus mechanical ventilation. One-hit VILI can occur in ventilated patients with initially healthy lungs, who are often vulnerable because of cardiac conditions, major surgery or trauma that may lead to ARDS (Borges, 2015). Although two-hit VILI with ARDS more commonly leads to lung injury, one-hit VILI is interesting from the point-of-view of investigating the direct relationship between the (healthy) lung and the ventilator, without the complication of a prior lung injury.

Two-hit VILI can be due to either direct (pulmonary) or indirect (extrapulmonary) causes of ARDS. The current clinical guidelines on lung protective ventilation strategies apply equally to both pulmonary and extrapulmonary ARDS.

Mechanical ventilation is currently understood to cause lung injury via two main mechanisms: volutrauma and atelectrauma (Dreyfuss & Saumon, 1992; MacIntyre, 2005; Slutsky & Ranieri, 2013). These are illustrated in Figure 2.5, where it can be seen that both these mechanisms lead to a cascade of biotrauma events, such as localised oedema, inflammation and increased alveolar-capillary permeability that may lead to the translocation of mediators, causing systemic inflammation and multiple-organ failure. A recent study in mice undergoing injurious mechanical ventilation demonstrated a synergy between atelectrauma and volutrauma, described as a "rich get

richer" effect, whereby atelectrauma induces alveolocapillary leak, and volutrauma exacerbates it, leading to worsening biotrauma (Hamlington *et al.*, 2018).

### 2.6.1 Volutrauma

Volutrauma refers to the volume of air in the alveoli as causing over-distension such that damage to the fragile tissue structure occurs. Early mechanical ventilation was initially applied to patients with healthy lungs who were undergoing surgery or with paralytic polio, where low pressures could be applied and gas exchange adequately maintained (Slutsky, 2015).

However, with the increasing use of mechanical ventilation, patients with injured lungs under respiratory distress were put on ventilators (Slutsky & Ranieri, 2013). In these patients, however, higher pressures were required to maintain adequate gas exchange, which led to alveolar rupture and air leaks (Dreyfuss & Saumon, 1992). This injury was initially termed barotrauma, referring to the airway pressure applied by the ventilator, which was thought to be causing damage.

The term was brought into question by subsequent studies on rabbits where the chest wall was constrained, in order to limit the inspiratory lung volume, but keeping the (high) airway pressure (i.e., the peak inspiratory pressure) the same, which resulted in less oedema and injury in this group of animals (Hernandez *et al.*, 1989). These findings supported the concept that it is the transpulmonary pressure that determines over-distension: restraint of the outward expansion of the chest wall can lead to a positive intrapleural pressure and therefore an overall lower transpulmonary pressure (Slutsky & Ranieri, 2013; Yoshida *et al.*, 2012). This concept is also demonstrated by musicians playing instruments: high pressure in the airways do not lead to lung injury, since the airway (or alveolar) pressure is counteracted by the *positive* intrapleural pressures generated by tensioning the chest wall muscles (Slutsky & Ranieri, 2013).

### 2.6.2 Atelectrauma

Atelectrauma refers to the repeated opening and closing of lung regions, resulting in cyclical stresses which eventually causes structural damage to the alveoli (Slutsky &

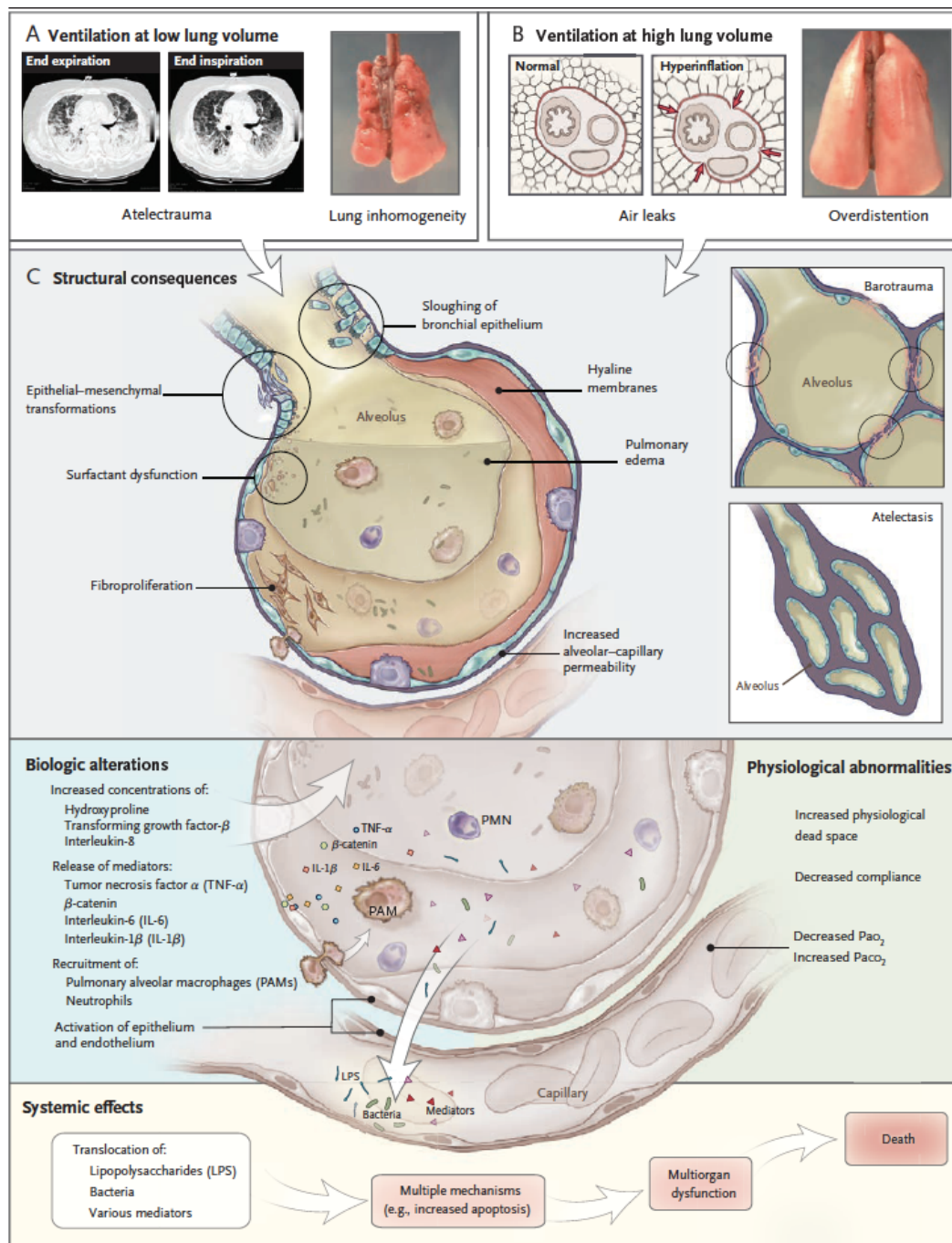


FIGURE 2.5: Illustration of the over-distension (volutrauma) and under-distension (atelectasis) of lung tissue leading to ventilator-induced lung injury and broader systemic effects, such as multiple-organ dysfunction and death. Reproduced with permission from Slutsky & Ranieri (2013), copyright Massachusetts Medical Society.

Ranieri, 2013). Atelectasis (collapse) is thought to occur upon expiration in ARDS patients if the end-expiratory pressure is set at atmospheric pressure (i.e., zero PEEP), as was the case in the early days of mechanical ventilation. One explanation for this is that the surfactant in the alveoli is disrupted in ARDS such that the surface tension causing the alveoli to recoil is higher than usual, tending to collapse alveoli at end-expiration and making it difficult to inhale, i.e., a decrease in lung compliance (Lewis & Jobe, 1993). Although it is not possible to distinguish collapse from oedema on end-expiratory CT images (Hubmayr, 2002), end-expiratory atelectasis has been observed *in vivo* with video microscopy in experimental models of lung injury in animals, as shown in Figure 2.6 (Christley *et al.*, 2013; Schiller *et al.*, 2001). Additionally, recruitable atelectasis may be distinguished when both end-inspiratory and end-expiratory CT images are available (Cereda *et al.*, 2017).

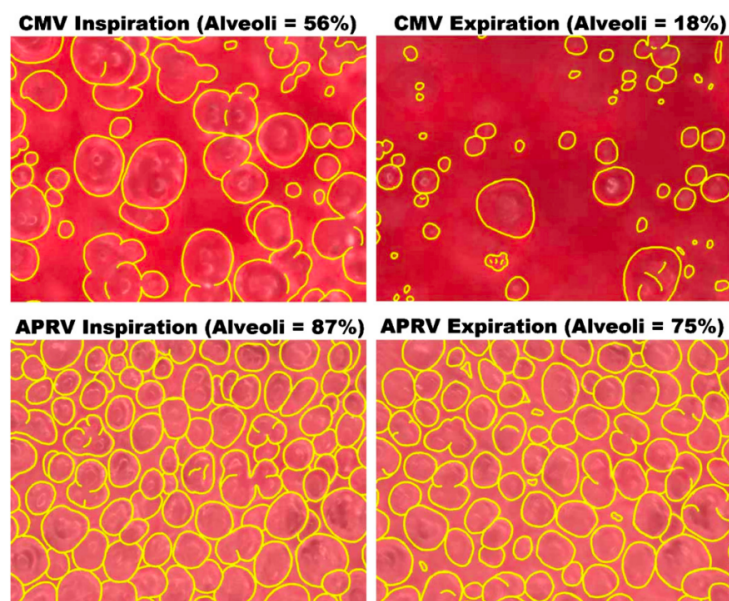


FIGURE 2.6: Alveolar collapse captured with video microscopy at end-expiration (top right panel, 'CMV Expiration'). In this study by Christley *et al.* (2013), conventional mechanical ventilation (CMV) was compared to airway pressure release ventilation (APRV). Yellow circles indicate individual alveoli.

### 2.6.3 Positive-end expiratory pressure (PEEP)

To help counter atelectasis, positive-end expiratory pressure (PEEP) was introduced in the early days of mechanical ventilation (Ashbaugh *et al.*, 1967; Webb & Tierney, 1974). It recruits (re-opens) previously closed alveoli and keeps the lung open at the

end of the breath cycle, at end-expiration, thus reducing alveolar collapse and the consequential cyclical stresses leading to atelectrauma (Caironi *et al.*, 2010; Slutsky & Hudson, 2006). This is an open lung approach, where higher PEEP is applied in response to worsening lung mechanics in ARDS, with the intention of decreasing the occurrence of stress raisers and reduce the heterogeneity of ventilation (Slutsky & Hudson, 2006). Whilst some PEEP is beneficial, it is not a panacea for VILI, as was initially thought. Too much PEEP can lead to over-distension and contribute to volutrauma, which is most pronounced in ARDS (Brower *et al.*, 2004; Gattinoni *et al.*, 2006). Furthermore, too much PEEP is known to have adverse effects on the pulmonary vasculature and haemodynamics (Vieillard-Baron *et al.*, 2016). Early investigations into the concept that too much PEEP may be causing over-distension studied various combinations of PEEP and peak inspiratory pressure (PIP) and their effect on lung injury in rat models (Dreyfuss & Saumon, 1993). It was found that applying a low or moderate tidal volume (via PIP), in combination with increasing levels of PEEP (i.e., increases in the end-expiratory lung volume), resulted in increasing lung injury, which they hypothesised to be due to the total end-inspiratory lung volume.

#### **2.6.4 Regional ventilation, heterogeneity and stress raisers**

Studies using clinical CT imaging show that volutrauma and atelectrauma occur as an uneven (heterogeneous) spatial distribution in ARDS patients (Cressoni *et al.*, 2013; Gattinoni *et al.*, 2001; Gattinoni & Pesenti, 2005). A study by Gattinoni & Pesenti (2005) using CT imaging in ARDS patients led to a renewed understanding of how lung injury manifests; as a patchy and unevenly distributed injury, rather than as an overall, evenly distributed injury. They quantified the reduced aeratable, i.e., healthy, volume of lung, which was termed baby lung, referring to the functional volume of the ARDS lung as being reduced to the size of a child's. They postulated that this heterogeneous distribution of ventilation may result in the over-inflation of the most compliant (i.e., healthy) zones, since these zones will likely receive most of the tidal ventilation. These studies corroborated an earlier study on models by Mead *et al.* (1970) by hypothesising (with evidence from CT imaging) that for the

ARDS lung, the increased local stresses (i.e., stress raisers) resulting from inhomogeneity due to oedema and inflammation may result in localised injury, despite a transpulmonary pressure that is deemed to be safe in a homogeneous lung (Cresoni *et al.*, 2013). CT evidence of the regional distribution of ventilation and injury led to the understanding that the decrease in compliance observed in ARDS patients was not because of a uniform, homogeneous distribution of tissue injury throughout the lung, but rather, from a reduction in the volume of normally aerated lung volume.

### 2.6.5 The role of CT imaging in ARDS and VILI

In many of the seminal studies described above, a vast improvement in understanding the spatial distribution of ventilation in ARDS has come from CT imaging of patients (Caironi *et al.*, 2010; Gattinoni *et al.*, 1987; Gattinoni *et al.*, 2001; Maunder *et al.*, 1986; Vieira *et al.*, 1999). In these studies, CT was able to provide three-dimensional information that reveals details about the inhomogeneity of ventilation that were not seen previously on two-dimensional chest radiographs (Pesenti *et al.*, 2016).

The challenge for safe mechanical ventilation lies in minimising both under-distension and over-distension of the alveoli throughout the lung, whilst still providing adequate ventilation to the patient to maintain arterial blood gases. This is a complex challenge, since the requirements are seemingly in conflict; apply upper limits on the tidal volume and PEEP to avoid over-distension (volutrauma), whilst still maintaining adequate ventilation to the patient, and enough PEEP to prevent the under-distension and collapse of distal airspaces that may lead to atelectrauma during the respiratory cycle.

Therefore, the key to providing safe mechanical ventilation lies in understanding the regional distribution and prevalence of over-distended and under-distended regions, and how this links to the ventilation parameters. The next section discusses various approaches for determining safe mechanical ventilation.

## 2.7 Safe mechanical ventilation in ARDS

The research to date shows that the initial lung injury in ARDS patients is spatially heterogeneous, which can lead to areas of both over-distension (volutrauma) and under-distension (atelectasis) during mechanical ventilation. Currently, a safe mechanical ventilation strategy is defined as one that prevents both volutrauma and atelectrauma, which are understood to be the main mechanisms of VILI. The aim of both clinical studies and pre-clinical experiments is to investigate variables and their correlation with indicators of safe mechanical ventilation in ARDS, such as survival statistics in the case of clinical data, or biological or physiological data in animal studies. The following section discusses approaches for determining safe mechanical ventilation relevant to this thesis.

### 2.7.1 Lung-protective ventilation in the clinic

Lung-protective ventilation is based on scientific evidence from clinical trials and expert consensus (Amato *et al.*, 2015; Brower *et al.*, 2000; Brower *et al.*, 2004; Fan *et al.*, 2017; Gattinoni *et al.*, 2017; Gattinoni *et al.*, 2018; Griffiths *et al.*, 2019; Papazian *et al.*, 2019). The guidelines currently include: low tidal volume combined with maximum limits on plateau pressure and PEEP; limiting the driving pressure; prone positioning of the patient to allow re-distribution of the transpulmonary pressure; and, the addition of some PEEP to avoid atelectasis and to aid in alveolar recruitment.

### 2.7.2 Transpulmonary pressure

Calculation of the transpulmonary pressure (see Equation 2.1) requires a measurement of the alveolar pressure, i.e., the plateau pressure from the ventilator (as shown in Figure 2.3), as well as an accurate measurement of the intrapleural pressure, which varies spatially throughout the lung. The main obstacle with this approach is obtaining accurate measures of the spatial distribution of intrapleural pressure throughout the lung. Clinically, an estimate of the intrapleural pressure can be obtained via the oesophagus, but this is sampled at one location and interpreted as a global value for the whole lung (Galetke *et al.*, 2007). Estimates of regional compliance rely on an

assumed constant transpulmonary pressure throughout the lung, resulting in the regional volume as an effective compliance (Kaczka *et al.*, 2011; Perchiazzi *et al.*, 2014; Wongviriyawong *et al.*, 2013). In the absence of a clinical oesophageal pressure measurement, the plateau pressure is monitored via the ventilator in an intensive care setting (Marino, 2014). This measure may be lower than the transpulmonary pressure, since it does not take the sub-atmospheric (negative) intrapleural pressure into account, thus providing an underestimate of the actual (resultant) pressures across the alveolar wall. This discrepancy becomes worse if a patient is in respiratory distress and generating very large sub-atmospheric intrapleural pressures, which can lead to over-distension and injury (volutrauma), despite ventilation with an acceptable plateau pressure (Slutsky & Ranieri, 2013).

### 2.7.3 Tidal volume

Evidence from clinical trial data showed an improvement in mortality between patients that were ventilated with a (reduced) tidal volume of 6 mL per kilogram of predicted body weight (despite an increase in hypercapnia), as compared to those with a tidal volume of 12 mL per kilogram of predicted body weight (Brower *et al.*, 2000; Sahetya *et al.*, 2017). This resulted in new clinical guidelines limiting the tidal volume to 6 mL per kilogram of predicted body weight, in an effort to mitigate volutrauma, with permissible hypercapnia. Whilst this measure scales the tidal volume to the predicted size of a patient's lung (i.e., anatomical size), it does not take into account the functional lung size, i.e., the healthy parts of the ARDS lung that have relatively normal compliance and ventilation (Gattinoni & Pesenti, 2005). This concept is called baby lung and it suggests that the tidal volume should perhaps be scaled to the ARDS patient's functional lung size for safe mechanical ventilation.

### 2.7.4 Pressure-volume curve

Modern mechanical ventilators can record pressure and volume data of ARDS patients for routine monitoring of pulmonary compliance. A reduced pulmonary compliance (compared to healthy reference values) indicates worsening lung function and injury. This is shown in the solid curve in Figure 2.7, where higher pressures are

required to achieve the same lung volume (Moloney & Griffiths, 2004).

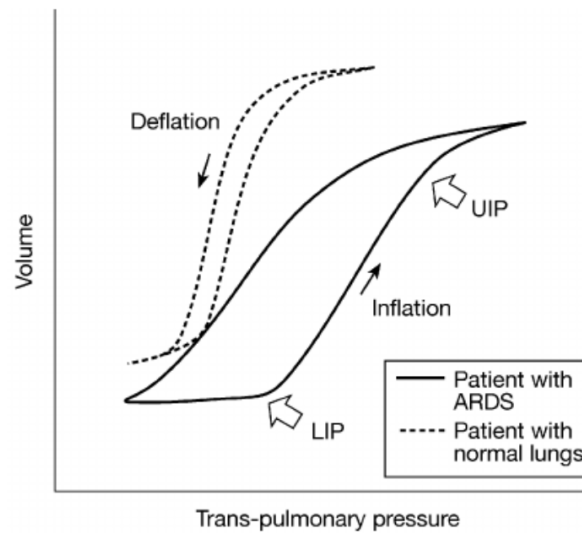


FIGURE 2.7: (a) Pressure-volume curves indicative of normal lungs (dashed) and for an ARDS patient (solid), where pulmonary compliance is decreased. Dynamic pulmonary compliance is the gradient of the curve, i.e.,  $dV/dP_{tp}$ . The lower inflection point (LIP) and the upper inflection point (UIP) are thought to indicate average recruitment and over-distension of the alveoli respectively (although, these are not strictly mathematical inflection points of the curve). Mechanical ventilation is thought to be injurious if it operates outside of the global optimal pulmonary compliance range, as measured by the LIP and the UIP (Moloney & Griffiths, 2004).

Slightly different pressure-volume curves exist for both the inspiratory and expiratory components of the breath cycle, even in healthy lungs (as shown by the dashed curve in Figure 2.7), whereby the difference in the inspiratory and expiratory curves, i.e., hysteresis, is due to the higher surface tension for the expiratory component, thus enabling lung recoil. This hysteresis can also be understood as the dissipation of energy when the surfactant molecules are pulled apart during expiration, enabling the surface tension to increase, aiding in lung recoil for expiration (Bachofen, 1968; Suki & Bates, 2011). There is an increase in hysteresis for ARDS patients, as shown in the solid curve in Figure 2.7, attributed to the disruption of surfactant in ARDS (Seeger *et al.*, 1993; Spadaro *et al.*, 2019).

Since ARDS manifests as a lung parenchymal problem, lung tissue (pulmonary) compliance is of most interest in ARDS for monitoring lung function (Hess, 2014). Clinically, the lower inflection point (LIP) on the pressure-volume curve is the point

where the slope begins to increase, as is shown in Figure 2.7. This is interpreted as the pressure value at which collapsed alveoli are re-opened and the forces of surface tension, which are often higher in the ARDS lung, are overcome. Similarly, the upper inflection point (UIP) on the pressure-volume curve indicates the (average) pressure at which alveoli can become over-distended; increasing pressure from here onwards results in little (or no) change in volume and indicates that the lung has reached a maximum volume limit, beyond which volutrauma may occur. This implies that safe ventilation of the lung occurs between the LIP and the UIP, indicating that the PEEP and the peak inspiratory pressure (or tidal volume in volume-controlled ventilation) can be safely set at these limits. Of note, the 'LIP' and the 'UIP' do not technically fulfill the mathematical definition of an inflection point.

Studies in animal models, using both X-ray computed tomography as well as biological indications of lung injury, have shown correlations between the inflection points and injury. However, these are global measures of the average critical pressures for recruitment and over-distension (Amini *et al.*, 2017; Terragni *et al.*, 2003). Therefore, due to the heterogeneity of ventilation and injury in ARDS, *local* LIPs and UIPs will be distributed throughout the lung, whereby injurious thresholds may be reached locally before the global inflection points on the pressure-volume curve (Harris, 2005; Hubmayr, 2002). Regional variability in inflection points was shown in a recent clinical study in ARDS patients using electrical impedance tomography to measure local lung volumes and plot regional pressure-volume curves (Scaramuzzo *et al.*, 2019).

### 2.7.5 End-inspiratory lung volume: tidal volume plus PEEP

The addition of some PEEP has long shown to be beneficial for reducing lung injury in mechanical ventilation in ARDS by keeping alveoli from collapsing at end-expiration (Webb & Tierney, 1974). However, the addition of PEEP must be used with caution, since it is the total end-inspiratory lung volume, or total lung stretch, that leads to volutrauma. Limiting the PEEP in combination with tidal volume was shown to prevent VILI in early studies on animals (Dreyfuss & Saumon, 1993). This understanding is reflected in current clinical guidelines, whereby PEEP is limited in

combination with a maximum tidal volume, based on population values from clinical trial data (Brower *et al.*, 2004). Subsequent studies by Vieira *et al.* (1999) used clinical CT imaging to assess the distribution of lung aeration in ARDS patients and found that increasing PEEP whilst keeping the tidal volume constant may result in over-distension rather than alveolar recruitment. This was shown specifically in patients where a lower inflection point is not present on the pressure-volume curve, indicating that the increase in volume is due to the healthy areas being over-inflated rather than more alveoli being recruited. In a study on mouse models of one-hit VILI, Seah *et al.* (2011) hypothesised that a "Vt-PEEP plane" exists in which the lungs can be safely ventilated without generating VILI. This is shown in Figure 2.8 which demonstrates the hypothesis that as VILI develops, the boundaries of the plane reduce, as shown by the dashed boundary, whereby both tidal volume (Vt) and PEEP should be adjusted in order to maintain protective (safe) ventilation. The solid boundary in the figure indicates the boundaries of safe ventilation; within it lie the ventilator settings for the mice ventilated with high Vt and some PEEP (filled square), the mice ventilated with zero PEEP and normal Vt (open circle), but not the high Vt *plus* zero PEEP group (filled circle), indicating the importance of adequately adjusting both PEEP and tidal volume for safe ventilation.

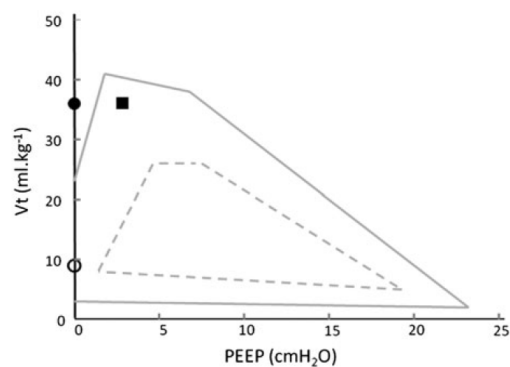


FIGURE 2.8: The "tidal volume (Vt) - PEEP plane" from a study by Seah *et al.* (2011), whereby protective (safe) ventilation occurs within the solid boundary. In this study, the filled circle represents the ventilator settings at which the high Vt/zero PEEP group of mice were ventilated, the open circle represents the zero PEEP group, and the filled square represents the settings for the high tidal volume group. It is hypothesised that as VILI develops, the boundaries of the plane reduce, as shown by the dashed boundary.

A more recent study by Protti *et al.* (2015) on pigs ventilated with different combinations of tidal volume and PEEP, shown in Figure 2.9, found that if the combination (i.e., total lung stretch) exceeded the lower limit of inspiratory capacity (a baseline measure of the whole lung from CT imaging), then VILI occurred, as defined by lung oedema. In this one-hit VILI model, the addition of PEEP was shown to be beneficial, but only if combined with a low tidal volume.

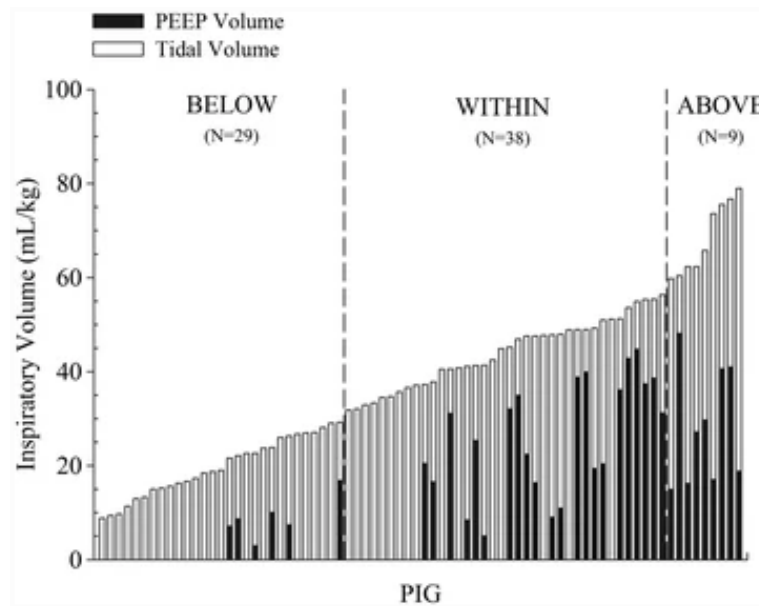


FIGURE 2.9: The combinations of tidal volume and PEEP in ventilated pigs from the study by Protti *et al.* (2015). The inspiratory volumes labelled "below", "within" and "above" are in reference to the normal (safe) inspiratory volume range.

More recent studies have quantified the regional distribution of ventilation with imaging under various combinations of PEEP and tidal volume in animal models of ARDS and VILI (Cereda *et al.*, 2017; Paula *et al.*, 2016; Wellman *et al.*, 2014; Xin *et al.*, 2018). These studies corroborate the heterogeneous distribution of ventilation using regional data from imaging (CT, PET). These important insights led to the understanding that although PEEP is beneficial, too much PEEP in combination with a safe tidal volume can nevertheless lead to regional over-distension and injury, which is amplified in ARDS. Indeed, it has been remarked that any additional PEEP that is ineffective in recruitment should be avoided. Furthermore, in order to reduce the risk of volutrauma, in certain cases, a closed lung approach with permissible atelectasis may be safer, i.e., leaving injured areas of the lung closed until they heal (Pelosi

*et al.*, 2018; Vieira *et al.*, 1999).

### 2.7.6 Additional considerations for safe mechanical ventilation

Novel approaches continue to be postulated for safe mechanical ventilation in ARDS, some of which are outlined below, but not directly relevant to this thesis:

- limiting the driving pressure:  $P_{plateau} - PEEP$  (Amato *et al.*, 2015)
- mechanical power: a unifying equation taking into account both the ventilator settings and global lung mechanics as variables (Gattinoni *et al.*, 2016)
- ergotrauma: the amount of energy dissipation across the lung tissues (Marini, 2018)
- time-controlled adaptive ventilation: suggests that a pause at end-inspiration may be better for recruitment than increasing PEEP (Nieman *et al.*, 2018)
- limiting the stress index from the pressure-time curve (Henderson *et al.*, 2017)
- high frequency oscillation ventilation in mild ARDS: allowing smaller tidal volumes with a higher respiratory rate (Herrmann *et al.*, 2020)
- open versus closed lung approaches: permissible atelectasis (Pelosi *et al.*, 2018)
- improving patient-ventilator synchrony (Yoshida *et al.*, 2012)
- patient prone positioning (Johnson *et al.*, 2017; Pelosi *et al.*, 1998; Scholten *et al.*, 2017; Xin *et al.*, 2018)

This section has outlined a number of approaches for determining whether mechanical ventilation is safe and not causing further damage to the lungs, i.e., not causing ventilator-induced lung injury. Lung volumes give key insights into the spatial distribution and the changes in the lung mechanics, as a surrogate for pulmonary compliance, and in the absence of being able to measure the spatial distribution of transpulmonary pressures. Therefore, the main focus of this thesis (Chapter 4) is on quantifying the volume of air in the lung under various ventilator settings. Measurement of the volume of air in the lungs at end-inspiration and end-expiration is used to gauge whether volutrauma (over-distension) and / or atelectasis (collapse)

is occurring during mechanical ventilation. Furthermore, the *distribution* of the air in the lungs is critical to understanding whether interventions, such as titrating levels of PEEP and patient prone positioning, are effective in improving ventilation and mitigating VILI. *In vivo* imaging studies have been pivotal in elucidating this current understanding.

In addition, safe mechanical ventilation also applies to the structures (airways and blood vessels) in the lung, ensuring that they are not damaged or incur adverse functional changes during mechanical ventilation. This will be discussed in the next section.

## 2.8 Airways and the pulmonary vasculature in ARDS and VILI

Previous studies have shown that mechanical ventilation can adversely affect the airways and the pulmonary blood vessels structurally and have functional consequences, such as for dead space ventilation (Nickles *et al.*, 2014), gas trapping (Jain & Sznajder, 2007), distal airway closure (Chen *et al.*, 2018), and on haemodynamics and cardiac output (Broccard *et al.*, 1998; Hamlington *et al.*, 2018).

Dead space is the volume of air in the lung that does not participate in gas exchange. It has two components: anatomic dead space; the volume of air in the conducting airways, and physiologic (or alveolar) dead space; the volume of air in the alveoli (West, 2012). Positive-pressure mechanical ventilation has been shown to distend the airways and contribute to an increase in anatomic dead space in mice (Nickles *et al.*, 2014). Furthermore, it has been postulated that mechanical ventilation distends the airways such that increased circumferential strain may lead to injury if wall tension exceeds safe limits (Sinclair *et al.*, 2007). In contrast, mechanical ventilation at low volumes, i.e., one-hit VILI, may damage peripheral airways and thus contribute to an increase in airway resistance, as demonstrated in animal studies (Broseghini *et al.*, 1988; D'Angelo *et al.*, 2002; Lu & Rouby, 2000). Similarly, distal airway dysfunction is thought to be partially responsible for increased gas trapping during mechanical ventilation, as shown in studies with clinical CT imaging (Jain & Sznajder, 2007).

The ability to measure the pulmonary vasculature relates directly to ventilation and perfusion which has implications for hypoxia in ARDS (Pesenti *et al.*, 2016; Terragni *et al.*, 2003). Moderate hypertension has been found in patients with ARDS and animal studies show that mechanical ventilation can cause altered haemodynamics, affecting right ventricular afterload and venous return (Vieillard-Baron *et al.*, 2016). The pulmonary vasculature can respond to local hypoxia by constricting small arterioles to reduce perfusion, known as hypoxic pulmonary vasoconstriction (HPV), in order to maintain adequate oxygenation for ventilation-perfusion matching (Naeije & Brimiouille, 2001). The protective function of HPV may be disrupted in ARDS patients, however the exact mechanisms are yet unknown (Sylvester *et al.*, 2012). In the context of a two-hit VILI model with ARDS, it has been shown that knock-out mice with Nlrp3- and Casp1-deficiency are protected from hypoxaemia, indicating a protective dynamic vascular response (Jones *et al.*, 2014).

Studies to date have shown that positive-pressure mechanical ventilation can affect the structure of the airways and the pulmonary blood vessels, which may adversely affect lung mechanics and lead to worsening hypoxia (Broccard *et al.*, 1998; Chen *et al.*, 2018; Hamlington *et al.*, 2018; Jain & Sznajder, 2007; Nickles *et al.*, 2014).

A better understanding of the effect of mechanical ventilation requires both clinical and experimental approaches. Clinical approaches have the advantage of analysing data with human anatomy, physiology and the complexities of the clinic. The drawback is that it is difficult to isolate variables and to control external factors. Furthermore, conservative approaches need to be taken, since no additional harm to patients can ensue from interventions in clinical trials. This is where experimental studies on laboratory animals can push the boundaries, especially at the extremes of ventilation parameters such as very low or very high pressures or volumes, to deliberately investigate the mechanisms leading to volutrauma and atelectrauma.

## 2.9 Mouse models of ARDS and VILI

Animal models provide the ability to study the lungs *in vivo* in an intact organism, allowing for investigation of the systemic effects of ARDS and VILI, such as multiple-organ failure. Potentially injurious ventilation protocols with specific combinations

of PIP and PEEP enable precise questions about the mechanisms of volutrauma and atelectrauma in VILI to be investigated. Furthermore, reductionist animal models can be studied with knock-out variants and novel interventions.

Animal studies of VILI and ARDS include small animals, such as mice, rats and rabbits, as well as bigger animals, such as pigs and sheep (Cannizzaro *et al.*, 2011; Frank *et al.*, 2008; Paula *et al.*, 2016; Wellman *et al.*, 2014; Xia *et al.*, 2011). The advantages of using mice in lung research is their similarity to human physiology, the ease of upscaling numbers for statistical power, the ability to manipulate their DNA to produce transgenic animals, or for testing novel therapeutics *in vivo* (Nichane *et al.*, 2017).

Since mice are not mini humans, the aim of experiments with animals is to model the salient characteristics of lung injury in humans. Whilst human data on ARDS and VILI is collected from patients in the clinic, it is often difficult to isolate variables and conditions - an advantage that animal models have. Furthermore, in ARDS patients, it is difficult to clearly separate the contribution of prior lung injury to that caused by the ventilator, whereas in animal models, the effects of the ventilator can be isolated in experiments (Pinhu *et al.*, 2003). Animal models provide the opportunity to test a clinical hypothesis with scientific rigour (Uhlig & Kuebler, 2018).

A comprehensive review by Matute-Bello *et al.* (2008) classified various animal models of ARDS and acknowledged the relevance of a synergistic model of mechanical ventilation (two-hit VILI) as having direct impact in clinical practice, which is the focus of the studies conducted in this thesis. A subsequent consensus definition resulted in the American Thoracic Society (ATS) workshop report (Matute-Bello *et al.*, 2011), which acknowledged that absence of one or more clinical criteria in an animal model does not render established models invalid, acknowledging the practical limitations of fulfilling all the clinical definitions in animal models. The report outlined three established models of lung injury in animals: ventilator-induced lung injury (VILI), endotoxin-induced lung injury (indirect, extrapulmonary ARDS), and lung injury by live bacteria (direct, pulmonary ARDS). The latter two models are often used in combination with mechanical ventilation, i.e., as two-hit VILI, for clinical relevance. As the ATS workshop report points out, animal models are generally required to be reductionist in order to study a specific phenomenon, and therefore

the chosen mouse model may not replicate a clinical scenario of ARDS with all the complexities of the intensive care unit, such as volume support to prevent cardiovascular failure, or hyperoxia from increased oxygen levels. This may explain in part why, despite many positive outcomes in animal models, translation to the clinic has been elusive (Uhlig & Kuebler, 2018).

Table 2.1 summarises the main parameters for injurious and protective mechanical ventilation in mouse models (Cannizzaro *et al.*, 2011; Jones *et al.*, 2014; Kim *et al.*, 2017; Lex & Uhlig, 2017; Lovric *et al.*, 2018). Depending on the mode of ventilation, either a set peak inspiratory pressure (PIP) or a set tidal volume  $V_T$  is delivered. For pressure-controlled ventilation, a set PIP is delivered. For volume-controlled ventilation, a set  $V_T$  is delivered. The positive end-expiratory pressure (PEEP) can be set in either mode. The duration of ventilation for animal models of VILI varies between 2 - 5 hours on the ventilator for most studies in mice, although ventilation of up to 7 hours has been achieved on mice (Lex & Uhlig, 2017). The respiratory rate is adjusted according to the tidal volume, in order to keep to a required minute volume, depending on the model used.

The mouse models investigated in this thesis are either one-hit VILI or two-hit VILI, whereby the mechanical ventilation is either injurious or protective, as per Table 2.1 (Allen *et al.*, 2006; Cannizzaro *et al.*, 2011; Reiss *et al.*, 2011; Wolthuis *et al.*, 2009; Zosky *et al.*, 2009). Epidemiological data from studies into ARDS shows that mortality is highest in patients with sepsis, pneumonia or aspiration as the initial insult, which supports the rationale for investigating a mouse model of direct ARDS (pneumonia) in Chapter 5 and a mouse model of indirect ARDS (sepsis) in Chapter 4 (Bellani *et al.*, 2016; Rubenfeld & Herridge, 2007).

TABLE 2.1: Guideline values for ventilation parameters in mouse models of VILI: peak inspiratory pressure (PIP), positive end-expiratory pressure (PEEP), and tidal volume ( $V_T$ ).

VILI model	PIP (H <sub>2</sub> O)	PEEP (H <sub>2</sub> O)	$V_T$ (mL/kg)
injurious	20 - 30	0	15 - 24
protective	12 - 16	1 - 4	7 - 12

### 2.9.1 Measurement of lung function in mice

For mouse models of VILI and ARDS, the lung function parameters that are of most interest are lung volume and tissue compliance. Compliance (inverse of elastance) can be measured *in vivo* in mice with the forced oscillation technique (FOT), either with a wave-tube technique (Cannizzaro *et al.*, 2011; Zosky *et al.*, 2008), or with specialised animal ventilators that provide flow and pressure-volume data for lung mechanics (Schuessler & Bates, 1995). Animal plethysmographs can also be used to measure lung volumes, where the thoracic gas volume is used as an estimate of the functional residual capacity or end-expiratory lung volume (Janosi *et al.*, 2006). The lung clearance index from multiple breath washout (MBW) techniques can be used in mice to determine heterogeneity of ventilation (Dharmakumara *et al.*, 2014). Whilst these techniques were adapted from human lung function tests and are designed to be used *in vivo*, accuracy of the measurements can be challenging in mice due to their small size (Bates & Irvin, 2003; Irvin & Bates, 2003). Furthermore, these techniques provide global data on lung function, and cannot provide information on the regional distribution of the volume of air in the lung.

### 2.9.2 Measurement of the lung structures in mice

Measurements of the airways and blood vessels in mice can be determined from post-mortem whole resin casts, histological slices, or with precision-cut lung slice techniques *in vitro* for dynamic measurements (Faffe *et al.*, 2002; Faight *et al.*, 2017; Donovan *et al.*, 2015). These techniques are primarily used for determining gross anatomy and re-modelling, or for measurement of localised responses to a specific intervention or treatment. These techniques cannot be performed *in vivo* in intact animals. Imaging techniques are required to provide regional, whole organism, *in vivo* information on morphology and to capture insights into dynamic changes in small animals (Badea *et al.*, 2012; Nickles *et al.*, 2014).

Whilst techniques such as FOT, MBW and pressure-volume loops continue to be of widespread use in the clinic, their suitability in mice for experimental studies in VILI and ARDS is limited to global values of lung function. In order to gain a detailed spatial map of how mechanical ventilation affects the lungs in mouse models

of VILI, it is vital to capture the regional distribution of air in the lungs. This is where *in vivo* X-ray imaging techniques in mice and small animals have the advantage of providing high resolution, regional measurements that are non-invasive. These will be discussed in the next section.

## 2.10 *In vivo* X-ray imaging of mice for ARDS and VILI

Key breakthroughs in understanding ARDS and VILI have come from clinical computed tomography imaging (Gattinoni *et al.*, 2001). Early two-dimensional chest radiographs gave limited regional information. However, the advent of CT enabled three-dimensional information to be reconstructed from a series of two-dimensional chest radiograph projections. Clinical CT scans provided *in vivo* cross-sections of the lung and showed for the first time *in vivo* that ARDS and VILI manifests as a patchy, regionally distributed lung injury (Maunder *et al.*, 1986). This section explores the requirements of CT imaging for mouse models of ARDS and VILI, including spatial and temporal resolution for dynamic imaging, on both a synchrotron source and with laboratory imaging.

### 2.10.1 CT imaging for VILI and ARDS

Whilst computed tomography (CT) has been a long-standing clinical and research tool for whole-lung imaging, other modalities have emerged alongside, such as positron emission tomography (PET), magnetic resonance imaging (MRI), and electrical impedance tomography (EIT) (Pesenti *et al.*, 2016; Robertson & Buxton, 2012). These modalities continue to play important roles for functional lung imaging in the clinic, for both research and diagnostic purposes (Wongviriyawong *et al.*, 2013), however, for experimental studies, these modalities are mainly used on larger animals, such as pigs and sheep, since they have limited spatial resolution (Wellman *et al.*, 2014; Vidal Melo *et al.*, 2003). CT imaging has excellent contrast, high spatial resolution and signal-to-noise ratio, which are important criteria for high quality imaging of the biological structures in small animals Dubsy *et al.* (2010) and Fouras *et al.* (2009). The volume of air in the lungs from CT images is measured from the CT density of the

voxels by converting the greyscale intensity values to Hounsfield Units (HU) (Kalendar, 2011). As described in Section 2.6.4, the regional distribution of air throughout the lung in ARDS and VILI is used as a measure of ventilation heterogeneity and regional lung function (Bayat *et al.*, 2015). Since the lungs are constantly moving, breath-hold techniques are required for static imaging, where movement is restricted for the duration of image acquisition to avoid image blur. Two static CT images along the breath cycle can give dynamic information; for example, a common method for determining the whole lung tidal volume is calculated by subtracting the volume of air in the end-expiratory image from the end-inspiratory image. Furthermore, this information can be used to measure regional volumetric strain, defined as change in volume divided by initial volume, i.e., tidal volume divided by functional residual capacity (or end-expiratory lung volume), as described by Fuld *et al.* (2008). For regional tidal volumes, the region of interest in the two images must be co-registered and aligned for accurate comparison (Yin *et al.*, 2009). A recent study on VILI with various tidal volume and PEEP combinations used CT breath-hold techniques with co-registration of eight regions of equal tissue volume along the ventral-dorsal axis in pigs (Paula *et al.*, 2016). This study found that local strain limits correlating with injury were reached, despite global measurements remaining below the injury threshold. Another study of a two-hit VILI model in rats with acid aspiration used paired static breath-hold CT images to map the end-inspiratory and end-expiratory volume of air for each voxel across the whole lung Cereda *et al.* (2017). They found that animals that had large differences in regional end-inspiratory and end-expiratory volume of air at the onset of ventilation corresponded with worsening injury, as measured by survival statistics after one and two hours of mechanical ventilation. Depending on the image acquisition time, breath-hold techniques may allow a redistribution of air, or result in regional recruitment or de-recruitment Paula *et al.*, 2016. Since measurement of the regional distribution of air is a central question for many studies in ARDS and VILI, dynamic CT imaging can be used to overcome this.

### 2.10.2 Dynamic CT imaging

*In vivo* four-dimensional computed tomography (4DCT) requires the image acquisition to be gated to either the breathing cycle (with a ventilator) for lung imaging, or

to the heartbeat for cardiac imaging (Dubsky *et al.*, 2017). 4DCT results in a series of phase-binned CT images throughout the cycle (Herrmann *et al.*, 2017; Herrmann *et al.*, 2020). For lung imaging, it offers the advantage of no breath-hold, avoiding the possibility of a re-distribution of gases in the lungs during a respiratory pause. 4DCT is mostly used as an experimental technique, due to the relatively high dose of radiation imparted to the subject. Consideration of the radiation dose for pre-clinical imaging depends on the question being asked and whether the study is terminal or longitudinal (Vande Velde *et al.*, 2015). 4DCT in the clinic is mostly reserved for the purposes of radiotherapy planning for lung tumor treatment, due to the high radiation dose (Yamamoto *et al.*, 2009). Dubsky *et al.* (2012) developed a four-dimensional X-ray velocimetry (4DXV) method to enable dynamic information in the lung to be captured throughout the breath cycle from 4DCT images. 4DXV is derived from particle image velocimetry (PIV), which is a well-established technique in the field of fluid dynamics and is based on obtaining an optical measurement of displacement from patterns of tracer particles or speckle (Adrian, 2005). In the case of 4DCT combined with PIV, the speckle patterns in the lung are used in place of seeding tracer particles to track the lung motion for specified interrogation windows. Displacement vectors in three dimensions are determined statistically with the use of cross-correlation functions to obtain the displacement field. This method can be applied to high-resolution CT images, where there is sufficient speckle structure, i.e., air-tissue contrast (Dubsky *et al.*, 2012). Furthermore, the tissue expansion values can be directly obtained from the displacement field on a region-by-region basis, thus mapping regional tidal volume across the entire lung. With 4DXV, image registration of CT image pairs is not required for measurements of the regional tidal volumes. For mice, their small size and fast respiratory rate requires both high resolution and high speed imaging for successful dynamic imaging. Synchrotron facilities with small animal imaging capabilities, as well as specialised laboratory imaging facilities, are designed for this purpose.

### 2.10.3 Synchrotron imaging

Synchrotron imaging facilities provide a high brightness, coherent light source that can be specifically adjusted for the imaging of biological tissues and configured for

phase contrast X-ray imaging (Murrie *et al.*, 2015). Phase contrast X-ray imaging is an improvement on conventional X-ray imaging, whereby refraction and wave interference is exploited to provide edge-enhancing effects to greatly improve image contrast, especially at air-tissue boundaries, which is especially applicable to imaging of the lungs and soft tissue (Kitchen *et al.*, 2008; Stampanoni *et al.*, 2011). Furthermore, the high photon flux of the synchrotron beam allows for reduced exposure time, allowing for high speed dynamic imaging with a fast detector. This was demonstrated in a study of ventilated mice using X-ray velocimetry with phase contrast images, whereby the lung motion over the breath cycle captured alterations in regional motion in mice with bleomycin-induced lung disease before global changes in lung function were detected (Fouras *et al.*, 2012). Extension of this technique to three-dimensional CT imaging resulted in the 4DXV technique, which was validated with synchrotron imaging on mice and rabbit pups, demonstrating the capability of this new technique to capture regional lung function, such as tidal volumes, regional flow through the airway tree, and the regional time constant (Dubsky *et al.*, 2012). Additional recent studies on ventilated mice using synchrotron 4DXV imaging include tracking the airways in response to methacholine in asthma models (Dubsky *et al.*, 2017), and cardiac gating to measure cardiogenic airflow in the lungs (Dubsky *et al.*, 2018). In addition to whole organism imaging, recent synchrotron microscopy studies with CT imaging of individual alveoli with breath-hold techniques in rats and mice demonstrate the heterogeneous inflation patterns at the alveolar level during mechanical ventilation (Lovric *et al.*, 2017a; Lovric *et al.*, 2017b). Imaging with synchrotron X-rays is expensive and these large-scale facilities are not always in proximity to the home institution, therefore, there remains considerable interest in translating *in vivo* imaging techniques to laboratory X-ray systems.

#### **2.10.4 Laboratory imaging**

Early optimisation of compact laboratory-based imaging included a cone-beam X-ray source and propagation-based phase contrast X-ray imaging with conventional polychromatic X-ray sources (Feldkamp *et al.*, 1984; Ng *et al.*, 2012; Ritman, 2005;

Wilkins *et al.*, 1996). However, for dynamic *in vivo* imaging of small animals, compact laboratory facilities must provide both high spatial resolution and high temporal resolution. This can be achieved with a high powered, micro-focus X-ray source, at energies suitable for the imaging of biological tissues (Larsson *et al.*, 2011), coupled with a high speed detector and geometric magnification. Ideally, the facility is located adjacent to animal housing, including animal surgery and tissue laboratory facilities.

The pre-clinical X-ray facility in the New Horizons biomedical engineering research facility at Monash University is designed for this purpose. Comprising a state-of-the-art liquid-metal jet X-ray source (Excillum D2+, Excillum AB, Kista, Sweden) and an efficient flat-panel detector (PaxScan 2020, Varian Medical Systems, Palo Alto, CA, USA), it is specifically designed for high-resolution and high-speed *in vivo* imaging of mouse lungs. Pre-commissioning simulation studies of this system investigated imaging speeds for X-ray velocimetry suited to the respiratory rates of mice, balancing exposure times long enough to minimise image noise, yet short enough to minimise motion blur (Murrie *et al.*, 2016). The results in Chapter 3 of this thesis build upon these preliminary simulations by testing the operational configurations for *in vivo* 4DCT lung imaging of mice.

Similar X-ray laboratories around the world produce high quality, high resolution tomographic lung imaging of detailed biological structures, such as of individual alveoli in mice and small animals (Larsson *et al.*, 2016). However, these are mostly either static breath-hold *in vivo* images (Brooks *et al.*, 2019), or post-mortem techniques at longer exposure times with the aim of capturing the fine structures in the samples (Romell *et al.*, 2019). The Munich Compact Light Source is a laboratory-based, high brightness X-ray source, aiming to provide an imaging capability similar to a synchrotron light source, but with the accessibility and lower cost of conventional X-ray sources (Gradl *et al.*, 2018).

Whilst compact imaging systems are currently a research tool, a long-term focus is to translate this technology to the clinic for improved imaging quality of biological soft tissues for diagnostic purposes (Stampanoni *et al.*, 2011; Tapfer *et al.*, 2012).

### 2.10.5 Contrast in X-ray CT imaging

Measurement of biological structures requires a sharp edge with minimal blurring in order to obtain accurate measurements of diameters, cross-sectional areas or the volumes of interest in the images. Good contrast is also required for qualitative assessment of structural patterns in the lung; accurately identifying a known pattern is directly linked to diagnoses, such as ARDS, fungal infections or tumors, and may directly inform patient treatment options. In addition, the success of automating pattern recognition with machine learning currently relies on high quality images with good contrast (Brooks *et al.*, 2019; Gerard *et al.*, 2020; Sluimer *et al.*, 2005). Laboratory and clinical X-ray sources are polychromatic and lower in coherence and brightness than synchrotron X-rays. Therefore, they are limited in the level of phase contrast that can be achieved. Often, other contrast-enhancing techniques are required, such as the administration of contrast agents (Badea *et al.*, 2012). In mice, the resolution and contrast required for imaging of the airways depends on the research question: for asthma studies, the internal diameter (lumen) of the airways as well as the wall thickness are of interest for determining the response to either short-term or long-term stimuli and for testing the efficacy of novel bronchodilators (Dubsky *et al.*, 2017; Lam *et al.*, 2018). Much higher resolution combined with phase contrast, however, is required for the imaging of the mucosal airway liquid layer in mouse models of cystic fibrosis, and therefore these studies usually require a synchrotron light source (Parsons *et al.*, 2008). In order to enhance the contrast between the airways and the lung tissue, images are ideally taken at end-expiration and additional post-processing may be required for segmenting the airways from the image. *In vivo* imaging of the pulmonary blood vessels from CT images usually requires the administration of a radio-opaque contrast agent in order to segment these from the lung tissue in the images. Whilst this vastly improves the contrast, the administration of substances during imaging is not a trivial undertaking in a small animal, such as a mouse, especially for dynamic CT imaging (Badea *et al.*, 2012; Kuebler, 2011; Sonobe *et al.*, 2011). Furthermore, the administration of intravenous contrast substances is invasive, potentially toxic, and may influence the experimental results or require additional control animals. In order to overcome these challenges, Samarage *et al.*

(2016) developed a contrast-free post-processing technique, with *in vivo* images from a laboratory X-ray scanner, based on calibrating the measurements from iodine contrast images against contrast-free images. Chapter 5 builds on this work and demonstrates successful application of this technique to 4DCT images of live mice. Other approaches for distinguishing the components in the lung beyond the two categories of air-like and water-like substances, for example, the distinction between air, blood and tissue volumes can give functional information regarding the cardiopulmonary effects of mechanical ventilation (Badea *et al.*, 2012; Porra *et al.*, 2017). This can be achieved with the administration of contrast agents combined with dual-energy CT imaging on synchrotron facilities or in customised laboratory systems with dual X-ray tubes, although new technology for commercial spectral X-ray imaging is also emerging (Badea *et al.*, 2008; Panta *et al.*, 2018).

Ultimately, the choice of imaging modality depends on the research questions and the study design. For mouse models of VILI and ARDS, CT is ideally suited for high resolution images of ventilation distribution and the high flux and short exposure times required for dynamic imaging. X-ray is an ubiquitous medical imaging modality, both as static chest X-ray imaging, static CT (including contrast-based CT angiography), and, less commonly, as dynamic 4DCT. Current contrast-based clinical CT angiography can cause contrast medium-induced nephropathy, especially in vulnerable patients with impaired kidney function, therefore, translation of contrast-free CT angiography to the clinic would be an invaluable diagnostic tool. It is logical to develop experimental techniques on an X-ray CT platform, in order to enable translation to commercial pre-clinical scanners and to the clinic. However, when considering translation of this technique to the clinic, radiation dose becomes paramount. A simple chest X-ray delivers the lowest radiation dose to the patient, whereas there is a marked increase in radiation for a static thoracic CT, with 4DCT giving the highest dose and is therefore mostly reserved for lung tumor treatment planning. Whilst implementation of dynamic CT as a routine diagnostic tool for ARDS and VILI may not be on the near-term horizon due to radiation dose, it nevertheless remains an important tool for fundamental investigations using animal models. A compact system capable of high quality CT imaging of small animals enables proof-of-concept or longitudinal experiments to be conducted within an accessible

facility with the required laboratory infrastructure nearby.

## 2.11 Summary

A review of the current literature in ARDS and VILI demonstrates that there is an incomplete understanding of how the ventilation parameters link to the regional distribution of air in the lung (Beitler *et al.*, 2016; Gattinoni *et al.*, 2017; Henderson *et al.*, 2017). A review of the studies to date shows that both over-distension of the alveoli (volutrauma) and derecruitment of the alveoli (atelectrauma) are understood to be the main mechanisms of VILI in ARDS (Fan *et al.*, 2017; Slutsky & Ranieri, 2013). In addition, pre-existing, patchy lung injury in ARDS results in greater ventilation inhomogeneity during mechanical ventilation, increasing the likelihood of tissue injury from volutrauma and atelectrauma (Caironi *et al.*, 2010).

A better understanding of how the ventilator settings relate to the regional distribution of volutrauma and atelectrauma would enable adjustments to be made to the ventilation protocol in order to provide safe mechanical ventilation. *In vivo* X-ray CT imaging provides a static snapshot of the distribution of air in the lung and has been pivotal in advancing our understanding of ARDS in the clinic to date (Gattinoni *et al.*, 1987; Maunder *et al.*, 1986). However, in order to capture the functional changes associated with VILI, imaging at both high resolution and high speed is required (Dubsky *et al.*, 2012). A recently-developed dynamic 4DCT pre-clinical imaging technique is capable of this and provides a high resolution spatial map of the volume of air throughout the lung during mechanical ventilation (Preissner *et al.*, 2018b). Therefore, the overall aim of this research project is to use this state-of-the-art laboratory-based imaging system to obtain dynamic images of the mechanically-ventilated lung *in vivo* to investigate mouse models of VILI. The specific research aims are outlined in the next section.

## 2.12 Research Aims

The overall aim of this research project is to use a laboratory-based imaging system, with the unique capability of both high resolution and high speed *in vivo* imaging, to

obtain dynamic 4DCT images of the mechanically-ventilated lung, in order to investigate the mechanisms of volutrauma and atelectrauma from regional lung volumes, as well as to obtain quantitative measurements of the airways and the pulmonary vasculature in mouse models of VILI. The three specific aims of the research in this thesis are:

1. The first aim of the research presented in this thesis is to characterise the laboratory X-ray imaging system for resolution, speed and contrast - the parameters pertinent to high quality dynamic (4DCT) *in vivo* lung imaging.
2. The second aim is to obtain regional lung volumes (i.e., the tidal volume and the end-expiratory volume) from dynamic 4DCT images acquired with the laboratory system and to map these to regional biomarkers of lung tissue injury. The linking of lung volumes with biomarkers for the same lung regions is crucial for understanding the effects of mechanical ventilation on regional lung injury.
3. The third aim is to use dynamic 4DCT images from the laboratory system to measure the volume of air in the airways and the volume of the pulmonary vasculature in the mouse lung, in order to observe changes in these structures occurring as a result of mechanical ventilation.



## 3 Characterising the X-ray system for dynamic *in vivo* lung imaging

### 3.1 High resolution propagation-based imaging system for *in vivo* dynamic computed tomography of lungs in small animals

---

Preissner M., Murrie R. P., Pinar I., Werdiger F., Carnibella R. P., Zosky G. R., Fouras A. and Dubsky S.

Published in *Physics in Medicine and Biology*, 2018

---

The ability to obtain high quality four-dimensional computed tomographic (4DCT) images of mice or small animals *in vivo* in a readily-accessible laboratory environment enables pilot or longitudinal experiments to be conducted, which are often too costly for synchrotron imaging (Gradl *et al.*, 2018). This was the motivation behind the development of a customised laboratory X-ray imaging system employing a state-of-the-art micro-focus, liquid metal-jet X-ray source (Larsson *et al.*, 2011; Murrie *et al.*, 2016). The system was specifically designed for both high resolution and high speed lung imaging with short exposure times, which current commercially-available micro-CT systems were unable to provide.

The journal article in this chapter investigated the laboratory X-ray imaging system for resolution, speed and contrast - the parameters pertinent to high quality dynamic *in vivo* lung imaging, i.e., 4DCT imaging. Tests using phantoms demonstrated superior spatial resolution and image contrast for low density materials, such as the air-tissue contrast found in lungs. High quality *in vivo* 4DCT images of mechanically-ventilated mouse lungs provided proof-of-concept of the quality of the X-ray imaging system for live imaging studies. To our knowledge, these were the first 4DCT images obtained with a liquid-metal jet X-ray source. Furthermore, the quality factor devised by Kalender *et al.* (2005), based on resolution, radiation dose and noise,

was used to compare the performance of the system to other commercially-available pre-clinical systems. The laboratory system was found to have the highest quality factor, as well as the shortest CT scan time, indicating superior imaging quality combined with high speed imaging.

The results in the journal article for this chapter demonstrate the capability of a unique, laboratory-based imaging facility for studies of lung mechanics in mice. It demonstrates that this facility provides both high resolution and high speed imaging of mechanically ventilated mouse lungs. The results provide a foundation for the *in vivo* studies in Chapter 4 and Chapter 5. Furthermore, the system provides an *in vivo* tool available for respiratory research that was previously not possible in a laboratory set-up. This research tool enables lung function and structure of mouse models of other respiratory diseases to be investigated (Murrie *et al.*, 2020). The dynamic imaging that this system provides is especially important for studies of VILI and ARDS where it is critical that there is no pause in ventilation during imaging, thus avoiding the re-distribution of air that may occur with static, breath-hold CT imaging techniques (Motta-Ribeiro *et al.*, 2018; Paula *et al.*, 2016).

## OPEN ACCESS



## NOTE

RECEIVED  
3 January 2018REVISED  
15 March 2018ACCEPTED FOR PUBLICATION  
22 March 2018PUBLISHED  
20 April 2018

Original content from  
this work may be used  
under the terms of the  
[Creative Commons  
Attribution 3.0 licence](#).

Any further distribution  
of this work must  
maintain attribution  
to the author(s) and the  
title of the work, journal  
citation and DOI.



## High resolution propagation-based imaging system for *in vivo* dynamic computed tomography of lungs in small animals

M Preissner<sup>1</sup>, R P Murrie<sup>1</sup>, I Pinar<sup>1</sup>, F Werdiger<sup>1</sup>, R P Carnibella<sup>2</sup>, G R Zosky<sup>3</sup>, A Fouras<sup>3,4</sup> and S Dubsy<sup>1</sup><sup>1</sup> Department of Mechanical and Aerospace Engineering, Monash University, Melbourne, Victoria, Australia<sup>2</sup> 4Dx Limited, Melbourne, Victoria, Australia<sup>3</sup> School of Medicine, Faculty of Health, University of Tasmania, Hobart, Tasmania, Australia<sup>4</sup> Biomedical Imaging Research Institute, Cedars-Sinai Medical Center, Los Angeles, CA, United States of AmericaE-mail: [melissa.preissner@monash.edu](mailto:melissa.preissner@monash.edu) and [stephen.dubsy@monash.edu](mailto:stephen.dubsy@monash.edu)**Keywords:** 4DCT, *in vivo*, x-ray imaging, functional imaging, biological imaging, tomographySupplementary material for this article is available [online](#)

### Abstract

We have developed an x-ray imaging system for *in vivo* four-dimensional computed tomography (4DCT) of small animals for pre-clinical lung investigations. Our customized laboratory facility is capable of high resolution *in vivo* imaging at high frame rates. Characterization using phantoms demonstrate a spatial resolution of slightly below 50  $\mu\text{m}$  at imaging rates of 30 Hz, and the ability to quantify material density differences of at least 3%. We benchmark our system against existing small animal pre-clinical CT scanners using a quality factor that combines spatial resolution, image noise, dose and scan time. *In vivo* 4DCT images obtained on our system demonstrate resolution of important features such as blood vessels and small airways, of which the smallest discernible were measured as 55–60  $\mu\text{m}$  in cross section. Quantitative analysis of the images demonstrate regional differences in ventilation between injured and healthy lungs.

### 1. Introduction

Computed tomography is the most widely used clinical imaging technique for investigating lung diseases, owing to its ability to noninvasively resolve the structures within the lung in detail. Four dimensional computed tomography (4DCT) allows the lung structures to be imaged over the breathing cycle, and provides the opportunity for further analysis to calculate functional parameters such as specific ventilation (Brennan *et al* 2015). However, producing high-resolution *in vivo* computed tomography scans of lungs in the pre-clinical laboratory setting remains difficult. Until now, scanners and techniques have suffered from either relatively poor spatial resolution, or require scan times that are prohibitive for practical *in vivo* imaging.

Synchrotron facilities provide excellent imaging of the lungs in small animals, due to their high brilliance and coherence, providing air-tissue contrast through phase-contrast imaging (Kitchen *et al* 2004, Fouras *et al* 2009, 2012, Sera *et al* 2013). Due to the limited accessibility of synchrotron sources, laboratory pre-clinical imaging facilities that are capable of providing high quality imaging would open up new possibilities for studies that require pre-treatment, or for longitudinal studies that require repeated imaging over days or weeks (Krenkel *et al* 2016). Previous studies on *in vivo* CT imaging on a pre-clinical facility show excellent results for phase-contrast (dark-field) imaging in a laboratory setting, albeit with longer exposure times (i.e. 10s) (Tapfer *et al* 2012, Bech *et al* 2013).

Here we present the development and characterization of a laboratory x-ray system for dynamic *in vivo* imaging of lungs in small animals. Using a high-brightness liquid-metal-jet x-ray source, we have achieved propagation-based phase enhancement to produce high-resolution, four-dimensional computed tomography of mechanically ventilated mice, previously only achievable using synchrotron facilities (Stahr *et al* 2016, Dubsy *et al* 2017). Phase enhancement in the lung tissue acts to improve contrast at the air/tissue interfaces, rather than generating phase fringes (for retrieval). Using phantoms, we characterize the spatial resolution of our system, and demonstrate the contrast resolution for quantitative imaging of the lung.

Accepted quality standards and customized phantoms enable quality control and robust performance testing for clinical cone-beam computed tomography (DIN 2013, Steiding *et al* 2014). Currently, no such standards for pre-clinical (micro-CT) scanners exist. In order to address the issue of quality assurance in micro-CT, Kalender *et al* propose a method that tests a combination of dose, resolution, noise and scan time (Kalender *et al* 2005). To benchmark our system against current scanners, we adopt the quality factor, which amalgamates these important parameters into a single index for comparison between systems. Finally, we present *in vivo* 4DCT images of mouse lungs to demonstrate the quality of imaging that our system achieves for pre-clinical investigations.

## 2. Methods

### 2.1. X-ray imaging set-up

Figure 1 shows the laboratory set-up. The high-brightness x-ray source (Excillum D2 + , Excillum AB, Kista, Sweden) has a liquid-metal-jet anode (gallium alloy) which enables higher electron beam power (70 kVp, 250W) with a micro-focus spot of between 15 and 20  $\mu\text{m}$ . It has a polychromatic x-ray beam with characteristic x-ray peaks at 8 keV and 24 keV (Larsson *et al* 2011). A high-speed flat panel detector (PaxScan 2020, Varian Medical Systems, Palo Alto, CA, USA) is mounted at a distance of 3363 mm from the x-ray source. The geometric magnification ( $M$ ) is adjusted by translating the stage for the distances  $R_1$  and  $R_2$  (Zaber Technologies, Vancouver, Canada). The detector has a pixel size of  $194 \times 194 \mu\text{m}$  and is capable of achieving a frame rate of up to 30 Hz with an 18 ms exposure time.

The range of geometric magnification achievable with the current set-up of this system is 7.2–12.0, where  $M = (R_1 + R_2)/(R_1)$ . The corresponding range of field of view is between 16.1 and 27 mm. The effective pixel size of the projection images for this magnification range is between 16 and 27  $\mu\text{m}$ . Phase enhancement is achieved via a propagation distance and can be seen in the fringes of the projection image in figure 1(B). The phase enhancement can also be quantified with an effective object-image distance,  $z_{\text{eff}} = R_1 R_2 / (R_1 + R_2)$  (Wilkins *et al* 1996, Mayo *et al* 2002). Our set-up has  $z_{\text{eff}}$  values of between 257 mm and 402 mm, which is a practical compromise between exploiting the phase enhancement our system provides without compromising the flux required for dynamic imaging with short exposure times.

Table 1 shows the two main combinations of x-ray spot size, power and projections per CT used for dynamic lung imaging. The standard setting is based on a larger spot size, fewer projections and lower power (with a lower radiation dose), whereas the maximum setting has a smaller spot size and a higher power, resulting in better image quality (as defined by the quality factor described below), with a higher radiation dose as the trade-off.

### 2.2. Phantom imaging and dose measurement

Resolution testing was carried out with phantoms. The CT resolution was measured using a line pair phantom (Micro-CT bar pattern phantom, QRM GmbH, Möhrendorf, Germany). A customized 3D printed rod (FullCure720, Objet Eden260V, Stratasys Ltd) was used to test noise. The contrast resolution was tested with a low contrast phantom with three inserts (Micro-CT Low Contrast Phantom V2, QRM GmbH, Germany). The radiation dose rate was measured using a pencil beam dosimeter (TNT 12000WD wireless detector and 500–100 CT ion chamber, Fluke Biomedical, Washington, USA).

### 2.3. *In vivo* 4DCT imaging

The use of eight-week old BALB/c female mice for *in vivo* imaging was approved by the local Animal Ethics Committee of Monash University (Monash University Research Platform, Melbourne, VIC, Australia) and conducted in accordance with the guidelines set out in the Australian code of practice for the care and use of animals for scientific purposes. Mice were anaesthetized with an intraperitoneal injection of ketamine (Parnell Australia Pty Ltd, Alexandria NSW, Australia) and xylazine (Xylazil-20, Troy Laboratories Pty Ltd, Smithfield NSW, Australia), surgically intubated and placed upright in a custom sample mount with ventilator attachments, which is 3D printed and can therefore be made to the size and shape of the sample, e.g. mouse or small rat. Mice were ventilated at a peak inspiratory pressure of 20 cm H<sub>2</sub>O and zero positive end-expiratory pressure with an inspiratory-expiratory ratio of 1:1 (300 ms : 300 ms). The animal was placed on a ventilator (AccuVent, Notting Hill Devices, Melbourne, Australia) and secured on the rotating stage. Image acquisition was synchronized with the ventilator. Projection images were obtained over multiple breath cycles for a 360° rotation of the sample. The respiratory rate of the animal ( $RR$ , breaths per minute) determines the number of phases ( $n$ ) acquired in the 4DCT:  $n = 60f/RR$ , where  $f$  is the image acquisition rate (Hz). The rotational speed of the stage ( $\omega$ , degrees per second) is determined by the total number of projections required for the 4DCT:  $\omega = 360^\circ f/np$ , where  $p$  is the number of projections per phase, i.e. 400 projections for the standard setting or 800 projections for the maximum setting (table 1). The projections are allocated (binned) into discrete phases of the respiratory cycle. The binned projection images are then reconstructed using filtered back-projection based on the Feldkamp–

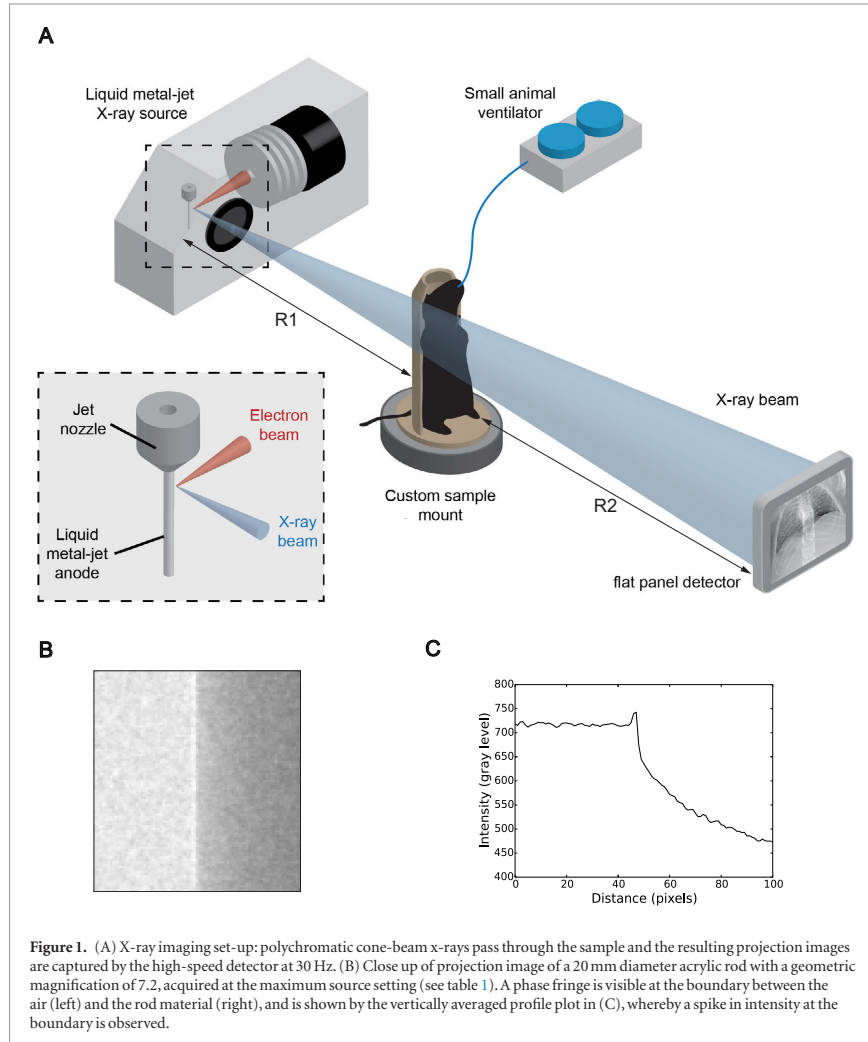


**Figure 1.** (A) X-ray imaging set-up: polychromatic cone-beam x-rays pass through the sample and the resulting projection images are captured by the high-speed detector at 30 Hz. (B) Close up of projection image of a 20 mm diameter acrylic rod with a geometric magnification of 7.2, acquired at the maximum source setting (see table 1). A phase fringe is visible at the boundary between the air (left) and the rod material (right), and is shown by the vertically averaged profile plot in (C), whereby a spike in intensity at the boundary is observed.

**Table 1.** X-ray imaging settings used for small animal lung imaging.

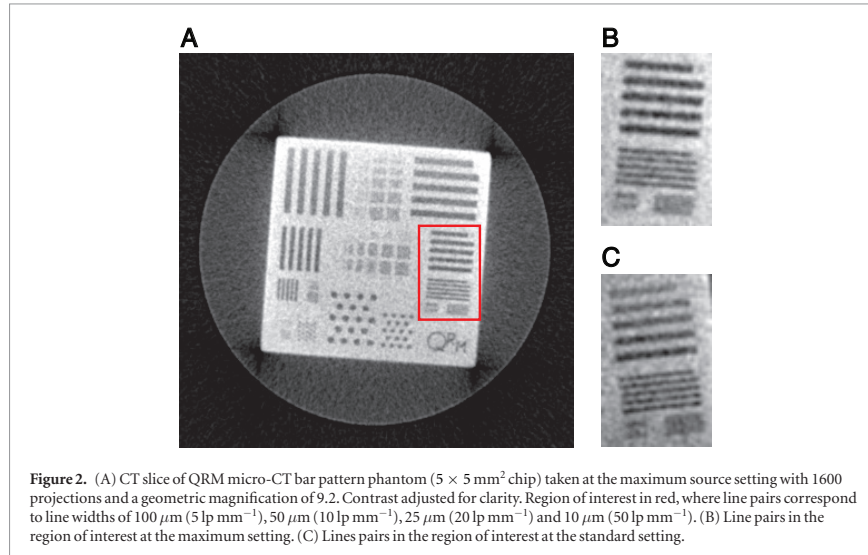
Setting	X-ray spot ( $\mu\text{m}$ )	Power (W)	Projections per CT	Scan time per CT (s)	Usage
Standard	20	200	400	16	Continuous usage
Maximum	15	250	400–800	16–32	Limited usage

Davis–Kress cone-beam CT reconstruction algorithm to obtain 3D cross-sectional images (Feldkamp *et al* 1984, Yang *et al* 2006).

### 3. Results and discussion

#### 3.1. CT resolution

The resolution for CT images was tested using a high precision bar pattern (line pair) phantom for micro-CT (QRM GmbH, Möhrendorf, Germany) at the standard and maximum settings (table 1). The images are shown in figure 2. Note that the corner artifacts are due to beam hardening. Based on visual inspection of the line pairs in the image, the spatial resolution lies between 10 line pairs per mm ( $1\text{p mm}^{-1}$ ), i.e.  $50\ \mu\text{m}$  line widths, where



the bars can be resolved, and  $20 \text{ lp mm}^{-1}$ , i.e.  $25 \mu\text{m}$  line widths, where the bars can no longer be resolved. For a more accurate measure of the spatial resolution, the modulation transfer function (MTF) of the system was calculated based on the standard definition by Boreman (2001). The 10% MTF was calculated as  $11 \text{ lp mm}^{-1}$  for the standard source setting and  $12 \text{ lp mm}^{-1}$  for the maximum source setting.

### 3.2. Radiation dose

Reducing the radiation dose received by the animal is important to avoid unwanted interference in experimental results or ill-effects from radiation, particularly in the case of longitudinal studies (Boone *et al* 2004, Vande Velde *et al* 2015). The dose rate was measured as  $5.01 \text{ mGy s}^{-1}$  air kerma using a pencil-beam dosimeter (TNT 12000WD wireless detector and 500–100 CT ion chamber, Fluke Biomedical, Washington, USA). The total dose for a CT obtained with the standard setting is 30 mGy, whereas the total dose for a CT on the maximum setting is 60 mGy.

### 3.3. Low contrast phantom

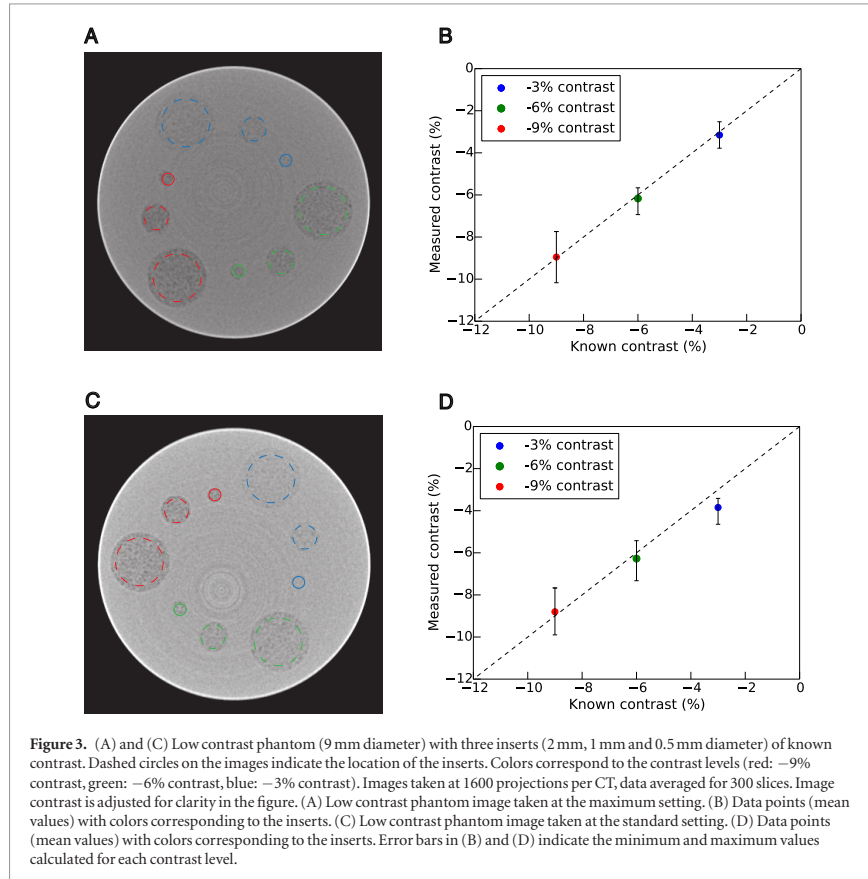
Figure 3 shows CT images of a phantom with three inserts of low contrast (due to air bubbles) with known contrast levels of  $-3\%$ ,  $-6\%$  and  $-9\%$  ( $\pm 0.1\%$ ) as compared to the background material made of a proprietary epoxy resin (QRM GmbH, Möhrendorf, Germany). Each contrast level has three inserts of varying diameter sizes: small (0.5 mm), medium (1 mm) and large (2 mm). Intensity values were measured for each of the inserts (nine in total) using ImageJ software (Schindelin *et al* 2012). The contrast ( $c$ ) was determined by comparing the intensity values ( $I$ ) of the inserts to the background material,  $c = 1 - ((I_{\text{insert}} - I_{\text{air}})/(I_{\text{resin}} - I_{\text{air}}))$ . These were plotted against the known contrast values and shows excellent agreement between the measured and known values. This demonstrates that the system is capable of detecting low contrast levels in samples such as the tissue-air contrast found in the lungs.

### 3.4. Noise

We adopted an approach similar to Kalender *et al* for the calculation of noise for use in their quality factor equation, whereby noise was defined as the standard deviation (in HU) for a  $10 \text{ mm}^2$  region of interest in a 32 mm diameter water phantom (Kalender *et al* 2005). We used a 3D printed 24 mm diameter rod (FullCure720, Objet Eden260V, Stratasys Ltd) made of a material that has properties similar to an acrylic, and as such, has properties similar to water (Ionita *et al* 2014). A region of interest was converted to Hounsfield Units (HU) with ImageJ (Schindelin *et al* 2012) using the following relationship between intensity ( $I$ ) and HU:

$$I = (HU + HU_{\text{shift}}) \left( \frac{65535}{HU_{\text{range}}} \right). \quad (1)$$

For our system, the value for  $HU_{\text{shift}}$  is 3072 and the value for  $HU_{\text{range}}$  is 8191, based on calibrations of the attenuation coefficient ( $\mu$ ) for water and air at an effective photon energy of 20 keV (Seltzer 1993), and using



the standard formula for calculating Hounsfield Units:  $HU = 1000(\mu_{material} - \mu_{air})/(\mu_{water} - \mu_{air})$  (Kalender 2011). The standard deviation was determined to be 520 HU for the standard setting and 198 HU for the maximum setting, using equation (1).

### 3.5. Quality factor versus scan time

Kalender *et al* utilize a combination of dose, resolution and noise to characterize various systems in high speed mode and high quality mode, and represent this as the quality factor,  $Q$ , given by equation (2): where;  $\rho_{10\%} = 10\%$  MTF ( $\text{lp mm}^{-1}$ ),  $\sigma = \text{noise}$  (standard deviation as HU),  $D = \text{dose}$  (mGy) (Kalender *et al* 2005).

$$Q = 1000 \frac{\rho_{10\%}^2}{\sigma \sqrt{D}} \quad (2)$$

The ratio of quality factor to scan time ( $Q/T$ ) in high speed mode for one CT is shown in figure 4 for our system for both the standard and maximum settings. These values are compared to four commercially available micro-CT scanners (Scanners (A)–(D) in figure 4) (Kalender *et al* 2005), as well as for a current state-of-the-art commercially available micro-CT scanner (Scanner (E) in figure 4), for which the values of dose (19 mGy), resolution ( $4.85 \text{ lp mm}^{-1}$ ) and scan time (26 s, based on 514 projections per CT) were obtained from the current literature and technical notes available from the manufacturer (Behrooz *et al* 2016, Ghani *et al* 2016). The noise for this system was estimated as the same as for the Excillum at the maximum setting (i.e. 198 HU). As scan time increases, the quality factor does not increase. This is due to the squared weighting of the resolution (10% MTF) and the increased dose; longer scan times do not significantly improve resolution, but they do significantly increase the radiation dose received by the sample, thus resulting in a lower quality factor. For terminal *in vivo* imaging, where the dose is less significant than for longitudinal imaging, we compared the devices without the dose component in the quality factor (figure 4(B)), i.e.  $Q' = 1000(\rho_{10\%}^2)/\sigma$ .

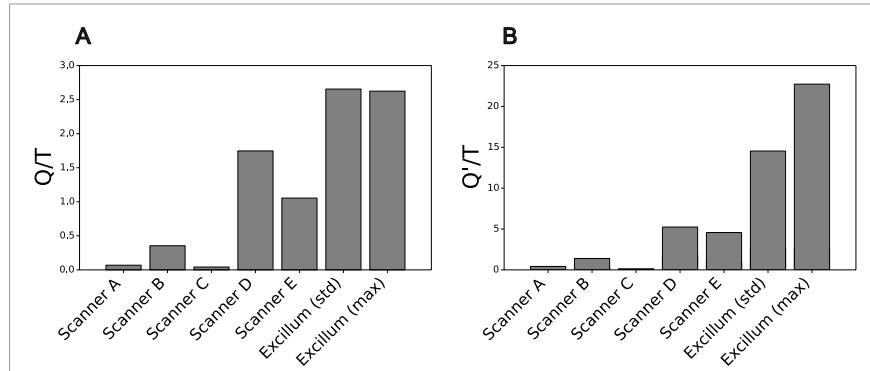


**Figure 4.** (A) Comparison of scanners in high speed mode using the ratio of quality factor (Q) to scan time (T), Q/T, where the quality factor includes radiation dose. (B) Comparison of scanners in high speed mode without taking dose into account, where Q' does not include dose (e.g. for terminal studies).

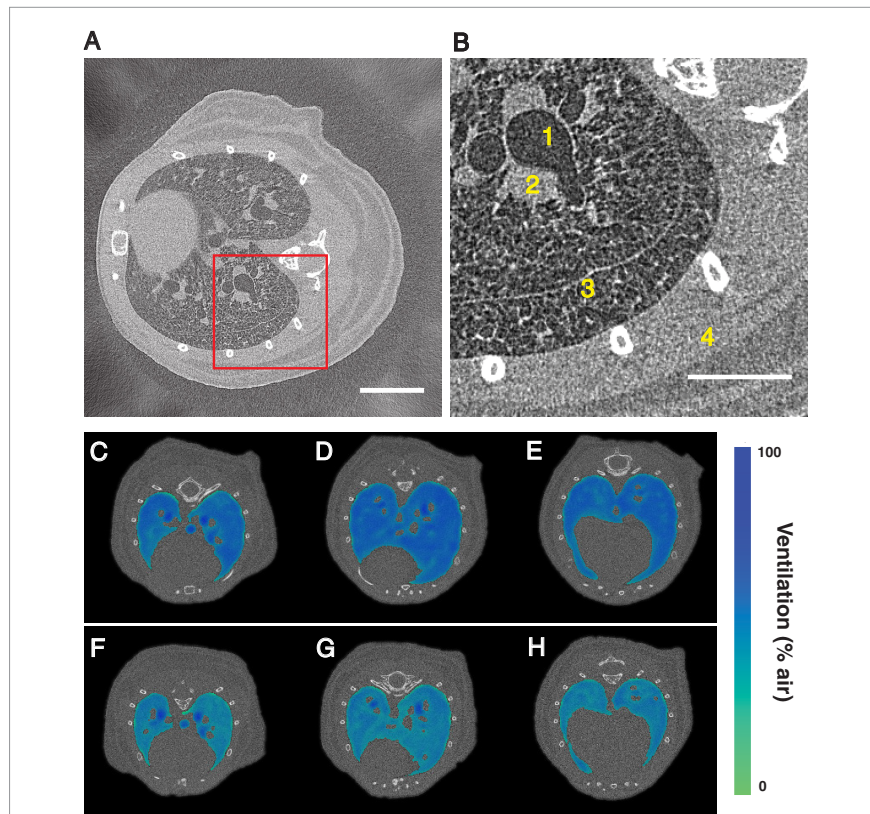


**Figure 5.** CT slices from 4DCT *in vivo* imaging of BALB/c mice taken at 30 Hz with an 18 ms exposure time (see supplementary material 5). (A) Healthy mouse, with region of interest in red. Scale bar represents 4 mm. (B) Close up of region of interest shows airways (1), blood vessels (2), lobe fissures (3) and fat and muscle layers (4). Scale bar represents 2 mm. (C)–(H) Sequence of CT slices at end-expiration with contours (percentage of air) demonstrating differences in volume of air and distribution of air at 0 hours mechanical ventilation (C)–(E), and after 2 h of high pressure mechanical ventilation (F)–(H).

### 3.6. *In vivo* 4DCT images of mice

The CT slices in figure 5 are from a typical *in vivo* 4DCT image obtained on our system (supplementary material 5 ([stacks.iop.org/PMB/63/08NT03/mmedia](https://stacks.iop.org/PMB/63/08NT03/mmedia))). The images are of healthy BALB/c mice. The images were taken at the maximum setting (table 1), i.e. 800 projections per CT and a scan time of 32 s at an image acquisition rate of 30 Hz and an 18 ms exposure time (with inspiratory and expiratory times of 300 : 300 ms). These *in vivo* CT images demonstrate the high quality images that are achievable with this laboratory set-up. Pertinent features in the lung parenchyma, such as the small airways (or alveolar clusters) can be discerned in our 4DCT images. A selection of these were manually measured (figure 5) using ImageJ and found to be approximately 55–60  $\mu\text{m}$  in cross section, which is consistent with other studies (Irvin and Bates 2003). There are some artifacts (blurring) around the heart and at edges of the lungs and rib-cage bones, due to motion blur (figure 5(A)). The images in figures 5(C)–(H) demonstrate the application of Hounsfield Units for calculating the volume of air in the lungs. In these images, the relative volumes are mapped onto the CT slices. The ability to accurately quantify absolute lung volumes is important in order to determine lung function, for example, in determining the functional residual capacity on a regional level. There are many potential applications for high quality dynamic CT reconstructions, for example to be used for 3D x-ray velocimetry analysis, such as that based on the technique by Dubsky *et al* (2012). High quality images also enable the accurate segmentation of airways (Kim *et al* 2016, Dubsky *et al* 2017) and pulmonary vasculature (Samarage *et al* 2016), which is essential for obtaining regional (e.g. lobar or sub-lobar) information about the lungs in order to determine heterogeneity in disease models (Stahr *et al* 2016).

## 4. Conclusion

The research presented in this paper demonstrates the optimization of a customized laboratory facility for the purposes of lung x-ray imaging in small animals. The key feature of our system is imaging at high speed with high image quality (10% MTF of 12 lp  $\text{mm}^{-1}$  for a CT taken at 30 frames per second), which is a prerequisite for functional imaging. The ratio of quality factor to scan time (Q/T) demonstrates that the facility has an excellent balance between imaging speed, resolution, contrast and radiation dose, which is essential for quality control in small animal imaging. Such information is necessary in deciding on the design of future *in vivo* studies with the capabilities of the system in mind and for translation to the clinic. The advantages of a customized in-house facility enables complex and longitudinal animal studies that would otherwise not be possible. Furthermore, the system can be configured and adapted to the specific imaging requirements. For example, the effective propagation distance can be adjusted from pure absorption to phase enhancement, and the magnification and field of view can be configured for specific studies (e.g. mouse, rat), or for a specific region of interest.

## Acknowledgments

This work was funded in part by: National Health and Medical Research Council Project Grant 1077905, National Health and Medical Research Council Development Grant APP1055116 and Australian Research Council Discovery Grant DP150102240. C R Samarage for assistance with figure 1. H D Jones for expertise in preparing animals for *in vivo* imaging (figures 5(A) and (B)). E Bennett for preparing animals for *in vivo* imaging (figures 5(C)–(H)). S Irvine for assistance with *in vivo* imaging. K Hourigan for guidance and manuscript editing. This project was also supported by the Multi-modal Australian ScienceS Imaging and Visualization Environment (MASSIVE).

## Disclosures

A Fouras, R P Carnibella, S Dubsky and R P Murrie have beneficial interest in 4Dx Limited.

## ORCID iDs

M Preissner  <https://orcid.org/0000-0003-2144-9467>

S Dubsky  <http://orcid.org/0000-0001-8355-7362>

## References

- Bech M, Tapfer A, Velroyen A, Yaroshenko A, Pauwels B, Hostens J, Bruyndonckx P, Sasov A and Pfeiffer F 2013 *In-vivo* dark-field and phase-contrast x-ray imaging *Sci. Rep.* **3** 3209
- Behrooz A, Tseng J-C and Meganck J 2016 *Image Resolution in Micro-CT: Principles and Characterization of the Quantum FX and Quantum GX System* (Technical Note)
- Boone J M, Velazquez O and Cherry S R 2004 Small-animal x-ray dose from micro-CT *Mol. Imaging* **3** 149–58
- Boreman G D 2001 *Modulation Transfer Function in Optical and Electro-Optical Systems* (Bellingham, WA: SPIE Press)

- Brennan D et al 2015 Clinical validation of 4-dimensional computed tomography ventilation with pulmonary function test data *Int. J. Radiat. Oncol. Biol. Phys.* **92** 423–9
- DIN 6868-161 2013 Image quality assurance in diagnostic x-ray departments—part 161: RoV acceptance testing of dental radiographic equipment for digital cone-beam computed tomography
- Dubsky S, Hooper S B, Siu K K W and Fouras A 2012 Synchrotron-based dynamic computed tomography of tissue motion for regional lung function measurement *J. R. Soc. Interface* **9** 2213–24
- Dubsky S, Zosky G R, Perks K, Samarage C R, Henon Y, Hooper S B and Fouras A 2017 Assessment of airway response distribution and paradoxical airway dilation in mice during methacholine challenge *J. Appl. Physiol.* **122** 503–10
- Feldkamp L A, Davis L C and Kress J W 1984 Practical cone-beam algorithm *J. Opt. Soc. Am. A* **1** 612
- Fouras A, Kitchen M J, Dubsky S, Lewis R A, Hooper S B and Hourigan K 2009 The past, present, and future of x-ray technology for *in vivo* imaging of function and form *J. Appl. Phys.* **105** 102009
- Fouras A, Allison B J, Kitchen M J, Dubsky S, Nguyen J, Hourigan K, Siu K K W, Lewis R A, Wallace M J and Hooper S B 2012 Altered lung motion is a sensitive indicator of regional lung disease *Ann. Biomed. Eng.* **40** 1160–9
- Ghani M U, Zhou Z, Ren L, Wong M, Li Y, Zheng B, Yang K and Liu H 2016 Investigation of spatial resolution characteristics of an *in vivo* microcomputed tomography system *Nucl. Instrum. Methods Phys. Res.* **807** 129–36
- Ionita C N, Mokin M, Varble N, Bednarek D R, Xiang J, Snyder K V, Siddiqui A H, Levy E I, Meng H and Rudin S 2014 Challenges and limitations of patient-specific vascular phantom fabrication using 3D Polyjet printing *Proc. SPIE Int. Soc. Opt. Eng.* **9038** 90380M
- Irvin C G and Bates J H T 2003 Measuring lung function in mice: the challenge of size *Respir. Res.* **4** 1
- Kalender W A, Durkee B, Langner O, Stepina E and Karolczak M 2005 Comparative evaluation: acceptance testing and constancy testing for micro-CT scanners *Biomed. Technol.* **50** 1192–3
- Kalender W A 2011 *Computed Tomography: Fundamentals, System Technology, Image Quality, Applications* (New York: Wiley)
- Kim E H, Preissner M, Carnibella R P, Samarage C R, Bennett E, Fouras A, Zosky G R and Jones H D 2016 Novel analysis of 4DCT imaging quantifies progressive increases in anatomic dead space during mechanical ventilation in mice *J. Appl. Physiol.* **123** 578–84
- Kitchen M J, Paganin D, Lewis R A, Yagi N, Uesugi K and Mudie S T 2004 On the origin of speckle in x-ray phase contrast images of lung tissue *Phys. Med. Biol.* **49** 4335–48
- Krenkel M, Töpferwien M, Dullin C, Alves F and Salditt T 2016 Propagation-based phase-contrast tomography for high-resolution lung imaging with laboratory sources *AIP Adv.* **6** 035007
- Larsson D H, Takman P A C, Lundström U, Burvall A and Hertz H M 2011 A 24 keV liquid-metal-jet x-ray source for biomedical applications *Rev. Sci. Instrum.* **82** 123701
- Larsson D H, Lundström U, Westermark U K, Arsenian Henriksson M, Burvall A and Hertz H M 2013 First application of liquid-metal-jet sources for small-animal imaging: high-resolution CT and phase-contrast tumor demarcation *Med. Phys.* **40** 021909
- Mayo S C, Miller P R, Wilkins S W, Davis T J, Gao D, Gureyev T E, Paganin D, Parry D J, Pogany A and Stevenson A W 2002 Quantitative x-ray projection microscopy: phase-contrast and multi-spectral imaging *J. Microsc.* **207** 79–96
- Samarage C R, Carnibella R, Preissner M, Jones H D, Pearson J T, Fouras A and Dubsky S 2016 Technical note: contrast free angiography of the pulmonary vasculature in live mice using a laboratory x-ray source *Med. Phys.* **43** 6017–23
- Schindelin J et al 2012 Fiji: an open-source platform for biological-image analysis *Nat. Methods* **9** 676–82
- Seltzer S M 1993 Calculation of photon mass energy-transfer and mass energy-absorption coefficients *Radiat. Res.* **136** 147–70
- Sera T, Yokota H, Tanaka G, Uesugi K, Yagi N and Schroter R C 2013 Murine pulmonary acinar mechanics during quasi-static inflation using synchrotron refraction-enhanced computed tomography *J. Appl. Physiol.* **115** 219–28
- Stahr C S et al 2016 Quantification of heterogeneity in lung disease with image-based pulmonary function testing *Sci. Rep.* **6** 29438
- Steiding C, Kolditz D and Kalender W A 2014 A quality assurance framework for the fully automated and objective evaluation of image quality in cone-beam computed tomography *Med. Phys.* **41** 31901
- Tapfer A et al 2012 Experimental results from a preclinical x-ray phase-contrast CT scanner *Proc. Natl Acad. Sci.* **109** 39
- Vande Velde G, De Langhe E, Poelmans J, Bruyndonckx P, d'Agostino E, Verbeken E, Bogaerts R, Lories R and Himmelreich U 2015 Longitudinal *in vivo* microcomputed tomography of mouse lungs: no evidence for radiotoxicity *Am. J. Physiol. Lung Cell. Mol. Physiol.* **309** L271–9
- Wilkins S W, Gureyev T E, Gao D, Pogany A and Stevenson A W 1996 Phase-contrast imaging using polychromatic hard x-rays *Nature* **384** 335–8
- Yang K, Kwan A L C, Miller D F and Boone J M 2006 A geometric calibration method for cone beam CT systems *Med. Phys.* **33** 1695–706

## 4 Dynamic *in vivo* imaging for regional lung function in VILI

### 4.1 Introduction and aims

Previous work has shown that so-called protective ventilation strategies in healthy mice can still lead to lung injury (Cannizzaro *et al.*, 2011). These studies used the forced oscillation technique to obtain global pulmonary function, as well as biomarkers to ascertain tissue injury post-mortem. Although biomarkers can provide sensitive measures of regional tissue inflammation and injury post-mortem, they cannot determine the mechanism of the regional injury. Conversely, although global pulmonary function testing provides an insight into the mechanism of injury, it does not provide information on the regional lung mechanics.

Imaging fills these gaps by mapping the regional volume of air throughout the lung *in vivo* as an indication of regional lung mechanics (Dubsky *et al.*, 2012). While lung volumes may be indicators of lung injury, this needs to be confirmed with known biomarkers of injury. Therefore, a crucial aspect of the studies in this chapter was to also assess the lung tissue for various biomarkers of injury. The objective of these studies was to map the regional volume data directly to a suite of biomarkers of lung injury known to be implicated in mouse models of VILI (Cannizzaro *et al.*, 2011). The two methods complement each other by providing correlations between the regional injury and the volume of air in the region. For example, a positive correlation between the biomarker and tidal stretch implies that the injury is related to a high lung volume mechanism, and a negative correlation implies that the injury is related to a low lung volume mechanism.

The work in this chapter addresses the second aim of the thesis, namely, to obtain lung volumes for ten regions in the mouse lung from dynamic 4DCT images

acquired with the laboratory system described in Chapter 3. The regional volumes obtained from imaging were the tidal volume and the end-expiratory volume (also denoted functional residual capacity in some figures). In addition, the ten regions in the lung were assessed for various biomarkers of lung injury.

Two studies of lung injury were investigated in this chapter: 1. a model of one-hit VILI using injurious mechanical ventilation and no initial lung injury, and 2. a model of two-hit VILI with extrapulmonary ARDS and protective mechanical ventilation. The terms one-hit VILI and two-hit VILI refer to mechanical ventilation irrespective of the ventilation parameters, as described in Section 2.9 of Chapter 2.

Post-processing analysis developed by the author specifically for these studies included a method for customised sub-lobe slicing for the left lobe, and for calculation of the regional end-expiratory volume. These techniques are based on the 4DXV voxel-tracking technique and have the advantage that they do not require image registration (Dubsky *et al.*, 2012).

The results of the studies were published in two journal articles as joint first author and are included in Appendix A (Yen & Preissner *et al.*, 2019, Yen & Preissner *et al.*, 2020).

## 4.2 Mouse models and study design

The mouse models and experimental design for the two studies are shown in Figure 4.1. The mouse models and ventilation strategies were designed by Professor Graeme Zosky, University of Tasmania, based on previous work (Cannizzaro *et al.*, 2011). The lung tissue analysis was performed by Dr Seiha Yen from the University of Tasmania.

Seven week old BALB/c female mice (20.9 +/- 1.3 g) were obtained from the Monash University Animal Research Platform and experiments were approved by the Monash University Animal Ethics Committee. The mice were surgically intubated and were attached to a small animal ventilator ventilator (AccuVent, Notting Hill Devices, Melbourne, VIC, Australia) (Kitchen *et al.*, 2010). Further details of the mouse preparation is given in the journal article by Yen & Preissner *et al.* (2019) in

Appendix A. The two mouse models of lung injury are described in the following sections.

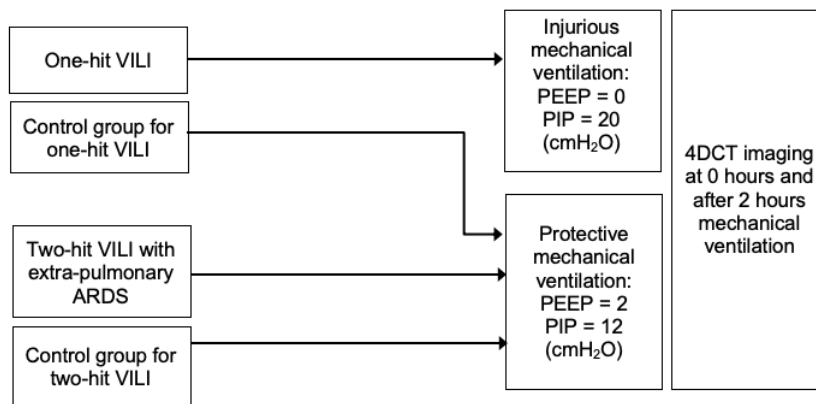


FIGURE 4.1: Schematic showing the two mouse models used in the studies, including treatment, ventilation parameters and imaging times.

#### 4.2.1 Mouse model of one-hit VILI

The first study used a mouse model of one-hit VILI in which mice ( $n = 8$ ) were ventilated for two hours with an injurious ventilation protocol: a positive inspiratory pressure (PIP) of 20  $\text{cmH}_2\text{O}$ , zero positive end-expiratory pressure (PEEP), and a respiratory rate of 100 breaths per minute. These were compared to a control group ( $n = 6$ ), which were ventilated with a lung-protective ventilation strategy with a PIP of 12  $\text{cmH}_2\text{O}$ , a PEEP of 2  $\text{cmH}_2\text{O}$  and a respiratory rate of 225 breaths per minute.

#### 4.2.2 Mouse model of two-hit VILI

The most common cause of ARDS is sepsis and patients with sepsis-related ARDS have the highest hospital mortality (Bellani *et al.*, 2016; Rubenfeld & Herridge, 2007). Therefore sepsis was the focus of the two-hit VILI mouse model studied in this chapter. The study used a mouse model of extrapulmonary ARDS plus protective mechanical ventilation. The ARDS was initiated via endotoxaemia with an intraperitoneal injection of lipopolysaccharide (LPS). The mice ( $n = 7$ ) were given an intraperitoneal injection of a 200  $\mu\text{L}$  bolus of 0.9% saline with 10  $\text{mg}/\text{kg}$  lipopolysaccharide (derived from *E. coli* O111:B4, InvivoGen, San Diego, CA, USA) four hours prior to

baseline imaging, as a model of whole body sepsis (Matute-Bello *et al.*, 2008). These were compared to a control group ( $n = 5$ ) that were given an intraperitoneal injection of saline solution (200 uL bolus of 0.9% saline).

Both groups were ventilated for two hours with a ventilation protocol based on a lung-protective ventilation strategy: a PIP of 12 cmH<sub>2</sub>O, a PEEP of 2 cmH<sub>2</sub>O and a respiratory rate of 225 breaths per minute.

### 4.2.3 Ventilation strategies

The ventilation strategies are shown in the pressure trace in Figure 4.2. Both of the studies used pressure-controlled ventilation (Kitchen *et al.*, 2010). The ventilation strategy with a low positive inspiratory pressure (PIP) and some positive end-expiratory pressure (PEEP) aimed to provide a lung protective strategy, whereby the PEEP protects the alveoli from collapse, and a low PIP results in a low tidal volume to protect from over-distension, the value of which is dependent on the compliance of the lungs. In contrast, the injurious ventilation strategy aimed to induce VILI, via volutrauma from a high PIP, as well as atelectrauma from zero PEEP, resulting in alveolar collapse and cyclical stresses as the ventilation cycles from zero to 20 cmH<sub>2</sub>O. The respiratory rates were altered to match minute ventilation (i.e., total volume of air per minute) between groups.

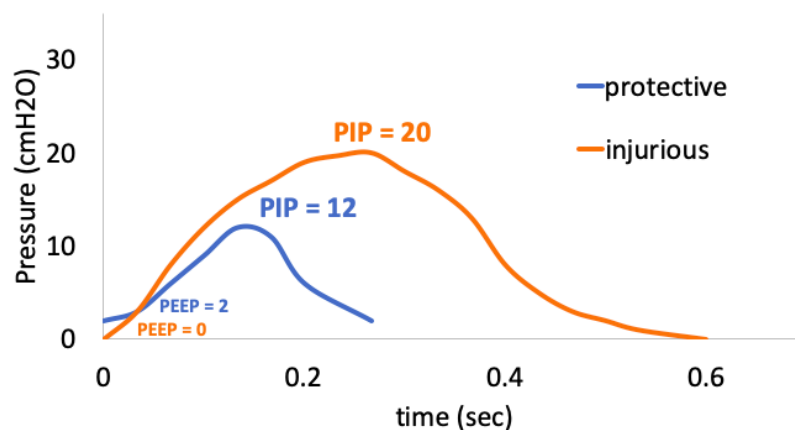


FIGURE 4.2: A representation of pressure (relative to atmosphere) versus time showing the two ventilation strategies used in the studies: protective (225 breaths per minute) and injurious (100 breaths per minute).

#### 4.2.4 Regions of interest in the lung

The ten regions of interest for the studies in this chapter are shown in Figure 4.3 (Yen & Preissner *et al.*, 2019). These regions were chosen to map the volume data from imaging with biomarkers of lung injury in tissue of the same region. The lobes on the right side are R1, R2, R3 and R4. These are commonly known as the cranial (R1), middle (R2), caudal (R3), and accessory (R4) lobes in mice. The six regions in the left lobe are labelled as L1-L6.

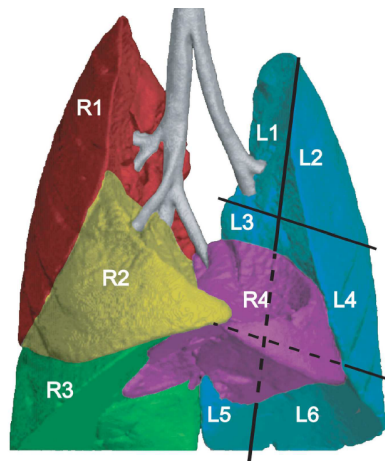


FIGURE 4.3: Pseudo-colouring of a volumetric rendering of a CT image from the one-hit VILI study. The labels indicate the ten regions in the images that were used for tissue matching: four right lobes (R1-R4) and six regions in the left lobe (L1-L6) (Yen & Preissner *et al.*, 2019).

#### 4.2.5 Analysis of lung tissue

Analysis of biomarkers of injury in the lung tissue was a crucial objective of these studies. This enabled the regional biomarkers to be mapped to the regional lung volumes from *in vivo* imaging, in order to investigate correlations between tissue injury in the region and the volume of air in the region (as shown in Figures 4.12 and 4.15 of this chapter). Mice were euthanased and the lungs were dissected *en bloc*. The lobes were removed intact, whereby the left lobe was cut into six sections as per Figure 4.4.

The lung sections were stored in RNAlater (Sigma-Aldrich) and RNA extraction

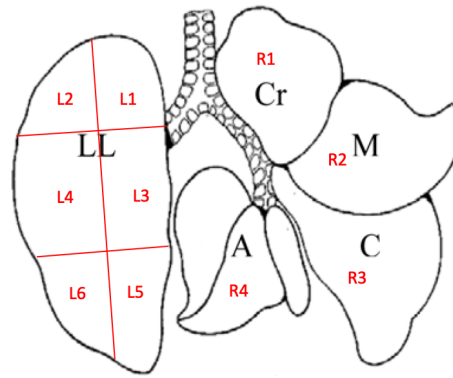


FIGURE 4.4: A representation of the ten regions of the murine lung for tissue analysis in the two VILI studies. LL = left lung (L1 - L6), Cr = cranial lobe (R1), M = median lobe (R2), C = caudal lobe (R3) A = accessory lobe (R4) (Ruiz Júnior *et al.*, 2005).

(miRNeasy Mini Kit, Qiagen) and analysis was performed at the University of Tasmania. For the one-hit VILI study (Yen & Preissner *et al.*, 2019), the lung tissue sections were assessed for 21 genes associated with VILI, whereas a sub-set of seven genes were assessed in the two-hit VILI study (Yen & Preissner *et al.*, 2020). These are listed in Figure 4.5.

Gene Function	Gene Name
Inflammation	<i>Ccl2</i> ●
	<i>Cxcl2</i> ●
	<i>Elane</i>
	<i>IL-1<math>\beta</math></i> ●
	<i>IL-6</i> ●
	<i>Mpo</i> ●
	<i>Tnf-<math>\alpha</math></i> ●
	<i>RAGE</i>
	<i>Ang-2</i>
	Surfactant
<i>Cdh1</i>	
Epithelial-mesenchymal response	<i>Ctnnb1</i>
	<i>Egfr</i>
	<i>Tgfb1</i>
	<i>Vim</i>
	<i>Wnt1</i>
Transcription, cell signaling	<i>c-fos</i>
	<i>Mapk1</i>
	<i>Nfe2l2</i> ●
Anticoagulant	<i>Nfkb1</i>
	<i>Plat</i>

FIGURE 4.5: The 21 VILI-related genes for which the lung tissue regions were assessed in the one-hit VILI study. The seven gene names marked with red dots were assessed in the two-hit VILI study. Modified from Table 1 in Yen & Preissner *et al.* (2019).

Each lung region was weighed and the mass recorded. These were averaged,  $m_{ave,r}$ , for all the mice in each study, as follows

$$m_{ave,r} = \frac{\sum_1^n m_r}{n}, \quad (4.1)$$

where  $n$  denotes the total number of mice in the study,  $r$  denotes the region (i.e., R1 - R4, L1 - L6), and  $m_r$  is the mass of the region per mouse.

The mass fraction,  $f_m$ , for each region was calculated as follows

$$f_m = \frac{m_{ave,r}}{m_{ave,tot}}, \quad (4.2)$$

where  $r$  denotes the region (i.e., R1 - R4, L1 - L6),  $m_{ave,r}$  is the average mass for each region given by Equation 4.1, and  $m_{ave,tot}$  is the average of the total mass of the whole lung for all the mice in the study.

The mass fractions were used to determine the slicing of left lobe from the imaging data, as described in Section 4.4.5.

### 4.3 Dynamic *in vivo* 4DCT imaging

The journal article in Chapter 3 describes the laboratory X-ray imaging system used to capture the four-dimensional computed tomography (4DCT) imaging data for these studies (Preissner *et al.*, 2018b).

A movie of the 4DCT images can be accessed online via the supplementary material from Preissner *et al.* (2018b): <https://iopscience.iop.org/article/10.1088/1361-6560/aab8d2/data>

The laboratory system comprises a state-of-the-art liquid metal-jet X-ray source (D2+, Excillum AB, Kista, Sweden) and a high-speed detector, able to capture images at up to 30 frames per second (PaxScan 2020, Varian Medical Systems, Palo Alto, CA, USA). The imaging was phase-averaged such that the total number of breaths, or phases in the 4DCT,  $p$ , was determined by

$$p = 60f/RR, \quad (4.3)$$

where  $RR$  is the respiratory rate in breaths per minute, and  $f$  is the image acquisition rate in Hertz, set at 30 frames per second for all imaging in this chapter.

The geometric magnification,  $M$ , was determined by

$$M = (R1 + R2) / R1, \quad (4.4)$$

where  $R1$  is the source-to-sample distance, and  $R2$  is the sample-to-detector distance.

$R1$  and  $R2$  were fixed for all the images in the studies. The system is designed with an increased propagation distance ( $R2$ ), resulting in phase fringes in the images at the boundaries of different materials for improved contrast and sharpness, which can be seen in Figure 1, Panel B in Preissner *et al.* (2018b).

Figure 4.6 shows representative global volumes,  $EEV$  and  $V_T$ , and the respiratory rates for both the injurious and protective ventilation strategies, as measured from the 4DCT images. The data points show the time points (phases) in the 4DCT, each of which is a CT image snapshot at that point in the breath cycle. The mice were imaged whilst on the ventilator at baseline (0 hours) and after two hours of mechanical ventilation.

4DCT dynamic imaging does not require a breath-hold for the acquisition of the projection images. A phase-averaged snapshot of the lungs is captured at various points along the breath cycle. Whilst dynamic CT results in a much higher dose of radiation to the animal than two static CTs (e.g., an end-inspiratory CT and end-expiratory CT for tidal volume), it does not require the ventilator to be paused for the duration of image capture. This has the advantage of avoiding changes in lung mechanics that may occur during ventilation pauses, such as air redistribution, thus capturing the true dynamics of the lungs during ventilation (Motta-Ribeiro *et al.*, 2018; Paula *et al.*, 2016). Imaging dynamically during mechanical ventilation without pausing the ventilator also reduces stress relaxation due to the viscoelasticity of the lung (Suki *et al.*, 2011) and is a more realistic measurement of the lung mechanics during mechanical ventilation.

Post-processing of the projection images is described next, including the specific methods developed to segment the lung into customised regions (as described in

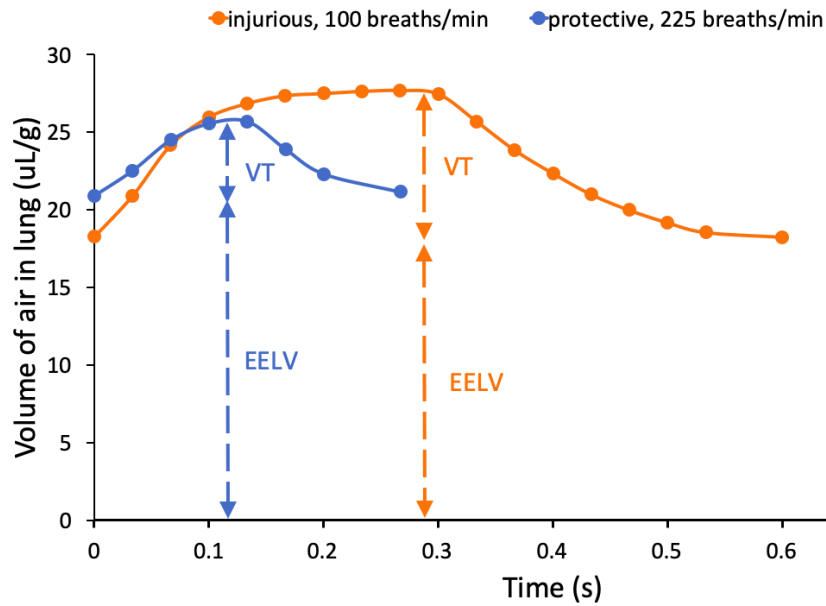


FIGURE 4.6: Representative volume traces from the 4DCT data showing tidal volume ( $V_T$ ) and the end-expiratory lung volume (EELV) for the whole lung. The data points show the time points (phases) in the 4DCT. Data are for two different mice ventilated with either the protective or the injurious ventilation strategy. The lung volumes are normalised to the weight of the mouse. The total lung stretch (or end-inspiratory lung volume) is defined as the sum of these two volumes, i.e.,  $EELV + V_T$ .

Section 4.2.4) in order to map the volumes from imaging data directly with biomarkers from lung tissue of the same region.

#### 4.4 Post processing of imaging data

The 4DCT imaging data was processed according to the flowchart in Figure 4.7. The main post processing steps are described in detail in this section.

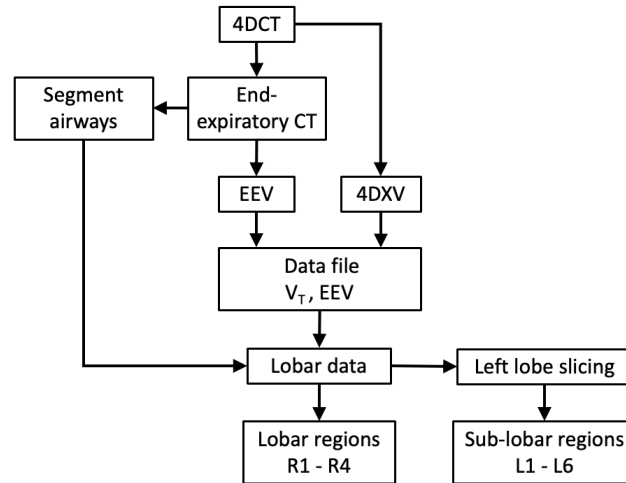


FIGURE 4.7: Flowchart showing the post processing tasks for the 4DCT imaging data and analysis of the regional distribution of tidal volume ( $V_T$ ) and end-expiratory volume (EEV).

#### 4.4.1 CT reconstruction and lung mask

Firstly, the projection images in the 4DCT were binned into the phases of the breath cycle. The CT images were reconstructed from the projection images using the Feldkamp Davis Kress algorithm for X-ray cone beam geometry (Feldkamp *et al.*, 1984). 3D image processing software (Avizo, Thermofisher Scientific) was used to manually create a binary mask containing the lung parenchyma from the CT at the start of inspiration using a flood-fill technique with a greyscale range that includes all the voxels inside the lung. For the VILI mouse model data, the mask did not include the larger blood vessels. For the ARDS mouse model, due to the presence of oedematous, patchy regions in the 2-hour image, the lung masks included the blood vessels, in order to ensure that the oedematous regions were captured in the data analysis. It is crucial that the lung masks contain all the voxels inside the lung, including injured or oedematous regions, since this determines which data is included in the analysis.

#### 4.4.2 Airway tree segmentation

The airways were segmented in a similar process to the lung masks, using the CT with the lowest amount of air, i.e., at end-expiration, in order to obtain the best contrast, as shown in Figure 4.8. Prior to manual segmentation, a Hessian filter was applied to the image in order to enhance the vessel-like structures, i.e., the airways,

to provide a better segmentation (Dubsky *et al.*, 2017; Frangi *et al.*, 1998). 3D image processing software (Avizo, Thermofisher Scientific) was used to create a connected centreline tree from the segmented airways. The centreline tree was then used to identify the airway of interest, i.e., the airway that supplies the lobe of interest, in order to obtain the volume data for the four lobar regions of interest in these studies. This technique, described in previous studies as the airway tree link (ATL) method, enables the lobes to be automatically aligned without the need for image registration techniques (Dubsky *et al.*, 2012; Dubsky *et al.*, 2017; Stahr *et al.*, 2016).

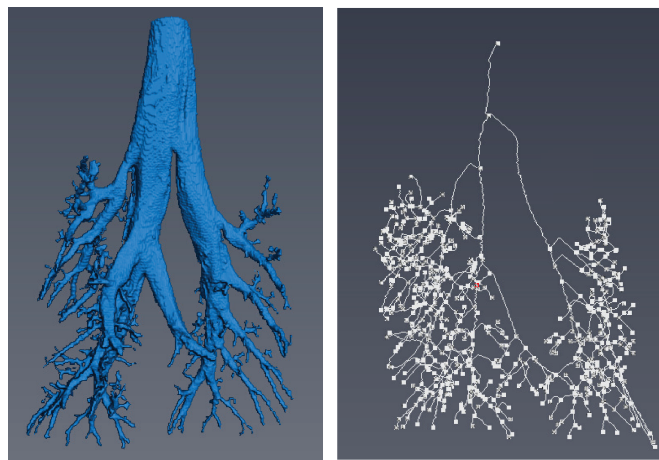


FIGURE 4.8: Airways from a CT image in the 4DCT sequence. The left panel shows the segmented airways after the filter is applied. The right panel shows the centreline tree. The main bronchus supplying the left lobe and the four main airways on the right side of the lung were used to isolate the main lobes using the airway tree link (ATL) technique.

#### 4.4.3 Data file

The output of the processing for the  $V_T$  and EEV values were contained in a data file that uses a grid based on the interrogation regions used in the "4DXV" step in Figure 4.7. The EEV values were appended to the file containing the 4DXV (i.e.,  $V_T$ ) data.

#### 4.4.4 Lobar regions

The end-expiratory volume and the tidal volume was determined for each of the four lobar regions, R1-R4, as shown in Figure 4.3. In order to automate this measurement

for the lobes, the airway tree link (ATL) technique was used (Dubsky *et al.*, 2012; Dubsky *et al.*, 2017; Stahr *et al.*, 2016). The ATL technique associates the voxels in the data file (for either  $V_T$  or EEV values) to the supplying airway of the lobe, as shown in Figure 4.8.

#### 4.4.5 Sub-lobar regions

The left lobe was sliced in the images specifically to match the dissection and slicing of the left lobe that was used for the tissue analysis described in Section 4.2.5. A customised technique was developed by the author specifically for these studies to slice the left lobe into the six sections, labelled L1 to L6 in Figure 4.3. This was critical to allow the novel correlations of the regional lung volumes with tissue biomarkers, as shown in Figures 4.12 and 4.15.

The image slicing process is illustrated in Figure 4.9. Firstly, the left lobe was isolated from the image with the airway tree link (ATL) technique, as illustrated in panel a) (Dubsky *et al.*, 2017; Stahr *et al.*, 2016). It was then rotated around the z-axis (x-y plane), such that the sternum was at 12 o'clock, as per panel b). The data was further rotated around the y-axis (y-z plane), as shown in panel c), in order to best match the orientation that was used for slicing the lobe tissue in the laboratory.

The image was then sliced at three positions in the x-y plane, as shown in panel b): firstly at the extremities of the lobe,  $y_{min}$  and  $y_{max}$ , and then at a distance half-way,  $y_{mid}$ , such that  $y_1 = y_2$ . The location of  $y_{mid}$  corresponds closely with the entry point of the main bronchus into the left lobe, which was used as a location guide for the tissue slicing. These same cutting planes are shown in panel c).

The rotated array was then sliced at two locations, approximately one-third ( $z_{max\_2}$ ) and two-thirds ( $z_{max\_3}$ ) from the origin to mimic the tissue cuts, as shown in panel c) in Figure 4.9.

In order to obtain a best match with the tissue sections, the six sections from the left lobe image were also based on the average mass per section as a fraction of the whole left lobe tissue, i.e., the mass fraction, as described by Equation 4.2 in Section 4.2.5. An analogue of the mass fraction was determined for each left lobe section in the 3D imaging data, termed the volume fraction, and was given by

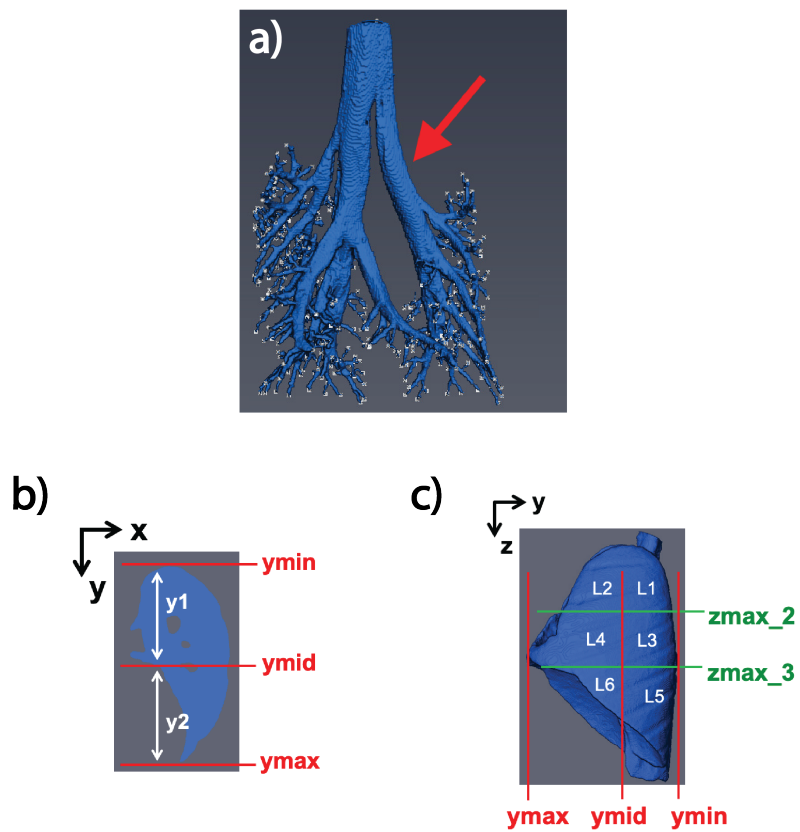


FIGURE 4.9: Left lobe slicing technique. The segmented airway tree with centrelines was used to isolate the left lobe (panel (a), red arrow). The isolated left lobe data is rotated and cut in the x-y plane (b) and y-z plane (c), to match tissue slicing of the six sub-lobar regions, L1 - L6.

$$f_V = \frac{V_{ave,r}}{V_{ave,tot}}, \quad (4.5)$$

where  $V_{ave,r}$  is the volume of the region (in voxels) averaged for all the animals in the study, and  $V_{ave,tot}$  is the average of the total volume of the whole lung (in voxels) for all the mice in the study.

The average volume for the region,  $V_{ave,r}$ , was given as follows

$$V_{ave,r} = \frac{\sum_1^n V_r}{n}, \quad (4.6)$$

where  $n$  denotes the total number of mice in the study,  $r$  denotes the region (i.e., R1 - R4, L1 - L6), and  $V_r$  is the volume of the region (in voxels) per mouse.

A balance between matching the tissue mass fractions to the volume fractions from the imaging data, whilst adhering to the cutting planes shown in Figure 4.9, was the aim in slicing the left lobe image data.

#### 4.4.6 Tidal volume

The 4DXV algorithm developed by Dubsy *et al.* (2012) was used to determine how the tidal volume was distributed throughout the whole lung on a voxel by voxel basis, as shown in Figure 4.10.

The 4DXV technique is derived from particle image velocimetry (Adrian, 2005), and is based on obtaining a measurement of displacement from the patterns of speckle in high-resolution CT images, arising from the air-tissue contrast in the lungs (Dubsy *et al.*, 2012). The lung motion is tracked for specified interrogation windows and the displacement vectors in three dimensions are determined statistically with the use of cross-correlation functions to obtain the displacement field. From this, the tissue expansion values can be directly obtained from the divergence of the displacement field, as described by

$$\nabla \cdot \mathbf{v} = \frac{du}{dx} + \frac{dv}{dy} + \frac{dw}{dz}, \quad (4.7)$$

where  $u$ ,  $v$  and  $w$  are the tissue displacement vectors in the  $x$ ,  $y$ ,  $z$  directions.

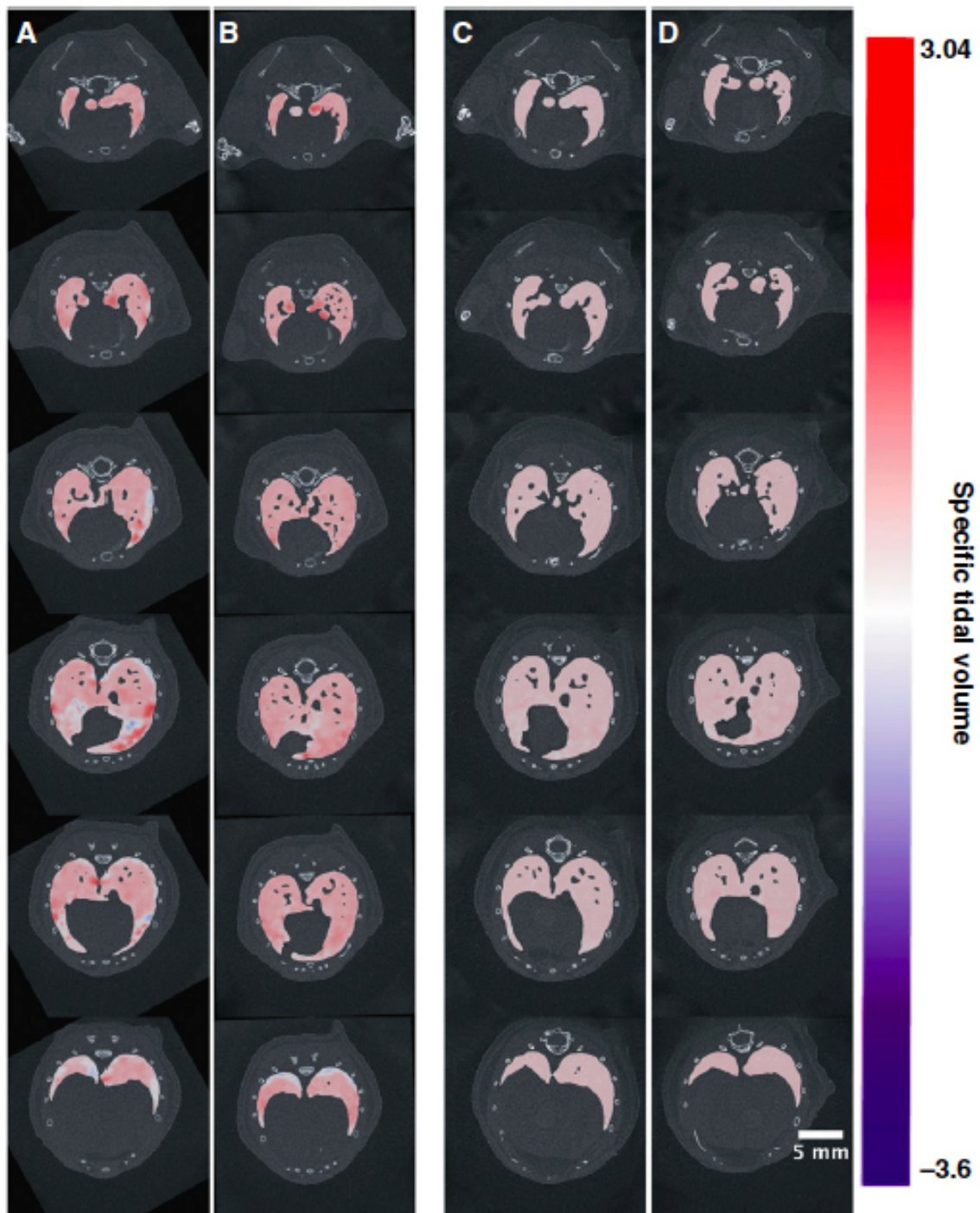


FIGURE 4.10: Contours showing regional tidal volume for two groups of mice after 2 hours of mechanical ventilation. Cross-sectional images for injurious ventilation (panels A and B) and protective ventilation (panels C and D) are shown (Yen & Preissner *et al.*, 2019).

The divergence between end-expiration and end-inspiration is the tidal volume. With 4DXV, image registration across the image pairs is not required to calculate the regional tidal volumes throughout the whole lung.

The equation for volume flux,  $(\nabla \cdot \mathbf{v})dx.dy.dz$ , can be used to convert these values to volume units. However, since the image magnification was the same for all the images, i.e.,  $dx.dy.dz = \text{constant}$ , this conversion was not used in these studies. Instead, the divergence was kept in voxels, as per Equation 4.7, and these were summed for each of the ten regions in order to obtain the regional tidal volume in voxels, as follows

$$V_{Tregion} = \sum_1^{n_{vx}} (\nabla \cdot \mathbf{v})_{voxel}, \quad (4.8)$$

where  $n_{vx}$  is the total number of voxels in the region of interest.

#### 4.4.7 End-expiratory volume

The findings in Chapter 3 demonstrate that the X-ray imaging system is capable of detecting low contrast levels in samples, such as the air-tissue contrast found in lungs (Preissner *et al.*, 2018b). This is critical for determining the amount of air in the lungs with quantitative CT. Quantitative CT was used to determine the end-expiratory volume (EEV) using Hounsfield Units (HU), similar to the methods used in other studies (Fuld *et al.*, 2008). The greyscale intensity data for the end-expiratory CT was converted to Hounsfield Units, as described in Preissner *et al.* (2018b) in Chapter 3. Each voxel was then converted to a fraction of air,  $f_{air}$ , as described by

$$(f_{air})_{voxel} = \frac{HU_{voxel}}{HU_{air}}, \quad (4.9)$$

where  $HU_{air}$  has a value of -1000 by definition.

The EEV method was specifically developed for these studies and appended to the 4DXV file structure, in order to use the airway tree link (ATL) method.

In order to determine the EEV for each region,  $EEV_{region}$ , the fraction of air for each voxel,  $(f_{air})_{voxel}$ , as described by Equation 4.9, was summed for all the voxels in the region of interest, as given by

$$EEV_{region} = \sum_1^{n_{vox}} (f_{air})_{voxel}, \quad (4.10)$$

where  $n_{vox}$  is the total number of voxels in the region of interest.

## 4.5 Data analysis

### 4.5.1 Normalising the values

In order to give a measure of the tidal volume ( $V_T$ ) and the EEV scaled to the size of the region in each mouse, the values were normalised to the sum of the voxels in the region at end-expiration (EE) at the same baseline ventilation pressures. Equations 4.11 and 4.12 describe the method for normalising the volumes, as follows

$$sV_T = \frac{V_{Tregion}}{n_{EE}}, \quad (4.11)$$

$$sEEV = \frac{EEV_{region}}{n_{EE}}, \quad (4.12)$$

where  $sV_T$  and  $sEEV$  denote the specific volumes,  $V_{Tregion}$  and  $EEV_{region}$  are the tidal volume and the end-expiratory volume for the region, respectively, and  $n_{EE}$  is the number of voxels in the region from the end-expiratory CT image.

### 4.5.2 Total stretch

The total end-inspiratory volume, also referred to as total stretch, or total distension, for a region was defined as  $sEEV + sV_T$ . This was investigated in order to understand the impact of too much PEEP on volutrauma, i.e., PEEP plus tidal volume. The literature is described in detail in Chapter 2, Section 2.7, whereby over-distension from total end-inspiratory volume is known to lead to volutrauma in the presence of low or moderate tidal volumes (Protti *et al.*, 2015).

### 4.5.3 Statistical analysis of imaging data

Statistical analysis of the imaging data was conducted as described in Yen & Preissner *et al.* (2019) and Yen & Preissner *et al.* (2020) in Appendix A. Briefly, two-way

repeated measures ANOVA was applied to the imaging data, both between groups and between regions, whereby differences were deemed statistically significant if  $P < 0.05$ . Linear regression analysis was used to determine associations between the biomarkers of tissue injury (gene expression) and the specific lung volumes. The tissue analysis and statistical analysis for both of the studies was completed by Dr Seiha Yen at the University of Tasmania.

## 4.6 Results and Discussion

The results for the one-hit VILI study were published as a joint first author journal article (Yen & Preissner *et al.* 2019) in the American Journal of Respiratory Cell and Molecular Biology. The results for the two-hit VILI study were published as a joint first author journal article (Yen & Preissner *et al.* 2020) in the American Journal of Physiology - Lung Cellular and Molecular Physiology. The journal articles are included in Appendix A.

All the imaging data was processed by the author and customised post-processing techniques were developed for the calculation of EEV and customised sub-lobar slicing of the left lung, as described in Section 4.4. This customisation of the imaging data was critical for comparison with the regional injury biomarkers, in order to elucidate how the volume in the region related to tissue injury.

The regional volumes, sEEV, sV<sub>T</sub> and total stretch (sEEV + sV<sub>T</sub>) from imaging, and the correlations with biomarkers are presented as extracts from the published journal article in the next sections.

### 4.6.1 One-hit VILI study

The results of the study of the mouse model of one-hit VILI with injurious ventilation resulted in a published journal article as joint first author, included in Appendix A (Yen & Preissner *et al.*, 2019).

Figure 4.11, shows box plots (median, interquartile range and 10th to 90th percentile) of the specific volumes from imaging for both the injurious ventilation and the protective ventilation groups. The ten regional volumes shown here are specific

end-expiratory volume (denoted specific functional residual capacity, sFRC, in the figure), specific tidal volume ( $sV_T$ ) and total stretch, defined as  $sFRC + sV_T$ .

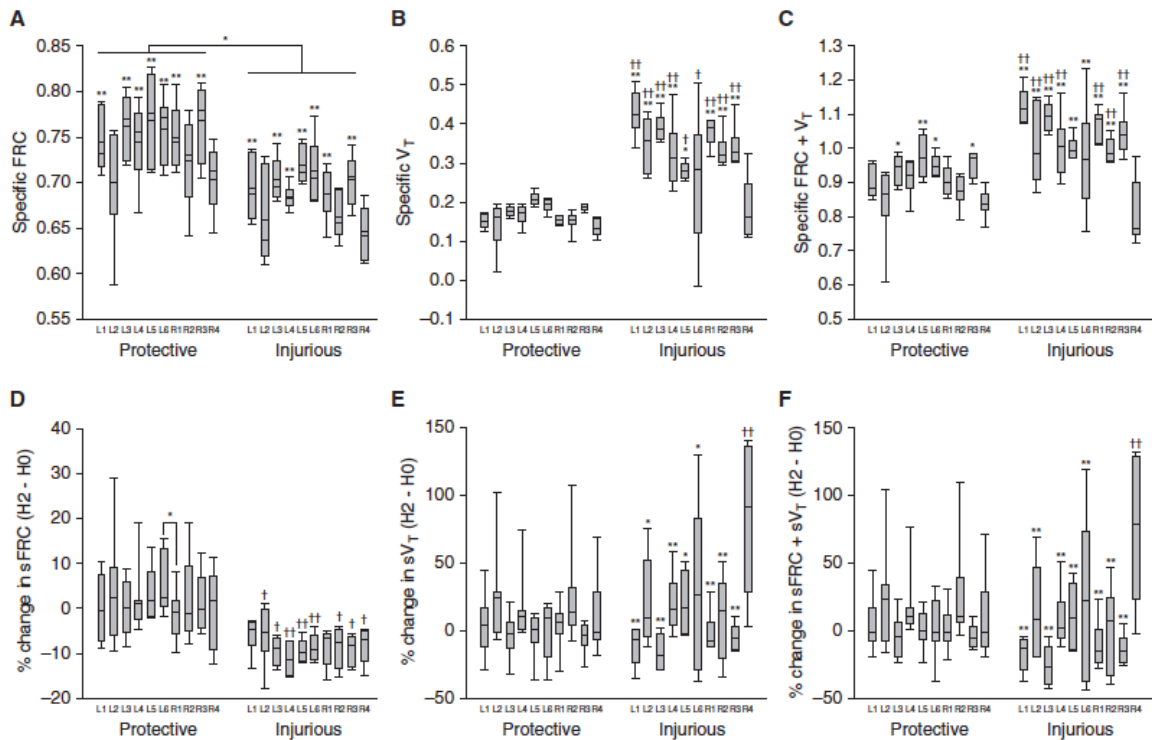


FIGURE 4.11: Box plots from Yen & Preissner *et al.* (2019) of the regional specific tidal volume ( $sV_T$ ) and regional specific end-expiratory volume (denoted sFRC) from imaging. The one-hit VILI study investigated protective and injurious mechanical ventilation on healthy mice. H0 denotes the values at baseline (i.e., 0 hours mechanical ventilation), and H2 denotes the values after 2 hours of mechanical ventilation.

Highlights from the imaging data at baseline include:

- a significant difference in the sEEV (sFRC) between the groups, which reflects the increased PEEP for the protective group (panel A Figure 4.11).
- a significant difference in the  $sV_T$  and total stretch (sEEV +  $sV_T$ ) between the groups for all of the regions except R4, which reflects the higher PIP value in the injurious group (panels B and C in Figure 4.11).

These results at baseline are somewhat to be expected as an outcome of the very different ventilation strategies in these groups, however, perhaps more interesting is the variation across regions, as determined by the significant difference between

regions: sEEV varied regionally in both groups, whereas the  $sV_T$  at baseline was more homogeneous in the protective ventilation group than in the injurious group.

The data at two hours ventilation are presented in Figure 4.11 in panels D, E and F as a percent change in specific volume from 0 hours to two hours ventilation. The global values were computed as a sum of all the regional specific volumes, and reported as a change between 0 hours (H0) and two hours (H2) of mechanical ventilation.

Highlights from these data after two hours of mechanical ventilation are as follows:

- there was no significant change in the average global sEEV,  $sV_T$ , or the total stretch in the protective group.
- the sEEV in the injurious group was decreased after two hours of mechanical ventilation for all of the regions except L1, potentially due to a change in mechanical properties of these regions as a result of the injurious ventilation, potentially due to VILI. However the change in  $sV_T$  as an average value across all regions in this group was minimal.
- in the injurious group, there were *regional* changes in  $sV_T$  and total stretch despite no significant changes in the *global* total stretch after two hours of mechanical ventilation.

Figure 4.12 shows the correlations between lung injury for three biomarkers and regional volumes using linear regression analysis (Yen & Preissner *et al.*, 2019).

Three of the genes studied, IL-6, Ccl2 and Ang-2 (from a set of 21 genes shown in Figure 4.5) showed an overall positive correlation with  $sV_T$ . This shows that tissue injury is clearly linked to over-distension, driven by the regional tidal volume, as shown in panels B, D, F in Figure 4.12. Overall, the data in panels A, C and E in Figure 4.12 shows no significant correlation between regional sEEV (sFRC) and tissue injury markers, indicating that injury due to low volumes is not occurring in these regions.

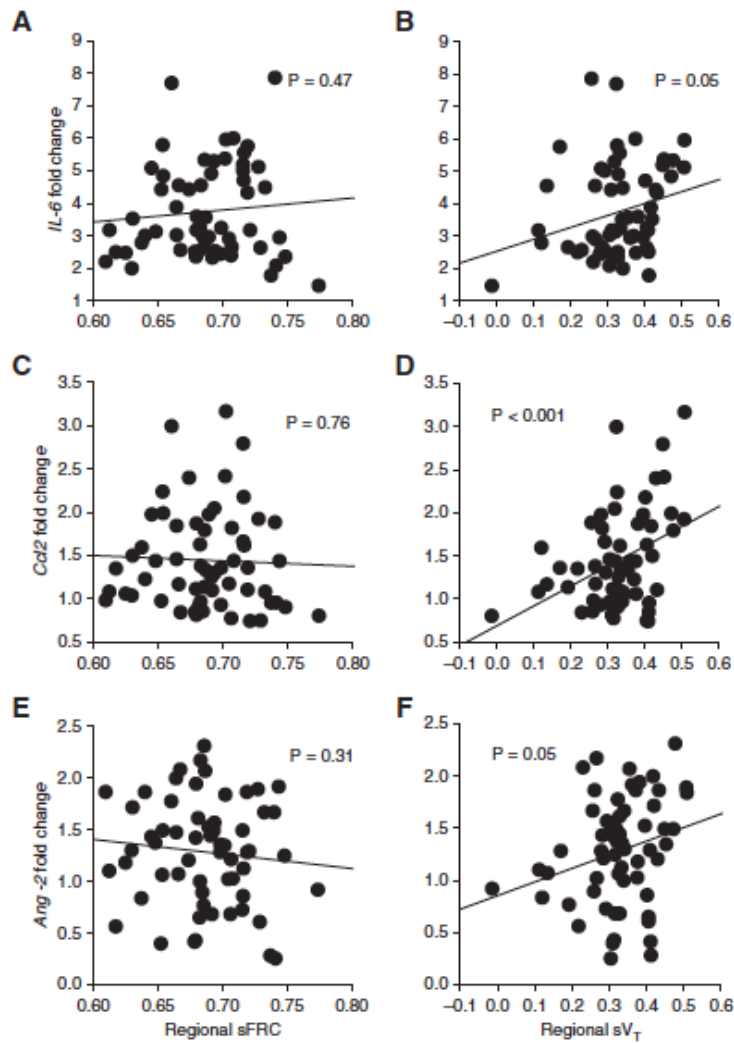


FIGURE 4.12: Scatter plots from Yen & Preissner *et al.* (2019) showing correlation between regional gene expression for three genes (IL-6, Ccl2 and Ang-2) and lung volumes from imaging for the one-hit VILI study. Linear regression lines are shown as a visual aid. Where significance levels are marginal (i.e.,  $P = 0.05$ ), for panels B and F,  $r^2 = 0.063$  in both cases.

#### 4.6.2 Two-hit VILI study

The results of the two-hit VILI study were reported in a published journal article as joint first author in Appendix A (Yen & Preissner *et al.*, 2020). The two-hit VILI study used a mouse model of extra-pulmonary ARDS, whereby the initial injury was endotoxaemia incurred via lipopolysaccharide (LPS), as outlined in Section 4.2 of this chapter.

Figure 4.13 shows imaging data for EEV and VT for the two-hit VILI study mapped throughout the whole lung for representative mice from each group in the study. The regions R1 and L2 for representative mice from each of the groups (control mouse in panel A, and two-hit VILI in panel B) demonstrate an increase in sEEV for the two-hit VILI (extrapulmonary ARDS) group, which is also seen in Figure 4.14 from the box plots across all mice. This may indicate gas-trapping at end-expiration for these regions.

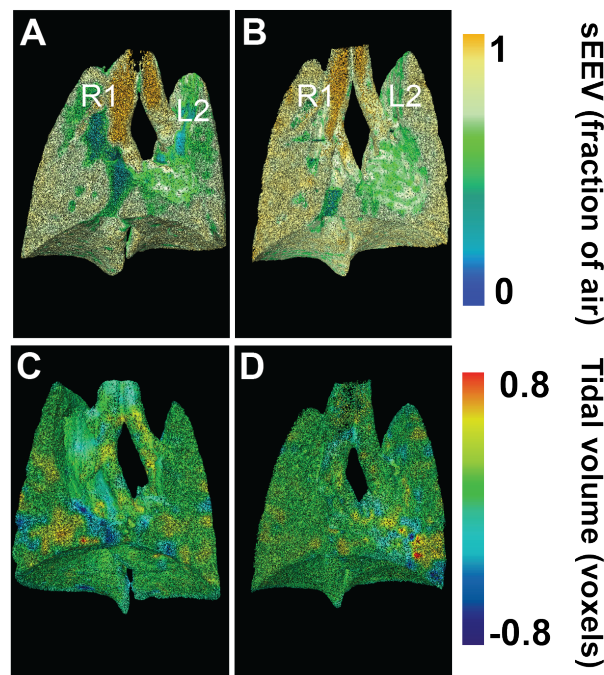


FIGURE 4.13: Volume-rendered images showing the contours for regional end-expiratory volume, sEEV (A, B) and tidal volume (C, D) at baseline for the two-hit VILI (ARDS) study. Panel A demonstrates decreased sEEV for regions R1 and L2 in mice from the control group, as compared to the LPS group in panel B. The tidal volume distribution is relatively homogeneous for both the lungs in panel C (control) and the lungs in panel D (LPS / ARDS).

Box plots with the normalised values for the regional specific lung volumes ( $sV_T$ )

and sEEV, denoted sFRC) from the mouse model of two-hit VILI with extra-pulmonary ARDS are shown in Figure 4.14. To allow between-region comparisons via two-way repeated measures ANOVA, region R4 was used as a reference.

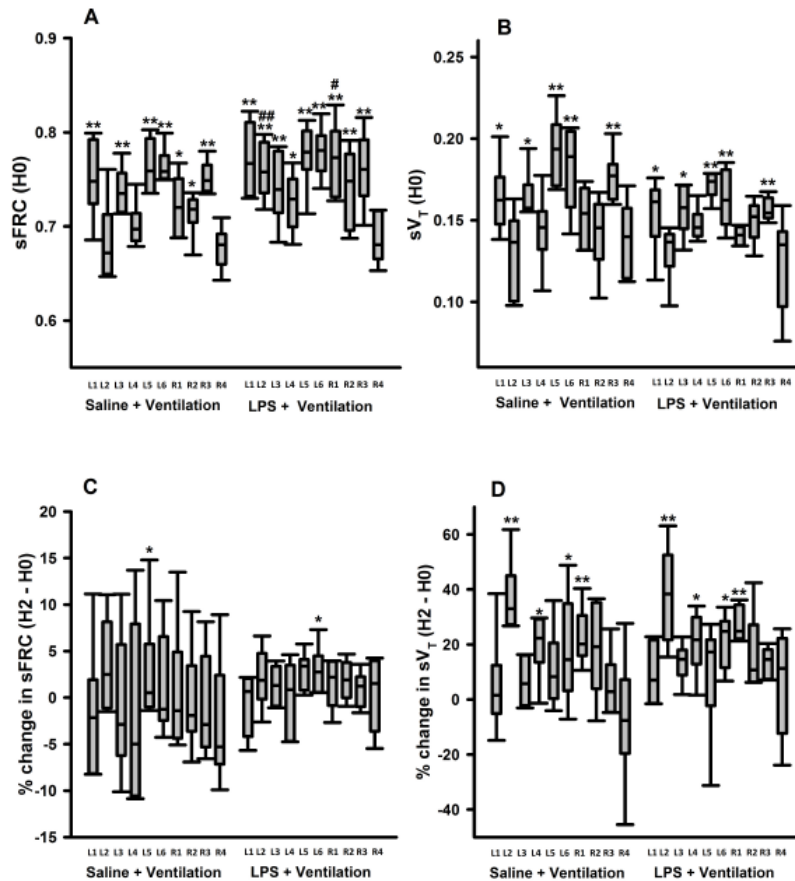


FIGURE 4.14: Box plots of regional lung volumes from imaging for the two-hit VILI study, i.e., extra-pulmonary ARDS plus mechanical ventilation. (Unpublished data. Reproduced with permission from S. Yen).

Overall, and in contrast to the one-hit VILI study, this study indicated that under-ventilation is linked to injury in two-hit VILI with extra-pulmonary ARDS.

Some overall observations from the regional volume data from imaging:

- $sV_T$  at baseline was significantly different when compared across the regions within each group, indicating heterogeneity of ventilation for both groups, independent of initial injury.
- there was no significant change in the regional  $sV_T$  for the two-hit VILI group after two hours of mechanical ventilation.

- a regional difference in sEEV (sFRC) at baseline for the control group was observed for some regions (L1, L3, L5, L6, R1, R2, R3) as compared to R4, whereas in the group with the initial injury, all regions had a higher sEEV (sFRC) than in R4.

Figure 4.15 shows the correlation between two genes, TNF-alpha and IL-6, as biomarkers of lung injury, and the regional lung volumes, sEEV and  $sV_T$ , at baseline (H0). There was no relationship between the values of  $sV_T$  and injury. For sEEV, TNF-alpha had a positive correlation with regional volumes, indicating volutrauma from PIP or possibly air-trapping, whereas IL-6 showed a negative correlation with regional sEEV, indicating that the IL-6 related lung injury in those regions is due to under-distension or atelectasis.

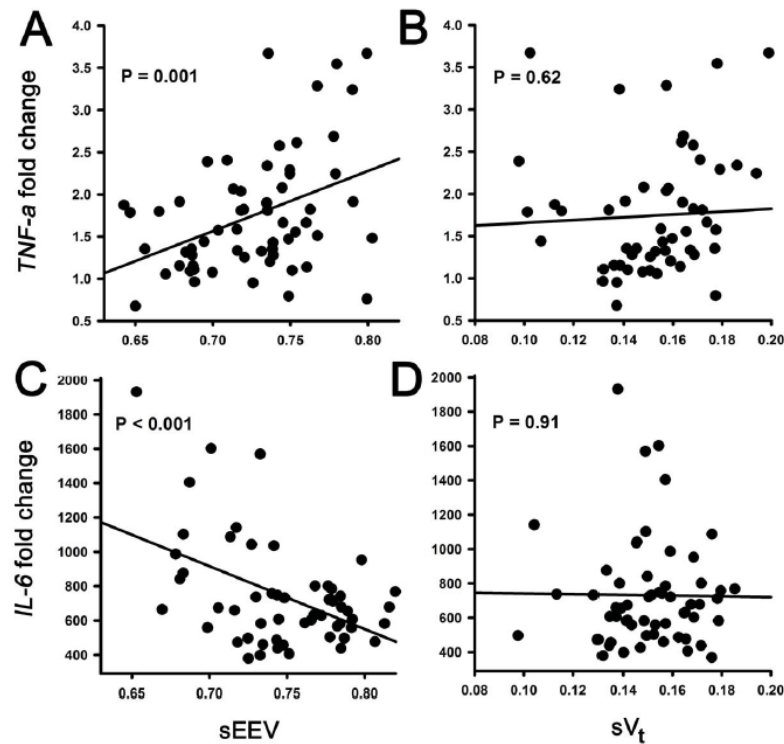


FIGURE 4.15: Relationship between biomarkers of regional lung injury and regional lung volumes, specific end-expiratory volume, sEEV, and specific tidal volume,  $sV_T$ , at baseline mechanical ventilation, H0 (Yen & Preissner *et al.*, 2020). Linear regression lines are shown as a visual aid.

Additional analysis of the data from Figure 4.15, using a concept similar to the  $V_t$ -PEEP plane by Seah *et al.* (2011) described in Section 2.7.5, is shown in Figure 4.16.

The scatterplots show specific tidal volume ( $sV_T$ ) plotted against specific end-expiratory volume (sEEV), whereby an increasing circle size indicates higher relative gene expression, i.e., more injury. The solid lines were drawn arbitrarily to enclose regions that correspond to minimal relative gene expression (i.e., smaller circle sizes), whereby the circles represent gene expression for TNF-alpha in panel A, and in panel B, the circles represent IL-6 gene expression. The dashed line indicates the difference in the two fields, i.e., the region enclosed by solid lines in panel A is shown as dashed in panel B, and vice versa. This indicates that the combination of volumes (sVT and sEEV) that result in less injury for the one-hit VILI (control) group in panel A do not necessarily also result in less injury for the two-hit VILI (endotoxaemic) group. In other words, it shows that pre-existing lung injury affects the combinations of  $sV_T$  and sEEV that minimise regional lung tissue injury.

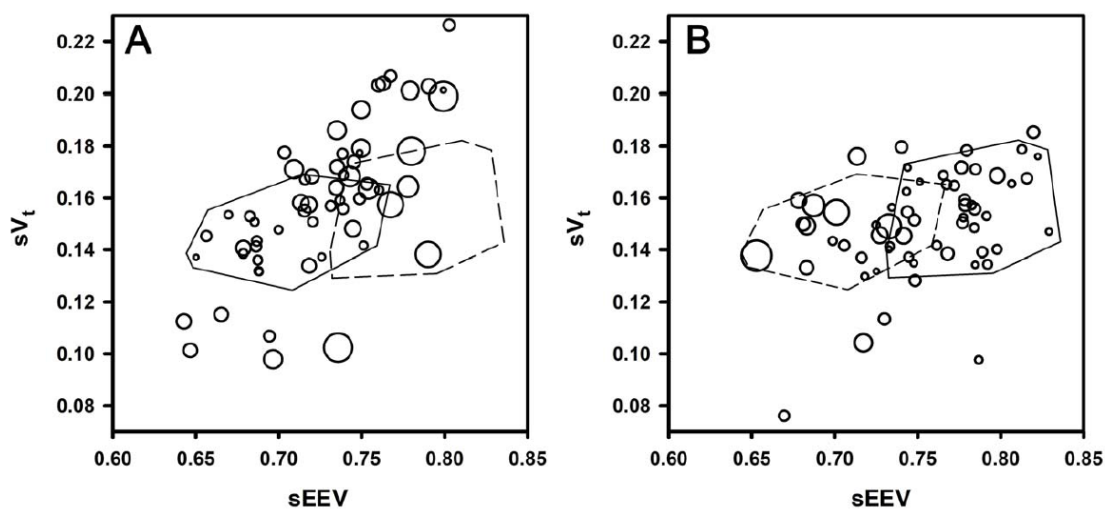


FIGURE 4.16: Scatterplots from Yen & Preissner et al. (2020) of specific tidal volume ( $sV_T$ ) and specific end-expiratory volume (sEEV) for the control group (panel A) and the endotoxaemic group (panel B). Circle size is scaled to relative gene expression: TNF-alpha in panel A and IL-6 in panel B. Circles enclosed by the solid line indicate combinations of  $sV_T$  and sEEV that correspond to minimal gene expression (arbitrarily drawn to enclose the smaller circles), indicating less injury. The dashed region in panel A is a representation of the solid region in panel B, and vice versa, indicating the different effects on lung injury for the same range of regional volumes in each group.

## 4.7 Conclusions

The studies in this chapter investigated the link between regional lung volumes and regional inflammatory markers in mouse models of VILI. These studies presented, for the first time, a direct mapping of regional injury biomarkers to regional *in vivo* lung function in mouse models of VILI. This was made possible with laboratory-based dynamic X-ray CT imaging (Preissner *et al.*, 2018b).

The dynamic imaging facility enabled the regional distribution of tidal volume and end-expiratory volume to be captured throughout the lung *in vivo* in high resolution. In addition, total end-inspiratory volume, the sum of the end-expiratory volume and tidal volume, was used to investigate the role of total stretch, shown in previous studies to lead to lung injury in the presence of moderate tidal volumes (Protti *et al.*, 2015).

Tissue analysis methods using biomarkers are able to sensitively measure local bio-trauma. Combining this information with *in vivo* imaging can elucidate the mechanism, or the driver, of the injury.

These two methods complemented each other by providing correlations between the injury and the volume in the region of interest. The correlations are the most striking aspect of these studies, and in particular, the trend for a positive correlation with regional specific tidal volume and regional injury, which corroborates the current understanding of injury via a high lung volume, i.e., volutrauma, in a one-hit VILI model. Similarly striking is the link between regional lung injury and specific end-expiratory volume in the two-hit VILI model with ARDS, indicating that under-ventilation is the driver of injury in two-hit VILI with ARDS.

Additional studies are required to clearly separate the effects of injury due to high volume, i.e., volutrauma (high PIP), and injury due to low volume, i.e., atelectasis (zero PEEP), which was not possible with the data from the injurious ventilation model. Mapping more combinations of tidal volume and PEEP will allow further exploration of the link between the ventilator settings and regional lung volumes and tissue injury.

This chapter applies a unique approach of anatomical (lobar) and customised

---

sub-lobar segmentation and region alignment without the need for image registration by applying the 4DXV and airway tree link methods. Analysis developed specifically for these studies enabled customised sub-lobar slicing to match the tissue regions in the left lobe, in addition to building on previous work by applying advanced imaging techniques, such as 4DXV and the airway tree link method, for tracking regional volumes. The methods developed within this chapter for the analysis of dynamic X-ray images of mechanically ventilated lungs provide a vital tool for further exploration of VILI.



## 5 Dynamic *in vivo* imaging of structures in the lung

This chapter contains two studies investigating the structures in the mouse lung during mechanical ventilation using the laboratory X-ray imaging system described in Chapter 3. It comprises two published papers: one investigating the airways, one investigating the pulmonary vasculature.

### 5.1 Novel analysis of 4DCT imaging quantifies progressive increases in anatomic dead space during mechanical ventilation

---

Kim E. H.\*, Preissner M.\*, Carnibella R. P., Samarage C. R., Bennett E., Fouras A., Zosky G. R. and Jones H. D.

Published in the Journal of Applied Physiology, 2016

\* The asterisk indicates joint first author, whereby both authors contributed equally to the work.

---

The aim of the study in this journal article was to investigate the effect of prolonged mechanical ventilation on the large airways ( $\geq 0.2$  mm diameter) in mouse models of one-hit VILI and two-hit VILI with pulmonary ARDS. This study observed distension of the airways during mechanical ventilation, which led to an increase in anatomic dead space.

The laboratory imaging system described in Chapter 3 was used to obtain the 4DCT images. The airways were segmented from the CT images at end-inspiration and end-expiration in order to obtain the airway tidal volume. The four-dimensional X-ray velocimetry (4DXV) technique was used to obtain the lung parenchymal tidal volume (Dubsky *et al.*, 2012). The total tidal volume was defined as the lung parenchymal tidal volume plus the airway tidal volume. The results in this study showed

that the dead space fraction significantly increased over time with mechanical ventilation, but was independent of the initial lung injury, i.e., pulmonary ARDS.

The dead space fraction was calculated as a ratio of airway tidal volume to total tidal volume, which indicates the proportion of the tidal volume delivered by the ventilator that increased anatomic dead-space as opposed to expanding the alveoli and participating in gas exchange. This is an important insight demonstrating that the ventilator also affects the airways and may have consequences for ventilator settings in the clinic.

This technique can also be applied more broadly to models of VILI and ARDS: it provides information on the distribution of airway diameters throughout the lung and can be used in combination with measurements of regional lung volumes to determine how changes in the structure of the airways may affect regional ventilation heterogeneity (Chen *et al.*, 2018; Jain & Sznajder, 2007). Furthermore, this technique can be used in other models of respiratory disease, such as asthma (Dubsky *et al.*, 2017), or cystic fibrosis (Murrie *et al.*, 2020), where changes in airway calibre or airway collapse plays a vital functional role.

*J Appl Physiol* 123: 578–584, 2017.  
First published June 8, 2017; doi:10.1152/jappphysiol.00903.2016.

## RESEARCH ARTICLE

# Novel analysis of 4DCT imaging quantifies progressive increases in anatomic dead space during mechanical ventilation in mice

Elizabeth H. Kim,<sup>1\*</sup> Melissa Preissner,<sup>2\*</sup> Richard P. Carnibella,<sup>3</sup> Chaminda R. Samarage,<sup>3</sup> Ellen Bennett,<sup>4</sup> Marcio A. Diniz,<sup>5</sup> Andreas Fouras,<sup>3,6</sup> Graeme R. Zosky,<sup>4</sup> and Heather D. Jones<sup>1,6</sup>

<sup>1</sup>Department of Medicine and Women's Guild Lung Institute, Cedars-Sinai Medical Center, Los Angeles, California;

<sup>2</sup>Department of Mechanical and Aerospace Engineering, Monash University, Melbourne, Victoria, Australia; <sup>3</sup>4Dx Limited, Melbourne, Victoria, Australia; <sup>4</sup>School of Medicine, Faculty of Health, University of Tasmania, Hobart, Tasmania, Australia; <sup>5</sup>Biostatistics and Bioinformatics Research Center, Cedars-Sinai Medical Center, Los Angeles, California; and

<sup>6</sup>Biomedical Imaging Research Institute, Cedars-Sinai Medical Center, Los Angeles, California

Submitted 12 October 2016; accepted in final form 4 June 2017

**Kim EH, Preissner M, Carnibella RP, Samarage CR, Bennett E, Diniz MA, Fouras A, Zosky GR, Jones HD.** Novel analysis of 4DCT imaging quantifies progressive increases in anatomic dead space during mechanical ventilation in mice. *J Appl Physiol* 123: 578–584, 2017. First published June 8, 2017; doi:10.1152/jappphysiol.00903.2016.—Increased dead space is an important prognostic marker in early acute respiratory distress syndrome (ARDS) that correlates with mortality. The cause of increased dead space in ARDS has largely been attributed to increased alveolar dead space due to ventilation/perfusion mismatching and shunt. We sought to determine whether anatomic dead space also increases in response to mechanical ventilation. Mice received intratracheal lipopolysaccharide (LPS) or saline and mechanical ventilation (MV). Four-dimensional computed tomography (4DCT) scans were performed at onset of MV and after 5 h of MV. Detailed measurements of airway volumes and lung tidal volumes were performed using image analysis software. The forced oscillation technique was used to obtain measures of airway resistance, tissue damping, and tissue elastance. The ratio of airway volumes to total tidal volume increased significantly in response to 5 h of mechanical ventilation, regardless of LPS exposure, and airways demonstrated significant variation in volumes over the respiratory cycle. These findings were associated with an increase in tissue elastance (decreased lung compliance) but without changes in tidal volumes. Airway volumes increased over time with exposure to mechanical ventilation without a concomitant increase in tidal volumes. These findings suggest that anatomic dead space fraction increases progressively with exposure to positive pressure ventilation and may represent a pathological process.

**NEW & NOTEWORTHY** We demonstrate that anatomic dead space ventilation increases significantly over time in mice in response to mechanical ventilation. The novel functional lung-imaging techniques applied here yield sensitive measures of airway volumes that may have wide applications.

anatomic dead space; mechanical ventilation; four-dimensional computed tomography; velocimetry

ACUTE RESPIRATORY DISTRESS SYNDROME (ARDS) is a severe, life-threatening form of respiratory failure characterized by its acute onset, diffuse lung inflammation, and severe hypoxemia

\* E. H. Kim and M. Preissner contributed equally to this work.

Address for reprint requests and other correspondence: H. D. Jones, 9600 Advanced Health Sciences Pavilion, 127 San Vicente Blvd., Los Angeles, CA 90048 (e-mail: heather.jones@cshs.org).

(19, 27). Many physiological abnormalities are associated with ARDS, including poor gas exchange and decreased lung compliance. Increased dead space is another well-recognized physiological disturbance in the ARDS lung (14, 15, 23), and recent studies have demonstrated that it is an early prognostic marker of mortality (5, 14, 15, 23). Increased dead space in ARDS is primarily attributable to increased alveolar dead space through ventilation/perfusion heterogeneity and shunt (6, 28). However, positive pressure ventilation and positive end-expiratory pressure (PEEP) increase anatomic dead space, which is the volume of air in the upper airways that does not participate in gas exchange (6, 9, 30). Therefore the effects of mechanical ventilation on anatomic dead space might play a role in the increased dead space of ARDS, although increased anatomic dead space has not yet been linked to increased mortality in this disease.

In vivo studies of small animal airway morphology and responses of the airways to mechanical ventilation are challenging, and novel approaches have been used to overcome the size limitations. Sinclair et al. (32) ventilated rats using tantalum dust to provide contrast during microfocal X-ray imaging of the airways and demonstrated increased airway distension and strain with increasing tidal volumes and PEEP. Nickles et al. (22) used a flat-panel volume micro-CT scanner to acquire high-spatial resolution images of the trachea, the right and left main bronchi, and the large segmental bronchi of mice and demonstrated a similar, large increase in upper airway volumes with mechanical ventilation compared with spontaneous breathing. These authors also elegantly demonstrated an increase in inflammatory cytokine production in isolated tracheas exposed to ventilation. However, in vivo responses of airways to prolonged exposure to mechanical ventilation have not been examined to date.

The aim of this study was to determine how the large airways respond over time to positive pressure ventilation. We addressed this by applying four-dimensional computed tomography (4DCT) to mice in a model of prolonged (5 h) mechanical ventilation. We used intensity-based thresholding and skeletonization-based image-processing techniques to analyze CT images to directly measure the airway volumes. We applied X-ray velocimetry to the same image data to generate detailed three-dimensional tissue expansion maps (7, 10, 21, 25), which allowed us to precisely measure lung tidal volumes. Combining these measurements, we estimated the relative contribution

of airway volumes to the total tidal volume,  $V_{aw}/V_t$ , and discovered that this ratio increases over time in response to mechanical ventilation.

#### METHODS

**Animals.** Eight-week-old BALB/c female mice ( $n = 11$ ) were obtained from Monash Animal Research Platform (Monash University, Melbourne, VIC, Australia). All experiments were approved by the local Animal Ethics Committee of Monash University (Melbourne, VIC, Australia) and conducted in accordance with the guidelines set out in the Australian Code of Practice for the Care and Use of Animals for Scientific Purposes.

**Administration of intratracheal reagents.** Mice were transiently anesthetized with isoflurane (Piramal Healthcare, Bethlehem, PA) and suspended from their incisors for intratracheal instillation of lipopolysaccharide (LPS, *Escherichia coli*; 0111:B4, ultrapure; InvivoGen, San Diego, CA;  $n = 6$ ) or saline alone (Pfizer, Bentley, WA, Australia;  $n = 5$ ). LPS was diluted in saline (100  $\mu\text{g}/\text{ml}$ ), and both groups received 2  $\mu\text{l}/\text{g}$  body wt of solution intratracheally (total volumes ranged from 45 to 60  $\mu\text{l}$ ). We demonstrated in a prior study that this dose of intratracheal LPS (0.2 mg/kg) does not cause lung injury alone, but can lead to lung injury in conjunction with injurious mechanical ventilation (13). Following instillation, mice were allowed to recover from anesthesia and returned to their cages.

**Tracheostomy and mechanical ventilation.** Ninety minutes after intratracheal LPS or saline, mice were anesthetized with intraperitoneal injections of a mix of ketamine (Parnell Australia, Alexandria, NSW, Australia) and xylazine (Xylazil-20; Troy Laboratories, Smithfield, NSW, Australia) at doses of 150 and 10 mg/kg, respectively. Each mouse was securely restrained in a custom-built acrylic chassis (7) in a supine position, and a surgical tracheostomy was performed as previously described (35). Mice were then ventilated using pressure control ventilation on a mouse ventilator (4Dx; Melbourne, VIC, Australia) with an inspiratory pressure of 20  $\text{cmH}_2\text{O}$ , zero positive end-expiratory pressure (PEEP), and inspiratory and expiratory times of 300 ms each (a respiratory rate of 100 breaths/min). Tidal volumes with these settings were  $\sim 250$   $\mu\text{l}$  for a 20-g mouse, or 12.5  $\mu\text{l}/\text{g}$  (12.5 ml/kg). Mice underwent mechanical ventilation (MV) for a total of 5 h and were imaged at the onset of MV and after 5 h of MV.

Subcutaneous saline (500  $\mu\text{l}$ ) was administered at the onset of MV and after 3 h of MV. Repeat doses of anesthesia were administered as subcutaneous injections as needed (usually every 2–3 h). Mice were kept warm using pocket warmers wrapped around the lower abdomen and legs.

**Imaging protocol.** Imaging was conducted in the Laboratory for Dynamic Imaging at Monash University (Melbourne, VIC, Australia). The X-ray-imaging setup consisted of a high-brightness microfocus (15- $\mu\text{m}$  spot size) X-ray source (Excillum, Kista, Sweden; 16, 17). This X-ray source (70 kV, 250 W) produces a spectrum with a characteristic peak at 25 keV. A high-speed complementary metal-oxide semiconductor (CMOS) flat-panel detector (PaxScan; Varian Medical Systems, Palo Alto, CA) with an isotropic pixel size of 0.194 mm was used to capture images at a frame rate of 30 Hz and an exposure time of 18 ms. The system enables appreciable propagation-based phase contrast, which results in lung tissue speckle patterns, based on the contrast between air and soft tissue (17). The mouse was positioned in the acrylic chassis in front of the X-ray beam in the upright position. A high-precision rotary stage (Zaber Technologies, Vancouver, BC, Canada) was used to rotate the mice 360 deg under mechanical ventilation for the 4DCT scan. The imaging was synchronized with ventilation and gated to obtain 800 projection images of the lungs at end-expiration and end-inspiration for CT reconstruction. The radiation dose delivered (equating to 1,600 projections with 18-ms exposure times and an air kerma rate of 5.01 mGy/s) was measured to be 120 mGy, which is 1.8% of the  $\text{LD}_{50/30}$  (the dose of radiation

expected to cause death to 50% of an exposed population within 30 days;  $\sim 7$  Gy) for BALB/c mice (24).

A calibration scan of an acrylic cylinder with fiducials (34) was performed before and after the mouse scans. This process captures the tilt angle and center of rotation of the scan necessary for accurate CT reconstruction results. The source-to-isocenter of the rotation stage and source-to-detector distances were 374 and 3,315 mm, respectively, resulting in an effective isotropic voxel size of 21.9  $\mu\text{m}$  for the entire imaging system.

**Image analysis.** The airway trees at the end-expiratory (Fig. 1, A and D) and end-inspiratory (Fig. 1, B and E) phases of the respiratory cycle were extracted in a two-stage process. Using Avizo (FEI Visualization Sciences Group, M $\acute{e}$ rinac, France) 3D visualization and analysis software, the airways were first segmented using a threshold-based flood fill technique. The root of the airway tree was then specified manually, and the centerline tree was extracted using a skeletonization procedure. We included airways with diameters  $\geq 0.2$  mm for analysis as this was the smallest airway diameter that could be reliably resolved (data not shown).

Two investigators (H. D. Jones and E. H. Kim) independently calculated the volumes for each airway tree using the open-source software ParaView (1). Given the diameter threshold, not all subsegmental airways were present on all airway tree reconstructions for the same mouse, and therefore only airways that were present on all four airway trees (0-h MV and 5-h MV end-expiratory and end-inspiratory scans) were measured. We compared the volume measurements between the two investigators and found excellent interobserver agreement (intraclass correlation coefficients of 0.97–1.0).

We used the term “airway tidal volume” ( $\Delta V_{aw}$ ) to denote the difference between the end-inspiratory airway tree volume and the end-expiratory airway tree volume. Lung parenchymal tidal volumes were calculated using velocimetry analysis (7, 8; Fig. 1, C and F). Total lung tidal volumes ( $V_t$ ) were calculated by adding airway volumes and parenchymal tidal volumes. The anatomic dead space fraction was calculated as the ratio of airway volume to total tidal volume ( $V_{aw}/V_t$ ).

**Lung function.** Lung mechanics were assessed using a modification of the forced oscillation technique as described previously (36). Briefly, during 6-s pauses in ventilation at elastic equilibrium lung volume, an oscillatory signal, delivered from a loudspeaker via a wave tube, was introduced via the tracheal cannula. The oscillatory signal contained nine frequencies ranging from 4 to 38 Hz and was used to calculate the respiratory system impedance spectrum ( $Z_{rs}$ ). A four-parameter model with constant phase tissue impedance (11) was fitted to the  $Z_{rs}$  to calculate the airway resistance ( $R_{aw}$ ), tissue damping ( $G$ ), and tissue elastance ( $H$ ). These measurements were made at baseline, 2.5 h, and 5 h into the ventilation period.

**Statistics.** Between-group comparisons for airway volumes ( $V_{aw}$ ), airway tidal volumes ( $\Delta V_{aw}$ ), total lung tidal volumes ( $V_t$ ),  $V_{aw}$ -to- $V_t$  ratios, and lung function were made using a two-way repeated-measures ANOVA (treatment  $\times$  time) with Holm-Sidak post hoc tests. Data are presented as means (SD), and  $P < 0.05$  was considered statistically significant. Relationships between  $V_{aw}/V_t$  and lung mechanics ( $R_{aw}$ ,  $G$ , and  $H$ ) were assessed by Pearson correlation.

Intraclass correlation coefficients (ICC) were calculated considering a two-way mixed model to evaluate the interobserver agreement for airway measurements for four time points as well as their respective 95% confidence interval. Values close to 1 indicate excellent agreement, and values close to 0 indicate poor agreement. In addition, an  $F$ -test was computed to evaluate the null hypothesis of ICC = 0; a  $P$  value  $< 0.05$  rejects this hypothesis.

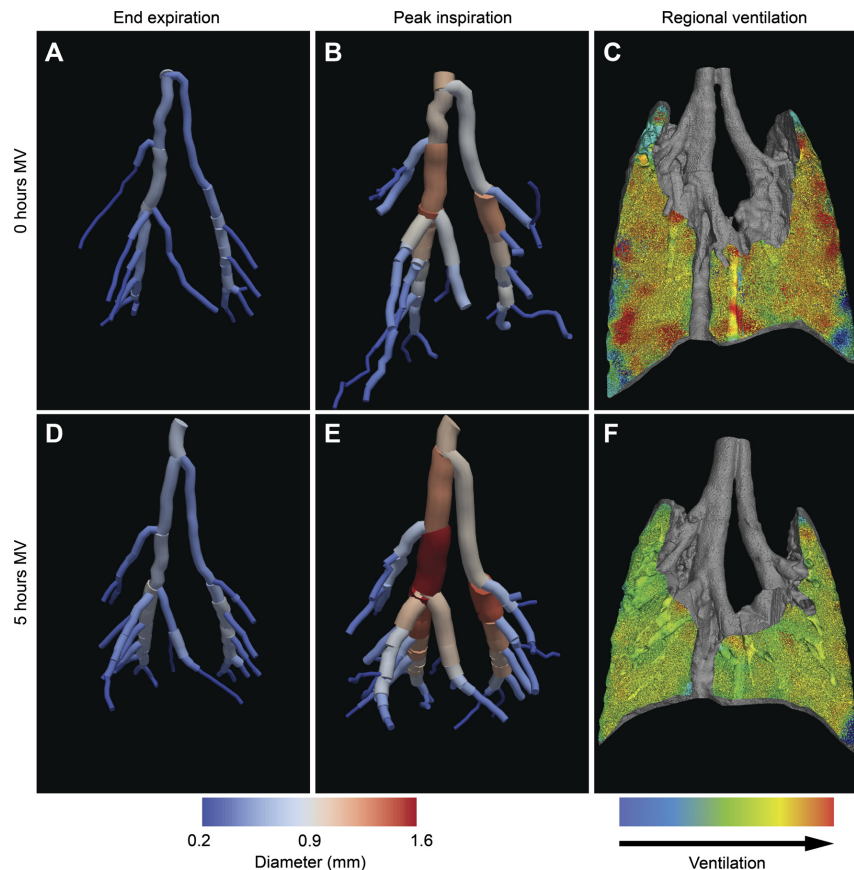


Fig. 1. Analysis of large airway volumes and regional ventilation. Three-dimensional reconstructions of the larger airways ( $>0.2$  mm) of each mouse were performed at end-expiration (A and D) and end-inspiration (B and E), and regional tidal ventilation (C and F) was measured for scans performed at the onset of mechanical ventilation (0-h MV; A–C) and after 5 h of mechanical ventilation (5-h MV; D–F). Only airways that were determined to be present on all four airway images were selected for volume measurements.

## RESULTS

**Anatomic dead space fraction increases with mechanical ventilation.** Five hours of mechanical ventilation led to increases in both the large airway volumes,  $V_{aw}$  ( $P < 0.0001$ ; Fig. 2A), and the change in volume between end-expiration and end-inspiration, which we termed the airway tidal volume,  $\Delta V_{aw}$  ( $P < 0.0001$ ; Fig. 2B). In contrast, mechanical ventilation had minimal effect on total tidal volume,  $V_t$  ( $P = 0.09$ ; Fig. 2C), such that the ratio of  $V_{aw}$  to  $V_t$ , or the anatomic dead space fraction, increased after 5 h of ventilation compared with baseline ( $P < 0.0001$ ; Fig. 2D). There was no difference between the LPS- and saline-treated mice for any of these parameters (airway volumes,  $P = 0.94$ ;  $\Delta V_{aw}$ ,  $P = 0.63$ ;  $V_t$ ,  $P = 0.12$ ;  $V_{aw}/V_t$ ,  $P = 0.19$ ). Individual mice demonstrated a consistent increase in  $V_{aw}/V_t$  for both saline+MV and LPS+MV conditions (Fig. 2E).

**Tissue elastance increases in response to mechanical ventilation.** We measured airway resistance (Raw), tissue damping (G), and tissue elastance (H) to determine whether a change in any lung function parameters mirrored the changes seen in  $V_{aw}$  and  $V_{aw}/V_t$  in response to mechanical ventilation. There was no effect of LPS challenge ( $P = 0.69$ ) or mechanical ventilation ( $P = 0.54$ ) on Raw (Fig. 3A). H increased by the end of the ventilation period ( $P = 0.04$ ), but there was no difference between LPS+MV and saline+MV treatment groups ( $P = 0.35$ ; Fig. 3B). In contrast, whereas LPS challenge had no effect on baseline G ( $P = 0.47$ ), ventilation increased G in the LPS+MV group (5 h,  $P = 0.002$ ) such that G was significantly higher by the end of the ventilation period in the LPS+MV group compared with the saline+MV group ( $P = 0.008$ ; Fig. 3C). Whereas no correlation was seen between Raw and  $V_{aw}/V_t$

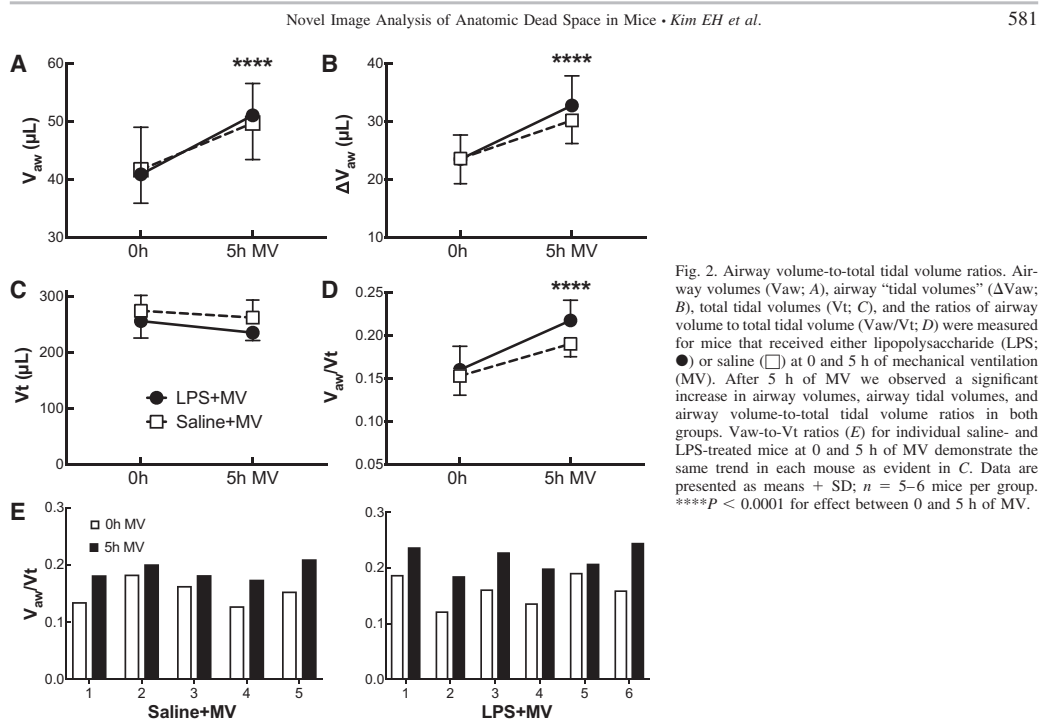


Fig. 2. Airway volume-to-total tidal volume ratios. Airway volumes ( $V_{aw}$ ; A), airway "tidal volumes" ( $\Delta V_{aw}$ ; B), total tidal volumes ( $V_t$ ; C), and the ratios of airway volume to total tidal volume ( $V_{aw}/V_t$ ; D) were measured for mice that received either lipopolysaccharide (LPS; ●) or saline (□) at 0 and 5 h of mechanical ventilation (MV). After 5 h of MV we observed a significant increase in airway volumes, airway tidal volumes, and airway volume-to-total tidal volume ratios in both groups.  $V_{aw}$ -to- $V_t$  ratios (E) for individual saline- and LPS-treated mice at 0 and 5 h of MV demonstrate the same trend in each mouse as evident in C. Data are presented as means + SD;  $n = 5-6$  mice per group. \*\*\*\* $p < 0.0001$  for effect between 0 and 5 h of MV.

( $r = -0.22$ ,  $P = 0.44$ ) or between  $H$  and  $V_{aw}/V_t$  ( $r = 0.38$ ,  $P = 0.19$ ). G showed a significant correlation with  $V_{aw}/V_t$  ( $r = 0.72$ ,  $P = 0.003$ ).

#### DISCUSSION

We used a mouse model to determine whether mechanical ventilation, with or without LPS challenge, impacted anatomic dead space. The main finding of this report is that the anatomic dead space fraction,  $V_{aw}/V_t$ , is significantly increased in response to 5 h of mechanical ventilation. Additionally, airway excursion during inspiration, which we termed the airway "tidal volume," also increases in response to prolonged mechanical ventilation. To our knowledge, this is the first time that airway volumes have been shown to increase over time on mechanical ventilation.

This study builds on prior work characterizing airway volumes during mechanical ventilation (22, 32). We took advantage of the enhanced contrast between air and soft tissue that is possible with phase contrast X-ray technology (due to the refractive index between the 2 materials) to obtain detailed images of the airways and lung parenchyma. We used 4DCTs to capture dynamic information about airway distension during the respiratory cycle that might have been lost by comparing static inspiratory and expiratory CTs, which are susceptible to gas redistribution during the required breath holds (26). Our technique improves on prior imaging techniques by providing higher resolution of airways compared with flat-plate micro-CT (22), and our image analysis with thresholding and

skeletonization allowed continuous measurements of all subsegmental airways  $>0.2$  mm compared with focal measurements at specified points in the airways (22, 32). Furthermore, we demonstrated that the airway volumes continue to increase over time in response to mechanical ventilation, which suggests dynamic changes in the anatomic dead space in response to this stimulus, and has not been previously reported.

There is strong evidence from older literature (6, 9, 30) showing that anatomic dead space increases with positive pressure ventilation. For example, anatomic dead space was shown to increase in direct relationship to increasing levels of PEEP in dogs, an effect ascribed to increased functional residual capacity (from increased PEEP) and the mechanical effects of increased lung volumes on conducting airway caliber (6, 9). Indeed, Severinghaus and Stupfel demonstrated a linear relationship between anatomic dead space and functional residual capacity and also between anatomic dead space and tidal volumes (30). In the same report, the authors described an increase in anatomic dead space with conditions that caused decreased compliance and noted that "under the conditions of constant ventilation, a decreased compliance is followed by increased positive pressure during inspiration, and it is this pressure which distends the anatomic dead space" (30). These same authors demonstrated a substantial (30%) increase in anatomic dead space in human subjects injected with atropine and concluded that the bronchomotor tone controls the volume of anatomic dead space (31) suggesting that airway stiffness is a determinant of the response.

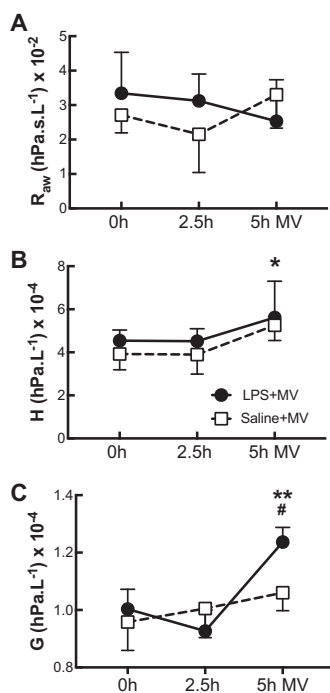


Fig. 3. Lung mechanics during prolonged mechanical ventilation. Lung mechanics of mice that received either lipopolysaccharide (LPS; ●) or saline (□) were assessed using a forced oscillation technique (see METHODS) at 0, 2.5, and 5 h of mechanical ventilation (MV). Airway resistance ( $R_{aw}$ ; A), tissue elastance ( $H$ ; B), and tissue damping ( $G$ ; C) are shown. Data are presented as means  $\pm$  SD;  $n = 3-4$  mice per group. \* $P < 0.05$  for both LPS and saline groups at 0 and 5 h of MV; \*\* $P < 0.005$  for LPS mice at 5 h of MV; # $P < 0.05$  for LPS vs. saline groups at 5 h of MV.

Applying these observations to our model, we cannot attribute the increased airway tidal volumes to increased functional residual capacity because we did not apply PEEP. Furthermore, we used a pressure control mode of ventilation and did not observe significant changes in tidal volumes after 5 h of MV (Fig. 2B). We observed decreased parenchymal compliance, reflected as increased elastance (Fig. 3B) in both groups in response to 5 h of MV, which is consistent with findings from prior studies of lung mechanics in ventilated mice (3). However, we cannot attribute the increased airway volumes to decreased compliance as per the mechanism postulated by Severinghaus and Stupfel (30), because we used pressure control ventilation and hence the positive pressure was fixed in our study. Furthermore, total tidal volumes did not decrease, suggesting a minimal effect of the changes in compliance. We observed an increase in tissue damping that was restricted to the LPS-challenged mice (Fig. 3C) and suggests that LPS exposure in this model has resulted in peripheral airway inhomogeneity (18). However, this finding is unlikely to play a role in the airway dilatation as it was only found in LPS-exposed

mice, whereas both saline- and LPS-exposed mice had similar increases in airway volumes.

Another possible mechanism of increased anatomic dead space in this study is increased airway compliance, either from decreased bronchomotor tone due to factors secreted in response to mechanical ventilation or from mechanical disruption of airway structural integrity with continuous exposure to positive pressure ventilation. The prior work by Sinclair et al. (32) and Nickles et al. (22) sets the stage for understanding how this might occur. Sinclair et al. demonstrated significant increases in airway strain with the application of positive pressure ventilation, and Nickles et al. showed that inflammatory cytokines such as IL-1 $\beta$ , which are known to affect cell-cell tight junctions (2, 4), are secreted by isolated trachea in response to ventilation. These observations suggest that the changes we observed over time in airway volumes in response to mechanical ventilation may represent a pathological response of the airways to prolonged exposure to positive pressure.

A further consideration is the possibility that the intrabronchial airway surface fluid lining becomes thinner over the course of 5-h MV from the drying effects of the nonhumidified air used in mouse ventilators. Indeed, a high-resolution phase contrast X-ray-imaging approach has previously been used to specifically examine the airway surface liquid layer and to visualize mucocilliary transport of debris within a live mouse airway to a resolution of 2–5  $\mu\text{m}$  (33). However, the resolution of our technique is ~50–60  $\mu\text{m}$  (29; unpublished data), which is below the range of airway surface liquid layer thicknesses in mice of 10–30  $\mu\text{m}$  (20), and therefore we would be unable to detect changes in the airway surface liquid layer in our study. In any case, a thinning of the airway surface liquid layer would not explain the changes in airway volumes over the respiratory cycle because the thickness of the airway surface liquid layer would not change from inspiration to expiration. Hence the dynamic changes we detect over the course of 5-h MV likely reflect actual airway excursion rather than thinning of the fluid lining the airways due to drying.

Our study has several limitations. The first and most obvious is that mouse airways are orders of magnitude smaller than human airways, and it is unlikely that the trachea and mainstem bronchi in humans demonstrate marked dilatation over time on MV. However, these structures have intact cartilaginous rings, and although the mouse trachea also has cartilaginous rings, the murine main bronchi and segmental airways do not and therefore are more comparable to distal airways in humans (12). It is plausible to consider that the progressive effects of mechanical ventilation that we observed in the mouse airways may have corollaries in the noncartilaginous airways in humans, and this question needs to be the subject of future study.

We did not observe increased elastance in response to LPS exposure compared with saline exposure, which was unexpected. In prior work, we found that intratracheal LPS plus volume control mechanical ventilation in male C57BL/6 mice caused significantly worse lung injury compared with saline plus mechanical ventilation controls (13). However, in this study we used female BALB/c mice and pressure control ventilation, and it is likely that strain, sex, and ventilation mode played a significant role in susceptibility to acute lung injury under these conditions.

In summary, we applied a novel functional lung-imaging technique to image the motion of lung tissue and airways in mechanically ventilated mice and detected a significant increase in airway volumes and airway expansion over time on mechanical ventilation. This report builds on prior studies showing increased airway volumes during positive pressure ventilation, and we have demonstrated that airway volumes continue to increase with prolonged exposure to positive pressure ventilation in the absence of increased tidal volumes. Mechanisms of this progressive increase in airway volumes remain to be elucidated but may represent pathological responses to mechanical ventilation. Furthermore, our novel imaging technique demonstrates a degree of resolution of airway morphology and volume measurements heretofore not possible, and the ability to image the airways in mice *in vivo* with this degree of resolution opens the door to many further applications in airway and other lung diseases.

#### ACKNOWLEDGMENTS

We thank Dr. William Parks and Dr. Wolfgang Kuebler for thoughtful discussions and editorial advice.

#### GRANTS

This work was funded by National Heart, Lung, and Blood Institute Grant 125806 (H. D. Jones), National Health and Medical Research Council Project Grant 1077905 (G. R. Zosky), NHMRC Development Grant APP1055116 (A. Fouras), and a Multi-modal Australian Sciences Imaging and Visualization Environment grant (MASSIVE Project NCLy40; A. Fouras).

#### DISCLOSURES

A. Fouras is founder and CEO of 4Dx. C. R. Samarage and R. Carnibella are employees and have stock ownership in 4Dx. H. D. Jones has stock ownership in 4Dx.

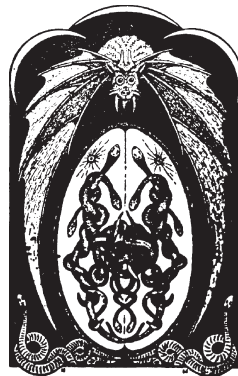
#### AUTHOR CONTRIBUTIONS

M.P., R.C., A.F., G.R.Z., and H.D.J. conceived and designed research; E.H.K., M.P., R.C., E.B., and H.D.J. performed experiments; E.H.K., M.P., R.C., C.R.S., E.B., M.A.D., A.F., G.R.Z., and H.D.J. analyzed data; E.H.K., M.P., R.C., E.B., M.A.D., G.R.Z., and H.D.J. interpreted results of experiments; M.P., R.C., C.R.S., G.R.Z., and H.D.J. prepared figures; M.P., G.R.Z., and H.D.J. drafted manuscript; E.H.K., M.P., R.C., C.R.S., M.A.D., A.F., G.R.Z., and H.D.J. edited and revised manuscript; E.H.K., M.P., R.C., C.R.S., E.B., M.A.D., A.F., G.R.Z., and H.D.J. approved final version of manuscript.

#### REFERENCES

- Ahrens J, Geveci B, Law C. ParaView: an end-user tool for large data visualization. In: *Visualization Handbook*, edited by Hansen CD and Johnson CR. New York: Elsevier, 2005, p. 717–731. doi:10.1016/B978-012387582-2/50038-1.
- Al-Sadi R, Ye D, Dokladny K, Ma TY. Mechanism of IL-1beta-induced increase in intestinal epithelial tight junction permeability. *J Immunol* 180: 5653–5661, 2008. doi:10.4049/jimmunol.180.8.5653.
- Cannizzaro V, Hantos Z, Sly PD, Zosky GR. Linking lung function and inflammatory responses in ventilator-induced lung injury. *Am J Physiol Lung Cell Mol Physiol* 300: L112–L120, 2011. doi:10.1152/ajplung.00158.2010.
- Capaldo CT, Nusrat A. Cytokine regulation of tight junctions. *Biochim Biophys Acta* 1788: 864–871, 2009. doi:10.1016/j.bbame.2008.08.027.
- Charron C, Repesse X, Bouferrache K, Bodson L, Castro S, Page B, Jardin F, Vieillard-Baron A. PaCO<sub>2</sub> and alveolar dead space are more relevant than PaO<sub>2</sub>/FiO<sub>2</sub> ratio in monitoring the respiratory response to prone position in ARDS patients: a physiological study. *Crit Care* 15: R175, 2011. doi:10.1186/cc10324.
- Coffey RL, Albert RK, Robertson HT. Mechanisms of physiological dead space response to PEEP after acute oleic acid lung injury. *J Appl Physiol Respir Environ Exerc Physiol* 55: 1550–1557, 1983.
- Dubsky S, Hooper SB, Siu KK, Fouras A. Synchrotron-based dynamic computed tomography of tissue motion for regional lung function measurement. *J R Soc Interface* 9: 2213–2224, 2012. doi:10.1098/rsif.2012.0116.
- Dubsky S, Jamison RA, Higgins SP, Siu KK, Hourigan K, Fouras A. Computed tomographic X-ray velocimetry for simultaneous 3D measurement of velocity and geometry in opaque vessels. *Exp Fluids* 52: 543–554, 2012. doi:10.1007/s00348-010-1006-x.
- Dueck R, Wagner PD, West JB. Effects of positive end-expiratory pressure on gas exchange in dogs with normal and edematous lungs. *Anesthesiology* 47: 359–366, 1977. doi:10.1097/0000542-197710000-00007.
- Fouras A, Allison BJ, Kitchen MJ, Dubsky S, Nguyen J, Hourigan K, Siu KK, Lewis RA, Wallace MJ, Hooper SB. Altered lung motion is a sensitive indicator of regional lung disease. *Ann Biomed Eng* 40: 1160–1169, 2012. doi:10.1007/s10439-011-0493-0.
- Hantos Z, Adamicza A, Govaerts E, Daróczy B. Mechanical impedances of lungs and chest wall in the cat. *J Appl Physiol* (1985) 73: 427–433, 1992.
- Hyde DM, Hamid Q, Irvin CG. Anatomy, pathology, and physiology of the tracheobronchial tree: emphasis on the distal airways. *J Allergy Clin Immunol* 124, Suppl: S72–S77, 2009. doi:10.1016/j.jaci.2009.08.048.
- Jones HD, Crother TR, Gonzalez-Villalobos RA, Jupelli M, Chen S, Dagvadorj J, Ardití M, Shimada K. The NLRP3 inflammasome is required for the development of hypoxemia in LPS/mechanical ventilation acute lung injury. *Am J Respir Cell Mol Biol*, 50: 270–280, 2014. doi:10.1165/rcmb.2013-0087OC.
- Kallet RH, Alonso JA, Pittet JF, Matthay MA. Prognostic value of the pulmonary dead-space fraction during the first 6 days of acute respiratory distress syndrome. *Respir Care* 49: 1008–1014, 2004.
- Kallet RH, Zhuo H, Liu KD, Calfee CS, Matthay MA; National Heart Lung and Blood Institute ARDS Network Investigators. The association between physiologic dead-space fraction and mortality in subjects with ARDS enrolled in a prospective multi-center clinical trial. *Respir Care* 59: 1611–1618, 2014. doi:10.4187/respcare.02593.
- Kitchen MJ, Buckley GA, Leong AF, Carnibella RP, Fouras A, Wallace MJ, Hooper SB. X-ray specks: low dose *in vivo* imaging of lung structure and function. *Phys Med Biol* 60: 7259–7276, 2015. doi:10.1088/0031-9155/60/18/7259.
- Larsson DH, Lundström U, Westermark UK, Arsenian Henriksson M, Burvall A, Hertz HM. First application of liquid-metal-jet sources for small-animal imaging: high-resolution CT and phase-contrast tumor demarcation. *Med Phys* 40: 021909, 2013. doi:10.1118/1.4788661.
- Lutchen KR, Hantos Z, Peták F, Adamicza A, Suki B. Airway inhomogeneities contribute to apparent lung tissue mechanics during constriction. *J Appl Physiol* (1985) 80: 1841–1849, 1996.
- Matthay MA, Ware LB, Zimmerman GA. The acute respiratory distress syndrome. *J Clin Invest* 122: 2731–2740, 2012. doi:10.1172/JCI60331.
- Morgan KS, Donnelly M, Paganin DM, Fouras A, Yagi N, Suzuki Y, Takeuchi A, Uesugi K, Boucher RC, Parsons DW, Siu KK. Measuring airway surface liquid depth in *ex vivo* mouse airways by X-ray imaging for the assessment of cystic fibrosis airway therapies. *PLoS One* 8: e55822, 2013. doi:10.1371/journal.pone.0055822. [Erratum. *PLoS One* 9 (May): e97829, 2014. doi:10.1371/journal.pone.0097829.]
- Ng I, Paganin DM, Fouras A. Optimization of in-line phase contrast particle image velocimetry using a laboratory X-ray source. *J Appl Phys* 112: 074701, 2012. doi:10.1063/1.4757407.
- Nickles HT, Sumkauskaitė M, Wang X, Wegner I, Puderbach M, Kuebler WM. Mechanical ventilation causes airway distension with proinflammatory sequelae in mice. *Am J Physiol Lung Cell Mol Physiol* 307: L27–L37, 2014. doi:10.1152/ajplung.00288.2013.
- Nuckton TJ, Alonso JA, Kallet RH, Daniel BM, Pittet JF, Eisner MD, Matthay MA. Pulmonary dead-space fraction as a risk factor for death in the acute respiratory distress syndrome. *N Engl J Med* 346: 1281–1286, 2002. doi:10.1056/NEJMoa012835.
- Okunieff P, Wu T, Huang K, Ding I. Differential radioprotection of three mouse strains by basic or acidic fibroblast growth factor. *Br J Cancer Suppl* 27: S105–S108, 1996.
- Parsons DW, Morgan K, Donnelly M, Fouras A, Crosbie J, Williams I, Boucher RC, Uesugi K, Yagi N, Siu KK. High-resolution visualization of airspace structures in intact mice via synchrotron phase-contrast X-ray imaging (PCXI). *J Anat* 213: 217–227, 2008. doi:10.1111/j.1469-7580.2008.00950.x.
- Paula LF, Wellman TJ, Winkler T, Spieth PM, Güldner A, Venegas JG, Gama de Abreu M, Carvalho AR, Vidal Melo MF. Regional tidal

- lung strain in mechanically ventilated normal lungs. *J Appl Physiol* (1985) 121: 1335–1347, 2016. doi:10.1152/jappphysiol.00861.2015.
27. Ranieri VM, Rubenfeld GD, Thompson BT, Ferguson ND, Caldwell E, Fan E, Camporota L, Slutsky AS; ARDS Definition Task Force. Acute respiratory distress syndrome: the Berlin definition. *JAMA* 307: 2526–2533, 2012. doi:10.1001/jama.2012.5669.
28. Robertson HT, Swenson ER. What do dead-space measurements tell us about the lung with acute respiratory distress syndrome? *Respir Care* 49: 1006–1007, 2004.
29. Samarage CR, Carnibella R, Preissner M, Jones HD, Pearson JT, Fouras A, Dubsky S. Technical Note: contrast free angiography of the pulmonary vasculature in live mice using a laboratory X-ray source. *Med Phys* 43: 6017–6023, 2016. doi:10.1118/1.4964794.
30. Severinghaus JW, Stupfel M. Alveolar dead space as an index of distribution of blood flow in pulmonary capillaries. *J Appl Physiol* 10: 335–348, 1957.
31. Severinghaus JW, Stupfel M. Respiratory dead space increase following atropine in man, and atropine, vagal or ganglionic blockade and hypothermia in dogs. *J Appl Physiol* 8: 81–87, 1955.
32. Sinclair SE, Molthen RC, Haworth ST, Dawson CA, Waters CM. Airway strain during mechanical ventilation in an intact animal model. *Am J Respir Crit Care Med* 176: 786–794, 2007. doi:10.1164/rccm.200701-088OC.
33. Siu KK, Morgan KS, Paganin DM, Boucher R, Uesugi K, Yagi N, Parsons DW. Phase contrast X-ray imaging for the non-invasive detection of airway surfaces and lumen characteristics in mouse models of airway disease. *Eur J Radiol* 68, Suppl: S22–S26, 2008. doi:10.1016/j.ejrad.2008.04.029.
34. Yang K, Kwan AL, Miller DF, Boone JM. A geometric calibration method for cone beam CT systems. *Med Phys* 33: 1695–1706, 2006. doi:10.1118/1.2198187.
35. Zosky GR, Cannizzaro V, Hantos Z, Sly PD. Protective mechanical ventilation does not exacerbate lung function impairment or lung inflammation following influenza A infection. *J Appl Physiol* (1985) 107: 1472–1478, 2009. doi:10.1152/jappphysiol.00393.2009.
36. Zosky GR, Janosi TZ, Adamicza A, Bozanich EM, Cannizzaro V, Larcombe AN, Turner DJ, Sly PD, Hantos Z. The bimodal quasi-static and dynamic elastance of the murine lung. *J Appl Physiol* (1985) 105: 685–692, 2008. doi:10.1152/jappphysiol.90328.2008.



## 5.2 Application of a novel *in vivo* imaging approach to measure pulmonary vascular responses in mice

---

Preissner M., Murrie R. P., Bresee C., Carnibella R. P., Fouras A., Weir E. K., Dubsky S., Pinar I. P. and Jones H. D.

Published in *Physiological Reports*, 2018

---

The aim of the study in this journal article was to investigate the pulmonary vasculature in mice during mechanical ventilation. The contrast-free pulmonary angiography (CFPA) technique (Samarage *et al.*, 2016) was applied to measure the responses of the pulmonary vasculature in mice under various conditions. The co-authored journal article describing the CFPA technique is included in Appendix B.

One group of mice was given a hypoxic/hypercarbic gas mixture and then imaged on the laboratory X-ray system, providing information on the changes in the total number of vessels during recovery. A separate group of healthy mice were used to investigate the pulmonary vasculature over the breath cycle during mechanical ventilation, whereby the volume of blood and the number of vessels was measured in order to capture the intra-breath changes.

The results of this study demonstrated proof-of-concept that contrast-free imaging of mice on the laboratory X-ray system can capture dynamic, quantitative information about the pulmonary vasculature, down to diameters of approximately 60  $\mu\text{m}$ . These results indicate that mechanical ventilation may adversely affect the delicate blood vessels and have implications on the haemodynamics in ARDS and VILI. Since the CFPA technique is a post-processing technique applied on the 4DCT images acquired on the laboratory X-ray system, it can simultaneously provide information on the pulmonary vasculature in addition to the functional information obtained from regional lung volumes, as described in Chapter 4.

Furthermore, since no contrast agents are required to be administered to the animal, this CFPA technique has the advantage of imaging in the same animal over time, which is especially pertinent to small animals where the administration of contrast agents may be technically challenging and invasive, especially for CT imaging where rotation of the animal is usually required.

Moderate hypertension has been found in patients with ARDS (Vieillard-Baron *et al.*, 2016), indicating that constriction of the pulmonary blood vessels plays a role in impaired respiratory function in these patients. Therefore, animal studies may benefit from simultaneous analysis of both regional lung function and the pulmonary vasculature, in order to better understand the causes of impaired respiratory function in VILI and ARDS.

# Physiological Reports

Open Access

Physiological Reports ISSN 2051-817X

ORIGINAL RESEARCH

## Application of a novel *in vivo* imaging approach to measure pulmonary vascular responses in mice

Melissa Preissner<sup>1</sup>, Rhiannon P. Murrie<sup>1</sup>, Catherine Bresee<sup>2</sup>, Richard P. Carnibella<sup>3</sup>, Andreas Fouras<sup>1,3,5</sup>, E. Kenneth Weir<sup>4</sup>, Stephen Dubsy<sup>1</sup>, Isaac P. Pinar<sup>1,a</sup> & Heather D. Jones<sup>5,a</sup>

1 Department of Mechanical and Aerospace Engineering, Monash University, Melbourne, Victoria, Australia

2 Cedars-Sinai Medical Center, Biostatistics & Bioinformatics Research Institute, Los Angeles, California

3 4Dx Limited, Melbourne, Victoria, Australia

4 Department of Medicine, University of Minnesota, Minneapolis, Minnesota

5 Department of Biomedical Sciences, Cedars-Sinai Medical Center, Biomedical Imaging Research Institute, Los Angeles, California

### Keywords

4DCT, *in vivo* imaging, micro-CT, pulmonary vasculature.

### Correspondence

Heather Jones, Biomedical Imaging Research Institute, Department of Biomedical Sciences, Cedars-Sinai Medical Center, 8700 Beverly Blvd., Los Angeles, CA 90048.

Tel: +1 310-423-1837

Fax: +1 310-967-0639

E-mail: heather.jones@cshs.org

### Funding Information

This work was funded by National Institutes of Health grant K08HL125806 (HJ), National Health and Medical Research Council (NHMRC) Project Grant APP1055116 (AF), and a Multi-modal Australian ScienceS Imaging and Visualisation Environment grant (MASSIVE project number NCLy40)(AF), Australian Research Council - Discovery Project DP150102240 (grant recipient Andreas Fouras), Australian Research Council - Discovery Early Career Researcher Award DE180101133 (grant recipient Stephen Dubsy).

Received: 21 August 2018; Accepted: 24 August 2018

doi: 10.14814/phy2.13875

*Physiol Rep*, 6 (18), 2018, e13875,  
<https://doi.org/10.14814/phy2.13875>

<sup>a</sup>These authors contributed equally to this work.

### Abstract

Noninvasive imaging of the murine pulmonary vasculature is challenging due to the small size of the animal, limits of resolution of the imaging technology, terminal nature of the procedure, or the need for intravenous contrast. We report the application of laboratory-based high-speed, high-resolution x-ray imaging, and image analysis to detect quantitative changes in the pulmonary vascular tree over time in the same animal without the need for intravenous contrast. Using this approach, we detected an increased number of vessels in the pulmonary vascular tree of animals after 30 min of recovery from a brief exposure to inspired gas with 10% oxygen plus 5% carbon dioxide (mean  $\pm$  standard deviation: 2193  $\pm$  382 at baseline vs. 6177  $\pm$  1171 at 30 min of recovery;  $P < 0.0001$ ). In a separate set of animals, we showed that the total pulmonary blood volume increased ( $P = 0.0412$ ) while median vascular diameter decreased from 0.20 mm (IQR: 0.15–0.28 mm) to 0.18 mm (IQR: 0.14–0.26 mm;  $P = 0.0436$ ) over the respiratory cycle from end-expiration to end-inspiration. These findings suggest that the noninvasive, nonintra-venous contrast imaging approach reported here can detect dynamic responses of the murine pulmonary vasculature and may be a useful tool in studying these responses in models of disease.

## Introduction

*In vivo* imaging techniques to study the pulmonary vasculature in mice provide valuable information on pulmonary physiology and mechanisms of disease. For example, elegant experiments using intravital microscopy of the murine pulmonary microcirculation have provided novel insights into such processes as hypoxic pulmonary vasoconstriction (Tabuchi et al. 2008; Wang et al. 2012; Goldenberg et al. 2015), leukocyte migration (Ichimura et al. 2005), and endothelial calcium signaling (Kieffmann et al. 2009; Rowlands et al. 2011). Single-photon emission computed tomography (SPECT) imaging can characterize lung perfusion patterns in mice (Jobse et al. 2012; Koba et al. 2013) but the low resolution of this technique is an inherent limitation. Resin instillation has also been used to generate a detailed radiopaque cast of the murine vasculature, which can then be imaged using high-resolution micro-CT scanning (Molthen et al. 2004; Faight et al. 2017), but this technique is a terminal procedure. To date, quantitative *in vivo* imaging of the murine pulmonary vascular tree has required both intravenous contrast and synchrotron-based radiation (Sonobe et al. 2011; Porra et al. 2017).

Previously, this approach required synchrotron-based x-ray sources (Kitchen et al. 2005; Morgan et al. 2014). However, recent advances in compact imaging have made it possible to perform high resolution, high speed imaging in a laboratory (Tuohimaa et al. 2007; Pfeiffer et al. 2008; Bech et al. 2013; Zhou et al. 2013; Larsson et al. 2016; Preissner et al. 2018). These recent advances in preclinical imaging provide further steps toward development in the area of clinical applications (Bravin et al. 2013). A number of authors on this study used laboratory-based 4DCT x-ray imaging and postimage acquisition analysis (Samarage et al. 2016) to generate three-dimensional, quantitative pulmonary vascular trees from scans acquired without intravenous contrast. We compared the measurements of vessel diameters obtained using this method to measurements obtained in the same animals via pulmonary angiography with intravenous contrast and found excellent correlation. Here, we describe the application of this technique to characterize the pulmonary vascular response over time in mice to exposure to hypoxic/hypercarbic gas exposure and recovery from such exposure, and the changes in pulmonary blood volume during inspiration with positive pressure mechanical ventilation. We noted dynamic changes in the number of vessels detected before and after brief hypoxic/hypercarbic gas exposure, which we hypothesize may reflect dilatation or constriction of vessels near the limit of detection. Furthermore, we demonstrate an increase in pulmonary blood volume but a decrease in median vessel diameter with

inspiration during positive pressure ventilation. We propose that this novel imaging and image analysis approach will be a useful technique for studying *in vivo* pulmonary vascular responses in small animal models of lung disease.

## Methods

### Ethical approval and animals

Eight-week old BALB/c female mice ( $n = 7$ ) were obtained from the Monash Animal Research Platform (Monash University, Melbourne, VIC, Australia). All experiments were approved by the local Animal Ethics Committee of Monash University (Ethics Project MARP/2014/137; Melbourne, VIC, Australia) and conducted in accordance with the guidelines set out in the Australian Code of Practice for the Care and Use of Animals for Scientific Purposes. Authors of this manuscript understand the ethical principles under which the Journal of Physiology operates and our work complies with the animal ethics as outlined in the journal (Grundy 2015).

### Mechanical ventilation

Mice were anesthetized with intraperitoneal injections of a mix of ketamine (Parnell Australia Pty Ltd, Alexandria NSW, Australia) and xylazine (Xylazil-20, Troy Laboratories Pty Ltd, Smithfield NSW, Australia) at doses of 150 mg/kg and 10 mg/kg respectively. The depth of anesthesia was determined to be adequate by the absence of a toe-pinch reflex. During housing, prior to anesthesia, mice were provided with food and water *ad libitum*. Each mouse was orotracheally intubated and securely restrained in a custom-built chassis (Dubsky et al. 2012) in a supine position. Mice were then ventilated using pressure control ventilation on a mouse ventilator (AccuVent, Notting Hill Devices, Melbourne, VIC, Australia). For the hypoxia/hypercarbia experiment ( $n = 4$  mice, identified as M1 to M4), the ventilator settings were: inspiratory pressure of 18 cmH<sub>2</sub>O, 2 cmH<sub>2</sub>O positive end-expiratory pressure (PEEP), and inspiratory and expiratory times of 200 ms each (a respiratory rate of 150 breaths/min). Tidal volumes with these settings were  $8.5 \pm 2.1 \mu\text{L/gm}$  (mL/kg). For the Expiration/Inspiration experiment ( $n = 3$  mice, identified as M5 to M7), ventilator settings were: inspiratory pressure of 20 cmH<sub>2</sub>O, 2 cmH<sub>2</sub>O PEEP, and inspiratory and expiratory times of 300 msec each (a respiratory rate of 100 breaths/min). Tidal volumes with these settings were calculated as  $9.1 \pm 0.8 \mu\text{L/gm}$  (mL/kg). All tidal volumes were calculated from the CT images. Subcutaneous saline (500  $\mu\text{L}$ ) was administered at the onset of mechanical ventilation (MV). Mice were kept warm using pocket warmers wrapped around the lower abdomen and

legs. The end point of the study was euthanasia via cervical dislocation under anesthesia.

### Hypoxia/CO<sub>2</sub> protocol

Mice were imaged at baseline on room air ("Baseline"), and then the inhaled gas for the ventilator was changed to 10% oxygen, 5% carbon dioxide, and 85% nitrogen balance. We used a gas with both decreased oxygen and increased carbon dioxide concentrations based on literature suggesting that increased inhaled carbon dioxide concentrations would enhance hypoxic vasoconstrictor effects on the pulmonary vasculature (Hyde et al. 1964; Noble et al. 1981; Orchard et al. 1983; Lumb and Slinger 2015). Inhaled oxygen percentage was measured using an oxygen controller (ProOX 110, BioSpherix, Parish, NY) to ensure inhaled oxygen had reached 10%, which takes approximately 5 min (Fig. 2) due to gas mixing within the ventilator lines, and then animals were imaged again immediately ("10%O<sub>2</sub> + 5%CO<sub>2</sub>"), with a 10 sec delay while researchers moved from the x-ray imaging room to the control room. It was not possible to wait for longer periods of hypoxic/CO<sub>2</sub> gas exposure before imaging, because the animals became dysynchronous with the ventilator within 8 min of exposure to hypoxic/CO<sub>2</sub> gas (and 4DCT imaging scans required 5 min to obtain). Animals were then switched back to room air, and the inhaled oxygen concentration was monitored to ensure return to 21%. Animals were imaged again after 10 min ("10 m Post") and 30 min ("30 m Post") of ventilation with oxygen concentration greater than or equal to 19% (about 4 min after stopping hypoxic gas due to mixing within ventilator lines, Fig. 2). Arterial oxygen saturations were measured in mice before the Baseline and 10 m Postscans using a MouseOX pulse oximeter (STARR Life Sciences, Oakmont, PA). After imaging, oxygen saturations for one animal (M4) were monitored during re-exposure to hypoxic/CO<sub>2</sub> gas, and then on return to room air to generate the data for Figure 2.

### Imaging protocol

Imaging was conducted at the Laboratory for Dynamic Imaging, Monash University (Melbourne, VIC, Australia). The imaging for the hypoxia/CO<sub>2</sub> experiment utilized a prototype small animal high-speed, high-resolution microfocus x-ray imaging system (Kim et al. 2017; Preissner et al. 2018). For the Expiration/Inspiration ("Expir/Inspir") experiment, a commercial version of the x-ray imaging system was used (Notting Hill Devices, Melbourne, Australia). Both instruments utilized microfocus x-ray sources and a high-speed flat-panel detector (PaxScan, Varian Medical Systems, Palo Alto, CA). Taking into

account geometric magnification, images are captured at a frame rate of 30 Hz and an exposure time of 18 msec with an effective pixel size of 19  $\mu$ m. The mouse was positioned in the chassis in front of the x-ray beam in the upright position. A high precision rotary stage (Zaber Technologies, Vancouver, Canada) was used to rotate the mice 360 degrees under mechanical ventilation for the four-dimensional computed tomography (4DCT) scan. The imaging was synchronized with ventilation and gated to obtain 800 projection images of the lungs for CT reconstruction. A calibration scan of an acrylic cylinder with fiducials (Yang et al. 2006) was performed before and after the mouse scans. This process captures the tilt angle and center of rotation of the scan necessary for accurate CT reconstruction results. Mice were imaged four times for the hypoxia/CO<sub>2</sub> experiment, and once for the Expiration/Inspiration experiment, and subsequently euthanized.

### Image analysis

Each 4DCT scan from all animals was phase-binned and synchronized with the ventilator. CT analysis was performed using the peak inspiration CT reconstruction for the hypoxia/CO<sub>2</sub> experiment, and using CT reconstructions from end-expiration ("Expiration") and end-inspiration ("Inspiration") phases of the respiratory cycle for the Expiration/Inspiration experiment.

The segmentation of the pulmonary vasculature was based on the contrast-free pulmonary angiography (CFPA) technique by Samarage et al. (2016). This technique uses a Hessian-based filter that uses multiple Gaussian scales to detect the probability of a tube-like structure in the 3D image (Frangi et al. 1998). The algorithm defines a sharp threshold below which no vessels will be detected, which in our case, is in the range of 0.04–0.06 mm in diameter. The filtered image is used to obtain a 3D centerline tree of the segmented vessels with measurements of diameters mapped at equi-distant points along the tree ("Measurements"). From this, various parameters, such as the distribution of diameters along the tree and the number of segments in the tree can be extracted. For the purposes of this study, we define a vessel as the segment between branching points along the centerline tree ("Vessels"). The segmentation was applied to the whole lung in order to capture the full range of visible pulmonary vessels, including the large conduit vessels.

### Pulmonary blood vessel volume calculation

The volume of the pulmonary blood vessels (outer diameter) for animals from the Expiration/Inspiration experiment (mice identified as M5 to M7) was calculated by

obtaining a cylindrical volume for each segment in the centerline tree, i.e., by calculating the Euclidean distance between the points and using the branch (i.e., vessel) diameter obtained from the filtered image (described above) at each point. The individual segment volumes were then summed to obtain the aggregate volume for the lung, including the large conduit vessels.

### Tidal volume calculations

The tidal volumes for the hypoxia/CO<sub>2</sub> mice (M1–M4) at baseline were calculated by converting the image to Hounsfield Units (HU) in order to obtain a quantitative measure of fraction of air per voxel, based on the standard definition of HU (Kalender 2005). The fractions were summed for the whole lung parenchyma and converted to volumes for both the end-inspiration and the end-expiratory images. The difference was calculated as the tidal volume (Fuld et al. 2008). The tidal volumes for the Expiration/Inspiration mice (M5, M6, M7) were estimated from the difference in the fraction of air in the lungs between inspiration and expiration in the CT images (Fuld et al. 2008).

### Heart rate measurements

Heart rates in the Expiration/Inspiration experiment (mice identified as M5 to M7) were measured using real-time x-ray videos of the thorax that were obtained during CT image acquisition (Videos S1–S3). The number of heart beats for a 10 sec period was counted, and that number was multiplied by 6 to obtain beats per minute.

### Statistical analysis

Changes in the median vessel diameters were tested across animals over time using generalized linear mixed modeling techniques to adjust for the repeated measures within each animal and fitted to a gamma distribution given the skewed nature of the data. Average number of vessels and diameter measurements were tested across time with repeated measures ANOVA (hypoxia/CO<sub>2</sub> model) or paired T-test (Expir/Inspir model). Correlations between number of vessels and number of diameter measurements was constructed using mixed model linear regression to account for repeated measures across animals. Residuals were inspected to confirm the overall fit of all modeling. For all testing the level of significance was set at a two-sided *P*-value of <0.05 and post hoc testing was adjusted for multiple comparisons with Tukey T-tests. Data are presented as means ± standard deviations (SD) or median ± interquartile range (IQR). Analysis was performed using SAS v9.4 software.

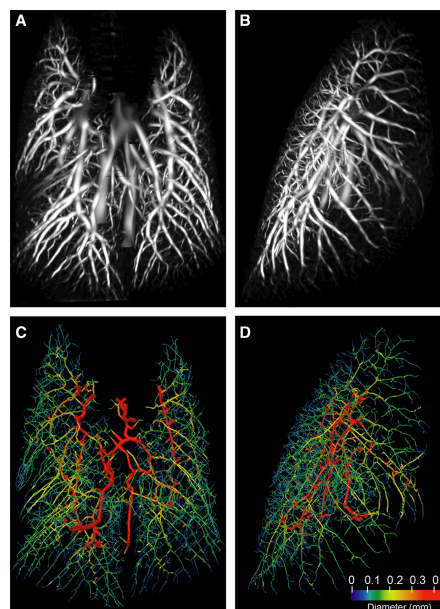


**Figure 1.** Murine pulmonary vasculature derived from a CT scan without intravenous contrast. A healthy 8 week old BALB/c mouse was scanned once using dynamic x-ray imaging and end-inspiration images were segmented as described under Methods. (A, B) Probability field of the filtered image, as a maximum intensity projection (A, frontal; B, lateral); (C, D) Vessel diameters mapped to the centerline tree for the same animal/scan (C, frontal; D, lateral). Branch thickness is reduced by a factor of 6.8 for clarity.

## Results

### Vascular tree reconstructions

Reconstructed pulmonary vascular trees from the non-contrast CT scans were obtained using the CFFA image analysis technique developed and previously reported by some of the authors of this study (Samarage et al. 2016; Dubsky et al. 2017). Briefly, a filter is applied to the 3D CT image that detects tube-like (i.e., vessel-like) structures (Fig. 1) and provides a measurement of diameters at equi-spaced points along the vessels (see Methods for details). Using this approach, a three-dimensional vascular tree was generated for each scan (Dubsky et al. 2012). A range of 33,000 to 120,000 diameter measurements were obtained per vascular tree.

M. Preissner et al.

New Imaging Approach to Measure Pulmonary Vascular Responses in Mice

### Vessel diameter measurements during and after exposure to hypoxic/hypercarbic gas

To test the hypothesis that hypoxic/hypercarbic pulmonary vasoconstriction could be detected using a noninvasive imaging approach, four sequential x-ray 4DCT scans on each mouse were performed as follows: a baseline scan ventilating with room air ("Baseline"), a scan while ventilating with 10% oxygen and 5% carbon dioxide ("10%O<sub>2</sub> + 5%CO<sub>2</sub>"), and then two more scans after 10 and 30 min of ventilation with room air posthypoxic/hypercarbic gas exposure ("10 m Post" and "30 m Post"). All animals had oxygen saturations of 93% or greater at baseline and upon return to room air ventilation. Ventilation with 10%O<sub>2</sub> + 5%CO<sub>2</sub> gas was confirmed to induce severe hypoxia within minutes by measurement of noninvasive oxygen saturations in one sample mouse (M4) after imaging and prior to euthanasia (Fig. 2).

A three-dimensional vascular tree for each scan was generated and vessel diameters were measured as described above. Two of 16 total scans (mouse M1 at 10 m Post and mouse M2 at 10%O<sub>2</sub> + 5%CO<sub>2</sub>) were of insufficient quality to allow image analysis and so were excluded from this data set. At baseline, median vessel diameter was 0.20 mm (IQR: 0.15–0.29), which was unchanged during 10%O<sub>2</sub> + 5%CO<sub>2</sub> exposure (median 0.20; IQR: 0.15–0.29;  $P = 0.9347$ ), or at 30 m posthypoxia/CO<sub>2</sub> (median 0.20; IQR: 0.15–0.26;  $P = 0.9954$ ). However, at the 10 m posthypoxia/CO<sub>2</sub> time point, the median diameter was smallest at 0.18 mm (IQR: 0.13–

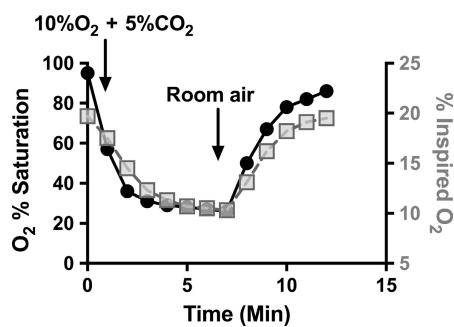


**Figure 2.** Changes in oxygen saturations in response to ventilation with hypoxic/CO<sub>2</sub> gas. Noninvasive oxygen saturations (filled circles, left y axis) in one animal (M4) were tracked at baseline on room air, during ventilation with 10%O<sub>2</sub> + 5%CO<sub>2</sub>, and during return to ventilation with room air after imaging was completed. Inspired oxygen concentration (grey squares, right y axis) was measured at the inspiratory limb of the ventilation circuit at the animal to determine rate of decline and recovery in actual inspired oxygen.

0.25) which was significantly different from baseline ( $P = 0.0025$ ), 10%O<sub>2</sub> + 5%CO<sub>2</sub> ( $P = 0.0095$ ) and 30 m post ( $P = 0.0062$ ); Fig. 3A, and Table 1).

Interestingly, the total number of diameter measurements acquired by the image analysis algorithm increased significantly at 30 min posthypoxia compared to all other time points (vs. baseline,  $P = 0.0024$ ; vs. 10%O<sub>2</sub> + 5%CO<sub>2</sub>,  $P = 0.0023$ ; and vs. 10 m posthypoxia,  $P = 0.0419$ ; Fig. 3B, Table 1). There are two possible explanations for this result from an image analysis perspective: (1) an increase in the length of vessels, which would lead the image analysis algorithm, which obtains diameter measurements of vessels at evenly spaced intervals, to generate more measurements per vessel; or (2) an increase in the total number of vessels detected, and therefore the number of vessels measured by the algorithm. For the purposes of this study, we defined a vessel as the segment between branching points along the centerline tree, and we assessed the number of individual vessels detected at each time point. The number of vessels detected increased and was significantly greater than all other time points at 30 min posthypoxia/CO<sub>2</sub> (vs. baseline,  $P = 0.0005$ ; vs. 10%O<sub>2</sub> + 5%CO<sub>2</sub>,  $P = 0.0005$ ; and vs. 10 m posthypoxia/CO<sub>2</sub>,  $P = 0.0063$ ; Fig. 3C, Table 1). Using the data from all scans in this report (i.e. both the hypoxia/CO<sub>2</sub> and Expiration/Inspiration experiments), we confirmed that the number of blood vessels imaged has a direct correlation with the number of diameter measurements acquired for each scan (Fig. 3D; Pearson's correlation:  $r = 0.9645$ ,  $P < 0.0001$ ).

We examined the distribution of diameter measurements in the hypoxia/CO<sub>2</sub> experiment for all mice over all time points. The peak number of diameter measurements, that is, the mode, was the same in all scans and occurred at a diameter of 0.16 mm (Fig. 4A).

### Pulmonary blood volume increases during positive pressure inspiration

We were interested in understanding how vascular volumes and diameters change over the respiratory cycle during positive pressure ventilation and whether noninvasive imaging and image analysis techniques could provide insight into this phenomenon. We scanned three mice and reconstructed the three-dimensional vascular tree from each animal using the CT scan data from the end-expiration ("Expiration") and end-inspiration ("Inspiration") phases of the respiratory cycle. We found that there was not a statistically significant difference in the number of diameter measurements ( $P = 0.1192$ ) nor vessels detected ( $P = 0.2690$ ) measured between Expiration and Inspiration (Fig. 3F, G). The median diameter did significantly decrease from 0.20 mm (IQR: 0.15–0.28)

New Imaging Approach to Measure Pulmonary Vascular Responses in Mice

M. Preissner et al.

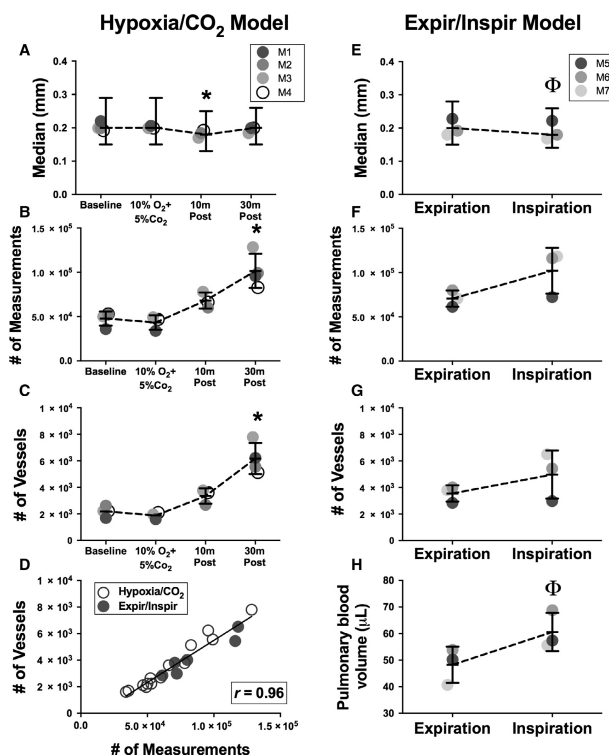


**Figure 3.** Measurements of changes in the murine pulmonary vascular tree during exposure to hypoxic/CO<sub>2</sub> gas and with positive pressure mechanical ventilation. Three-dimensional murine pulmonary vascular trees were reconstructed from CT scans performed without intravenous contrast. Median diameter measurements, numbers of diameter measurements and vessels, and pulmonary blood volumes were determined. (A, E) Median diameters ( $\pm$  IQR) of pulmonary vessels detected for individual mice in response to hypoxic/CO<sub>2</sub> gas exposure (animals M1-4) and from end-expiration to end-inspiration (animals M5-7); (B, F) Mean  $\pm$  SD number of diameter measurements that were able to be obtained from the vascular tree for each experiment; (C, G) Mean  $\pm$  SD number of vessels that were detected from the vascular tree for each experiment; (D) Correlation of number of diameter measurements obtained to number of vessels detected from each vascular tree for all scans ( $r = 0.96$ ,  $P < 0.0001$ ); (H) Mean  $\pm$  SD total pulmonary blood volume during positive pressure ventilation from end-expiration to end-inspiration. Baseline = no treatment; 10%O<sub>2</sub> + 5%CO<sub>2</sub> = during ventilation with 10% oxygen and 5% carbon dioxide; 10 m Post = 10 min of ventilation with room air after ventilation with 10%O<sub>2</sub> + 5%CO<sub>2</sub>; 30 m Post = 30 min of ventilation with room air after ventilation with 10% O<sub>2</sub> + 5%CO<sub>2</sub>. Expiration = data from vascular tree reconstructed from end-expiratory phase of CT scan; Inspiration = data from vascular tree reconstructed from end-inspiratory phase of same CT scan. \* $P < 0.001$  in comparison to all other timepoints. ( $P < 0.05$  in comparison to Expiration).

to 0.18 mm (IQR: 0.14–0.26) with inspiration ( $P = 0.0426$ ; Fig. 3E, Table 1). The mode for these scans, i.e., the peak number of measurements, occurred at 0.17 mm for both Inspiration and Expiration (Fig. 4B).

We hypothesized that total pulmonary blood volume would increase with inspiration due to lung expansion and concomitant vascular expansion. To test this

hypothesis, we measured vascular volumes as described in Methods, and found that pulmonary blood volume did indeed increase with inspiration ( $P = 0.0412$ ; Fig. 3H).

One mouse (M5) had less variation from Expiration to Inspiration (Fig. 3F–H, Fig. 5), and we wondered if this observation was due to low inspiratory volumes for this animal. To explore this possibility, we compared the

M. Preissner et al.

New Imaging Approach to Measure Pulmonary Vascular Responses in Mice

**Table 1.** Vessel diameter data

Group	Timepoint	Number of diameter measurements (Mean $\pm$ SD)	Number of vessels detected (Mean $\pm$ SD)	Median vessel diameter (mm) (IQR)
Hypoxia/CO <sub>2</sub> Model (n = 4 Mice)	Baseline	47,761 $\pm$ 8087	2193 $\pm$ 382	0.20 (0.15–0.29)
	10%O <sub>2</sub> +5%CO <sub>2</sub>	43,268 $\pm$ 8245	1890 $\pm$ 259	0.20 (0.15–0.29)
	10 m Post	68,065 $\pm$ 9172	3357 $\pm$ 583	0.18* (0.13–0.25)
	30 m Post	101,508* $\pm$ 19,257	6177* $\pm$ 1171	0.20 (0.15–0.26)
Exp/Inspir Model (n = 3 Mice)	Expiration	70,613 $\pm$ 9305	3558 $\pm$ 623	0.20 (0.15–0.28)
	Inspiration	102,123 $\pm$ 25,995	4976 $\pm$ 1812	0.18* (0.14–0.26)

Average number of diameter measurements, number of vessels detected, and median diameter measurements obtained from vascular trees for each animal across time points is shown.

\*Indicates that data are significantly different than all other time points within group,  $P < 0.05$ .

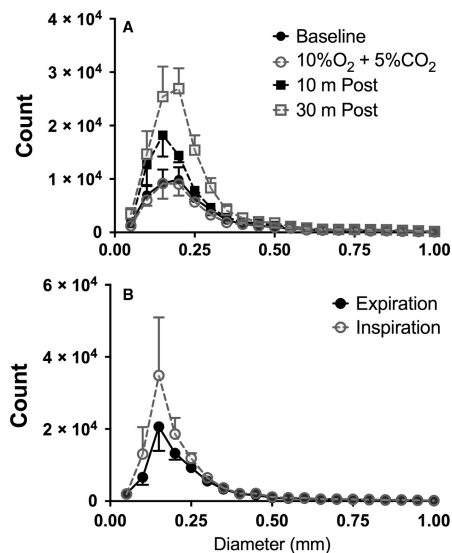


**Figure 4.** Distribution of diameter measurements from murine pulmonary vascular trees during exposure to hypoxia/hypercarbia (A) or from expiration to inspiration with positive pressure ventilation (B). Histogram of data counts are presented as the mean ( $\pm$  SD) across animals per 0.05 mm unit range of detected vessel diameters. The peak (mode) number of diameter measurements are at 0.16 mm for hypoxia/CO<sub>2</sub> data and 0.17 mm for Expir/Inspir data.

relative change in volume over the respiratory cycle for each animal and found that the tidal volumes for M5 (9.2  $\mu$ L/gm) were similar to those for M6 (9.9  $\mu$ L/gm)

and M7 (8.3  $\mu$ L/gm). However, we noted that the heart rate for M5 was approximately half, i.e. 138 beats per minute, (bpm) of that in M6 (257 bpm) and M7 (300 bpm) (Videos S1-S3).

## Discussion

In this study, we applied state-of-the-art lung imaging and image analysis techniques to examine the acute pulmonary vascular responses to hypoxic/CO<sub>2</sub> gas and positive pressure ventilation in mice. The main finding reported here is that it is now possible to use laboratory-based x-ray imaging technology to noninvasively measure dynamic changes over time in the pulmonary vasculature in live mice without intravenous contrast. We were able to characterize and quantify the number and distribution of vessel diameters, and the median and modal diameters before, during, and after exposure to hypoxic/CO<sub>2</sub> gas. Using this approach, we captured a significant increase in the number of pulmonary vessels detected by the image analysis algorithm 30 min after a brief exposure to hypoxic/CO<sub>2</sub> gas. In a separate experiment, we characterized the number and distribution of vessel diameters, the relative change in lung volumes, and the absolute change in pulmonary blood volumes over the respiratory cycle during positive pressure ventilation in mice.

Our original goal was to determine whether our *in vivo* imaging techniques could be used to detect vascular changes reflective of hypoxic pulmonary vasoconstriction (HPV). We performed our 10%O<sub>2</sub> + 5%CO<sub>2</sub> imaging during a 10 min period of exposure to hypoxic/CO<sub>2</sub> gas. We used 5% inspired CO<sub>2</sub> in the hypoxic gas mixture based on literature suggesting that elevated inspired carbon dioxide concentrations augment HPV responses (Noble et al. 1981; Koyama and Horimoto 1982; Orchard et al. 1983; Swenson et al. 1994) and we

New Imaging Approach to Measure Pulmonary Vascular Responses in Mice

M. Preissner et al.

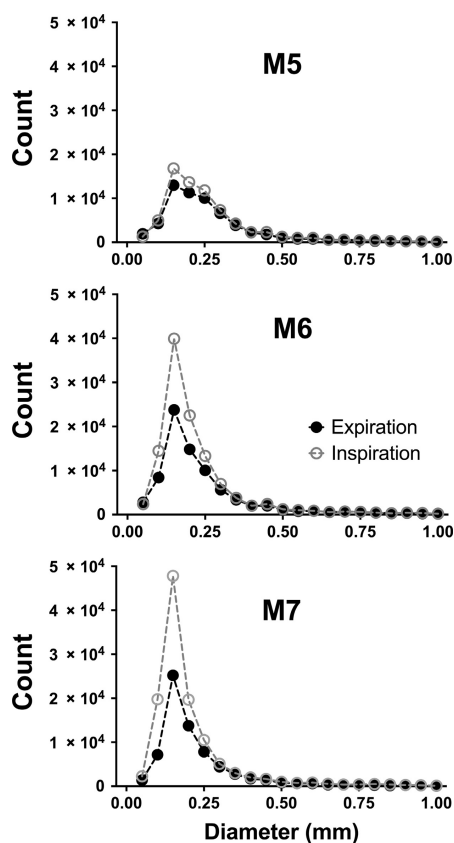


**Figure 5.** Distribution of diameter measurements from murine pulmonary vascular trees of individual animals from expiration to inspiration during positive pressure ventilation. Histograms of individual data counts are presented as observed numbers per 0.05 mm range of vessel diameters for animals M5-M7 in the Expiration/Inspiration model.

adapted a protocol used in isolated perfused lungs from BALB/c mice (the strain we used for this study) which included 5% CO<sub>2</sub> with hypoxic gas challenges to generate increases in pulmonary artery pressures (Weissmann et al. 2004). However, other data suggests that CO<sub>2</sub> may inhibit HPV (Emery et al. 1977; Chuang et al. 2010), and because we did not directly measure right ventricular pressures during this imaging experiment, we are unable to say with certainty the effect of our ventilatory conditions on HPV.

Indeed, it may not be possible to directly capture HPV using this imaging technique. The absolute cut-off for resolution of vessels based on the algorithm used in this study is 40–60 μm. That is, no vessels below 40–60 μm can be resolved and measured using this technique. The precapillary vessels that are generally considered to be involved in HPV are in the range of 30–50 μm in mice (Tabuchi et al. 2008) which would be below the limit of resolution, although murine HPV responses have been documented in vessels in the range of 70–100 μm (Paddenberg et al. 2006; Sonobe et al. 2011), and in a wide range of vessel sizes throughout the vascular tree in other species (Hillier et al. 1997; Sylvester et al. 2012). Another challenge to detecting HPV with this imaging approach is that the percent change in vessel diameters directly visualized during HPV may be relatively small at 7% (Tabuchi et al. 2008) to 40% (Paddenberg et al. 2006) and even if the vessels participating in HPV in mice can be visualized, subtle changes in diameter may not be detectable.

The anatomy of the pulmonary vasculature is one in which branching vessels increase in number with increasing generations of branching, and so the drop-off in the number of vessels detected at diameters below the mode (that is, the diameter at which the peak number of vessels are detected) represents a loss of detected vessels at smaller diameters (under the same imaging and ventilation conditions). This is an inherent limitation of many imaging approaches; there is a point at which the data obtained will be truncated.

The finding of a significant increase in the number of measurements obtained by the algorithm 30 min after exposure to hypoxic/CO<sub>2</sub> gas was striking and unexpected, and the physiological explanation seems unclear. To understand this finding, we first determined that the number of diameter measurements obtained by the algorithm reflects an increase in the number of vessels *detected*, rather than an increase in the length of existing vessels (which would also lead the algorithm to generate more diameter measurements). Next, we noted that the number of diameter measurements were increased specifically in the smaller diameter range, with the largest number detected at 170 μm. This suggests that vessels that were below the limit of resolution on the baseline and 10%O<sub>2</sub> + 5%CO<sub>2</sub> scans dilated into a detectable range on the later scans.

Our second aim in this study was to determine whether we could detect vascular changes over the respiratory cycle with positive pressure ventilation using a noninvasive, noncontrast imaging technique. Others have used *in vivo* imaging techniques with intravenous contrast to evaluate blood volume changes during mechanical ventilation. Badea et al. (2012) used dual energy micro-CT

imaging to study the volumes of air, lung tissue, and blood in mice during positive-pressure ventilation with an intravenous liposomal iodine preparation to allow for repeat measurements of blood volumes without the need for repeat iodine injections. These authors were interested in studying the relative distribution of these components with varying amounts of PEEP, and found regional differences in the blood volume variation over the respiratory cycle and in response to PEEP. Porra et al. (2017) also used dual energy x-ray imaging (which they termed K-edge subtraction imaging) performed at a synchrotron facility with intravenous iodine as a contrast agent to study regional changes in blood volume in rabbits over the respiratory cycle, again at different PEEP settings. They found that during positive pressure inspiration, regional blood volumes decreased.

Our findings add to these reports. We found a significant increase ( $P = 0.0412$ ) in total pulmonary blood volume with inspiration, while the median vessel diameter decreased from 0.20 to 0.18 mm ( $P = 0.0436$ ). We speculate that the increase in total blood volume with inspiration could reflect an increased blood volume in the conduit vessels. That is, with inspiration during positive pressure ventilation, larger (fewer) vessels may increase slightly in diameter, accounting for the increase in total pulmonary blood volume. The decrease in median vessel diameter may represent an actual decrease in individual vessel diameters. Alternatively, it may be due to the trend (although not statistically significant) toward an increased number of small vessels detected with inspiration, which would also shift the median diameter to the left. As with the Hypoxia/CO<sub>2</sub> data, this may suggest a dilatation of smaller vessels into the range of detection with inspiration.

This finding might at first glance seem to contradict the findings of Porra et al. However, we measured the pulmonary blood volume of noncapillary vessels only, because alveolar capillaries are below the limit of resolution for our technique. In contrast, Porra et al. specifically excluded larger vessels from their analysis because they were interested in the effects of positive pressure, lung tidal volumes, and PEEP on the capillary blood volume. Therefore, it is likely that we are capturing the increased blood volumes of extra-alveolar vessels due to radial traction from lung expansion, whereas Porra et al. measured the decreased volumes in alveolar vessels during inspiration related to positive alveolar pressures and compression. Lung blood volume during positive pressure ventilation varies depending on the balance of compression of the alveolar capillaries from intra-alveolar positive pressure versus increased interstitial radial tethering forces in extra-alveolar vessels with lung inflation, as well as the pressure gradients between pulmonary arteries and pulmonary veins (Permutt et al. 1961; Graham et al. 1982;

Brower et al. 1985; Kuebler 2017). In addition, changes in intrathoracic pressure caused by positive pressure ventilation alter the return of venous blood to the right side of the heart. For an excellent summary of this interesting physiology, we refer readers to Kuebler's commentary on Porra et al.'s work (Kuebler 2017). Determining the relative contributions of these various factors in our model was beyond the scope of this report. It is interesting to note that one of the mice (M5) had a heart rate that was half of the rate for M6 and M7 (as shown in Videos S1-S3) and that this animal had less variation in blood volume and other measures from expiration to inspiration.

There are several limitations to our data. First, we did not distinguish between pulmonary arteries and pulmonary veins for this analysis. Second, this technique provides robust data on vascular diameters, with 30,000 to over 100,000 measurements per vascular tree, but at the present time we are only able to report a distribution of data points rather than tracking changes in individual vessels. Finally, vascular diameters and pulmonary blood volumes do not reflect pulmonary blood flow, which is dependent on both cardiac output and pulmonary vascular resistance.

In summary, we report the application of a new *in vivo* imaging approach using advanced x-ray based imaging technology in conjunction with post-image acquisition analysis to generate three-dimensional pulmonary vascular trees from mice. This analysis provides detailed quantitative information about the number and diameter distributions of pulmonary vessels without the need for intravenous contrast. We applied this approach to measure the murine pulmonary vascular response during and after exposure to hypoxic/hypercarbic gas, and to characterize the pulmonary vascular bed over the respiratory cycle during positive pressure ventilation. An important read-out of this approach may be the change in the number of vessels detected as a reflection of small vessel dilatation into the limits of resolution. This noninvasive imaging modality provides information on the entire vascular bed and can be repeated in the same animal over time, adding a complementary approach to other *in vivo* and *ex vivo* methodologies to study the pulmonary vasculature in small animal models.

### Acknowledgments

The authors thank Drs. Wolfgang Kuebler and Erik Swenson for thoughtful discussions and editorial advice.

### Conflict of Interest

AF is CEO of 4Dx. AF, RC, HJ, and SD have stock ownership in 4Dx. AF holds a patent relating to CFPA, and HJ and AF hold a joint patent related to CFPA.

## References

- Badea, C. T., X. Guo, D. Clark, S. M. Johnston, C. D. Marshall, and C. A. Piantadosi. 2012. Dual-energy micro-CT of the rodent lung. *Am. J. Physiol. Lung Cell. Mol. Physiol.* 302:L1088–L1097.
- Bech, M., A. Tapfer, A. Velroyen, A. Yaroshenko, B. Pauwels, J. Hostens, et al. 2013. In-vivo dark-field and phase-contrast x-ray imaging. *Sci. Rep.* 3:3209.
- Bravin, A., P. Coan, and P. Suortti. 2013. X-ray phase-contrast imaging: from pre-clinical applications towards clinics. *Phys. Med. Biol.* 58:R1–R35.
- Brower, R., R. A. Wise, C. Hassapoyannes, B. Bromberger-Barnea, and S. Permutt. 1985. Effect of lung inflation on lung blood volume and pulmonary venous flow. *J. Appl. Physiol.* 1985:954–963.
- Chuang, I. C., H. P. Dong, R. C. Yang, T. H. Wang, J. H. Tsai, P. H. Yang, et al. 2010. Effect of carbon dioxide on pulmonary vascular tone at various pulmonary arterial pressure levels induced by endothelin-1. *Lung* 188:199–207.
- Dubsky, S., S. B. Hooper, K. K. W. Siu, and A. Fouras. 2012. Synchrotron-based dynamic computed tomography of tissue motion for regional lung function measurement. *J. R. Soc. Interface* 9:2213–2224.
- Dubsky, S., G. R. Zosky, K. Perks, C. R. Samarage, Y. Henon, S. B. Hooper, et al. 2017. Assessment of airway response distribution and paradoxical airway dilation in mice during methacholine challenge. *J. Appl. Physiol.* 1985:503–510.
- Emery, C. J., P. J. Sloan, F. H. Mohammed, and G. R. Barer. 1977. The action of hypercapnia during hypoxia on pulmonary vessels. *Bull. Eur. Physiopathol. Respir.* 13:763–776.
- Faigt, E. M., K. Verdelis, L. Zourelis, R. Chong, R. L. Benza, and K. J. Shields. 2017. MicroCT analysis of vascular morphometry: a comparison of right lung lobes in the SUGEN/hypoxic rat model of pulmonary arterial hypertension. *Pulm. Circ.* 7:522–530.
- Frangi, A. F., W. J. Niessen, K. L. Vincken, and M. A. Viergever. 1998. Multiscale vessel enhancement filtering. Pp. 130–137. *Medical Image Computing and Computer-Assisted Intervention*. Springer Verlag, Berlin, Germany.
- Fuld, M. K., R. B. Easley, O. I. Saba, D. Chon, J. M. Reinhardt, E. A. Hoffman, et al. 2008. CT-measured regional specific volume change reflects regional ventilation in supine sheep. *J. Appl. Physiol.* 1985:1177–1184.
- Goldenberg, N. M., L. Wang, H. Ranke, W. Liedtke, A. Tabuchi, and W. M. Kuebler. 2015. TRPV4 is required for hypoxic pulmonary vasoconstriction. *Anesthesiology* 122:1338–1348.
- Graham, R., C. Skoog, L. Oppenheimer, J. Rabson, and H. S. Goldberg. 1982. Critical closure in the canine pulmonary vasculature. *Circ. Res.* 50:566–572.
- Grundy, D. 2015. Principles and standards for reporting animal experiments in the journal of physiology and experimental physiology. *J. Physiol.* 593:2547–2549.
- Hillier, S. C., J. A. Graham, C. C. Hanger, P. S. Godbey, R. W. Glenny, and W. W. Wagner. 1997. Hypoxic vasoconstriction in pulmonary arterioles and venules. *J. Appl. Physiol.* 1985:1084–1090.
- Hyde, R. W., W. H. Lawson, and R. E. Forster. 1964. Influence of carbon dioxide on pulmonary vasculature. *J. Appl. Physiol.* 19:734–744.
- Ichimura, H., K. Parthasarathi, A. C. Issekutz, and J. Bhattacharya. 2005. Pressure-induced leukocyte margination in lung postcapillary venules. *Am. J. Physiol. Lung Cell. Mol. Physiol.* 289:L407–L412.
- Jobse, B. N., R. G. Rhem, C. A. McCurry, I. Q. Wang, and N. R. Labiris. 2012. Imaging lung function in mice using SPECT/CT and per-voxel analysis. *PLoS ONE* 7:e42187.
- Kalender, W. 2005. *Computed tomography: fundamentals, system technology, image quality, applications*. Publicis Corporate Pub, Erlangen.
- Kieffmann, R., M. N. Islam, J. Lindert, K. Parthasarathi, and J. Bhattacharya. 2009. Paracrine purinergic signaling determines lung endothelial nitric oxide production. *Am. J. Physiol. Lung Cell. Mol. Physiol.* 296:L901–L910.
- Kim, E. H., M. Preissner, R. P. Carnibella, C. R. Samarage, E. Bennett, M. A. Diniz, et al. 2017. Novel analysis of 4DCT imaging quantifies progressive increases in anatomic dead space during mechanical ventilation in mice. *J. Appl. Physiol.* 1985:578–584.
- Kitchen, M. J., D. Paganin, R. A. Lewis, N. Yagi, and K. Uesugi. 2005. Analysis of speckle patterns in phase contrast images of lung tissue. *Nucl. Instrum. Methods in Phys. Res. A* 548:240–246.
- Koba, W., L. A. Jelicks, and E. J. Fine. 2013. MicroPET/SPECT/CT imaging of small animal models of disease. *Am. J. Pathol.* 182:319–324.
- Koyama, T., and M. Horimoto. 1982. Pulmonary microcirculatory response to localized hypercapnia. *J. Appl. Physiol. Respir. Environ. Exerc. Physiol.* 53:1556–1564.
- Kuebler, W. M. 2017. Tides of blood: cyclic changes in lung blood volume during a single breath. *Am. J. Respir. Cell Mol. Biol.* 57:386–387.
- Larsson, D. H., W. Vågberg, A. Yaroshenko, A. Yildirim, and H. M. Hertz. 2016. High-resolution short-exposure small-animal laboratory x-ray phase-contrast tomography. *Sci. Rep.* 6:39074.
- Lumb, A. B., and P. Slinger. 2015. Hypoxic pulmonary vasoconstriction: physiology and anesthetic implications. *Anesthesiology* 122:932–946.
- Molthen, R. C., K. L. Karau, and C. A. Dawson. 2004. Quantitative models of the rat pulmonary arterial tree morphometry applied to hypoxia-induced arterial remodeling. *J. Appl. Physiol.* 1985:2372–2384. discussion 2354.

M. Preissner et al.

New Imaging Approach to Measure Pulmonary Vascular Responses in Mice

- Morgan, K. S., M. Donnelly, N. Farrow, A. Fouras, N. Yagi, Y. Suzuki, et al. 2014. *In vivo* x-ray imaging reveals improved airway surface hydration after Cystic Fibrosis airway therapy. *AJRCCM* 190:469–472.
- Noble, W. H., J. C. Kay, and J. A. Fisher. 1981. The effect of PCO<sub>2</sub> on hypoxic pulmonary vasoconstriction. *Can. Anaesth. Soc. J.* 28:422–430.
- Orchard, C. H., R. Sanchez de Leon, and M. K. Sykes. 1983. The relationship between hypoxic pulmonary vasoconstriction and arterial oxygen tension in the intact dog. *J. Physiol.* 338:61–74.
- Paddenberg, R., P. König, P. Faulhammer, A. Goldenberg, U. Pfeil, and W. Kummer. 2006. Hypoxic vasoconstriction of partial muscular intra-acinar pulmonary arteries in murine precision cut lung slices. *Respir. Res.* 7:93.
- Permutt, S., J. B. Howell, D. F. Proctor, and R. L. Riley. 1961. Effect of lung inflation on static pressure-volume characteristics of pulmonary vessels. *J. Appl. Physiol.* 16:64–70.
- Pfeiffer, F., M. Bech, O. Bunk, P. Kraft, E. F. Eikenberry, C. Brönnimann, et al. 2008. Hard-X-ray dark-field imaging using a grating interferometer. *Nat. Mater.* 7:134–137.
- Porra, L., L. Broche, L. Dégrugilliers, G. Albu, I. Malaspina, C. Doras, et al. 2017. Synchrotron Imaging Shows Effect of Ventilator Settings on Intra-breath Cyclic Changes in Pulmonary Blood Volume. *Am. J. Respir. Cell Mol. Biol.* 57:459–467.
- Preissner, M., R. P. Murrie, I. Pinar, F. Werdiger, R. P. Carnibella, G. R. Zosky, et al. 2018. High resolution propagation-based imaging system for *in vivo* dynamic computed tomography of lungs in small animals. *Phys. Med. Biol.* 63:08NT03.
- Rowlands, D. J., M. N. Islam, S. R. Das, A. Huertas, S. K. Quadri, K. Horiuchi, et al. 2011. Activation of TNFR1 ectodomain shedding by mitochondrial Ca<sup>2+</sup> determines the severity of inflammation in mouse lung microvessels. *J. Clin. Invest.* 121:1986–1999.
- Samarage, C. R., R. Carnibella, M. Preissner, H. D. Jones, J. T. Pearson, A. Fouras, et al. 2016. Technical Note: contrast free angiography of the pulmonary vasculature in live mice using a laboratory x-ray source. *Med. Phys.* 43:6017.
- Sonobe, T., D. O. Schwenke, J. T. Pearson, M. Yoshimoto, Y. Fujii, K. Umetani, et al. 2011. Imaging of the closed-chest mouse pulmonary circulation using synchrotron radiation microangiography. *J. Appl. Physiol.* 1985:75–80.
- Swenson, E. R., H. T. Robertson, and M. P. Hlastala. 1994. Effects of inspired carbon dioxide on ventilation-perfusion matching in normoxia, hypoxia, and hyperoxia. *Am. J. Respir. Crit. Care Med.* 149:1563–1569.
- Sylvester, J. T., L. A. Shimoda, P. I. Aaronson, and J. P. Ward. 2012. Hypoxic pulmonary vasoconstriction. *Physiol. Rev.* 92:367–520.
- Tabuchi, A., M. Mertens, H. Kuppe, A. R. Pries, and W. M. Kuebler. 2008. Intravital microscopy of the murine pulmonary microcirculation. *J. Appl. Physiol.* 1985:338–346.
- Tuohimaa, T., M. Otendal, and H. M. Hertz. 2007. Phase-contrast X-ray imaging with a liquid-metal-jet-anode microfocus source. *Appl. Phys. Lett.* 91:074104.
- Wang, L., J. Yin, H. T. Nickles, H. Ranke, A. Tabuchi, J. Hoffmann, et al. 2012. Hypoxic pulmonary vasoconstriction requires connexin 40-mediated endothelial signal conduction. *J. Clin. Invest.* 122:4218–4230.
- Weissmann, N., E. Akkayagil, K. Quanz, R. T. Schermuly, H. A. Ghofrani, L. Fink, et al. 2004. Basic features of hypoxic pulmonary vasoconstriction in mice. *Respir. Physiol. Neurobiol.* 139:191–202.
- Yang, K., A. L. Kwan, D. F. Miller, and J. M. Boone. 2006. A geometric calibration method for cone beam CT systems. *Med. Phys.* 33:1695–1706.
- Zhou, T., U. Lundström, T. Thüring, S. Rutishauser, D. H. Larsson, M. Stampanoni, et al. 2013. Comparison of two x-ray phase-contrast imaging methods with a microfocus source. *Opt. Express* 21:30183–30195.

### Supporting Information

Additional supporting information may be found online in the Supporting Information section at the end of the article.:

**Videos S1-S3:** Real-time imaging of mouse thorax during CT scan acquisition. Mice M5 through M7 are shown here on Videos S1-S3, respectively, in a real-time image that is visible in the control room while the 4DCT scan is acquired.

## 6 Conclusions and recommendations for future work

Despite numerous studies over the past fifty years, there remain significant gaps in the understanding of how mechanical ventilation ventilates - and injures - the lungs (Slutsky & Ranieri, 2013). Historically, examinations of lung tissue have shown that lung injury manifests in a patchy, heterogeneous manner (Dreyfuss & Saumon, 1992; Schiller *et al.*, 2001). More recently, both clinical and pre-clinical computed tomographic (CT) imaging has corroborated these findings with *in vivo* data, and numerous studies have shown that both over-distended and under-distended areas are present in acute respiratory distress syndrome (ARDS) during mechanical ventilation (MacIntyre, 2005). Measurement of the spatial distribution of ventilation in the lung with CT is therefore currently considered to be key in advancing our understanding of ventilator-induced lung injury (VILI). Furthermore, CT imaging also captures quantitative information on structures in the lung that may lead to functional disruption during mechanical ventilation, such as altered haemodynamics (Vieillard-Baron *et al.*, 2016), or an increase in anatomic dead space (Nickles *et al.*, 2014).

Consequently, there is currently no known ventilation formula to completely avoid injury to the lungs, despite the complexity of modern clinical ventilators and lung-protective ventilation guidelines. ARDS patients with respiratory failure are especially vulnerable and mortality in this cohort remains high, ranging from 34.9% to 46.1%, depending on the severity of ARDS (Bellani *et al.*, 2016). Ideally, safe ventilation strategies are tailored to the current condition of each patient and can adapt to the changing lung mechanics in order to maintain safe ventilation. This is currently done in the clinic to some extent, with intermittent measures of global lung mechanics from the ventilator. However, safe mechanical ventilation with these current methods cannot be guaranteed and VILI continues to be a risk for vulnerable

ARDS patients.

CT is a powerful imaging modality for investigating VILI and ARDS. CT image acquisition can be performed on many platforms, from the synchrotron to the clinic. High quality laboratory imaging offers the possibility of undertaking pilot or longitudinal studies that may be too costly for synchrotron imaging or not possible with commercially-available micro-CT systems. In addition, dynamic CT imaging offers the distinct advantage of capturing the lung motion without a breath-hold (Dubsky *et al.*, 2012). However, dynamic CT imaging on mice requires a laboratory set-up with fast imaging speeds and high resolution. This is possible on the facility located in the biomedical engineering precinct at Monash University (Preissner *et al.*, 2018b). All the studies on mouse models in this thesis were conducted at this laboratory facility.

In Chapter 3, the laboratory X-ray system, utilising a state-of-the-art liquid-metal jet X-ray source (Excillum D2+, Excillum AB, Kista, Sweden) combined with a high speed flat-panel detector, was investigated for its suitability for dynamic imaging of mouse lungs for the measurement of regional lung volumes. It was found to be capable of both high resolution and high speed imaging, providing superior imaging and the highest quality factor when compared with currently available micro-CT devices (Kalender *et al.*, 2005).

The link between regional lung function and regional lung injury in VILI and ARDS was investigated in Chapter 4. The studies used a unique approach of combining tailored imaging analysis for regional lung volumes with biomarkers of lung injury. This approach involved the development of customised methods to calculate the end-expiratory volume and of applying the four-dimensional X-ray velocimetry (4DXV) technique for the tidal volume, for ten regions in the lung. These were matched directly to biomarkers of injury for tissue in the same region. The mapping of these data showed that the one-hit VILI model had a clear link between regional lung injury and regional over-distension, driven by tidal volume (Yen & Preissner *et al.*, 2019). In contrast, regional lung injury in the two-hit VILI model was linked to low regional lung volumes, i.e., end-expiratory volume (Yen & Preissner *et al.*, 2020). The novel approach in these studies provided new insights into the regional mechanisms of VILI, i.e., volutrauma and atelectrauma, and how these relate to the

ventilator pressure settings of PIP and PEEP.

Chapter 5 investigated what happens to the airways in mouse models of VILI. Dynamic *in vivo* imaging showed that a significant increase in anatomic dead space fraction occurs during prolonged injurious mechanical ventilation, independent of initial lung injury (Kim & Preissner *et al.*, 2017). The dead space fraction was calculated as a ratio of airway tidal volume to total tidal volume. This indicates the proportion of the tidal volume delivered by the ventilator that is used to distend the airways, which may have adverse long-term effects on the structure and function of the airways. The calculation of the dead space fraction may provide an indication of how the ventilator is ventilating the lungs and have consequences for ventilator settings in the clinic, when combined with other indicators of VILI.

In addition, Chapter 5 contains proof-of-concept studies quantifying the pulmonary vasculature using the contrast-free angiography (CFPA) technique (Samarage *et al.*, 2016). Two studies on mice were undertaken: 1. detection of the number of vessels during recovery from exposure to hypoxic/hypercarbic gas, 2. measurements of the pulmonary vasculature at end-inspiration and end-expiration during mechanical ventilation (Preissner *et al.*, 2018a). Since the CFPA technique is a post-processing technique applied on the 4DCT images acquired on the laboratory X-ray system, it can simultaneously provide information on the pulmonary vasculature in addition to the regional lung volumes. Moderate hypertension has been found in patients with ARDS (Vieillard-Baron *et al.*, 2016), indicating that constriction of the pulmonary blood vessels plays a role in impaired respiratory function in these patients. Therefore, animal studies may benefit from simultaneous analysis of both regional lung function and the pulmonary vasculature with the CFPA technique, in order to better understand the causes of impaired respiratory function in VILI and ARDS.

Radiation dose for frequent CT imaging or for dynamic imaging is the largest hurdle for translation of this technology to the clinic. Ongoing efforts towards developing low dose imaging are encouraging (Dubsky *et al.*, 2010; Kitchen *et al.*, 2017). Therefore, although dynamic CT imaging may not yet be the solution for monitoring safe mechanical ventilation in the clinic, it will continue to be an essential research tool for investigating the effect of the ventilator on lung structure and function in

animal models.

Regional volume data at higher resolution than the ten regions studied in this thesis is possible on this laboratory system. This data can be used to understand ventilation heterogeneity. Information on heterogeneity of ventilation can also be combined with information on the airway diameters, to determine how airway closure or peripheral airway collapse relates to regional ventilation (Dubsky *et al.*, 2017). High resolution data from CT imaging provides patterns in the lung, therefore, this is an ideal platform for the development of machine learning algorithms to detect and classify pathophysiology in ARDS and VILI (Gerard *et al.*, 2020).

For the functional studies in Chapter 4, only a limited range of ventilation pressure combinations (PIP and PEEP) were used. There remains considerable scope for further combinations of PIP and PEEP to be explored with imaging to determine the effect on the regional distribution of ventilation, especially in ARDS models. In addition, other ventilation parameters may affect regional ventilation, such as the stress index (Henderson *et al.*, 2017), which remain to be explored more fully in combination with imaging. As alternative modes of safe ventilation in ARDS are postulated, such as time-controlled adaptive ventilation (Nieman *et al.*, 2018), or high frequency oscillation (Herrmann *et al.*, 2020), imaging provides a vital role for investigating how these modes affect the regional lung function and alveolar recruitment.

The research in this thesis uses mouse models to provide important insights into the effect of the ventilator settings on the regional volume distribution in the lungs. In addition, it provides insights into the effect of mechanical ventilation on the airways and the pulmonary vasculature. These insights were only made possible by combining state-of-the-art, high speed, high resolution imaging, combined with novel image analysis methods developed in this thesis. The studies investigated in this thesis provide a greater understanding of how the ventilator ventilates the lungs and pave the way towards providing safe mechanical ventilation in the clinic.

VILI is a complex research area and there remains an ongoing role for the engineer in understanding VILI and designing safe mechanical ventilation, alongside respiratory specialists, physiologists and critical care physicians (Kaczka & Nieman, 2019). It is vital that there is a multi-disciplinary effort to understand the mechanisms of VILI, in order to reduce the current unacceptably high mortality rates in

ARDS. The work in this thesis demonstrates that high quality, dynamic imaging is critical to advancing our understanding the effects of regional lung mechanics on the initiation and progression of VILI.



## **A Journal articles published from the studies in Chapter 4**

The two journal articles in this appendix were published as joint first author with the results from Chapter 4.

### **A.1 The link between regional tidal stretch and lung injury during mechanical ventilation**

Reprinted with permission of the American Thoracic Society. Copyright © 2020 American Thoracic Society. The American Journal of Respiratory Cell and Molecular Biology is an official journal of the American Thoracic Society.

## ORIGINAL RESEARCH

## The Link between Regional Tidal Stretch and Lung Injury during Mechanical Ventilation

Seiha Yen<sup>1\*</sup>, Melissa Preissner<sup>2\*</sup>, Ellen Bennett<sup>1</sup>, Stephen Dubsky<sup>2</sup>, Richard Carnibella<sup>3</sup>, Ronan O'Toole<sup>1</sup>, Louise Roddam<sup>1</sup>, Heather Jones<sup>4,5,6</sup>, Peter A. Dargaville<sup>7</sup>, Andreas Fouras<sup>3</sup>, and Graeme R. Zosky<sup>1,7</sup><sup>1</sup>School of Medicine and <sup>7</sup>Menzies Institute for Medical Research, College of Health and Medicine, University of Tasmania, Hobart, Tasmania, Australia; <sup>2</sup>Department of Mechanical and Aerospace Engineering, Monash University, Melbourne, Victoria, Australia; <sup>3</sup>4Dx Limited, Melbourne, Victoria, Australia; and <sup>4</sup>Biomedical Imaging Research Institute, <sup>5</sup>Department of Medicine, and <sup>6</sup>Women's Guild Lung Institute, Cedars-Sinai Medical Center, Los Angeles, California

ORCID ID: 0000-0001-9039-0302 (G.R.Z.).

## Abstract

The aim of this study was to assess the association between regional tidal volume ( $V_T$ ), regional functional residual capacity (FRC), and the expression of genes linked with ventilator-induced lung injury. Two groups of BALB/c mice ( $n = 8$  per group) were ventilated for 2 hours using a protective or injurious ventilation strategy, with free-breathing mice used as control animals. Regional  $V_T$  and FRC of the ventilated mice was determined by analysis of high-resolution four-dimensional computed tomographic images taken at baseline and after 2 hours of ventilation and corrected for the volume of the region (i.e., specific [s] $V_T$  and specific [s]FRC). RNA concentrations of 21 genes in 10 different lung regions were quantified using a quantitative PCR array.

sFRC at baseline varied regionally, independent of ventilation strategy, whereas s $V_T$  varied regionally depending on ventilation strategy. The expression of *IL-6* ( $P = 0.04$ ), *Ccl2* ( $P < 0.01$ ), and *Ang-2* ( $P < 0.05$ ) was associated with s $V_T$  but not sFRC. The expression of seven other genes varied regionally (*IL-1 $\beta$*  and *RAGE* [receptor for advanced glycation end products]) or depended on ventilation strategy (*Nfe2l2* [nuclear factor erythroid-derived 2 factor 2], *c-fos*, and *Wnt1*) or both (*TNF- $\alpha$*  and *Cxcl2*), but it was not associated with regional sFRC or s $V_T$ . These observations suggest that regional inflammatory responses to mechanical ventilation are driven primarily by tidal stretch.

**Keywords:** mechanical ventilation; regional tidal stretch; regional gene expression

Acute respiratory distress syndrome (ARDS) has a high mortality rate (1–3). Although the severity of ARDS is characterized by the degree of hypoxia (4), only a low percentage of patients with ARDS died of hypoxemia, with the majority dying as a result of multisystem organ failure (5). Unfortunately, although mechanical ventilation is necessary for patients with ARDS, it may also directly contribute to multisystem organ failure by inducing inflammation (6, 7).

Mechanical ventilation in ARDS aims to provide adequate gas exchange

while minimizing lung injury; however, it may damage the lung in a process known as “ventilator-induced lung injury” (VILI) (8–10). The impact of high tidal volume (high  $V_T$ ; overdistention) has been clearly demonstrated by the ARDSnet (NHLBI ARDS Network) study, which showed 22% lower mortality in patients ventilated at 6 ml/kg than in those receiving a traditional  $V_T$  of 12 ml/kg (11). However, only one intervention has proved to be effective in reducing mortality in ARDS since this study: prone positioning for patients with

severe ARDS (1, 2, 12, 13). This highlights the importance of the lung mechanical response to ventilation in determining patient outcomes.

Identifying the optimum ventilation strategy to minimize VILI is complicated by the heterogeneous nature of ARDS (14). In addition, both overdistention and atelectrauma can occur within the same lung (15, 16), and both can trigger an inflammatory response (biotrauma) (17–20). However, their relative contribution to overall biotrauma within an individual lung remains poorly understood

(Received in original form April 19, 2018; accepted in final form November 12, 2018)

\*These authors contributed equally to this work.

Supported by the National Health and Medical Research Council (1077905) and the Royal Hobart Hospital Research Foundation (15-027).

Author Contributions: S.Y., M.P., E.B., and G.R.Z.: conducted the experiments; S.Y., M.P., S.D., R.C., R.O'T., L.R., H.J., P.A.D., A.F., and G.R.Z.: analyzed the data generated; S.D., R.C., R.O'T., L.R., H.J., P.A.D., A.F., and G.R.Z.: conceptualized the study; and S.Y., M.P., E.B., S.D., R.C., R.O'T., L.R., H.J., P.A.D., A.F., and G.R.Z.: drafted the manuscript and approved the final version.

Correspondence and requests for reprints should be addressed to Graeme R. Zosky, Ph.D., M.Biostat., School of Medicine, College of Health and Medicine, University of Tasmania, Private Bag 34, Hobart, TAS 7001, Australia. E-mail: graeme.zosky@utas.edu.au.

Am J Respir Cell Mol Biol Vol 60, Iss 5, pp 569–577, May 2019

Copyright © 2019 by the American Thoracic Society

Originally Published in Press as DOI: 10.1165/rcmb.2018-0143OC on November 14, 2018

Internet address: www.atsjournals.org

ORIGINAL RESEARCH

(21). At the whole-lung level, we have previously shown an association between overdistention and the presence of pulmonary edema with protein leak and macrophage infiltration (21). However, we were unable to assess how these responses varied spatially, which may be an important determinant of outcome because studies have shown that ventilation causes a heterogeneous pattern of lung damage (15, 22) due to the inhomogeneous distribution of regional tidal strain (23).

The aim of this study was to assess the association between regional functional residual capacity (FRC) and regional  $V_T$  and the expression of markers of lung injury in response to mechanical ventilation. We investigated this in a mouse model by combining gene expression analysis with a recently developed lung-imaging technology that allows image capture at high speed and high resolution over the entire breathing cycle (24).

Methods

Animals

Six- to 9-week-old female BALB/c mice (Animal Research Platform, Monash University) were provided food and water *ad libitum* and housed in a 12-h/12-h light/dark cycle. All experiments were approved by the Monash University Animal Ethics Committees.

Animal Preparation and Ventilation

Mice were prepared as described previously (25). Briefly, they were anesthetized, tracheostomized, and mounted upright on a rotating stage (Zaber Technologies) in a customized holder. They were ventilated for 2 hours according to one of two protocols: 1) protective ( $n = 16$ ; 225 breaths/min; peak inspiratory pressure, 12 cm  $H_2O$ ; PEEP, 2 cm  $H_2O$ ) or 2) injurious ( $n = 16$ ; 144 breaths/min; peak inspiratory pressure, 20 cm  $H_2O$ ; positive end-expiratory pressure [PEEP], 0 cm  $H_2O$ ). Lung images of the ventilated groups were taken at baseline (H0) and after 2 hours (H2) of ventilation. Mice were killed by overdose with sodium pentobarbitone (200 mg/kg) before processing of the lung tissue for gene expression ( $n = 8$  per group) or immunohistochemistry ( $n = 8$  per group). A separate group of mice ( $n = 8$ ) served as unventilated control animals for gene expression.

X-Ray Imaging

For X-ray imaging, we used the liquid MetalJet X-Ray Source Technology (Excillum AB), enabling high-brightness and high-resolution imaging (26, 27). A high-speed detector (PaxScan; Varian Medical Systems) was used to capture projection images at 30 frames per second for four-dimensional computed tomographic reconstructions (28).

Post-Processing of Imaging Data

We applied a three-dimensional velocimetry technique to measure the regional  $V_T$  (24, 28, 29) by analyzing 400 frames per computed tomographic scan to calculate regional tissue expansion (24, 28, 29). To determine the regional FRC, we used the grayscale values (intensity), which were converted to Hounsfield units to determine the fraction of air for each voxel.

To assess the regional  $V_T$  and FRC, the scans were segmented into 10 regions (Figure 1). The airway tree was segmented (30) using a centerline tree extracted from an image of the airways filtered to accentuate cylindrical structures (31). The airway tree geometry was then used to segment the lung into five regions (left lobe and four right lobes [R1–R4]) by assigning voxels to the nearest supplying airway (see

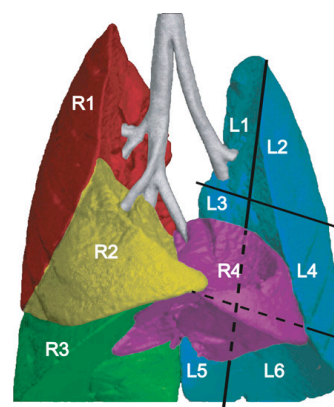


Figure 1. Regional lung segmentation. Schematic showing the segmentation approach for the assessment of regional lung volumes. This segmentation corresponded to the tissue sampling process for the assessment of gene expression. L = left lobe; R = right lobe.

References 24 and 29). The left lobe data were further segmented into six (L1–L6) volumes (Figure 1).

After segmentation of the lung imaging data, tissue expansion and volume of gas for each region were summed to provide the

Table 1. Relationship between Gene Expression, Ventilation Strategy, and Lung Region

Gene Function	Gene Name	Ventilation	Region	Ventilation × Region
Inflammation	<i>Ccl2</i>	0.07	<0.001	<0.001
	<i>Cxcl2</i>	<0.001	<b>0.04</b>	0.48
	<i>Elane</i>	0.12	0.30	0.13
	<i>IL-1β</i>	0.48	<b>0.02</b>	0.72
	<i>IL-6</i>	<0.001	0.08	<b>0.02</b>
	<i>Mpo</i>	0.14	0.35	0.70
	<i>Tnf-α</i>	<0.01	<0.01	0.86
	<i>RAGE</i>	0.34	<b>0.01</b>	0.86
	<i>Ang-2</i>	0.73	<0.001	0.75
	<i>Sftpb</i>	0.67	0.95	0.81
Surfactant	<i>Cdh1</i>	0.81	0.33	0.88
	<i>Ctnnb1</i>	0.65	0.87	0.78
	<i>Egfr</i>	0.22	0.24	0.88
	<i>Tgfb1</i>	0.39	0.67	0.90
	<i>Vim</i>	0.88	0.08	0.78
	<i>Wnt1</i>	<0.001	0.16	0.29
	<i>c-fos</i>	<0.01	0.59	0.93
Epithelial–mesenchymal response	<i>Mapk1</i>	0.99	0.37	0.54
	<i>Nfe2l2</i>	<0.001	0.81	0.87
	<i>Nfk1</i>	0.78	0.51	0.94
	<i>Plat</i>	0.14	0.14	0.97
Transcription, cell signaling				
Anticoagulant				

*P* values are for the main effects (ventilation, region) and the interaction term (ventilation × region) based on a two-way ANOVA for RNA expression relative to the housekeeping gene (*Rip37*). *P* values < 0.05 are in boldface type.

## ORIGINAL RESEARCH

regional values of  $V_T$  and FRC, respectively. To correct for variation in regional lung volumes, we calculated regional specific functional residual capacity ( $sFRC = \text{regional FRC/regional lung volume}$ ), specific tidal volume ( $sV_T = \text{regional } V_T/\text{regional lung volume}$ ), and regional lung distention ( $sFRC + sV_T$ ). Global values for these indices were also calculated. Data are presented as means(SD).

## Regional Gene Expression

After mice were killed, their lungs were removed *en bloc* and divided into 10 regions corresponding to the image segmentation (Figure 1). Each lung region was stored in RNeasy Lysis Buffer (Qiagen), and RNA extraction was performed with a miRNeasy Mini Kit (Qiagen).

The expression of 21 genes was assessed using reverse transcription–quantitative PCR (qPCR) arrays according to the manufacturer's instructions (Qiagen). VILI-related genes with known roles in inflammation, surfactant production, epithelial and mesenchymal responses, transcription/cell signaling, and coagulation were selected (Table 1). qPCRs were performed on a LightCycler 480 II instrument (Roche) in 96-well qPCR array plates. Gene expression relative to a housekeeping gene (*Rpl37*) was calculated using the comparative cycle threshold method and expressed as fold change relative to the average gene expression of the L1 region in the free-breathing control group.

## Immunohistochemistry

In a separate group of mice, after they were killed, lungs were instillation fixed *in situ* with 10% formalin at a transrespiratory pressure of 10 cm  $H_2O$  for 1 hour. The trachea was ligated, and the lung was removed *en bloc* and submerged in formalin before transfer to 70% ethanol. The fixed lungs were embedded in paraffin, and 5- $\mu\text{m}$  coronal sections were taken at the midline. Immunohistochemistry was performed using a horseradish peroxidase/diaminobenzidine (DAB) (ABC) detection immunohistochemistry kit (Abcam). Antigen retrieval was performed in a pressure cooker using a solution of 1 mM EDTA in citrate buffer (pH 6.0) for 10 minutes. Sections were stained using the following antibodies: anti-IL-6 (10 ng/ $\mu\text{L}$ , Ab208113; Abcam), anti-MCP-1 (anti-monocyte chemoattractant protein 1,

5 ng/ $\mu\text{L}$ ; Abcam), anti-p53 (0.5 ng/ $\mu\text{L}$ ; Abcam), antineutrophil (NIMP-R14, 5 ng/ $\mu\text{L}$ ; Abcam), or antirabbit IgG polyclonal (isotype control, 5 ng/ $\mu\text{L}$ ; Abcam). The antigen–antibody reaction was visualized after the application of DAB substrate in DAB chromogen solution for 5 minutes and counterstaining with hematoxylin. Slides were dehydrated and clear mounted for light microscopy. Images of the entire section were captured and analyzed using ImageJ software. The regional concentrations of IL-6, Ccl2 (MCP-1), and p53 in the left lobe were estimated by calculating the proportion of the positive

stain per unit area of tissue within each region after subtracting nonspecific staining based on the intensity of isotype control stain in the adjacent section. The regional number of neutrophils was counted in randomly selected images within each lung region and quantified as the number of cells per unit area.

## Data Analysis

Differences in  $sFRC$ ,  $sV_T$ , distention, and relative gene expression, both between regions and between ventilation protocols, were assessed using two-way repeated measures ANOVA with Holm-Sidak

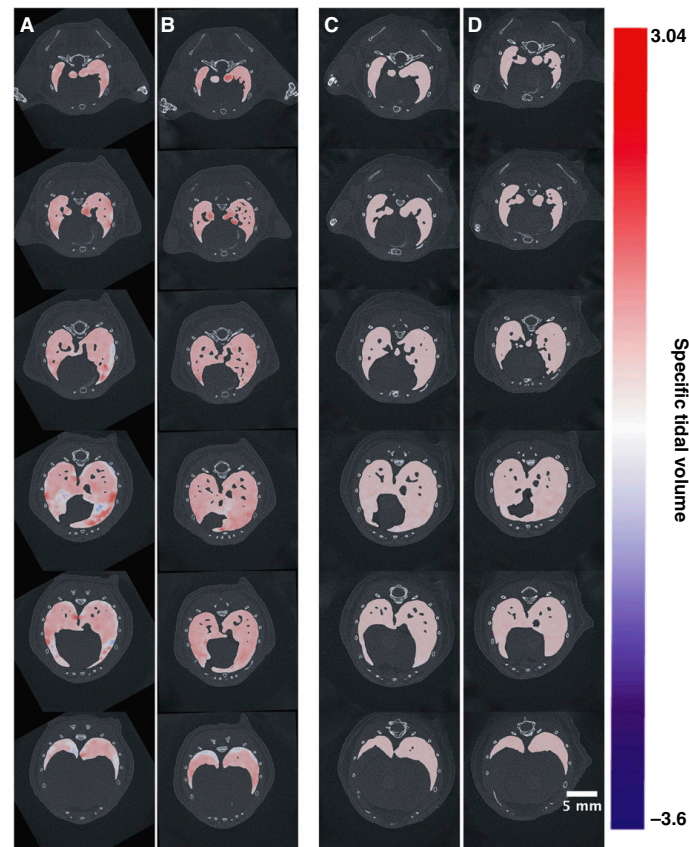


**Figure 2.** Imaging of lung motion during ventilation. Representative transverse images from the apex (top) to the base (bottom) of a mouse ventilated with an injurious strategy (A) at baseline and (B) after 2 hours of ventilation, as well as a mouse ventilated with a protective strategy (C) at baseline and (D) after 2 hours of ventilation. Tidal volume contours (arbitrary units) were normalized to the size of the whole lung. Scale bar: 5 mm.

ORIGINAL RESEARCH

*post hoc* tests (SigmaPlot version 12.5; Systat Software). Between-regions protein expression data (immunohistochemistry) were assessed by one-way ANOVA with Holm-Šidák *post hoc* tests. Data were transformed when necessary to satisfy the assumptions of normality and homoscedasticity of the variances. Associations between regional sFRC, sV<sub>T</sub>, distention, and regional RNA concentrations were assessed using linear regression analysis.

Results

Lung Motion

Qualitatively, lung stretch in the mice ventilated with the injurious protocol was heterogeneous and changed between baseline (H0) and after 2 hours (H2) of ventilation (Figures 2A and 2B), whereas

lung stretch with the protective protocol was more homogeneous (Figures 2C and 2D).

sFRC, sV<sub>T</sub>, and Distention at H0

At H0, global and regional sFRC values were higher in the protective group than in the injurious group ( $P < 0.01$ ) (Figure 3A). For both ventilation strategies, there were regional differences in sFRC ( $P < 0.001$ ), where sFRC was lower in the more distal regions (L2, R2, and R4;  $P < 0.05$ ). In general, regional sV<sub>T</sub> was higher in the injurious group in most regions, with the exception of R4 (Figure 3B). In animals receiving injurious ventilation, regional sV<sub>T</sub> was higher in proximal lung regions (L1 and R1;  $P < 0.001$ ), whereas protective ventilation showed homogeneous regional sV<sub>T</sub> at baseline (Figure 3B). Distention (sFRC + sV<sub>T</sub>) followed a pattern similar to that of sV<sub>T</sub> with higher distention in the injurious ventilation group, with the

exception of the three lower regions (L5,  $P = 0.51$ ; L6,  $P = 0.54$ ; R4,  $P = 0.76$ ) (Figure 3C).

Change in sFRC, sV<sub>T</sub>, and Regional Distention after 2 Hours of Ventilation

After 2 hours of ventilation, there was no change in sFRC (average change, 0.8%), sV<sub>T</sub> ( $\Delta = 3.2\%$ ), or regional distention ( $\Delta = 1.1\%$ ) in the protective group (Figures 3D–3F) compared with baseline. In contrast, sFRC was reduced in all lung regions in the injurious group ( $\Delta = 8.6\%$ ) (Figure 3D), whereas the change in global sV<sub>T</sub> was minimal ( $\Delta = 1.2\%$ ) (Figure 3E). On average, there was no significant change in global distention in the injurious group ( $\Delta = 5.5\%$ ;  $P = 0.76$ ) (Figure 3F). There were, however, significant regional differences in sV<sub>T</sub> and distention in the injurious group ( $P < 0.001$ ) (Figures 3E and 3F) between H0 and H2.

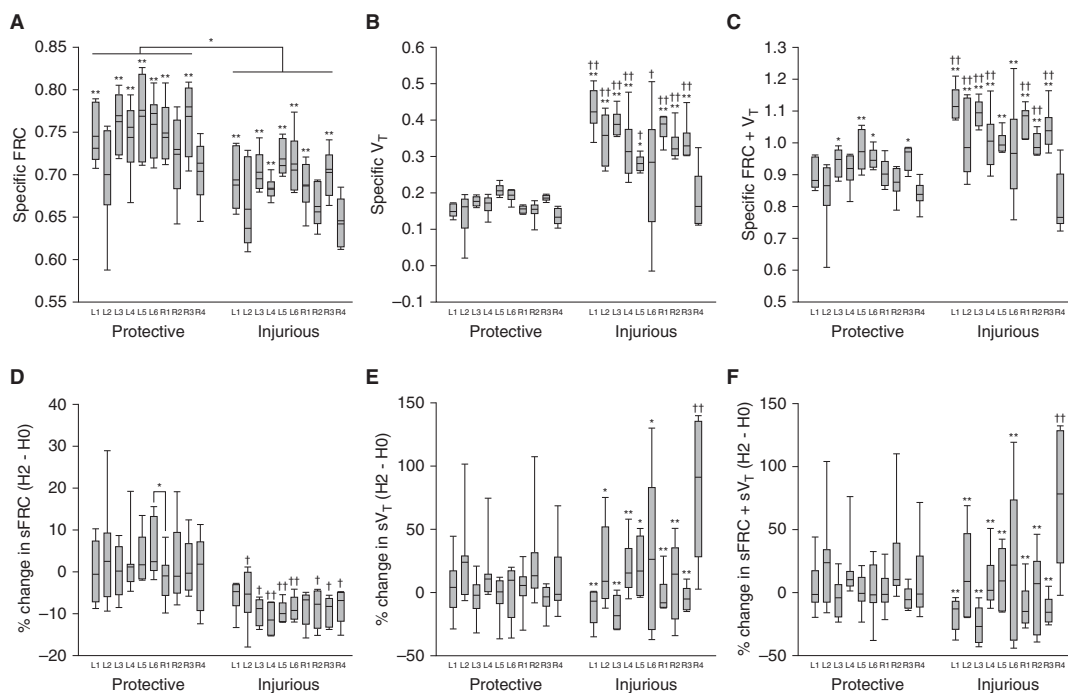


**Figure 3.** Effect of different ventilation strategies on lung volumes. Box plots (median, interquartile range, and 10th to 90th percentiles) for (A, B, and C, respectively) sFRC, sV<sub>T</sub>, and sFRC + sV<sub>T</sub> at baseline and the proportional change in (D, E, and F, respectively) sFRC, sV<sub>T</sub>, and sFRC + sV<sub>T</sub> after 2 hours of ventilation relative to baseline for each of 10 lung regions in mice ventilated with a protective or injurious strategy. \* $P < 0.05$  and \*\* $P < 0.001$  between ventilation strategies. † $P < 0.05$  and †† $P < 0.001$  compared with the same region in the protective group.  $n = 8$  mice per group. FRC = functional residual capacity; sFRC = specific FRC; sV<sub>T</sub> = specific tidal volume.

## ORIGINAL RESEARCH

## Regional Gene Expression

The expression of *IL-6* ( $P = 0.02$ ) and *Ccl2* ( $P < 0.001$ ) varied regionally, depending on the ventilation strategy (Table 1). In contrast, the expression levels of *Tnf- $\alpha$*  and *Cxcl2* varied independently with both region and ventilation strategy (Table 1). The expression of *IL-1 $\beta$* , *Ang-2* (angiopoietin 2), and *RAGE* (receptor for advanced glycation end products) varied regionally, but there was no influence of ventilation strategy on the expression of these genes. Expression levels of three genes (*Wnt1*,  $P < 0.001$ ; *c-fos*,  $P < 0.01$ ; *Nfe2l2* [nuclear factor erythroid-derived 2 factor 2],  $P < 0.001$ ) varied depending on ventilation strategy, but there were no significant differences in levels between lung regions (Table 1). There were no regional differences or associations with mechanical ventilation for the other genes measured (*Elane* [elastase neutrophil expressed], *Mpo* [myeloperoxidase], *SftpB* [surfactant-associated protein B], *Cdh1* [cadherin 1], *Cttnb1* [catenin- $\beta$ 1], *Egfr* [epidermal growth factor receptor], *TGF $\beta$ 1* [transforming growth factor- $\beta$ ], *Vim* [vimentin], *Mapk1* [mitogen-activated protein kinase], *Nfkb1* [NF- $\kappa$ B], and *Plat* [plasminogen activator, tissue]) (Table 1).

The expression of *IL-6* in the protective group was higher than in the free-breathing group, whereas the expression in the injurious group was higher again. However, regional differences were limited to the injurious group, with higher expression in the proximal (L1, L3, and R2) lung regions (Figure 4A). For *Ccl2*, the expression was elevated in some regions (R2,  $P = 0.03$ ; L3,  $P < 0.01$ ; L1,  $P = 0.03$ ), but only in the injurious group.

## Regional Immunohistochemistry (IL-6, Ccl-2, p53, and Neutrophils)

*Ccl2* was expressed in the airway epithelial cells and inflammatory cells (primarily macrophages) and diffusely throughout the lung parenchyma (Figures 5A and 5B). The concentration of *Ccl2* was highest in L1 and L3 ( $P < 0.05$ ) (Figure 6A) in the injurious group, which was consistent with the gene expression data (i.e., L1 and L3 had the highest *Ccl2* gene expression) (Figure 4B). Interestingly, we saw the same qualitative pattern in p53 protein expression (Figures 5B and 5C) whereby L1 and L3 had the highest expression ( $P < 0.05$ ) (Figure 6B). *IL-6* was expressed primarily in the airway epithelium (data not shown). In contrast to

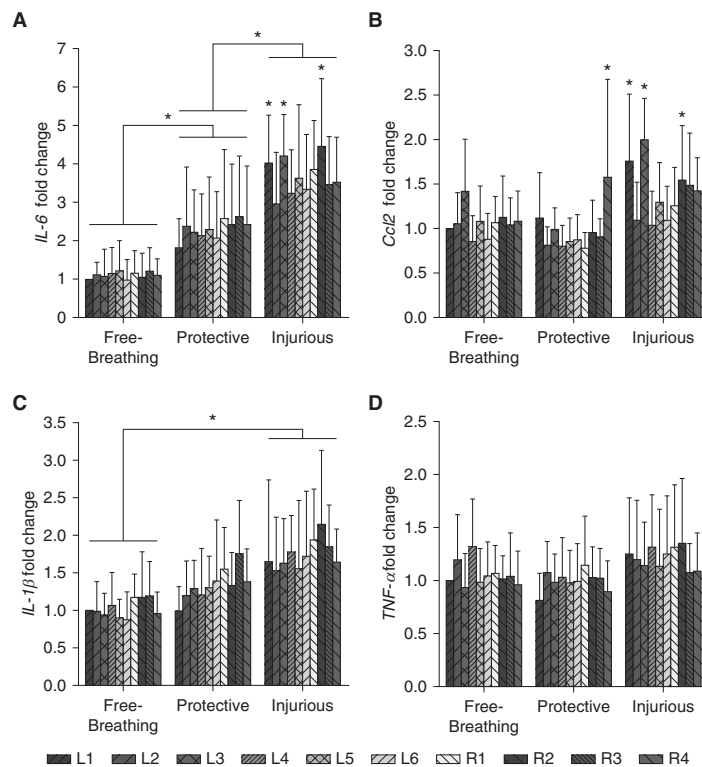


**Figure 4.** Regional gene expression measured by quantitative PCR array. Relative fold change of RNA concentrations was calculated using the comparative cycle threshold method relative to the housekeeping gene (*Rplp37*) and average cycle threshold of the L1 region in the free-breathing group for (A) *IL-6*, (B) *Ccl2*, (C) *TNF- $\alpha$* , and (D) *IL-1 $\beta$* . \* $P < 0.05$ . Data are shown as mean (SD).  $n = 8$  per group.

the other proteins, there were no significant regional differences in *IL-6* expression ( $P = 0.89$ ; data not shown). The number of neutrophils was higher ( $P = 0.007$ ) in the protective group ( $17 [2]/\text{mm}^2$ ) than in the injurious group ( $7 [2]/\text{mm}^2$ ), but there were no significant regional differences ( $P = 0.40$ ; data not shown).

Association between Regional Gene Expression and sFRC, sV<sub>T</sub>, and Regional Distention

The only genes that were significantly associated with any of imaging measures were *IL-6*, *Ccl2*, and *Ang-2* (Table 2). Expression of *IL-6* was positively associated with sV<sub>T</sub> and regional distention ( $P < 0.05$ ) but not with sFRC. Similarly, the expression of *Ccl2* was positively associated with sV<sub>T</sub>

and regional distention ( $P < 0.01$ ) but not with sFRC (Table 2 and Figure 7). Similarly, the expression of *Ang-2* was positively associated only with sV<sub>T</sub> ( $P < 0.05$ ) (Table 2 and Figure 7).

## Discussion

In this study, we assessed the impact of mechanical ventilation on regional lung volumes and gene expression. We found 1) a heterogeneous response to mechanical ventilation whereby sFRC varied regionally, independent of ventilation strategy, whereas sV<sub>T</sub> and distention (sFRC + sV<sub>T</sub>) varied regionally, depending on the ventilation strategy used; 2) an overall reduction in sFRC in response to 2 hours of

ORIGINAL RESEARCH

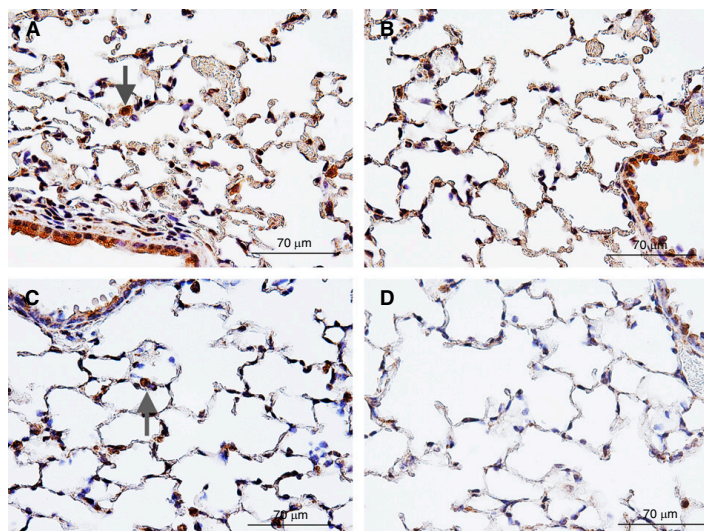


**Figure 5.** Qualitative regional expression of Ccl2 and p53. (A and B) Ccl2 staining was localized to the airway epithelium and inflammatory cells (macrophages; arrows) and was also expressed diffusely throughout the parenchyma. (C and D) The expression pattern of p53 was similar to that of Ccl2. There was regional variation (quantified in Figure 6) such that, for example, the expression levels of Ccl2 and p53 were higher in (A and C) the L1 region than in (B and D) the L2 region. Scale bars: 70  $\mu$ m.

injurious ventilation; 3) variations in regional gene expression levels that, in some cases (*IL-6*, *Ccl2*), depended on the ventilation strategy used; and 4) positive associations between the expression levels of *IL-6*, *Ccl2*, and *Ang-2* and regional stretch but not sFRC. Collectively, these

data highlight the complex and heterogeneous response of lung tissue to mechanical ventilation and how some but not all of the inflammatory response is linked to regional variations in tidal stretch. The lack of association between sFRC and altered gene expression suggests that

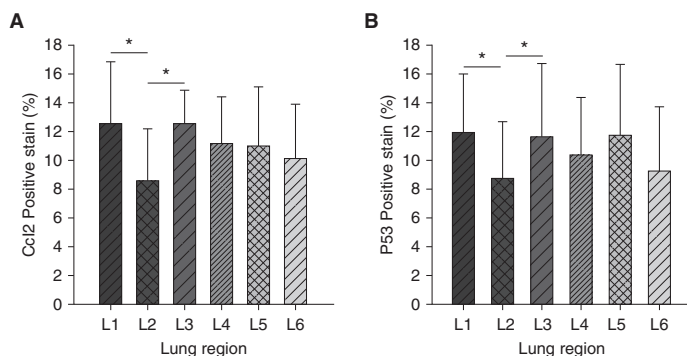


**Figure 6.** Regional expression of Ccl2 and p53 protein in the left lobe of the injurious ventilation group. The regional (L1–L6) proportion of positive staining tissue for (A) Ccl2 and (B) p53 protein (based on immunohistochemistry) per unit of tissue area after subtracting the background level of stain from the isotype control. \* $P < 0.05$ . Data are shown as mean (SD).  $n = 6$  per group.

overstretch is more detrimental than atelectasis.

We found that regional lung volumes varied in response to mechanical ventilation. This variability is consistent with that described in previous reports using larger-animal models and static lung volume measures (22, 23). Of interest is the fact that the regional variation in sFRC we observed was consistent between the protective and injurious ventilation strategies; the more distal regions of the lung seemed to be more susceptible to underventilation (i.e., low sFRC), whereas they were protected from overstretch. There was minimal change in sFRC and sV<sub>T</sub> over time in the protective group. In contrast, the injurious group showed a consistent loss of sFRC and significant variations in the sV<sub>T</sub> response over time, suggesting that this ventilation strategy alters the mechanical properties of the lung. The fact that we observed regional variations in lung stretch within minutes of mechanically ventilating the mice (i.e., at H0), as well as the fact that these regional variations were associated with altered gene expression, suggests that local lung injury may develop very soon after the commencement of ventilation.

The regional variations we observed in sV<sub>T</sub> were associated with the altered expression of *IL-6*, *Ccl2*, and *Ang-2*. *IL-6* is a key inflammatory cytokine (32) produced by epithelial cells and macrophages and is important in the progression of sepsis (17). *Ccl2*, or MCP-1, is responsible for the recruitment of macrophages to the site of inflammation (33, 34). The release of *IL-6* and *Ccl2* are closely linked (35), whereby *IL-6* induces *Ccl2* expression by peripheral blood mononuclear cells (36), whereas *Ccl2* induces the release of *IL-6* by human epithelial cells (37). Increasing concentrations of *IL-6* have been demonstrated in response to injurious ventilation in clinical (20) and experimental (17) studies. Similarly, injurious mechanical ventilation is associated with increasing concentrations of *Ccl2* in lung tissue (38), BAL, and plasma samples (7, 38). *Ang-2* is involved in the regulation of vascular endothelial permeability and is strongly linked to outcome in mechanically ventilated patients, particularly in those with ARDS (39). The link between the expression of this mediator and regional stretch highlights the role of overstretch in contributing to ventilator-induced vascular permeability and, potentially, edema,

## ORIGINAL RESEARCH

**Table 2.** Univariate Relationships between Gene Expression and Regional Lung Volume Indices

Gene Name	sFRC		sV <sub>T</sub>		Distention (sFRC + sV <sub>T</sub> )	
	R <sup>2</sup>	P Value	R <sup>2</sup>	P Value	R <sup>2</sup>	P Value
<i>Ccl2</i>	0.002	0.76	<b>0.157</b>	<b>&lt;0.01</b>	<b>0.121</b>	<b>&lt;0.01</b>
<i>Cxcl2</i>	<0.001	0.92	0.038	0.14	0.033	0.17
<i>IL-1β</i>	0.016	0.34	0.048	0.09	0.058	0.06
<i>IL-6</i>	0.009	0.47	<b>0.063</b>	<b>0.05</b>	<b>0.068</b>	<b>0.04</b>
<i>c-fos</i>	<0.001	0.92	0.025	0.23	0.022	0.26
<i>Tnf-α</i>	0.015	0.35	0.032	0.17	0.042	0.12
<i>Wnt1</i>	0.023	0.25	0.007	0.54	0.016	0.34
<i>Nfe2l2</i>	0.036	0.15	<0.001	0.98	0.04	0.64
<i>RAGE</i>	0.005	0.58	0.018	0.31	0.009	0.46
<i>Ang-2</i>	0.01	0.45	<b>0.063</b>	<b>0.05</b>	0.038	0.14

Definition of abbreviations: sFRC = specific functional residual capacity; sV<sub>T</sub> = specific tidal volume. R<sup>2</sup> and P values are from the linear regression analysis examining the association between gene expression and regional sFRC, sV<sub>T</sub>, and distention (sFRC + sV<sub>T</sub>). Only genes that showed significant variations by region and/or in response to ventilation were included in this analysis. P values < 0.05 are in boldface type.

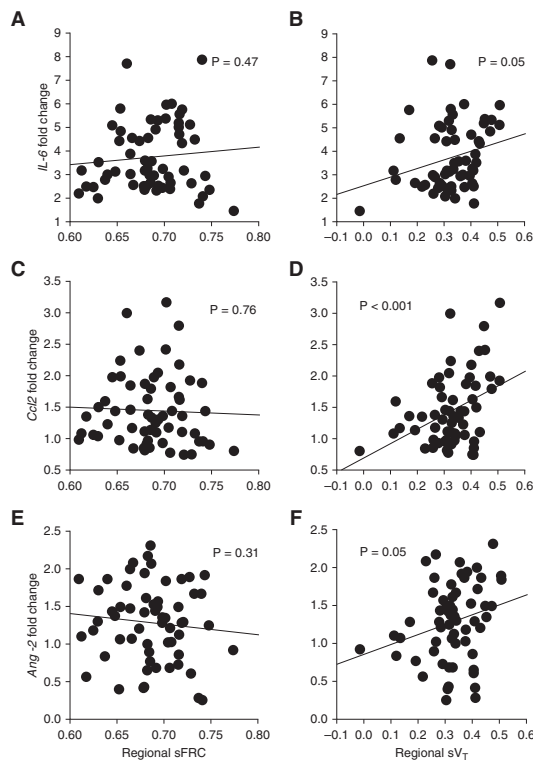


**Figure 7.** Relationship between regional gene expression (*IL-6*, *Ccl-2*, and *Ang-2* [angiopoietin 2]) and lung volumes. Scatterplots show the relationship between the fold change in regional gene expression of (A and B) *IL-6*, (C and D) *Ccl2*, and (E and F) *Ang-2*, and (A, C, and E) regional sFRC and (B, D, and F) regional sV<sub>T</sub> in the injurious group. Lines represent the predicted association based on linear regression analysis.

although we were not able to quantify the latter directly. Although demonstration of upregulation of these genes in response to mechanical ventilation is not novel, overstretch as the key driver of the expression of these mediators is suggested by the strong positive association between regional *IL-6*, *Ccl2*, and *Ang-2* expression; regional sV<sub>T</sub> and regional distention; and the absence of an association with sFRC. Given the importance of these mediators in multiorgan dysfunction (7, 40) and patient mortality (39), our data suggest that avoidance of regional overstretch during initiation of ventilation may be a critical determinant of patient outcome.

Although the expression levels of other genes (*Cxcl2*, *TNF-α*, *c-fos*, *Nfe2l2*, and *Wnt1*) were altered in response to the ventilation strategies used, their levels were not correlated with regional sFRC or sV<sub>T</sub>. *TNF-α* and *Cxcl2* are proinflammatory cytokines that are elevated in response to mechanical ventilation (41). *Nfe2l2*, *c-Fos*, and *Wnt1* are involved in transcription, cell signaling, and mesenchymal responses, respectively, and have previously been associated with the response to mechanical ventilation (17, 42, 43). In the case of *TNF-α*, *c-fos*, and *Wnt1*, the greatest expression was observed in the injurious group compared with the protective group, whereas the expression of *Nfe2l2* was equivalent between the protective and injurious groups, and the expression of *Cxcl2* was highest in the protective group compared with the injurious group. The expression pattern of *Cxcl2* matched our neutrophil data whereby there were no regional differences in neutrophil numbers, but there was an association with ventilation such that the greatest neutrophilia was observed in the protective ventilation group. These observations are consistent with the notion that *Cxcl2* is involved in the recruitment of neutrophils during the early stages of inflammation (44). These variations suggest that the pattern of expression is correlated with the ventilation strategy. However, none of these genes were associated with regional sFRC or sV<sub>T</sub>, suggesting that local factors may not be driving the altered expression of these pathways. Alternatively, upregulation of the expression of these genes may be binary and based on a low threshold of activation in response to mechanical stretch, although this does not explain the expression pattern in *Cxcl2*. Clearly, the

ORIGINAL RESEARCH

link between regional overstretch and underventilation and the subsequent activation of biological pathways is complex. Although we have identified a clear link between overstretch and the expression of *IL-6*, *Ccl2*, and *Ang-2*, the mechanical and biological processes regulating the altered expression of the other genes warrant further investigation.

To gain further insight into the key processes, using immunohistochemistry, we quantified *IL-6* and *Ccl2* protein expression to determine whether altered gene expression translated into protein synthesis and p53 expression to gain further insight into the cellular response. We found that *Ccl2* protein expression matched the gene data, whereas there was no difference in expression of *IL-6* protein. It is unclear whether the latter was due to a lack of translation or whether the timing was such that protein translation had not yet occurred. The pattern of p53 expression matched *Ccl2*. We assessed p53 as a potential marker of apoptosis (45); however, p53 has multiple functions in cell regulation. In this context, p53 has been shown to regulate *Ccl2* expression (46); thus, the association between the expression of these proteins is perhaps not surprising. This suggests that the

stretch-induced production of *Ccl2* may be regulated by p53; however, we are unable to rule out other roles for p53 in this context.

This study has several limitations. First, our injurious ventilation strategy comprised both high-pressure and zero PEEP, so we cannot separate the effect of each of these on the global expression levels of the genes we measured. However, our ability to calculate regional measures of sFRC and sVT means that we were able to identify how these factors influence regional gene expression levels. We were also limited by the fact that our observations were based primarily on correlation between gene expression and sVT, although the weight of evidence would suggest that the links we made were causal, and we were able to confirm increased *Ccl2* gene expression by immunohistochemistry.

In summary, we have demonstrated regional variations in sFRC and sVT in response to mechanical ventilation. By measuring the expression levels of a suite of genes, we were also able to assess the link between the mechanical response of the lung and alterations in regional gene expression. Interestingly, no alterations in gene expression levels were associated with markers of atelectasis, whereas alterations in expression of *IL-6* and *Ccl2* were clearly

linked to regional overstretch. There were a number of genes with altered expression levels with particular ventilation strategies, but not the regional mechanical response, which warrants further investigation. In the context of therapeutic approaches to improve outcomes in critically ill patients who are mechanically ventilated, our observations suggest that proinflammatory pathways are activated very early in response to mechanical stretch. What is unclear is whether this response resolves when stretch is subsequently reduced. Our data also indicate that *IL-6*, *Ccl2*, and *Ang-2* are the most sensitive to regional variation in stretch. However, the relative pathological significance of these mediators is unclear, with studies suggesting that upregulation of *IL-6* may be protective (47), whereas upregulation of *Ang-2* is detrimental (48); thus, the net effect may depend on the relative expression of these pathways. Further exploration of this interaction is necessary to further understand the pathogenesis of VILI. Our study clearly highlights the complexity of the link between mechanical ventilation and biotrauma. ■

Author disclosures are available with the text of this article at [www.atsjournals.org](http://www.atsjournals.org).

References

- Phua J, Badia JR, Adhikari NKJ, Friedrich JO, Fowler RA, Singh JM, et al. Has mortality from acute respiratory distress syndrome decreased over time? a systematic review. *Am J Respir Crit Care Med* 2009;179:220–227.
- Villar J, Blanco J, Kacmarek RM. Current incidence and outcome of the acute respiratory distress syndrome. *Curr Opin Crit Care* 2016;22:1–6.
- Bellani G, Laffey JG, Pham T, Fan E, Brochard L, Esteban A, et al.; LUNG SAFE Investigators; ESICM Trials Group. Epidemiology, patterns of care, and mortality for patients with acute respiratory distress syndrome in intensive care units in 50 countries. *JAMA* 2016;315:788–800.
- Ranieri VM, Rubenfeld GD, Thompson BT, Ferguson ND, Caldwell E, Fan E, et al.; ARDS Definition Task Force. Acute respiratory distress syndrome: the Berlin Definition. *JAMA* 2012;307:2526–2533.
- Montgomery AB, Stager MA, Carrico CJ, Hudson LD. Causes of mortality in patients with the adult respiratory distress syndrome. *Am Rev Respir Dis* 1985;132:485–489.
- Slutsky AS. History of mechanical ventilation: from Vesalius to ventilator-induced lung injury. *Am J Respir Crit Care Med* 2015;191:1106–1115.
- Imai Y, Parodo J, Kajikawa O, de Perrot M, Fischer S, Edwards V, et al. Injurious mechanical ventilation and end-organ epithelial cell apoptosis and organ dysfunction in an experimental model of acute respiratory distress syndrome. *JAMA* 2003;289:2104–2112.
- Carrasco Loza R, Villamizar Rodríguez G, Medel Fernández N. Ventilator-induced lung injury (VILI) in acute respiratory distress syndrome (ARDS): volutrauma and molecular effects. *Open Respir Med J* 2015;9:112–119.
- Bailey TC, Maruscak AA, Martin EL, Forbes AR, Petersen A, McCaig LA, et al. The effects of long-term conventional mechanical ventilation on the lungs of adult rats. *Crit Care Med* 2008;36:2381–2387.
- Dreyfuss D, Saumon G. Ventilator-induced lung injury: lessons from experimental studies. *Am J Respir Crit Care Med* 1998;157:294–323.
- Brower RG, Matthay MA, Morris A, Schoenfeld D, Thompson BT, Wheeler A; Acute Respiratory Distress Syndrome Network. Ventilation with lower tidal volumes as compared with traditional tidal volumes for acute lung injury and the acute respiratory distress syndrome. *N Engl J Med* 2000;342:1301–1308.
- Guérin C, Reignier J, Richard JC, Beuret P, Gacouin A, Boulain T, et al.; PROSEVA Study Group. Prone positioning in severe acute respiratory distress syndrome. *N Engl J Med* 2013;368:2159–2168.
- Cavalcanti AB, Suzumura EA, Laranjeira LN, Paisani DM, Damiani LP, Guimarães HP, et al.; Writing Group for the Alveolar Recruitment for Acute Respiratory Distress Syndrome Trial (ART) Investigators. Effect of lung recruitment and titrated positive end-expiratory pressure (PEEP) vs low PEEP on mortality in patients with acute respiratory distress syndrome: a randomized clinical trial. *JAMA* 2017;318:1335–1345.
- Gattinoni L, Marini JJ, Pesenti A, Quintel M, Mancebo J, Brochard L. The “baby lung” became an adult. *Intensive Care Med* 2016;42:663–673.
- Cressoni M, Chiurazzi C, Gotti M, Amini M, Brioni M, Algieri I, et al. Lung inhomogeneities and time course of ventilator-induced mechanical injuries. *Anesthesiology* 2015;123:618–627.
- Dargaville PA, Rimensberger PC, Frerichs I. Regional tidal ventilation and compliance during a stepwise vital capacity manoeuvre. *Intensive Care Med* 2010;36:1953–1961.
- Tremblay L, Valenza F, Ribeiro SP, Li J, Slutsky AS. Injurious ventilatory strategies increase cytokines and c-fos m-RNA expression in an isolated rat lung model. *J Clin Invest* 1997;99:944–952.
- Pugin J. Molecular mechanisms of lung cell activation induced by cyclic stretch. *Crit Care Med* 2003;31(4, Suppl):S200–S206.

## ORIGINAL RESEARCH

19. Vlahakis NE, Schroeder MA, Limper AH, Hubmayr RD. Stretch induces cytokine release by alveolar epithelial cells in vitro. *Am J Physiol* 1999;277:L167–L173.
20. Stüber F, Wrigge H, Schroeder S, Wetegrove S, Zinserling J, Hoefft A, et al. Kinetic and reversibility of mechanical ventilation-associated pulmonary and systemic inflammatory response in patients with acute lung injury. *Intensive Care Med* 2002;28:834–841.
21. Cannizzaro V, Hantos Z, Sly PD, Zosky GR. Linking lung function and inflammatory responses in ventilator-induced lung injury. *Am J Physiol Lung Cell Mol Physiol* 2011;300:L112–L120.
22. Wellman TJ, Winkler T, Costa EL, Musch G, Harris RS, Zheng H, et al. Effect of local tidal lung strain on inflammation in normal and lipopolysaccharide-exposed sheep. *Crit Care Med* 2014;42:e491–e500.
23. Paula LF, Wellman TJ, Winkler T, Spieth PM, Güldner A, Venegas JG, et al. Regional tidal lung strain in mechanically ventilated normal lungs. *J Appl Physiol (1985)* 2016;121:1335–1347.
24. Dubsy S, Hooper SB, Siu KKW, Fouras A. Synchrotron-based dynamic computed tomography of tissue motion for regional lung function measurement. *J R Soc Interface* 2012;9:2213–2224.
25. Zosky GR, Cannizzaro V, Hantos Z, Sly PD. Protective mechanical ventilation does not exacerbate lung function impairment or lung inflammation following influenza A infection. *J Appl Physiol (1985)* 2009;107:1472–1478.
26. Larsson DH, Takman PA, Lundström U, Burvall A, Hertz HMA. A 24 keV liquid-metal-jet x-ray source for biomedical applications. *Rev Sci Instrum* 2011;82:123701.
27. Samarage CR, Carnibella R, Preissner M, Jones HD, Pearson JT, Fouras A, et al. Technical note: contrast free angiography of the pulmonary vasculature in live mice using a laboratory x-ray source. *Med Phys* 2016;43:6017.
28. Kim EH, Preissner M, Carnibella RP, Samarage CR, Bennett E, Diniz MA, et al. Novel analysis of 4DCT imaging quantifies progressive increases in anatomic dead space during mechanical ventilation in mice. *J Appl Physiol (1985)* 2017;123:578–584.
29. Stahr CS, Samarage CR, Donnelley M, Farrow N, Morgan KS, Zosky G, et al. Quantification of heterogeneity in lung disease with image-based pulmonary function testing. *Sci Rep* 2016;6:29438.
30. Dubsy S, Zosky GR, Perks K, Samarage CR, Henon Y, Hooper SB, et al. Assessment of airway response distribution and paradoxical airway dilation in mice during methacholine challenge. *J Appl Physiol (1985)* 2017;122:503–510.
31. Frangi AF, Niessen WJ, Vincken KL, Viergever MA. Multiscale vessel enhancement filtering. In: Wells WM, Colchester A, Delp S, editors. Medical image computing and computer-assisted intervention — MICCAI'98: first international conference. MICCAI 1998. Lecture Notes in Computer Science, Vol. 1496. Berlin, Heidelberg: Springer; 1998. pp. 130–137.
32. Xing Z, Gauldie J, Cox G, Baumann H, Jordana M, Lei XF, et al. IL-6 is an antiinflammatory cytokine required for controlling local or systemic acute inflammatory responses. *J Clin Invest* 1998;101:311–320.
33. van Kooten C, van der Linde X, Woltman AM, van Es LA, Daha MR. Synergistic effect of interleukin-1 and CD40L on the activation of human renal tubular epithelial cells. *Kidney Int* 1999;56:41–51.
34. Prodjosudjadi W, Gerritsma JS, Klar-Mohamad N, Gerritsen AF, Bruijn JA, Daha MR, et al. Production and cytokine-mediated regulation of monocyte chemoattractant protein-1 by human proximal tubular epithelial cells. *Kidney Int* 1995;48:1477–1486.
35. Hosaka K, Rojas K, Fazal HZ, Schneider MB, Shores J, Federico V, et al. Monocyte chemotactic protein-1-interleukin-6-osteopontin pathway of intra-aneurysmal tissue healing. *Stroke* 2017;48:1052–1060.
36. Biswas P, Delfanti F, Bernasconi S, Mengozzi M, Cota M, Polentarutti N, et al. Interleukin-6 induces monocyte chemotactic protein-1 in peripheral blood mononuclear cells and in the U937 cell line. *Blood* 1998;91:258–265.
37. Viedt C, Dechend R, Fei J, Hänsch GM, Kreuzer J, Orth SR. MCP-1 induces inflammatory activation of human tubular epithelial cells: involvement of the transcription factors, nuclear factor- $\kappa$ B and activating protein-1. *J Am Soc Nephrol* 2002;13:1534–1547.
38. Altmeier WA, Matute-Bello G, Frevert CW, Kawata Y, Kajikawa O, Martin TR, et al. Mechanical ventilation with moderate tidal volumes synergistically increases lung cytokine response to systemic endotoxin. *Am J Physiol Lung Cell Mol Physiol* 2004;287:L533–L542.
39. Zinter MS, Spicer A, Orwoll BO, Alkhouli M, Dvorak CC, Calfee CS, et al. Plasma angiotensin-2 outperforms other markers of endothelial injury in prognosticating pediatric ARDS mortality. *Am J Physiol Lung Cell Mol Physiol* 2016;310:L224–L231.
40. Tesch GH, Schwarting A, Kinoshita K, Lan HY, Rollins BJ, Kelley VR. Monocyte chemoattractant protein-1 promotes macrophage-mediated tubular injury, but not glomerular injury, in nephrotoxic serum nephritis. *J Clin Invest* 1999;103:73–80.
41. Shosholcheva M, Jankulovski N, Kartalov A, Kuzmanovska B, Miladinova D. Synergistic effect of hyperoxia and biotrauma on ventilator-induced lung injury. *Pril (Makedon Akad Nauk Umet Odd Med Nauki)* 2017;38:91–96.
42. Shan Y, Akram A, Amatullah H, Zhou DY, Gali PL, Maron-Gutierrez T, et al. ATF3 protects pulmonary resident cells from acute and ventilator-induced lung injury by preventing Nrf2 degradation. *Antioxid Redox Signal* 2015;22:651–668.
43. Silva PL, Negrini D, Rocco PR. Mechanisms of ventilator-induced lung injury in healthy lungs. *Best Pract Res Clin Anaesthesiol* 2015;29:301–313.
44. De Filippo K, Dudeck A, Hasenberg M, Nye E, van Rooijen N, Hartmann K, et al. Mast cell and macrophage chemokines CXCL1/CXCL2 control the early stage of neutrophil recruitment during tissue inflammation. *Blood* 2013;121:4930–4937.
45. Ozaki T, Nakagawara A. Role of p53 in cell death and human cancers. *Cancers (Basel)* 2011;3:994–1013.
46. Tang X, Asano M, O'Reilly A, Farquhar A, Yang Y, Amar S. p53 is an important regulator of CCL2 gene expression. *Curr Mol Med* 2012;12:929–943.
47. Wolters PJ, Wray C, Sutherland RE, Kim SS, Koff J, Mao Y, et al. Neutrophil-derived IL-6 limits alveolar barrier disruption in experimental ventilator-induced lung injury. *J Immunol* 2009;182:8056–8062.
48. Bhandari V, Choo-Wing R, Lee CG, Zhu Z, Nedrelow JH, Chupp GL, et al. Hyperoxia causes angiotensin 2-mediated acute lung injury and necrotic cell death. *Nat Med* 2006;12:1286–1293.

**A.2 Interaction between regional lung volumes and ventilator induced lung injury in the normal and endotoxaemic lung**

*Am J Physiol Lung Cell Mol Physiol* 318: L494–L499, 2020.  
First published January 15, 2020; doi:10.1152/ajplung.00492.2019.

## RAPID REPORT

### Interaction between regional lung volumes and ventilator-induced lung injury in the normal and endotoxemic lung

Seiha Yen,<sup>1\*</sup> Melissa Preissner,<sup>2\*</sup> Ellen Bennett,<sup>1</sup> Stephen Dubsky,<sup>2</sup> Richard Carnibella,<sup>3</sup> Rhiannon Murrie,<sup>2</sup> Andreas Fouras,<sup>3</sup> Peter A. Dargaville,<sup>4</sup> and Graeme R. Zosky<sup>1,4</sup>

<sup>1</sup>School of Medicine, College of Health and Medicine, University of Tasmania, Hobart, Tasmania, Australia; <sup>2</sup>Department of Mechanical and Aerospace Engineering, Monash University, Melbourne, Victoria, Australia; <sup>3</sup>4Dx Limited, Melbourne, Victoria, Australia; and <sup>4</sup>Menzies Institute for Medical Research, College of Health and Medicine, University of Tasmania, Hobart, Tasmania, Australia

Submitted 2 December 2019; accepted in final form 6 January 2020

**Yen S, Preissner M, Bennett E, Dubsky S, Carnibella R, Murrie R, Fouras A, Dargaville PA, Zosky GR.** Interaction between regional lung volumes and ventilator-induced lung injury in the normal and endotoxemic lung. *Am J Physiol Lung Cell Mol Physiol* 318: L494–L499, 2020. First published January 15, 2020; doi:10.1152/ajplung.00492.2019.—Both overdistension and atelectasis contribute to lung injury and mortality during mechanical ventilation. It has been proposed that combinations of tidal volume and end-expiratory lung volume exist that minimize lung injury linked to mechanical ventilation. The aim of this study was to examine this at the regional level in the healthy and endotoxemic lung. Adult female BALB/c mice were injected intraperitoneally with 10 mg/kg lipopolysaccharide (LPS) in saline or with saline alone. Four hours later, mice were mechanically ventilated for 2 h. Regional specific end-expiratory volume (sEEV) and tidal volume (sVt) were measured at baseline and after 2 h of ventilation using dynamic high-resolution four-dimensional computed tomography images. The regional expression of inflammatory genes was quantified by quantitative PCR. There was a heterogeneous response in regional sEEV whereby endotoxemia increased gas trapping at end-expiration in some lung regions. Within the healthy group, there was a relationship between sEEV, sVt, and the expression of *Tnfa*, where high Vt in combination with high EEV or very low EEV was associated with an increase in gene expression. In endotoxemia there was an association between low sEEV, particularly when this was combined with moderate sVt, and high expression of *IL6*. Our data suggest that preexisting systemic inflammation modifies the relationship between regional lung volumes and inflammation and that although optimum EEV-Vt combinations to minimize injury exist, further studies are required to identify the critical inflammatory mediators to assess and the effect of different injury types on the response.

endotoxemia; inflammation; mouse model; regional lung imaging; ventilator-induced lung injury

## INTRODUCTION

Mortality rates due to acute respiratory distress syndrome (ARDS) remain high (3, 28). Mechanical ventilation, a lifesaving intervention in ARDS-related respiratory failure, may contribute to mortality by promoting inflammation in a process

known as ventilator-induced lung injury (VILI; 11, 26). The pathobiology of VILI is complex and is thought to occur through multiple mechanisms including overdistension due to high tidal volume (Vt) and/or end-inspiratory lung volume and atelectrauma due to low positive end-expiratory pressure (PEEP) and/or ventilation at low Vt (24).

When considering the competing priorities of maintaining adequate gas exchange while avoiding VILI, Seah et al. (22) proposed the concept of a Vt-PEEP plane, whereby a set of Vt-PEEP combinations exist that minimize lung injury. However, optimizing ventilation strategies to minimize VILI is complicated by the heterogeneous response within the lung to mechanical ventilation, whereby overdistension and atelectrauma may occur concurrently in different regions of the lung at a given PEEP and driving pressure (8, 20). We have recently measured the variations in regional Vt and end-expiratory volume (EEV) during ventilation of the naive mouse lung using four-dimensional computed tomography (4DCT) and found that regional Vt, but not EEV, was positively associated with the regional expression of *IL6* and C-C motif chemokine ligand 2 (*Ccl2*) suggesting that overdistension is the primary driver of VILI in the healthy lung (30).

4DCT imaging provides an opportunity to explore the Vt-PEEP plane concept at a regional level, using regional EEV as an indicator of the local PEEP effect and linking indexes of regional Vt and EEV to the local injury response. This allows multiple Vt-EEV combinations (analogous to global Vt and PEEP) to be matched with lung injury markers in one subject, thus overcoming the constraints associated with linkage of Vt-PEEP combinations with the lung injury response at a global level. Furthermore, performing this analysis regionally allows a greater variety and diversity of tidal stretch and regional EEV combinations to be examined.

When considering the relationship between lung volumes and injury, it is important to consider the effect of the prior lung injury (9), which precipitates the requirement for mechanical ventilation. For example, endotoxemia, as a model of sepsis, has been shown to modify the regional lung response to mechanical ventilation (29). The aim of this study was to assess the relationship between combinations of regional tidal volume and end-expiratory volume, as proxy measures of overdistension and atelectrauma, and the regional expression of inflammatory genes in the healthy and endotoxemic lung.

\* S. Yen and M. Preissner contributed equally to this work.

Address for reprint requests and other correspondence: G. R. Zosky, College of Health and Medicine, Univ. of Tasmania, Private Bag 34, Hobart, TAS 7001, Australia (e-mail: Graeme.Zosky@utas.edu.au).

**METHODS**

**Animals.** Adult female BALB/c mice were purchased from the Monash Animal Research Platform (Monash University, Melbourne, VIC, Australia). All mice were provided food and water ad libitum. All experiments complied with the guidelines of the National Health and Medical Research Council of Australia and were approved by the Monash University and University of Tasmania animal ethics committees.

**Animal treatment, preparation, and ventilation.** Mice were injected intraperitoneally with 200  $\mu$ L of 0.9% saline (10 mL/kg body wt) with, or without, 10 mg/kg lipopolysaccharide (LPS) derived from *E. coli* O111:B4 (InvivoGen, San Diego, CA). Four hours after injection, mice were anesthetized (400 mg/kg ketamine, 20 mg/kg xylazine; Troy Laboratories, Glendenning, NSW, Australia), tracheostomized, and ventilated with a small-animal ventilator (AccuVent 200; Notting Hill Devices, Melbourne, VIC, Australia) for 2 h at 225 breaths/min, with a peak inspiratory pressure of 12 cmH<sub>2</sub>O and a PEEP of 2 cmH<sub>2</sub>O.

Lung imaging was performed at baseline using a custom-built laboratory-based system with a liquid metal jet X-ray source (Excillum AB, Kista, Sweden) coupled with a high-speed detector (PaxScan; Varian Medical Systems, Palo Alto, CA) to capture 4DCT images. This system allowed us to capture high-brightness, high-resolution images at a high frame rate (400 projections per CT at 30 frames/s; 21). At the end of ventilation, mice were euthanized by sodium pentobarbitone overdose (200 mg/kg) before processing of the lung tissue for gene expression.

**Regional lung volumes.** 4DCT images were segmented into 10 regions (Fig. 1A) to calculate regional lung volumes as described previously (30; Fig. 1A). The lung regions were chosen arbitrarily to ensure a sufficient number of regions for assessment of regional variation, while allowing accurate image segmentation. The airway tree was manually segmented at end-expiration after applying a filter to identify the main airway supplying each lobe (25). A three-dimensional velocimetry technique, which dynamically tracks tissue deformation, was then applied to calculate regional Vt (12, 15, 25), whereas Hounsfield units were used to determine the aeration fraction to obtain estimates of regional EEV. To correct for the variation in regional lung size, we calculated specific EEV (sEEV = regional EEV/total volume of all voxels in the region) and specific tidal volume (sVt = regional Vt/total volume of all voxels in the region) for each region.

**Regional gene expression.** Lungs were removed en bloc, and tissue was collected from 10 regions corresponding to the regional image segmentation (30). Lung tissue was stored in RNAlater (Sigma) at  $-20^{\circ}$ C before processing. RNA extraction on the frozen samples and gene expression assessment using reverse transcription-quantitative PCR arrays were performed as described previously (30). The expression of seven VILI-related genes [*Tnfa*, *IL1b*, *IL6*, *Ccl2*, C-X-C motif chemokine ligand 2 (*Cxcl2*), myeloperoxidase (*Mpo*), and nuclear factor, erythroid 2-like 2 (*Nfe2l2*)] was assessed (30). Gene expression relative to the reference gene [ribosomal protein L37 (*Rpl37*)] was calculated using the  $2^{-\Delta\text{CT}}$  method (where CT is threshold cycle) and expressed as a fold change.

**Data analysis.** Between-group and between-region differences in sEEV, sVt, and relative gene expression were assessed using two-way repeated-measures ANOVA with Holm-Sidak post hoc tests (SigmaPlot v. 12.5; Systat Software Inc., San Jose, CA). Data were transformed where necessary to satisfy the assumptions of normality and homoscedasticity of the variances. Associations between regional sEEV, regional sVt, and regional mRNA levels were assessed using linear regression analysis.  $P < 0.05$  was considered statistically significant. A qualitative analysis of the sEEV-sVt plane and the expression of genes that were significantly associated with lung volumes in the regression analyses was conducted by constructing scatterplots of sVt against sEEV where the size of the points was proportional to the expression of the gene of interest.

**RESULTS**

**Effect of LPS on sEEV and sVt.** At baseline, the endotoxemic lung had higher sEEV in regions L2 ( $P < 0.001$ ) and R1 ( $P = 0.01$ ) compared with the healthy lung (Fig. 1, B and C). At baseline, sVt varied regionally ( $P < 0.001$ ) within groups, but there was no effect of endotoxemia on the response ( $P = 0.19$ ; Fig. 1, D and E). There was no difference between the endotoxemic and healthy lung in the regional change in sEEV ( $P = 0.55$ ) or sVt ( $P = 0.12$ ) after 2 h of ventilation.

**Regional gene expression.** Overall, the regional expression of all measured genes was higher in the endotoxemic lung ( $P < 0.001$  for all genes). The expression of *IL6* ( $P = 0.04$ ) varied regionally within the endotoxemic group, whereby expression in region R4 was higher than that in several other regions (e.g.,

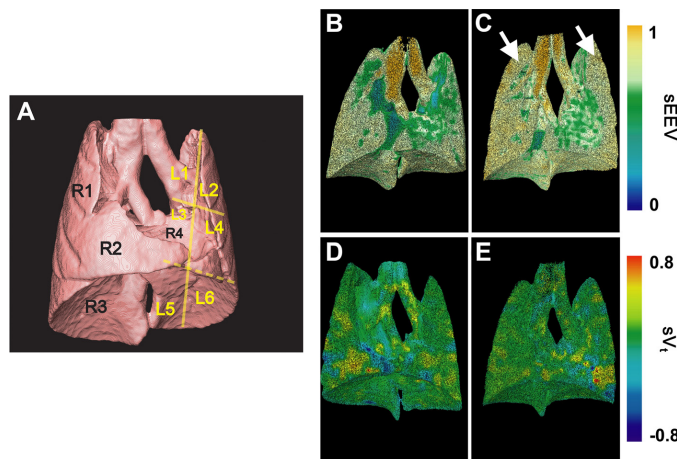
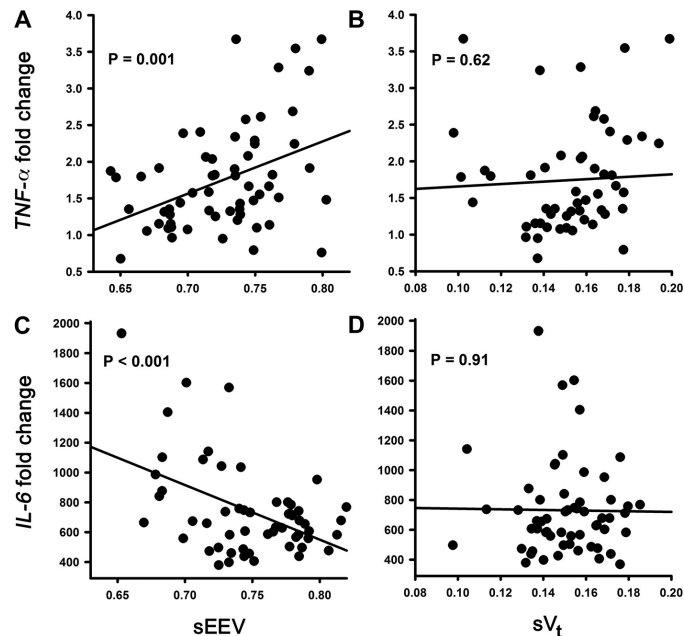


Fig. 1. Regional lung volumes: segmentation strategy and representative images. To allow associations between regional lung volumes and gene expression to be assessed, the lung was divided into 10 regions (A): 4 individual right lobes (regions R1–R4) and 6 regions in the left lobe (regions L1–L6). Representative three-dimensional images of specific end-expiratory volume (sEEV; B and C) and specific tidal volume (sVt; D and E) for a healthy lung (B and D) and an endotoxemic lung (C and E) at baseline. Endotoxemia was associated with an increase in sEEV in regions R1 and L2 (arrows), whereas regional sVt was relatively homogeneous.

L496

VENTILATOR-INDUCED LUNG INJURY IN ENDOTOXEMIA

Fig. 2. Association between regional gene expression and lung volume. Scatterplots showing the relationship between the fold change [relative to the ribosomal protein L37 (*Rpl37*) housekeeping gene] in regional gene expression of *Tnfa* (A and B; healthy lung) and *IL6* (C and D; endotoxemic lung), assessed after 2 h of ventilation, and specific end-expiratory volume (sEEV; A and C) and tidal volume (sVt; B and D) at baseline. Lines represent the predicted association based on linear regression analysis ( $P$  values shown).



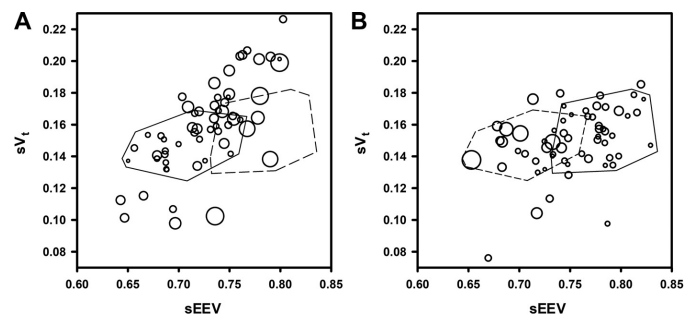
vs. region R1,  $P < 0.001$ ). In contrast, the expression of *Ccl2* varied regionally but only in the healthy lung, with higher expression in proximal regions of the left lobe (regions L1 and L3) and lower regions of the right lobes (regions R3 and R4). There was also regional variation in the expression of *Tnfa* ( $P = 0.02$ ) and *Cxcl2* ( $P = 0.005$ ), but this was independent of endotoxemia. There were no significant differences in regional mRNA levels of *IL1b* ( $P = 0.15$ ), *Mpo* ( $P = 0.25$ ), or *Nfe2l2* ( $P = 0.54$ ).

**Association between regional gene expression, sEEV, and sVt.** In the healthy lung, regional sEEV was positively associated with *Tnfa* ( $P = 0.001$ ) expression (Fig. 2A). In contrast, in endotoxemia, the expression of *IL6* ( $P < 0.001$ ) was negatively associated with sEEV (Fig. 2C). There were no further asso-

ciations between regional lung volumes and the expression of the other genes measured ( $P > 0.05$  for all analyses).

**sEEV-sVt plane and gene expression.** For the qualitative assessment of the relationship between the sEEV-sVt plane and gene expression, we only focused on genes with a significant association with measures of lung volume as described above (i.e., *Tnfa* and *IL6* in the healthy and endotoxemic groups, respectively). In the healthy lung, there was a wide distribution of sEEV-sVt combinations, although it should be noted that very few regions were in the top left quadrant (low sEEV and high sVt; Fig. 3A). On the basis of the relationship between the sEEV-sVt plane and the expression of *Tnfa* there were two clusters of injurious responses in the healthy lung: high sEEV in combination with high sVt or very low sEEV independent of

Fig. 3. Specific end-expiratory volume (sEEV)-tidal volume (Vt) planes and gene expression. Scatterplots of specific Vt (sVt) versus sEEV, with circles scaled to relative gene expression (larger circle equals higher expression), at baseline for *Tnfa*, assessed postventilation, in the ventilated healthy lung (A) and *IL6* in the ventilated endotoxemic lung (B). Regions enclosed by solid lines indicate arbitrarily drawn fields corresponding to minimal gene expression; regions delineated by dashed lines are shown to highlight the difference in fields between A and B. The combinations of sEEV-Vt that minimized *Tnfa* expression in the healthy lung were fundamentally different from those that minimized *IL6* expression after endotoxin exposure.



sVt (Fig. 3A). In the case of endotoxemia, there was a clear cluster of increased *IL6* expression in lung regions with low sEEV, in combination with relatively moderate Vt (Fig. 3B). However, it was clear that the sEEV-sVt combinations that resulted in minimum production of TNF- $\alpha$  in the healthy lung (Fig. 3A) and minimum production of IL-6 in the endotoxaemic lung (Fig. 3B) were distinct.

#### DISCUSSION

This study aimed to assess the regional response to mechanical ventilation in the setting of preexisting endotoxemia-induced inflammation with a focus on the interplay between end-expiratory volume, tidal volume, and the expression of inflammatory genes. We found a heterogeneous response in regional sEEV whereby pretreatment with endotoxin increased gas trapping at end-expiration in some, but not all, lung regions but had no effect on the regional sVt response. Within the healthy group there was a relationship between sEEV, sVt, and the expression of *Tnfa* such that both high Vt in combination with high EEV and high Vt in combination with very low EEV were associated with an increase in the expression of this gene, suggesting that in the healthy lung, the response of regional lung mechanics influences the expression of inflammatory genes. Although exposure to endotoxin increased the expression of all genes measured far above the changes induced by ventilation alone, there was an association between low sEEV (particularly when this was combined with moderate sVt) and high expression of *IL6*. The effect of endotoxemia on baseline sEEV, without a subsequent effect of endotoxemia on the change in sEEV after 2 h of ventilation, suggests that this may be due to the effect of prior inflammation on the local mechanical response. Collectively, these data suggest that a "Vt-PEEP" plane exists whereby the inflammatory response is minimized. However, the boundaries of this plane vary depending on the marker of inflammation used and are complicated by the effect of prior lung injury on regional lung mechanics.

We found regional variations in lung volumes, gene expression, and inflammation that were dependent on prior treatment with LPS. Whereas there was little effect on sVt, there were region-specific increases in sEEV in the endotoxaemic group, particularly in the regions proximal to the main bronchus. This suggests an element of end-expiratory gas trapping, although we are unable to rule out other causes of high EEV such as alterations in tethering forces and gas redistribution. Nonetheless, this result is consistent with the observation that the nondependent region of the lung in ARDS is less likely to collapse (7). It is possible that there were areas of dynamic airway collapse; however, in this scenario, gas trapping in the distal lung regions would be anticipated, which we did not observe. Related to this, prior lung injury resulting in decreased peripheral compliance could cause a redistribution of regional tidal volumes such that the central lung regions become more compliant as a result of the additional tidal stretch (15, 31). Alternatively, it is possible that this increase in sEEV represents local barotrauma at the pressure front of the ventilation waveform (2, 4, 23); however, we saw no evidence of overt lung injury in these regions in the endotoxaemic lung, and this is not consistent with the gene response we observed.

There was a positive correlation between *Tnfa* and regional sEEV in the group with healthy lungs. TNF- $\alpha$  is a proinflammatory cytokine that is produced in response to mechanical ventilation (17). Whereas some studies have shown that mechanical ventilation can enhance the production of TNF- $\alpha$  in the preinjured lung (1, 10, 19), others have found that ventilation alone has no effect on TNF production (18, 27) and that the absence of TNF- $\alpha$  may enhance the injury caused by mechanical ventilation (13). Our data suggest that the effect of mechanical ventilation on TNF- $\alpha$  production is related to regional tidal stretch (sVt), but only in the healthy lung. Interestingly, examination of the effect of combinations of sVt and sEEV on the expression of *Tnfa* suggests that an optimum ventilation strategy exists whereby moderate values of sVt in combination with low to moderate sEEV minimize the expression of this gene. In contrast, high sVt alone (i.e., regions at the upper end of the pressure-volume curve) and low sVt in combination with low EEV (i.e., regions at the lower end of the pressure-volume curve close to the lower inflection point) enhanced the expression of *Tnfa*. This observation is consistent with the proposed protective Vt-PEEP plane concept (22) and studies showing that both overdistension (14) and atelectasis (6) can promote ventilator-induced lung injury; however, this was not the case after endotoxin exposure.

In the endotoxaemic lung, there was a negative correlation between *IL6* and sEEV, but not sVt, suggesting that low end-expiratory lung volume is detrimental in the setting of systemic inflammation. The expression of IL-6 is associated with poor outcomes in ARDS (5, 16), so IL-6 is an important marker of disease pathogenesis. When examining the relationship between combinations of sVt and sEEV and the expression of *IL6* in the endotoxaemic mice, we made several important observations. First, whereas the range of sEEVs observed was similar to the healthy lung, the range of tidal volumes was much smaller suggesting a more homogeneous delivery of tidal volumes in the preinjured lung. Consistent with the regression analysis, lung regions exposed to low EEV had the highest expression of *IL6*. However, there was a striking difference between the sEEV-sVt combinations that minimized *Tnfa* expression in the healthy lung and the combinations that were associated with minimal *IL6* expression in the endotoxaemic lung, such that the regions were almost mutually exclusive. To determine whether this could be attributed to the effect of VILI or the effect of prior injury on regional lung mechanics, we assessed the effect of endotoxemia on the change in lung volumes and found no effect. This suggests that this relationship is primarily driven by the effect of prior injury on local lung mechanics. This is perhaps not surprising given the effect of injury on tissue compliance (15), consistent with the reduced range of Vt values we observed.

In this study, we assessed the expression of a range of genes that have previously been associated with ventilator-induced lung injury. However, it is unclear which of these, if any, are the most critical determinant of mortality in ARDS in response to mechanical ventilation. In addition, we only assessed one form of injury, and it is likely that the interaction between combinations of regional overdistension and low end-expiratory volumes, which may favor cyclic recruitment, and the injury response will vary depending on the nature of the preexisting lung injury (e.g., sepsis vs. aspiration). It should

L498

VENTILATOR-INDUCED LUNG INJURY IN ENDOTOXEMIA

also be acknowledged that we have only assessed gene expression in response to relatively short-term ventilation.

Nonetheless, our data clearly demonstrate the impact of combinations of tidal stretch and end-expiratory volume on the expression of inflammatory genes, particularly in the healthy lung. Importantly, we have shown that the interplay between the mechanical response of the lung tissue and the inflammatory response is fundamentally altered in preexisting lung injury, which is likely due to the effect of prior injury on tissue mechanics. These observations can help further research in this field with a view to understanding the impact of regional heterogeneity in the response to mechanical ventilation to guide the design of optimal ventilation strategies and improve patient outcomes.

#### GRANTS

This work was funded by National Health and Medical Research Council (Australia) Project Grant 1077905. S. Dubsky was supported by Australian Research Council Discovery Early Career Researcher Award DE180101133.

#### DISCLOSURES

S. Dubsky, R. Carnibella, and A. Fouras have financial interests in the commercialization of an imaging technology related to this publication. None of the other authors has any conflicts of interest, financial or otherwise, to disclose.

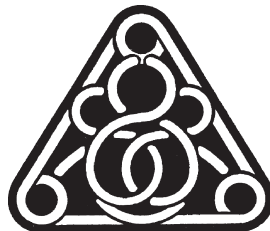
#### AUTHOR CONTRIBUTIONS

S.Y., M.P., S.D., A.F., P.A.D., and G.R.Z. conceived and designed research; S.Y., M.P., E.B., R.M., and G.R.Z. performed experiments; S.Y., M.P., E.B., S.D., R.C., R.M., and G.R.Z. analyzed data; S.Y., M.P., S.D., R.C., R.M., A.F., P.A.D., and G.R.Z. interpreted results of experiments; S.Y., M.P., and G.R.Z. prepared figures; S.Y., M.P., P.A.D., and G.R.Z. drafted manuscript; S.Y., M.P., E.B., S.D., R.C., R.M., A.F., P.A.D., and G.R.Z. edited and revised manuscript; S.Y., M.P., E.B., S.D., R.C., R.M., A.F., P.A.D., and G.R.Z. approved final version of manuscript.

#### REFERENCES

- Altemeier WA, Matute-Bello G, Frevert CW, Kawata Y, Kajikawa O, Martin TR, Glenn RW. Mechanical ventilation with moderate tidal volumes synergistically increases lung cytokine response to systemic endotoxin. *Am J Physiol Lung Cell Mol Physiol* 287: L533–L542, 2004. doi:10.1152/ajplung.00004.2004.
- Amato MB, Meade MO, Slutsky AS, Brochard L, Costa EL, Schoenfeld DA, Stewart TE, Briel M, Talmor D, Mercat A, Richard JC, Carvalho CR, Brower RG. Driving pressure and survival in the acute respiratory distress syndrome. *N Engl J Med* 372: 747–755, 2015. doi:10.1056/NEJMs1410639.
- Bellani G, Laffey JG, Pham T, Fan E, Brochard L, Esteban A, Gattinoni L, van Haren F, Larsson A, McAuley DF, Ranieri M, Rubenfeld G, Thompson BT, Wrigg H, Slutsky AS, Pesenti A; LUNG SAFE Investigators; ESICM Trials Group. Epidemiology, patterns of care, and mortality for patients with acute respiratory distress syndrome in intensive care units in 50 countries. *JAMA* 315: 788–800, 2016. doi:10.1001/jama.2016.0291.
- Bilek AM, Dee KC, Gaver DP III. Mechanisms of surface-tension-induced epithelial cell damage in a model of pulmonary airway reopening. *J Appl Physiol* (1985) 94: 770–783, 2003. doi:10.1152/jappphysiol.00764.2002.
- Calandra T, Gerain J, Heumann D, Baumgartner JD, Glauser MP. High circulating levels of interleukin-6 in patients with septic shock: evolution during sepsis, prognostic value, and interplay with other cytokines. *Am J Med* 91: 23–29, 1991. doi:10.1016/0002-9343(91)90069-A.
- Cipulli F, Vasques F, Duscio E, Romitti F, Quintel M, Gattinoni L. Atelectrauma or volutrauma: the dilemma. *J Thorac Dis* 10: 1258–1264, 2018. doi:10.21037/jtd.2018.02.71.
- Cressoni M, Cadringer P, Chiurazzi C, Amini M, Gallazzi E, Marino A, Brioni M, Carlesso E, Chiumello D, Quintel M, Bugeo G, Gattinoni L. Lung inhomogeneity in patients with acute respiratory distress syndrome. *Am J Respir Crit Care Med* 189: 149–158, 2014. doi:10.1164/rccm.201308-1567OC.
- Cressoni M, Chiurazzi C, Gotti M, Amini M, Brioni M, Algieri I, Cammaroto A, Rovati C, Massari D, di Castiglione CB, Nikolla K, Montaruli C, Lazzarini M, Dondossola D, Colombo A, Gatti S, Valerio V, Gagliano N, Carlesso E, Gattinoni L. Lung inhomogeneities and time course of ventilator-induced mechanical injuries. *Anesthesiology* 123: 618–627, 2015. doi:10.1097/ALN.0000000000000727.
- de Prost N, Ricard JD, Saumon G, Dreyfuss D. Ventilator-induced lung injury: historical perspectives and clinical implications. *Ann Intensive Care* 1: 28, 2011. doi:10.1186/2110-5820-1-28.
- Ding N, Wang F, Xiao H, Xu L, She S. Mechanical ventilation enhances HMGB1 expression in an LPS-induced lung injury model. *PLoS One* 8: e74633, 2013. doi:10.1371/journal.pone.0074633.
- Dreyfuss D, Saumon G. Ventilator-induced lung injury: lessons from experimental studies. *Am J Respir Crit Care Med* 157: 294–323, 1998. doi:10.1164/ajrcm.157.1.9604014.
- Dubsky S, Hooper SB, Siu KK, Fouras A. Synchrotron-based dynamic computed tomography of tissue motion for regional lung function measurement. *J R Soc Interface* 9: 2213–2224, 2012. doi:10.1098/rsif.2012.0116.
- Ehrhardt H, Pritske T, Oak P, Kossert M, Biebach L, Förster K, Koschig M, Alvira CM, Hilgendorff A. Absence of TNF- $\alpha$  enhances inflammatory response in the newborn lung undergoing mechanical ventilation. *Am J Physiol Lung Cell Mol Physiol* 310: L909–L918, 2016. doi:10.1152/ajplung.00367.2015.
- Güldner A, Braune A, Ball L, Silva PL, Samary C, Insoresi A, Huhle R, Rentzsch I, Becker C, Oehme L, Andreff M, Vidal Melo MF, Winkler T, Pelosi P, Rocco PR, Kotzerke J, Gama de Abreu M. Comparative effects of volutrauma and atelectrauma on lung inflammation in experimental acute respiratory distress syndrome. *Crit Care Med* 44: e854–e865, 2016. doi:10.1097/CCM.0000000000001721.
- Kim EH, Preissner M, Carnibella RP, Samarage CR, Bennett E, Diniz MA, Fouras A, Zosky GR, Jones HD. Novel analysis of 4DCT imaging quantifies progressive increases in anatomic dead space during mechanical ventilation in mice. *J Appl Physiol* (1985) 123: 578–584, 2017. doi:10.1152/jappphysiol.00903.2016.
- Meduri GU, Headley S, Kohler G, Stentz F, Tolley E, Umberger R, Leeper K. Persistent elevation of inflammatory cytokines predicts a poor outcome in ARDS. Plasma IL-1 $\beta$  and IL-6 levels are consistent and efficient predictors of outcome over time. *Chest* 107: 1062–1073, 1995. doi:10.1378/chest.107.4.1062.
- Nickles HT, Sumkauskaitė M, Wang X, Wegner I, Puderbach M, Kuebler WM. Mechanical ventilation causes airway distension with proinflammatory sequelae in mice. *Am J Physiol Lung Cell Mol Physiol* 307: L27–L37, 2014. doi:10.1152/ajplung.00288.2013.
- Okutani D, Han B, Mura M, Waddell TK, Keshavjee S, Liu M. High-volume ventilation induces pentraxin 3 expression in multiple acute lung injury models in rats. *Am J Physiol Lung Cell Mol Physiol* 292: L144–L153, 2007. doi:10.1152/ajplung.00002.2006.
- O'Mahony DS, Liles WC, Altemeier WA, Dhanireddy S, Frevert CW, Liggitt D, Martin TR, Matute-Bello G. Mechanical ventilation interacts with endotoxemia to induce extrapulmonary organ dysfunction. *Crit Care* 10: R136, 2006. doi:10.1186/cc5050.
- Paula LF, Wellman TJ, Winkler T, Spieth PM, Güldner A, Venegas JG, Gama de Abreu M, Carvalho AR, Vidal Melo MF. Regional tidal lung strain in mechanically ventilated normal lungs. *J Appl Physiol* (1985) 121: 1335–1347, 2016. doi:10.1152/jappphysiol.00861.2015.
- Preissner M, Murrin RP, Pinar I, Werdiger F, Carnibella RP, Zosky GR, Fouras A, Dubsky S. High resolution propagation-based imaging system for in vivo dynamic computed tomography of lungs in small animals. *Phys Med Biol* 63: 08NT03, 2018. doi:10.1088/1361-6560/aab8d2.
- Seah AS, Grant KA, Aliyeva M, Allen GB, Bates JH. Quantifying the roles of tidal volume and PEEP in the pathogenesis of ventilator-induced lung injury. *Ann Biomed Eng* 39: 1505–1516, 2011. doi:10.1007/s10439-010-0237-6.
- Sinclair SE, Molthen RC, Haworth ST, Dawson CA, Waters CM. Airway strain during mechanical ventilation in an intact animal model. *Am J Respir Crit Care Med* 176: 786–794, 2007. doi:10.1164/rccm.200701-088OC.
- Slutsky AS, Ranieri VM. Ventilator-induced lung injury. *N Engl J Med* 369: 2126–2136, 2013. doi:10.1056/NEJMr1208707.

25. Stahr CS, Samarage CR, Donnelley M, Farrow N, Morgan KS, Zosky G, Boucher RC, Siu KK, Mall MA, Parsons DW, Dubsky S, Fouras A. Quantification of heterogeneity in lung disease with image-based pulmonary function testing. *Sci Rep* 6: 29438, 2016. doi:10.1038/srep29438.
26. Tremblay LN, Slutsky AS. Ventilator-induced injury: from barotrauma to biotrauma. *Proc Assoc Am Physicians* 110: 482–488, 1998.
27. Tremblay L, Valenza F, Ribeiro SP, Li J, Slutsky AS. Injurious ventilatory strategies increase cytokines and c-fos m-RNA expression in an isolated rat lung model. *J Clin Invest* 99: 944–952, 1997. doi:10.1172/JCI119259.
28. Villar J, Blanco J, Kacmarek RM. Current incidence and outcome of the acute respiratory distress syndrome. *Curr Opin Crit Care* 22: 1–6, 2016. doi:10.1097/MCC.000000000000266.
29. Wellman TJ, Winkler T, Costa EL, Musch G, Harris RS, Zheng H, Venegas JG, Vidal Melo MF. Effect of local tidal lung strain on inflammation in normal and lipopolysaccharide-exposed sheep. *Crit Care Med* 42: e491–e500, 2014. doi:10.1097/CCM.0000000000000346.
30. Yen S, Preissner M, Bennett E, Dubsky S, Carnibella R, O'Toole R, Roddam L, Jones H, Dargaville PA, Fouras A, Zosky GR. The link between regional tidal stretch and lung injury during mechanical ventilation. *Am J Respir Cell Mol Biol* 60: 569–577, 2019. doi:10.1165/rmb.2018-0143OC.
31. Zosky GR, Janosi TZ, Adamicza A, Bozanich EM, Cannizzaro V, Larcombe AN, Turner DJ, Sly PD, Hantos Z. The bimodal quasi-static and dynamic elastance of the murine lung. *J Appl Physiol (1985)* 105: 685–692, 2008. doi:10.1152/jappphysiol.90328.2008.





## **B Related journal articles published during the PhD**

The two journal articles in this appendix were published as a co-author during the PhD candidature.

### **B.1 Technical Note: Contrast free angiography of the pulmonary vasculature in live mice using a laboratory X-ray source**

This open access article is licensed under the terms of the Creative Commons Attribution License: <https://creativecommons.org/licenses/by/4.0/>



## Technical Note: Contrast free angiography of the pulmonary vasculature in live mice using a laboratory x-ray source

Chaminda R. Samarage  
4Dx Limited, Melbourne 3000, Australia

Richard Carnibella  
4Dx Limited, Melbourne 3000, Australia and Department of Mechanical and Aerospace Engineering,  
Monash University, Melbourne 3800, Australia

Melissa Preissner  
Department of Mechanical and Aerospace Engineering, Monash University, Melbourne 3800, Australia

Heather D. Jones  
Department of Medicine and the Women's Guild Lung Institute, Cedars-Sinai Medical Center, Los Angeles,  
California 90048

James T. Pearson  
Department of Physiological, Monash University, Melbourne 3800, Australia; Monash Biomedical Imaging  
Facility Monash University, Melbourne 3800, Australia; and Australian Synchrotron,  
Melbourne 3168, Australia

Andreas Fouras<sup>a)</sup> and Stephen Dubsy<sup>a)</sup>  
4Dx Limited, Melbourne 3000, Australia and Department of Mechanical and Aerospace Engineering,  
Monash University, Melbourne 3800, Australia

(Received 6 March 2016; revised 15 August 2016; accepted for publication 30 September 2016;  
published 18 October 2016)

**Purpose:** *In vivo* imaging of the pulmonary vasculature in small animals is difficult yet highly desirable in order to allow study of the effects of a host of dynamic biological processes such as hypoxic pulmonary vasoconstriction. Here the authors present an approach for the quantification of changes in the vasculature.

**Methods:** A contrast free angiography technique is validated *in silico* through the use of computer-generated images and *in vivo* through microcomputed tomography ( $\mu$ CT) of live mice conducted using a laboratory-based x-ray source. Subsequent image processing on  $\mu$ CT data allowed for the quantification of the caliber of pulmonary vasculature without the need for external contrast agents. These measures were validated by comparing with quantitative contrast microangiography in the same mice.

**Results:** Quantification of arterial diameters from the method proposed in this study is validated against laboratory-based x-ray contrast microangiography. The authors find that there is a high degree of correlation ( $R = 0.91$ ) between measures from microangiography and their contrast free method.

**Conclusions:** A technique for quantification of murine pulmonary vasculature without the need for contrast is presented. As such, this technique could be applied for longitudinal studies of animals to study changes to vasculature without the risk of premature death in sensitive mouse models of disease. This approach may also be of value in the clinical setting. © 2016 Author(s). All article content, except where otherwise noted, is licensed under a Creative Commons Attribution (CC BY) license (<http://creativecommons.org/licenses/by/4.0/>). [<http://dx.doi.org/10.1118/1.4964794>]

Key words: pulmonary vasculature, x-ray, angiography, contrast free, lab-source

### 1. INTRODUCTION

Diseases of the lungs often involve derangements of complex physiological processes that cannot be effectively studied *in vitro* or in postmortem samples. In particular, *in vivo* imaging of the pulmonary vasculature and of dynamic processes such as hypoxic pulmonary vasoconstriction has proven to be challenging in small animals. Although recent advances such as the murine thoracic-window model and oxygen-saturation mapping techniques have added greatly to the ability to image pulmonary vascular responses *in vivo*, these approaches

are technically challenging and only provide information on a small area of the lung for each animal studied.<sup>1,2</sup> Other techniques that have been used to quantify the distribution of pulmonary blood flow in small animals include injection of fluorescent microspheres and postmortem histological quantification,<sup>3</sup> microcomputed tomography ( $\mu$ CT) imaging of the lungs with contrast agents either *in vivo*<sup>4</sup> or after radiopaque silicone polymer injection followed by *ex vivo* lung imaging,<sup>5</sup> and microangiography in mice using synchrotron radiation.<sup>6</sup> However, most of these methods preclude repeated imaging due to the terminal nature of the imaging procedures and



therefore prevent analysis of changes in the pulmonary distribution of blood flow over time or in correlation with changes in pulmonary lung function.

Vessel segmentation is a perennial problem in imaging research that has resulted in numerous studies.<sup>7,8</sup> However, much of this work has focused on human data.<sup>9,10</sup> Here, we present tools using a Hessian-based enhancement filter<sup>11</sup> to obtain quantitative vessel caliber measures from  $\mu$ CT images without contrast. Our aim was to assess the correlation between our contrast-free caliber measures and automated caliber measures from 2D contrast microangiography. We began by calibrating our measures using synthetic images, and then applied our technique to  $\mu$ CT images of live mice obtained using a laboratory x-ray source. Our method shows a high degree of correlation with quantitative 2D contrast microangiography in the same mice. Thus, for the first time, this method allows volumetric measurements of the entire pulmonary vasculature in mice in 3D, without the use of contrast agents or euthanasia.

## 2. MATERIALS AND METHODS

### 2.A. Experimental procedure

Eight-week old BALB/c female mice ( $n = 5$ ) were obtained from MARP (Monash University Research Platform, Monash University, VIC, Australia). All experiments were approved by the local Animal Ethics Committee of Monash University (Melbourne, VIC, Australia) and conducted in accordance with the guidelines set out in the Australian code of practice for the care and use of animals for scientific purposes. Mice were anesthetized with intraperitoneal injections of a mix of ketamine (Parnell Australia Pty Ltd., Alexandria NSW, Australia) and xylazine (Xylazil-20, Troy Laboratories Pty Ltd., Smithfield NSW, Australia) with doses of 150 mg/kg and 10 mg/kg, respectively. Mice were orotracheally intubated and allowed to continue breathing spontaneously while a customized 24-gauge BD Angiocath catheter (Becton-Dickinson, NJ, USA) was inserted into the jugular vein and advanced into the superior vena cava for administering contrast agents. The mouse was securely restrained in a custom-built acrylic chassis<sup>12</sup> in a supine position during the surgical procedure. Mice were then ventilated using pressure control ventilation on a mouse ventilator (AccuVent200 Small Animal Ventilator, Notting Hill Devices, Melbourne, VIC, Australia) with an inspiratory pressure of 20 cm H<sub>2</sub>O, zero positive end-expiratory pressure, and inspiratory and expiratory times of 300 ms each (a respiratory rate of 100 breaths/min). Tidal volumes with these settings were approximately 400  $\mu$ l for a 20-g mouse or 20  $\mu$ l/g (20 ml/kg). Mice were given a subcutaneous bolus of 100  $\mu$ l saline twice and ventilated for 10 min prior to imaging to allow equilibration and lung recruitment. Mice were kept warm using pocket warmers wrapped around the lower abdomen and legs.

### 2.B. Imaging protocol

Imaging was conducted in the Laboratory for Dynamic Imaging at Monash University (Melbourne, VIC, Australia). The x-ray imaging setup [see Fig. 1(A)] consists of a high

brightness x-ray source (Excillum AB, Kista, Sweden) that uses an x-ray beam generated from a liquid-metal-jet microfocus (15  $\mu$ m spot size) x-ray source.<sup>13,14</sup> This x-ray source (70 kV, 265 W) is polychromatic and unfiltered resulting in a characteristic peak at 25 keV. A high speed CMOS flat-panel detector (PaxScan, Varian Medical Systems, Palo Alto, CA, USA) with an isotropic pixel size of 0.194 mm was used to capture images at a frame rate of 30 Hz and an exposure time of 15 ms. The mouse was positioned in the acrylic chassis in front of the x-ray beam in the upright position. A high precision rotary stage (Zaber Technologies, Vancouver, Canada) was used to rotate the mice 360° under mechanical ventilation for the CT scan. The imaging was synchronized with ventilation and gated to obtain 800 projection images of the lungs at peak inspiration for CT reconstruction. The radiation dose delivered (equating to 800 projections with 15 ms exposure times and an air kerma rate of 5.01 mGy s<sup>-1</sup>) was measured to be 60.12 mGy, representing only 0.9% of the LD<sub>50/30</sub> (~7 Gy) for BALB/c mice.<sup>15</sup>

A calibration scan of an acrylic cylinder with fiducials<sup>16</sup> was performed before and after mouse scans. This process captures the tilt angle and center of rotation of the scan necessary for accurate CT reconstruction results. The source-to-isocenter of the rotation stage and source-to-detector distances were 374 and 3315 mm, respectively, resulting in an effective isotropic voxel size of 21.9  $\mu$ m for the entire imaging system.

For 2D microangiography imaging, which was conducted after  $\mu$ CT imaging, an iodinated contrast agent (Isovue 370, Bracco Diagnostics, Princeton, NJ, USA; 370 mg iodine per ml) was injected via the jugular vein cannula with a microinjection pump (PHD-2000, Harvard Apparatus, Holliston, MA, USA) that was programmed to deliver a bolus administration of 0.12 ml of iodine contrast agents at a speed of 11 ml/min. Image acquisition was initiated 1 s before iodine injection, and 200 frames were recorded for each scan. The exposure time and frame rate of image acquisition were the same as that used for  $\mu$ CT imaging. The lung vessels were imaged when ventilation was interrupted for a 5-s breath hold at peak inspiration to eliminate any blurring from lung movement. Mice were given at least 5 min to recover from each injection of contrast agents. Angiography was performed three times for each mouse: right anterior oblique, left anterior oblique, and frontal views (without rotation during imaging), in increments of 45°.

### 2.C. 2D microangiography analysis

The sequence of 2D angiography images was analyzed using a combination of both custom in-house software and tools from .<sup>17</sup> Figure 2(A) shows an unprocessed image of the lungs after contrast injection acquired over a breath hold. A background correction using the averaged image of the entire sequence was performed to enhance the intensity of the iodinated vessels within the image. To stabilize the changes to pixel intensities from changes in relative iodine levels within the vessels, a temporal moving average filter (five images either side) was applied to the background corrected image sequence. A frame from the processed image sequence [Fig. 2(B)] in which the vessels were most intensely filled with contrast agents was chosen for quantitative 2D microangiography measurements.

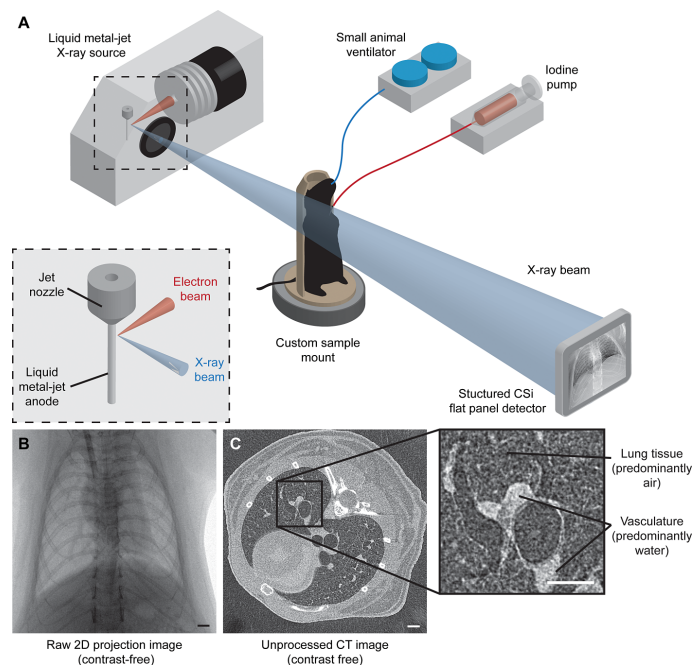


FIG. 1. X-ray imaging setup using a laboratory source. (A) BALB/c mice, intubated and mechanically ventilated, were placed in a custom sample mount on a rotating stage in between the source and detector. For 2D microangiography, an iodinated contrast agent was injected using a microsyringe pump during a breath-hold at peak inspiration, and images were captured from 3 views. For microcomputed tomography, the mouse was rotated while images were captured in synchronization with mechanical ventilation. (B) Raw 2D projection image of a frontal view using the laboratory x-ray imaging system described in (A). (C) Single slice from an unprocessed CT volume reconstructed using a cone-beam reconstruction technique. The technique presented in this study utilizes the contrast between air-filled lung tissue (see inset) and adjacent vasculature to quantify the vessel caliber. Scale bars represent 1 mm.

We used an automated plugin to (Ref. 18) that measures the diameter of a vessel,  $D_{ANG}$ , in an image using the full width at half-maximum approach. For a given line across a blood vessel, five measurements parallel to this line were obtained.

## 2.D. 3D CT image reconstruction and analysis

Image acquisition was synchronized with mechanical ventilation allowing image gating at peak inspiration when the contrast between lung tissue and adjacent blood vessels is maximal. A cone-beam reconstruction technique<sup>19</sup> was used to obtain a single CT volume of the lungs at peak inspiration where the contrast between lung tissue and adjacent blood vessels is maximal [see Fig. 1(C) inset].

A vesselness image filter based on Frangi *et al.*<sup>11</sup> was applied to this CT volume and the Hessian of the volume was calculated with a Gaussian kernel scale,  $S$ . Repeating over multiple scales, the local image gradients were matched to an ellipsoid to discriminate between plane-like structures and tubular structures. This filter produces a volume for the vesselness parameter, a measure relating to the likelihood that any given pixel belongs to a tubular structure, which we refer to as the probability volume. Figure 2(C) shows a

maximum intensity projection of the 3D probability volume after applying the filter to a  $\mu$ CT reconstruction of mouse lungs. In the probability volume structures that are tubular have much higher contrast than other structures in the volume. This enables a more accurate segmentation of tubular structures within the volume in contrast to the unprocessed CT volume. A flood-fill segmentation using Avizo (FEI VSG, France) was used to segment the pulmonary vasculature from the computed probability volume and a skeletonization procedure<sup>20</sup> was used to compute the centerline tree of the segmented pulmonary vasculature.

Our measures for vesselness were computed over a range of Gaussian kernel scales ( $1 \leq S \leq 30$ ). We also computed, for each voxel, the Gaussian scale ( $S_{MAX}$ ) that resulted in the highest value for vesselness which we captured in our probability volume. We refer to these data as the maximum kernel scale volume.

## 2.E. Calibration of Gaussian kernel scale to obtain vessel caliber

Values for  $S_{MAX}$  were calibrated using computer-generated images of long tubes that varied in diameter (see Fig. 3).

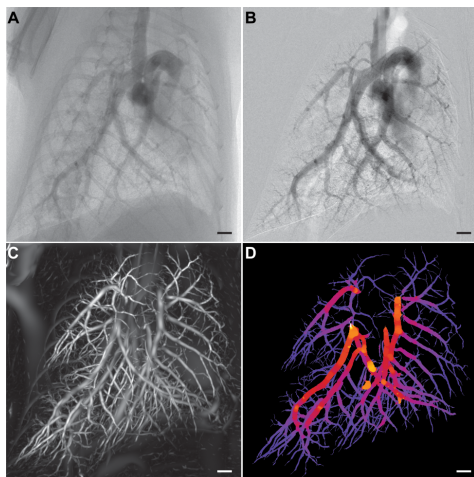


FIG. 2. 3D contrast-free diameter measurement of pulmonary vasculature. [(A) and (B)] 2D angiography with iodine bolus administration was used to validate our contrast-free vessel quantification method. (A) Unprocessed x-ray projection image with an iodinated contrast agent. Background correction and a moving average filter were used to enhance the contrast intensity in the image resulting in (B). (C) Maximum intensity projection through the probability volume (output from a Hessian-based vessel enhancement filter on a  $\mu$ CT volume without contrast agents) showing “vesselness.” (D) Maximum intensity projection of vasculature skeleton colored by our contrast-free vessel caliber measure. Scale bars represent 1 mm.

Tubes with diameters ranging between 3.14 and 62.8 px were placed in the volume and arbitrarily rotated in 3D ( $x = 30^\circ$ ,  $y = 15^\circ$  and  $z = 0^\circ$ ) to ensure tubes are randomly aligned in the images. Figure 3(A) shows the flowchart of the processes used to filter the images and perform a quantitative comparison between the two techniques highlighted in Secs. 2.C and 2.D, in a similar manner to the experimental data captured using the laboratory x-ray imaging system.

The 3D volume was generated (Sec. 1) and a maximal intensity forward projection was performed to generate projection views of the tubes similar to our experimental 2D microangiography data. These projection images were analyzed using the automated plugin (see Sec. 2.C) to obtain measures for tube diameter,  $D_{PROJ}$ . The 3D volume was then processed using Frangi’s Hessian-based vessel enhancement filter to obtain the probability volume and the  $S_{MAX}$  volume. The centerline tree was generated using the probability volume (Sec. 3) and measures of  $S_{MAX}$  were mapped to the tree. These data were forward projected (Sec. 4) to match the intensity forward projected views of the synthetic volume obtained in Sec. 2.

Line selections were drawn across each tube to simultaneously obtain measures for  $D_{PROJ}$  off the intensity projections [Fig. 3(B) blue line] and  $S_{MAX}$  off the  $S_{MAX}$  projected image [Fig. 3(B) red line]. We found that  $S_{MAX}$  is an excellent surrogate for vessel caliber demonstrating a linear correlation (slope = 0.3447;  $R = 0.99$ ) with automated vessel caliber measurements from intensity projection images [Fig. 3(C)].

## 2.F. Vessel diameter quantification and comparison

The centerline tree of the segmented vasculature was utilized to map values of  $S_{MAX}$  to 3D points along the vascular tree. Values for  $S_{MAX}$  were converted to contrast free vessel caliber estimates,  $D_{CT}$ , using the calibration results discussed in Sec. 2.E. This 3D volume was forward projected in increments of  $45^\circ$  to match the right anterior oblique, left anterior oblique, and frontal view obtained with 2D contrast microangiography. A typical resulting composite image of the segmented vasculature tree colored by  $D_{CT}$  is shown in Fig. 2(D). Line selections were drawn across blood vessels at multiple points in the image and measures  $D_{CT}$  and  $D_{ANG}$  (see Sec. 2.C) were obtained. Figure 4 shows that our contrast-free measures for vessel caliber,  $D_{CT}$ , show good correlation with quantitative 2D microangiography measures for vessel caliber,  $D_{ANG}$  (slope = 0.98; intercept = 0.17 mm;  $R = 0.91$ ).

## 2.G. Statistical methods

Linear regression was used to determine the relationship between  $S_{MAX}$  and  $D_{PROJ}$  using synthetic data [Fig. 3(C)]. Each point on Fig. 3(C) represents an average of 25 measurements. This relationship was used to calibrate measures for  $S_{MAX}$  to determine contrast-free vessel caliber,  $D_{CT}$ , obtained from  $\mu$ CT images of individual mice. Linear regression was used to determine the relationship between  $D_{CT}$  and caliber measures from 2D contrast microangiography,  $D_{ANG}$  (Fig. 4) using  $n = 500$  measures ( $n = 100$ /mouse).

## 3. RESULTS AND DISCUSSION

BALB/c mice ( $n = 5$ ) were imaged using a laboratory x-ray source (see methods) under mechanical ventilation [Figs. 1(A) and 1(B)] using a small-animal ventilator (see methods). Gated- $\mu$ CT imaging of breathing mice [Fig. 1(C)] was performed resulting in a single CT reconstruction of the murine lungs at peak inspiration. Hessian-based enhancement filters<sup>11</sup> are gaining popularity for vessel segmentation.<sup>8,10,21</sup> Most studies focusing on quantifying the pulmonary vasculature are based on humans.<sup>9</sup> To the best of our knowledge, no other group has quantified murine pulmonary vessel caliber using CT images without contrast agents.

Here, we apply a multi-scale Hessian-based enhancement filter to obtain vessel caliber measurements from CT images [Fig. 2(D)]. Figure 2(E) shows the composite image that incorporates the Gaussian scale used for vessel enhancement and the segmented pulmonary vasculature. We first calibrated the Gaussian kernel scale parameter using synthetic images of tubes with known diameters [Figs. 3(A) and 3(B)]. Using a similar analysis protocol to the experimental data, the Gaussian kernel scale measure was calibrated against vessel diameter measured from 2D intensity projection images of the synthetic tubes [Fig. 3(C)].

Our method was validated using 2D microangiography with contrast agents [Figs. 2(A) and 2(B)] in the same mice from three different views. The images are pre-processed using a digital subtraction<sup>22</sup> and averaging scheme to enhance the

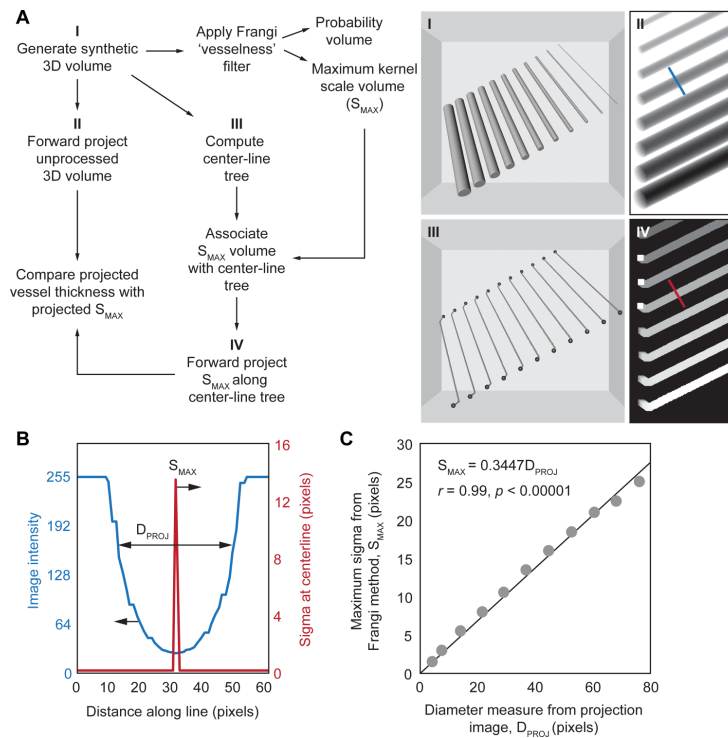


Fig. 3. Calibration of contrast-free vessel caliber with automated intensity-based caliber measures. (A) Workflow for utilizing a synthetic volume of tubes to determine the correlation between  $S_{MAX}$ , the maximum Gaussian kernel scale that maximizes the vesselness value in the Hessian-based vessel enhancement filter, and caliber measures from intensity projections of the volume. Forward projected centerline tree image in inset Sec. 4 has been thickened for clarity. (B) Example of the profiles across the line selection shown in insets Secs. 2 and 4 in (A). Vessel diameter in the intensity projected image (blue line),  $D_{PROJ}$ , was measured using an automatic full width at half-maximum approach.  $S_{MAX}$  is the maximum value in the line selection across the tube in the  $S_{MAX}$  forward projection image (red line). (C) Plot of  $S_{MAX}$  plotted against  $D_{PROJ}$  measured across multiple sections along each of the tubes in the image.

intensity of the pulmonary arteries. Figures 2(A) and 2(B) shows images obtained from microangiography before and after processing, respectively. Figures 2(A) and 2(B) are approximately  $\sim 0.6$  s after contrast administration. Failure to correctly place the catheter tip at the superior vena cava is one disadvantage of the conventional contrast microangiography approach that is eliminated with our new CT approach.

We probed corresponding images to obtain measures for vessel diameter,  $D_{CT}$  (after applying the calibration from synthetic testing), and vessel diameter from 2D angiography images ( $D_{ANG}$ ) at varying locations along the pulmonary vasculature (Fig. 4). Both pulmonary arteries and veins were segmented from the filtered CT volumes as evident in the image. Up to 16 generations of branches within the vasculature tree were visible in the segmented vasculature. With 2D angiography, a contrast medium was only highly visible in the arteries following a bolus injection. As a result, only pulmonary artery caliber measures were validated in this study. A total of 500 pulmonary arterial diameter measurements were obtained

for five mice with a fixed number of 100 measurements per mouse. Our results show that there is a good correlation between the vessel caliber measurements from 2D contrast angiography and our contrast-free CT method ( $R = 0.91$ ). The scatter of the points on the plot suggests that there are inaccuracies in both techniques used in this study. However, more importantly much of this scatter and the associated non-zero intercept may be the cause of a more fundamental difference in the two techniques. There is no significant difference between the  $x$ -ray absorption of blood and the arterial wall. As a result, the Hessian-based vessel enhancement approach used here increases the contrast in tubular structures between lung tissue (predominantly air) and other structures that are predominantly water [see Fig. 1(c) inset]. Thus, this would suggest that our approach detects the outer diameter of blood vessels, while the 2D contrast microangiography approach detects the inner diameter of blood vessels where there is an iodine-enhanced contrast. More work is warranted to assess the clinical applications of this approach which is outside of the scope of this study. Importantly, an alternative approach

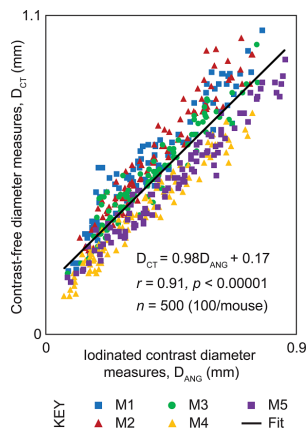


FIG. 4. Quantitative contrast-free vessel caliber measures in experimental data. Vessel caliber measurements from contrast-free  $\mu$ CT in live mice,  $D_{CT}$ , plotted against vessel diameter measured from 2D contrast microangiography images of the same mice.

may be to utilize both CT pulmonary angiography (CTPA) and CT to gauge wall thickness and vascular remodeling as well as overall vessel morphology.

#### 4. CONCLUSIONS

A tool for obtaining vessel caliber measures from (contrast free) CT images is presented. The laboratory-based imaging system used here yields images with sufficient resolution to resolve blood vessels *in vivo* with diameters ranging from 62  $\mu$ m and above in mice. The imaging system and the tools discussed here present an alternative angiography technique for small animal studies without the need for contrast agents, and theoretically could allow repeat imaging in the same animals over time as disease processes progress or in response to treatment.

Although this technique was pursued to permit better analysis of pulmonary perfusion patterns in murine models of lung disease, the obvious clinical applications cannot be overlooked. Acute pulmonary embolism (PE) is the migration of a blood clot from a deep vein in an extremity (usually the legs) through the right side of the heart and into the pulmonary arteries. PE is a common and sometimes fatal condition with mortality rates ranging from 14% to 28%,<sup>23</sup> to achieve the best outcomes for patients, PEs require rapid diagnosis and treatment.<sup>24–27</sup> Clinical signs and symptoms provide some clues towards a diagnosis of PE but ultimately a definitive diagnosis of PE requires imaging. Contrast-enhanced CT arteriography has rapidly replaced ventilation-perfusion scanning as the imaging modality of choice for diagnosing PE, especially with the advent of multi-detector CT scanners that allow analysis of the pulmonary arteries and detection of emboli at the subsegmental level.<sup>26,28–30</sup> However, CT angiography can cause contrast medium-induced nephropathy (CIN), which is the third most common cause of in-hospital acute

renal failure,<sup>31–33</sup> conferring significant morbidity and mortality. Therefore, a method of imaging the pulmonary vasculature without the use of contrast would represent a dramatic improvement in the risk/benefit profile of diagnostic testing for all patients suspected of having PEs and especially those who are at risk for CIN.

For the first time, we demonstrate a non-contrast approach to generate high fidelity, 3D quantification of the pulmonary vasculature in a murine model. It is not inconceivable that such a technique could be applied to human subjects for clinical applications including the detection of abnormalities in the pulmonary vasculature that correlate with PE. It is important to note that the radiation dose received by mice in this study is not high ( $\sim 60$  mGy), especially when considered relative to the  $LD_{50/30}$  ( $\sim 7$  Gy). Additionally, the scale of the vasculature in the mouse lung necessitates the use of a specialized microfocus x-ray source (such as liquid-metal-jet anode used here), to obtain the required resolution. A consequence of a liquid-metal anode is an energy spectrum that is weighted with low energy x-rays, contributing to a higher measured absorbed dose. When scaling the subject from the size of a mouse to a human, the concomitant scaling of the imaging technology allows features of the same relative size to be imaged with lower dose. We are confident that the resolution currently used in CTPA systems is sufficient for the clinical application of this technique, with a dose less than 7 mSv.<sup>34</sup> Studies to this end are currently underway.

#### ACKNOWLEDGMENTS

The authors thank Ellen Bennett with the preparation of mice for this study. This study was supported by the Multimodal Australian ScienceS Imaging and Visualisation Environment (MASSIVE Project No. NCIy40), the National Health and Medical Research Council of Australia (A.F.: NHMRC Development Grant No. APP1055116; J.T.P. Grant No. APP1064973), the National Institutes of Health (H.D.J.: NIH Grant No. 1 K08 HL125806-01), a grant from the Plum Foundation (H.D.J.) and a NHMRC Career Development Fellowship (A.F.: Grant No. APP1022721).

#### CONFLICT OF INTEREST DISCLOSURE

A.F. is Founder and C.R.S., R.C., H.D.J., and S.D. have beneficial interests in 4Dx, which is commercializing respiratory diagnostics technology.

<sup>a</sup>Co-corresponding authors: stephen.dubsky@monash.edu and andreas.fouras@monash.edu

<sup>1</sup>A. Tabuchi, M. Mertens, H. Kuppe, A. R. Pries, and W. M. Kuebler, "Intravital microscopy of the murine pulmonary microcirculation," *J. Appl. Physiol.* **104**(2), 338–346 (2008).

<sup>2</sup>W. M. Kuebler, "Real-time imaging assessment of pulmonary vascular responses," *Proc. Am. Thorac. Soc.* **8**(6), 458–465 (2011).

<sup>3</sup>R. W. Glenny, S. L. Bernard, and H. T. Robertson, "Pulmonary blood flow remains fractal down to the level of gas exchange," *J. Appl. Physiol.* **89**(2), 742–748 (2000).

<sup>4</sup>E. L. Ritman, "Micro-computed tomography of the lungs and pulmonary-vascular system," *Proc. Am. Thorac. Soc.* **2**(6), 477–480 (2005).

- <sup>5</sup>S. X. Vasquez, F. Gao, F. Su, V. Grijalva, J. Pope, B. Martin, J. Stinstra, M. Masner, N. Shah, D. M. Weinstein, R. Farias-Eisner, and S. T. Reddy, "Optimization of MicroCT imaging and blood vessel diameter quantitation of preclinical specimen vasculature with radiopaque polymer injection medium," *PLoS One* **6**(4), e19099 (2011).
- <sup>6</sup>T. Sonobe, D. O. Schwenke, J. T. Pearson, M. Yoshimoto, Y. Fujii, K. Umetani, and M. Shirai, "Imaging of the closed-chest mouse pulmonary circulation using synchrotron radiation microangiography," *J. Appl. Physiol.* **111**(1), 75–80 (2011).
- <sup>7</sup>D. Lesage, E. D. Angelini, I. Bloch, and G. Funka-Lea, "A review of 3D vessel lumen segmentation techniques: Models, features and extraction schemes," *Med. Image Anal.* **13**(6), 819–845 (2009).
- <sup>8</sup>R. D. Rudyanto, S. Kerkstra, E. M. van Rikxoort, C. Fetita, P.-Y. Brillet, C. Lefevre, W. Xue, X. Zhu, J. Liang, I. Öksüz, D. Ünay, K. Kadipaşaoğlu, R. S. J. Estépar, J. C. Ross, G. R. Washko, J.-C. Prieto, M. H. Hoyos, M. Orkisz, H. Meine, M. Hüllebrand, C. Stöcker, F. L. Mir, V. Naranjo, E. Villanueva, M. Staring, C. Xiao, B. C. Stoel, A. Fabijanska, E. Smistad, A. C. Elster, F. Lindseth, A. H. Foruzan, R. Kiros, K. Popuri, D. Cobzas, D. Jimenez-Carretero, A. Santos, M. J. Ledesma-Carbayo, M. Helmlberger, M. Urschler, M. Pienn, D. G. H. Bosboom, A. Campo, M. Prokop, P. A. de Jong, C. Ortiz-de-Solorzano, A. Muñoz-Barrutia, and B. van Ginneken, "Comparing algorithms for automated vessel segmentation in computed tomography scans of the lung: The VESSEL12 study," *Med. Image Anal.* **18**(7), 1217–1232 (2014).
- <sup>9</sup>E. U. Mumcuoğlu, F. R. Long, R. G. Castile, and M. N. Gurcan, "Image analysis for cystic fibrosis: Computer-assisted airway wall and vessel measurements from low-dose, limited scan lung CT images," *J. Digit. Imaging* **26**(1), 82–96 (2013).
- <sup>10</sup>M. Orkisz, M. Hernández Hoyos, V. Pérez Romanello, C. Pérez Romanello, J. C. Prieto, and C. Revol-Muller, "Segmentation of the pulmonary vascular trees in 3D CT images using variational region-growing," *IRBM* **35**(1), 11–19 (2014).
- <sup>11</sup>A. F. Frangi, W. J. Niessen, K. L. Vincken, and M. A. Viergever, "Multiscale vessel enhancement filtering," in *Medical Image Computing Computer-Assisted Intervention—MICCAI'98*, edited by W. M. Wells, A. Colchester, and S. Delp (Springer, Berlin, Heidelberg, 1998), pp. 130–137.
- <sup>12</sup>S. Dubsky, S. B. Hooper, K. K. W. Siu, and A. Fouras, "Synchrotron-based dynamic computed tomography of tissue motion for regional lung function measurement," *J. R. Soc. Interface* **9**(74), 2213–2224 (2012).
- <sup>13</sup>D. H. Larsson, U. Lundström, U. K. Westermarck, M. Arsenian Henriksson, A. Burvall, and H. M. Hertz, "First application of liquid-metal-jet sources for small-animal imaging: High-resolution CT and phase-contrast tumor demarcation," *Med. Phys.* **40**(2), 021909 (2013).
- <sup>14</sup>M. J. Kitchen, G. A. Buckley, A. F. T. Leong, R. P. Carnibella, A. Fouras, M. J. Wallace, and S. B. Hooper, "X-ray specks: Low dose *in vivo* imaging of lung structure and function," *Phys. Med. Biol.* **60**(18), 7259–7276 (2015).
- <sup>15</sup>P. Okunieff, T. Wu, K. Huang, and I. Ding, "Differential radioprotection of three mouse strains by basic or acidic fibroblast growth factor," *Br. J. Cancer, Suppl.* **27**, S105–S108 (1996).
- <sup>16</sup>K. Yang, A. L. C. Kwan, D. F. Miller, and J. M. Boone, "A geometric calibration method for cone beam CT systems," *Med. Phys.* **33**(6), 1695–1706 (2006).
- <sup>17</sup>J. Schindelin, I. Arganda-Carreras, E. Frise, V. Kaynig, M. Longair, T. Pietzsch, S. Preibisch, C. Rueden, S. Saalfeld, B. Schmid, J.-Y. Tinevez, D. J. White, V. Hartenstein, K. Eliceiri, P. Tomancak, and A. Cardona, "Fiji: An open-source platform for biological-image analysis," *Nat. Methods* **9**(7), 676–682 (2012).
- <sup>18</sup>M. J. M. Fischer, S. Uchida, and K. Messlinger, "Measurement of meningeal blood vessel diameter *in vivo* with a plug-in for ImageJ," *Microvasc. Res.* **80**(2), 258–266 (2010).
- <sup>19</sup>L. A. Feldkamp, L. C. Davis, and J. W. Kress, "Practical cone-beam algorithm," *J. Opt. Soc. Am. A* **1**(6), 612–619 (1984).
- <sup>20</sup>M. Sato, I. Bitter, M. A. Bender, A. E. Kaufman, and M. Nakajima, "Teasar: Tree-structure extraction algorithm for accurate and robust skeletons," in *Proceedings The Eighth Pacific Conference on Computer Graphics and Applications* (2000), pp. 281–449.
- <sup>21</sup>D. Jimenez-Carretero, A. Santos, S. Kerkstra, R. Dewi Rudyanto, and M. J. Ledesma-Carbayo, "3D Frangi-based lung vessel enhancement filter penalizing airways," in *2013 IEEE 10th International Symposium on Biomedical Imaging (ISBI)* (IEEE, 2013), pp. 926–929.
- <sup>22</sup>C. T. Badea, L. W. Hedlund, Y. Qi, B. Berridge, and G. A. Johnson, "*In vivo* imaging of rat coronary arteries using bi-plane digital subtraction angiography," *J. Pharmacol. Toxicol. Methods* **64**(2), 151–157 (2011).
- <sup>23</sup>S. Z. Goldhaber, "Pulmonary embolism," *Lancet* **363**(9417), 1295–1305 (2004).
- <sup>24</sup>R. D. Hull, G. E. Raskob, R. F. Brant, G. F. Pineo, and K. A. Valentine, "Relation between the time to achieve the lower limit of the APTT therapeutic range and recurrent venous thromboembolism during heparin treatment for deep vein thrombosis," *Arch. Intern. Med.* **157**(22), 2562–2568 (1997).
- <sup>25</sup>H. R. Büller, G. Agnelli, R. D. Hull, T. M. Hyers, M. H. Prins, and G. E. Raskob, "Antithrombotic therapy for venous thromboembolic disease: The seventh ACCP conference on antithrombotic and thrombolytic therapy," *Chest* **126**(Suppl.3), 401S–428S (2004).
- <sup>26</sup>V. F. Tapson, "Acute pulmonary embolism," *N. Engl. J. Med.* **358**(10), 1037–1052 (2008).
- <sup>27</sup>P. Egermayer and G. I. Town, "The clinical significance of pulmonary embolism: Uncertainties and implications for treatment—a debate," *J. Intern. Med.* **241**(1), 5–10 (1997).
- <sup>28</sup>M. Remy-Jardin, M. Pistolesi, L. R. Goodman, W. B. Gefer, A. Gottschalk, J. R. Mayo, and H. D. Sostman, "Management of suspected acute pulmonary embolism in the era of CT angiography: A statement from the Fleischner society," *Radiology* **245**(2), 315–329 (2007).
- <sup>29</sup>F. Lavorini, V. Di Bello, M. L. De Rimi, G. Lucignani, L. Marconi, G. Palareti, R. Pesavento, D. Prisco, M. Santini, N. Sverzellati, A. Palla, and M. Pistolesi, "Diagnosis and treatment of pulmonary embolism: A multidisciplinary approach," *Multidiscip. Respir. Med.* **8**:75 (2013).
- <sup>30</sup>R. S. Wiener, L. M. Schwartz, and S. Woloshin, "When a test is too good: How CT pulmonary angiograms find pulmonary emboli that do not need to be found," *BMJ* **347**, f3368 (2013).
- <sup>31</sup>T. Singh, K.-V. Lam, and C. Murray, "Low volume contrast CTPA in patients with renal dysfunction," *J. Med. Imaging Radiat. Oncol.* **55**(2), 143–148 (2011).
- <sup>32</sup>K. Nash, A. Hafeez, and S. Hou, "Hospital-acquired renal insufficiency," *Am. J. Kidney Dis.* **39**(5), 930–936 (2002).
- <sup>33</sup>D. A. Stenstrom, L. L. Muldoon, H. Armijo-Medina, S. Watnick, N. D. Doolittle, J. A. Kaufman, D. R. Peterson, J. Bubalo, and E. A. Neuwelt, "N-acetylcysteine use to prevent contrast medium-induced nephropathy: Premature phase III trials," *J. Vasc. Intervent. Radiol.* **19**(3), 309–318 (2008).
- <sup>34</sup>A. R. Hunsaker, M. T. Lu, S. Z. Goldhaber, and F. J. Rybicki, "Imaging in acute pulmonary embolism with special clinical scenarios," *Circ. Cardiovasc. Imaging* **3**(4), 491–500 (2010).

## **B.2 Real-time in vivo imaging of regional lung function in a mouse model of cystic fibrosis on a laboratory X-ray source**

This article is licensed under a Creative Commons Attribution 4.0 International License: <https://creativecommons.org/licenses/by/4.0/>

OPEN

## Real-time *in vivo* imaging of regional lung function in a mouse model of cystic fibrosis on a laboratory X-ray source

Rhiannon P. Murrie<sup>1\*</sup>, Freda Werdiger<sup>1</sup>, Martin Donnelley<sup>2,3</sup>, Yu-wei Lin<sup>4</sup>, Richard P. Carnibella<sup>5</sup>, Chaminda R. Samarage<sup>5</sup>, Isaac Pinar<sup>1</sup>, Melissa Preissner<sup>1</sup>, Jiping Wang<sup>4</sup>, Jian Li<sup>4</sup>, Kaye S. Morgan<sup>6</sup>, David W. Parsons<sup>2,3\*</sup>, Stephen Dubsky<sup>1</sup> & Andreas Fouras<sup>1,5</sup>

Most measures of lung health independently characterise either global lung function or regional lung structure. The ability to measure airflow and lung function regionally would provide a more specific and physiologically focused means by which to assess and track lung disease in both pre-clinical and clinical settings. One approach for achieving regional lung function measurement is via phase contrast X-ray imaging (PCXI), which has been shown to provide highly sensitive, high-resolution images of the lungs and airways in small animals. The detailed images provided by PCXI allow the application of four-dimensional X-ray velocimetry (4DxV) to track lung tissue motion and provide quantitative information on regional lung function. However, until recently synchrotron facilities were required to produce the highly coherent, high-flux X-rays that are required to achieve lung PCXI at a high enough frame rate to capture lung motion. This paper presents the first translation of 4DxV technology from a synchrotron facility into a laboratory setting by using a liquid-metal jet microfocus X-ray source. This source can provide the coherence required for PCXI and enough X-ray flux to image the dynamics of lung tissue motion during the respiratory cycle, which enables production of images compatible with 4DxV analysis. We demonstrate the measurements that can be captured *in vivo* in live mice using this technique, including regional airflow and tissue expansion. These measurements can inform physiological and biomedical research studies in small animals and assist in the development of new respiratory treatments.

The early diagnosis and ongoing monitoring of chronic lung diseases, such as chronic obstructive pulmonary disease (COPD), pulmonary fibrosis, cystic fibrosis (CF), asthma and lung cancer, is currently hampered by the inability to capture the complete spatial distribution of lung function<sup>1</sup>. Changes in pulmonary function are traditionally quantified clinically through global lung health measures such as pulmonary function tests, which produce whole-lung parameters such as FEV1 or Lung Clearance Index (LCI). Since they are measured at the mouth these tests are unable to accurately localise where in the lung any change in function originates. They can also be age- and effort-dependent, and their sensitivity means they can often only detect abnormalities in the advanced stages of disease.

Imaging modalities like high-resolution computed tomography (CT) can be used to detect structural changes such as bronchiectasis, bronchial wall thickening, mucus plugging and air trapping, but in clinical practice CT is typically combined with other non-invasive pulmonary function testing such as spirometry, forced oscillation technique (FOT), plethysmography, or multiple breath wash in/out techniques. CT has also been combined with

<sup>1</sup>Department of Mechanical and Aerospace Engineering, Monash University, Melbourne, Australia. <sup>2</sup>Robinson Research Institute and Adelaide Medical School, University of Adelaide, Adelaide, Australia. <sup>3</sup>Women's and Children's Hospital, North Adelaide, Australia. <sup>4</sup>Infection & Immunity Program, Monash Biomedicine Discovery Institute, and Department of Microbiology, Monash University, Melbourne, Australia. <sup>5</sup>4Dx Limited, Melbourne, Australia. <sup>6</sup>School of Physics and Astronomy, Monash University, Melbourne, Australia. \*email: [rhiannon.murrie@gmail.com](mailto:rhiannon.murrie@gmail.com); [david.parsons@sa.gov.au](mailto:david.parsons@sa.gov.au)

other techniques used to investigate thoracic dynamics<sup>2</sup>, such as the relation of diaphragmatic electric activity on lung aeration and collapse<sup>3</sup>, however this does not show localised lung dynamics or airflow. Disease location can be inferred via local assessment of structure such as with the PRAGMA-CF protocol<sup>4</sup>, but this technique extrapolates regional lung dysfunction through quantification of structural information captured from CT. Studies have also attempted to measure dynamic lung motion in humans by comparing CT scans at different respiratory phases (e.g. end-inspiratory and end-expiratory), to measure tissue deformation for tumour identification and tracking<sup>5,7</sup>. However, this type of technology has not become common clinical practice, and has not been widely utilised outside of tumour motion evaluation. Importantly, quantification of dynamic airflow with high resolution 3-dimensional spatial mapping is not yet available in clinical practice.

High-resolution CT imaging is now commonplace in small animals, enabling the identification of *structural* changes. However, pre-clinical studies of obstructive lung diseases (e.g. cystic fibrosis and asthma) in animal models also often lack robust *in vivo*, non-invasive techniques capable of identifying the location of *functional* deficits at high resolution (i.e. < 200  $\mu\text{m}$ ), and how they impact lung function. Typically, read-outs of lung function in these studies are global – such as airway resistance and compliance from lung mechanics testing using devices such as the flexiVent small animal ventilator (Scireq, Canada) – or they require euthanasia and post-mortem analysis of lung tissue using histological or biochemical tests to detect and localise disease. For longitudinal studies, the requirement for euthanasia means additional animals must be used for each time point, adding to the cost of such studies, and increasing the variability in results between animals. An ideal assessment technique would be able to obtain dynamic functional measures such as airflow in a regional manner to identify the location of any functional changes, and understand how they contribute to global changes in parameters such as FEV1.

To attempt to capture dynamic motion in pig lungs, Perchiazzi (2014) performed CT scans during multiple inspiratory hold manoeuvres at increasing pressures to quantify regional compliance<sup>8</sup>. However, because the motion of the lung parenchyma could not be tracked they used a registration algorithm to quantify the motion of manually identified landmarks at the edge and within transverse slices. Using this method they could create regional lung compliance maps. The methodologies we describe in this manuscript use custom designed hardware and software to enable two key evolutions: (1) Use of phase-contrast X-ray imaging to visualise the motion of the lung parenchyma in live mice on a laboratory source, and (2) performing CT acquisition during ventilated breathing without breath holds allows capture of the natural motion of the lung during respiration. Thus, we aim to use X-ray imaging methods to achieve effective, high-resolution *in vivo* data about the dynamic function of the lung. As in clinical studies, the availability of these methods in pre-clinical research would allow tracking of regional respiratory disease progression or response to therapies over time in the same animal, reduce animal numbers, improve statistical power, and provide additional information to researchers that is not currently available.

Phase-contrast X-ray imaging (PCXI) is capable of imaging soft tissues by enhancing the contrast of biological interfaces, a result of variations introduced to the phase of the X-ray wave by different materials. PCXI of the dense alveolar clusters in lung tissue produces a distinctive 'speckle' pattern<sup>9</sup>, and the motion of the speckle pattern during ventilation can be tracked via a technique known as X-ray velocimetry (XV)<sup>10</sup>. Lung expansion is a result of the volume of the thoracic cavity increasing by motion of the diaphragm, which causes air to flow through the bronchial airway tree inflating the lung tissue. As such, it is desirable to measure the regional lung tissue expansion and the airflow through each airway. Since XV can track lung tissue displacement and can be applied to 3-dimensional datasets (e.g. PCXI-CT), it can be used to capture lung expansion and contraction throughout the breath; a process we have termed 4DxV (with time being the fourth dimension). From these measurements the regional air volume in the lungs can be determined at multiple points throughout the breath. If this data is then associated with the airway tree structure, the time-varying airflow through each branch segment in the airway tree can be quantified<sup>11</sup>.

Structural changes from obstructive lung diseases such as asthma, COPD, emphysema and CF will alter the airflow within the bronchial tree and change the 4DxV lung expansion map, allowing poorly ventilated regions of the lung to be located. Restrictive lung diseases such as pulmonary fibrosis and interstitial lung disease, which can have a more widespread effect on the lung parenchyma and are often characterised by changes in lung tissue or chest wall stiffness, will also change the way the lungs expand on inhalation<sup>12,13</sup>. The 4DxV maps allow those regions of altered expansion to be identified<sup>14</sup>. The ability to monitor changes in local airflow is likely to be a useful indicator of disease progression or treatment effectiveness in many lung diseases.

The 4DxV functional lung imaging techniques were developed and validated using synchrotron radiation facilities<sup>11</sup>. For example, we have previously used 4DxV at the SPring-8 Synchrotron to demonstrate that  $\beta$ -ENaC mice – a recognised model of CF-like lung disease<sup>15</sup> – exhibit patchy lung disease, with the expiratory time constant used as a measure of regional lung function<sup>16</sup>. However, for this technique to be widely-adopted as a research tool, and move towards clinical diagnostic imaging, a more compact and accessible set-up is required<sup>17</sup>. Liquid-metal-jet anodes are a recent advance in laboratory X-ray source technology that reduce the impact of heat-load restriction associated with solid metal anodes, therefore providing both small spot sizes and relatively high flux<sup>18,19</sup>. Previous studies have shown that this small spot size provides sufficient coherence to produce PCXI lung speckle<sup>20</sup>, and that PCXI-CT of the lungs in post-mortem animals is achievable for structural characterization<sup>21–23</sup>.

The aim of the present experiment was to demonstrate the ability to visualise dynamic regional ventilation and airflow *in vivo* on a custom-built laboratory 4DxV system, using normal and  $\beta$ -ENaC mice. Our results demonstrate the successful translation of these techniques to a laboratory PCXI system, with the high speed, dynamic and functional imaging capabilities required to image live mice during ventilation. The ability to study lung diseases in small animal models using 4DxV technology has great potential; modern gene editing techniques have facilitated the cost-effective creation of new respiratory models, enabling cost-effective respiratory therapeutics

www.nature.com/scientificreports/

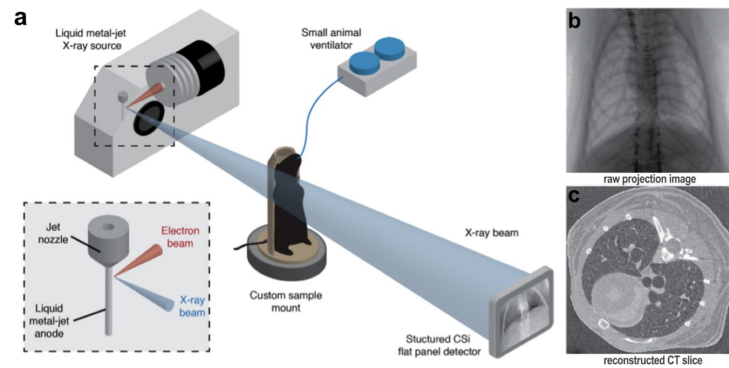


**Figure 1.** (a) Experimental image acquisition setup. Propagation-based phase contrast X-ray images of mouse lungs were acquired on a laboratory imaging setup consisting of a high brightness X-ray source with a liquid-metal-jet anode. Mice were non-surgically intubated and mechanically ventilated, then placed in a custom-built sample holder on a rotating stage for imaging. (b) Raw 2D projections were acquired over 360°, with images binned according to their time-point within the breath cycle. (c) CT volumes at each of the 15 time-points throughout the breath were then reconstructed from the binned projections, to produce a complete 4D CT dataset.

testing and physiology studies to be performed with high-throughput. Furthermore, a 2D version of the lung health assessment method developed and applied in these pre-clinical models is currently under review by the USA FDA under the 510(k) Premarket Notification scheme for use in humans to diagnose respiratory conditions in the clinic.

## Results and Discussion

We present dynamic 4DxV *in vivo* images of the lungs and airways of live mice acquired on a laboratory X-ray source at 30 frames per second. All images were acquired at the Laboratory for Dynamic Imaging at Monash University on a propagation-based phase contrast X-ray imaging setup that uses an Excillum D2 + X-ray source (Excillum AB, Kista, Sweden)<sup>24</sup>. Mice were anaesthetised, non-surgically intubated, and ventilated, and then 4-dimensional PCXI-CT images were acquired and processed to provide airway and lung measurements. These images are a volumetric CT that captures projection images of the entire lung in the frame. Figure 1 shows the imaging setup, with experimental and post-processing details located in the Methods sections.

The radiation dose at a source power of 265 W and a  $60 \times 15 \mu\text{m}$  spot size was 7.2 mGy/s. The scans described here delivered between 1.47–1.74 Gy, well below the dose required to damage lung tissue and the lethal dose measure ( $LD_{50/30}$ ) which is approximately 7.5 Gy for BALB/C mice and 8.3 Gy for C57BL/6 mice<sup>25</sup> (note previous work at a synchrotron delivered 10–15 Gy<sup>11</sup>). The resolution of the system was suitable for segmenting 60  $\mu\text{m}$  diameter airways.

Figure 2 shows a visual representation of the air distribution within the airway tree of a normal Swiss mouse throughout the breath cycle. At the start of the breath ( $t = 0$  ms) the volume of air in the lungs is the functional residual capacity, and then air begins to flow into the trachea and first bronchial bifurcation ( $t = 33$  ms). At mid-inspiration ( $t = 66$  ms) the primary airway branches are aerated and air begins to flow into the lower generation branches. At peak inspiration ( $t = 233$  ms) the airways are maximally aerated and fresh air is supplied to the alveoli. At mid-expiration ( $t = 433$  ms) the air is expelled from the lower generation branches during exhalation. Finally, close to the end of the breath ( $t = 466$  ms) the airways return toward their relaxed state. The progression of balanced aeration at each bifurcation of the bronchi at each phase of the breath shows that there are no obstructions present in the airway tree of this normal animal. The movement of the air volume to the lowest generation of airways measured (the 6<sup>th</sup> generation) shows uniform aeration to each region of each lobe of the lungs.

Figure 3 shows the results of the 4DxV analysis on the lungs of a healthy littermate control (left) and a diseased  $\beta$ -ENaC mouse (right). The expiratory time constant of the airflow through the airway tree (top row), and the corresponding 4DxV lung tissue maximal expansion maps (bottom row) demonstrate that the flow of air from the supplying branches directly impacts the aeration of the lung tissue. The healthy control mouse clearly exhibits uniform aeration throughout the airway tree (Fig. 3a), which translates to homogeneous expansion (and thus aeration) of the lung tissue in both left and right lung lobes (Fig. 3c). In a healthy lung (e.g. Fig. 3c) the centre of each lobe expands the most, as this region contains the alveoli that are closest to the airway branches that supply the fresh air. Alveoli on the edges of the lobes are supplied by the smallest terminal airways furthest away from the primary branches, and thus aerate last, even in a healthy lung.

For the diseased  $\beta$ -ENaC mouse the expiratory time constant (Fig. 3b) shows that it takes longer for the air to be expelled from the left lung, with a higher local expiratory time constant (yellow/orange/red) seen for these airways likely due to the patchy CF-like obstructive airway disease present in this animal. In Fig. 3d, a dramatic

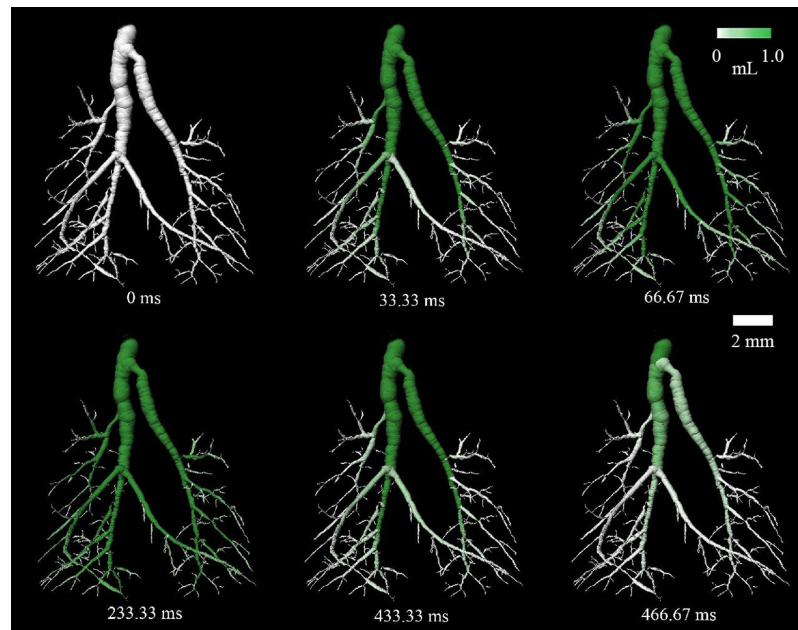


**Figure 2.** Aeration of the bronchial tree in a normal Swiss mouse. The white-green scale bar shows the measured air volume, relative to end-expiration, that has passed that location in the airway tree until that time point in the breath. This figure also demonstrates the high resolution of the airway tree branches achievable on a laboratory imaging system. Note that only six of the fifteen available time-points are shown here.

reduction in regional expansion of the left lung is seen, as represented by the large light blue area. This directly correlates to reduced aeration for these regions of the lung, and thus a reduction in local lung function for this mouse.

### Conclusions

We have demonstrated the ability to perform *in vivo* 4DxV regional imaging of the lungs and airways in live mice, at 30 frames per second and at high resolution (60  $\mu\text{m}$ ) on a laboratory X-ray source, to obtain functional information on dynamic airflow. The dynamic process of airflow through the airway tree and the resulting expansion and ventilation of the lung tissue was measured using lung tissue motion measures from X-ray velocimetry. The data we acquired matches the findings from our previous 4DxV imaging studies using  $\beta$ -ENaC mice at SPring-8 Synchrotron<sup>16</sup>, where we found that  $\beta$ -ENaC animals exhibited patchy lung disease that was detectable via 4DxV, an increased regional time constant and mucus obstructed airways that matched the location of the functional defects (detected histologically by AB/PAS staining). This allows us to validate the successful translation of this technique to a custom-designed compact laboratory XV setup, which is a pivotal step in the pathway to preclinical and clinical application of this technique.

While the synchrotron set-up that we have used in other studies offers higher spatial resolution, stronger phase contrast and higher x-ray flux than this laboratory set-up, our custom-designed laboratory setup was still able to track the local motion and hence function of the lung. The laboratory source does deliver low-energy x-ray radiation that is not present at the synchrotron, which will contribute to the radiation dose without contributing significantly to image quality, however the magnification present at the laboratory set-up enables the use of a detector with larger pixels and a thicker scintillator, requiring less incident radiation (and hence dose) for the same number of detector counts.

The ability to obtain these high quality 4D CT and 4DxV lung images without the need for synchrotron access shows the likely impact this technology can have for *in vivo* studies on pulmonary disease physiology, disease detection and monitoring, and respiratory treatment effects. The ability to perform this technique in the laboratory makes longitudinal studies on disease progression and treatment response feasible, in a non-invasive and non-terminal way, at readily accessible and compact laboratory facilities - a task which is difficult at limited-access facilities, like a synchrotron. Future studies will examine larger cohorts of animals, and be designed to both understand disease and enable continued development of novel outcome assessment measures based on the 4DxV data.

www.nature.com/scientificreports/

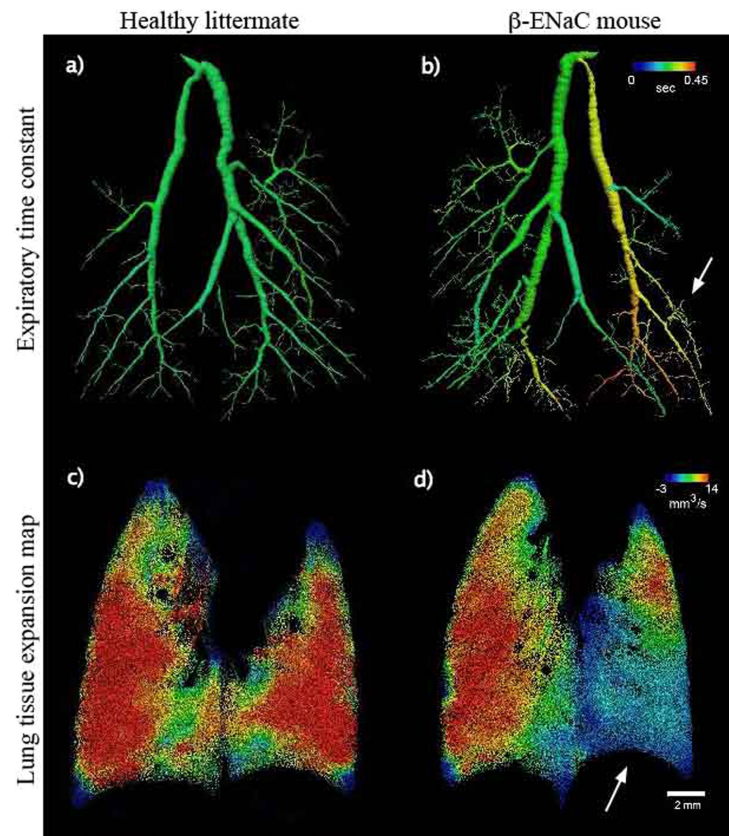


**Figure 3.** Two-dimensional projection images showing lung function analysis in a model of CF lung disease. (a,b) Airway segmentation from the 4DxV analysis of a healthy littermate and  $\beta$ -ENaC mouse, respectively, coloured by the local expiratory time constant. The lower part of the left anatomical lobe of the  $\beta$ -ENaC mouse shows an increased expiratory time constant (arrow), compared to both the right anatomical lobe and the littermate mouse. (c,d) The corresponding lung tissue expansion at the peak of the breath shows a clear reduction in expansion evident in the lower right anatomical lobe of the  $\beta$ -ENaC mouse (arrow), in comparison to the healthy littermate, in which the lung tissue expansion appears more uniform. The 4DxV expansion map around the heart is sparse due to cardiac motion artefacts.

Our study is a demonstration that a wealth of lung function information can be obtained from measures of lung motion in a laboratory setting. These 4DxV techniques are a novel tool that will enable localised quantification of a range of respiratory diseases to be made in small animal models, and in the future will likely facilitate advances in patient diagnosis, treatment and monitoring.

### Methods

**Experimental procedure.** All experiments were approved by the Monash University Animal Ethics Committee and conformed to the guidelines set out in the NHMRC Australian Code of Practice for the Care and Use of Animals for Scientific Purposes. All animals were supplied by the Monash Animal Research Platform.

The mouse used to demonstrate airway segmentation and airflow (Fig. 2) was a 9 week-old female Swiss mouse. The mouse was anaesthetised with isoflurane and orotracheally (non-surgically) intubated. Medical grade oxygen containing isoflurane (2%) was continually administered through a small animal ventilator (Accuvent 200, Notting Hill Devices, Melbourne, Australia) to maintain anaesthesia.

The pair of mice shown in Fig. 3 included one 8 week old  $\beta$ -ENaC-Tg female and one 8 week old female littermate control ( $\beta$ -ENaC negative).  $\beta$ -ENaC over-expressing mice are a well-established model of cystic fibrosis lung disease as they overproduce mucus that obstructs airways<sup>15</sup>. Mice were anaesthetised by intraperitoneal

Figure	PIP (cm H <sub>2</sub> O)	PEEP (cm H <sub>2</sub> O)	Inspiratory/expiratory time (ms)	Respiratory rate (breaths/min)	Time points per breath	Projections per time point	Total number of projections over 360°	Radiation dose (mGy/s)
2	12	2	250/250	120	15	400	6000	~7
3	12	2	150/350	120	15	480	7200	~6

**Table 1.** Ventilation and imaging parameters used in the airway analysis imaging.

(i.p.) injection with a mixture of 150 mg/kg ketamine (Parnell Australia Pty Ltd, Alexandria NSW, Australia) and 10 mg/kg xylazine (Xylazil-20, 60 Troy Laboratories Pty Ltd, Smithfield NSW, Australia), orotracheally intubated, and ventilated.

In all cases, mice were mounted vertically in a custom 3D-printed mouse holder for image acquisition, and the ventilation settings found in Table 1 were applied. Mice were humanely killed at the completion of imaging.

**Imaging procedure.** All imaging was performed in the Laboratory for Dynamic Imaging at Monash University (Melbourne, Australia)<sup>24</sup>. The imaging setup can be seen in Fig. 1, and consisted of a high brightness X-ray source (Excillum AB, Kista, Sweden) with a liquid-metal-jet anode and a characteristic peak of 24 keV, as per the manufacturer data sheet<sup>21</sup>. Imaging was performed at 70 kVp with a 15 μm spot size and at a power of 265 W. A high-speed CMOS flat-panel detector (PaxScan, Varian Medical Systems, Palo Alto, CA, USA) with an isotropic pixel size of 194 μm was used to capture images at 30 frames per second (fps) with an 18 ms exposure. The source-to-isocenter of the rotational imaging stage (R<sub>1</sub>) and source-to-detector (R<sub>2</sub>) distances were 0.36 m and 3.0 m respectively, resulting in an effective pixel size of 20 μm. A 2.7 m vacuum tube in front of the detector reduced image noise due to scattering in air. The radiation dose was measured using a dosimeter (Fluke Biomedical, TNT12000 DoseMate, USA). A high-precision rotation stage (Zaber Technologies, Vancouver, Canada) was used to rotate the mice 360 degrees whilst breathing to obtain a 4-dimensional CT. The CT parameters used to obtain the images in this paper can be found in Table 1. Images were obtained at 30 frames per second (Hz) and image acquisition was triggered by the ventilator so that all images were acquired at the same points throughout the breathing cycle. This allowed all images to be binned to 15 time points over the respiratory cycle; in reference to the parameters used for Fig. 2 this provided 400 projections for each time point in the breath over 360 degrees for post-processing. The total CTXV image acquisition took ~3.5 minutes.

**Image reconstruction and analysis.** A cone-beam reconstruction technique<sup>26</sup> was used to produce CT reconstruction volumes for each time point in the breath, resulting in 15 complete volumes that each represent a different time point in the breath. A calibration scan of an acrylic cylinder with fiducial markers<sup>27</sup> was imaged after each mouse to calculate the centre of rotation and projection angles used for the CT reconstruction.

Airways were segmented using an image filter based on Frangi *et al.*<sup>28,29</sup>. Local image gradients were matched to an ellipsoid, based on a Gaussian kernel scale, to differentiate tubular structures from plane-like structures. Tubular structures were computed over a range of 1–30 Gaussian kernel scales. This filter returns a probability value that any given pixel is part of a tubular structure, which, when segmented in Avizo (FEI VSG, France) using a flood-fill segmentation, returns a more accurate segmentation of the airways than segmenting the unprocessed CT volume alone. The airway segmentation was performed on the first of the 15 CT volumes (i.e. at the start of the breath before inspiration), because the volume of air throughout the distal gas exchange spaces is at a minimum at this time-point, creating maximal contrast to isolate the airways.

To extract functional respiratory data measurements (e.g. those represented in Fig. 3), the CT volumes were smoothed with a Gaussian filter to reduce noise, and the lung speckle visibility was enhanced using a bandpass filter. A 3-dimensional (3D) cross-correlation based technique was then used to measure the lung displacement between successive frames in the breath. The cross-correlation analysis was performed with interrogation regions of 32 × 32 × 32 voxels, with a 50% overlap between successive interrogation regions. The expansion field of the lung tissue was then calculated from the local gradients of the vectors. This information was displayed on a CT reconstruction of the lung tissue (see Fig. 3). The airflow through the airway tree was determined by associating the lung expansion data with the segmented airway tree through the Airway Tree Link (ATL) analysis method as described previously in Dubsy *et al.*<sup>11</sup>. As the air volume at the terminal airways can be calculated from the expansion data for the connected regional lung tissue, and the flow through the entire bronchial tree can be calculated by recursively summing the airflows in daughter segments at each bifurcation, with the assumption that the flow through a parent segment must equal the sum of the flow from the two supplying daughter segments and that airway compression effects are negligible due to the tidal breathing regime provided by the ventilator. This quantitative airflow measurement was then overlaid on the structural CT segmentation of the airways to visually present airflow through the bronchial tree (Fig. 2).

The expiratory time constant for the airway trees (Fig. 3a,b) is a standardised dynamic-change calculation that describes the time required for the lung volume to decrease by 63% (~1-(1/e)), where e is the mathematical constant known as Euler's number) of the complete expired volume and describes the system's resistance and compliance. The Airway Tree Link analysis described above allowed the volume at each branch of the airway to be quantified, which in turn is then be used to calculate the time required for the local air volume in each branch to reduce by 63% of the tidal volume.

www.nature.com/scientificreports/

**Code availability.** The 4DxV analysis code that supports the findings in this study is not publicly available due to patent restrictions. Code may however be available from the authors upon reasonable request and with permission of Monash University and 4Dx Limited.

#### Data availability

The data that support the findings of this study are available on reasonable request from the corresponding authors.

Received: 23 January 2019; Accepted: 15 November 2019;

Published online: 16 January 2020

#### References

1. Donnelly, M. & Parsons, D. W. Gene Therapy for Cystic Fibrosis Lung Disease: Overcoming the Barriers to Translation to the Clinic. *Front Pharmacol* **9** (2018).
2. Simon, B. A., Christensen, G. E., Low, D. A. & Reinhardt, J. M. Computed tomography studies of lung mechanics. *Proc. Am. Thorac. Soc.* **2**(517–521), 506–517 (2005).
3. Pellegrini, M. *et al.* The Diaphragm Acts as a Brake during Expiration to Prevent Lung Collapse. *Am. J. Respir. Crit. Care Med.* **195**, 1608–1616 (2017).
4. Rosenow, T. *et al.* PRAGMA-CF. A Quantitative Structural Lung Disease Computed Tomography Outcome in Young Children with Cystic Fibrosis. *Am. J. Respir. Crit. Care Med.* **191**, 1158–1165 (2015).
5. Chen, D., Xie, H., Zhang, S. & Gu, L. Lung respiration motion modeling: a sparse motion field presentation method using biplane x-ray images. *Phys. Med. Biol.* **62**, 7855–7873 (2017).
6. Guerrero, T., Zhang, G., Huang, T. C. & Lin, K. P. Intrathoracic tumour motion estimation from CT imaging using the 3D optical flow method. *Phys. Med. Biol.* **49**, 4147–4161 (2004).
7. Zhang, G. *et al.* Use of three-dimensional (3D) optical flow method in mapping 3D anatomic structure and tumor contours across four-dimensional computed tomography data. *J. Appl. Clin. Med. Phys.* **9**, 59–69 (2008).
8. Perchiazzi, G. *et al.* Regional distribution of lung compliance by image analysis of computed tomograms. *Respir. Physiol. Neurobiol.* **201**, 60–70 (2014).
9. Kitchen, M. J. *et al.* On the origin of speckle in x-ray phase contrast images of lung tissue. *Phys. Med. Biol.* **49**, 4335–4348 (2004).
10. Dubsky, S. *et al.* Computed tomographic x-ray velocimetry. *Appl. Phys. Lett.* **96** (2010).
11. Dubsky, S., Hooper, S. B., Siu, K. K. & Fouras, A. Synchrotron-based dynamic computed tomography of tissue motion for regional lung function measurement. *J. R. Soc. Interface* **9**, 2213–2224 (2012).
12. Chung, M. P. & Rhee, C. H. Airway obstruction in interstitial lung disease. *Curr. Opin. Pulm. Med.* **3**, 332–335 (1997).
13. Plantier, L. *et al.* Physiology of the lung in idiopathic pulmonary fibrosis. *Eur. Respir. Rev.* **27** (2018).
14. Fouras, A. *et al.* Altered Lung Motion is a Sensitive Indicator of Regional Lung Disease. *Ann. Biomed. Eng.* **40**, 1160–1169 (2011).
15. Mall, M., Grubb, B. R., Harkema, J. R., O'Neal, W. K. & Boucher, R. C. Increased airway epithelial Na<sup>+</sup> absorption produces cystic fibrosis-like lung disease in mice. *Nat. Med.* **10**, 487–493 (2004).
16. Stahr, C. S. *et al.* Quantification of heterogeneity in lung disease with image-based pulmonary function testing. *Sci. Rep.* **6**, 29438 (2016).
17. Bravin, A., Coan, P. & Suortti, P. X-ray phase-contrast imaging: from pre-clinical applications towards clinics. *Phys. Med. Biol.* **58**, R1–35 (2013).
18. Hemberg, O., Otendal, M. & Hertz, H. M. Liquid-metal-jet anode electron-impact x-ray source. *Appl. Phys. Lett.* **83**, 1483–1485 (2003).
19. Tuohimaa, T., Otendal, M. & Hertz, H. M. Phase-contrast x-ray imaging with a liquid-metal-jet-anode microfocus source. *Appl. Phys. Lett.* **91** (2007).
20. Zanette, I. *et al.* Speckle-Based X-Ray Phase-Contrast and Dark-Field Imaging with a Laboratory Source. *Phys. Rev. Lett.* **112** (2014).
21. Espes, E. *et al.* Liquid-metal-jet x-ray tube technology and tomography applications. In *Developments in X-Ray Tomography IX*, Vol. **9212** (SPIE Proceedings, 2014).
22. Krenkel, M., Tappervien, M., Dullin, C., Alves, F. & Salditt, T. Propagation-based phase-contrast tomography for high-resolution lung imaging with laboratory sources. *AIP Advances* **6** (2016).
23. Larsson, D. H., Vågberg, W., Yaroshenko, A., Yildirim, A. O. & Hertz, H. M. High-resolution short-exposure small-animal laboratory x-ray phase-contrast tomography. *Sci. Rep.* **6**, 39074 (2016).
24. Preissner, M. *et al.* High resolution propagation-based imaging system for *in vivo* dynamic computed tomography of lungs in small animals. *Phys. Med. Biol.* **63**, 08NT03 (2018).
25. Okunieff, P., Wu, T., Huang, K. & Ding, I. Differential radioprotection of three mouse strains by basic or acidic fibroblast growth factor. *Br. J. Cancer Suppl.* **27**, S105–108 (1996).
26. Feldkamp, L. A., Davis, L. C. & Kress, J. W. Practical cone-beam algorithm. *J. Opt. Soc. Am. A* **1**, 612–619 (1984).
27. Yang, K., Kwan, A. L., Miller, D. F. & Boone, J. M. A geometric calibration method for cone beam CT systems. *Med. Phys.* **33**, 1695–1706 (2006).
28. Dubsky, S. *et al.* Assessment of airway response distribution and paradoxical airway dilation in mice during methacholine challenge. *J. Appl. Physiol.* **122**, 503–510 (2017).
29. Frangi, A. F., Niessen, W. J., Vincken, K. L. & Viergever, M. A. Multiscale vessel enhancement filtering. In *Medical Image Computing and Computer-Assisted Intervention — MICCAI'98* 130–137 (1998).

#### Acknowledgements

This project was supported in part by the NHMRC (projects GNT1079712 and GNT1055116) and the Cystic Fibrosis Foundation (FOURAS1510). KM was supported by a Veski VPRF and completed this work with the support of the TUM Institute for Advanced Study, funded by the German Excellence Initiative and the European Union Seventh Framework Program under grant agreement no 291763 and co-funded by the European Union. MD was supported by a Robinson Research Institute Career Development Fellowship. JL is an NHMRC Senior Research Fellow and is supported by the National Institute of Allergy and Infectious Diseases of the National Institutes of Health (R01 AI132681).

#### Author contributions

A.F. and S.D. designed the techniques. A.F., D.P., M.D., and J.L. designed the experiments. A.F., S.D., C.S., and R.C. wrote the analysis code. R.M., F.W., Y.L., R.C., I.P., K.M., M.D. and D.P. performed the experiments. R.M., C.S., F.W., Y.L., M.P., R.C. and I.P. analysed the data. R.M. wrote the paper. M.D. edited final drafts. A.F., S.D., J.W., J.L., K.M., M.D. and D.P. provided overall guidance and supervision of the project. All authors discussed the results and commented on the manuscript.

www.nature.com/scientificreports/

#### Competing interests

A.F., C.S., R.C., R.M., S.D. and D.P. have beneficial interests in 4Dx Limited, a company commercialising respiratory diagnostics technology. A.F., S.D. and C.S. are listed on patents filed by Monash University and 4Dx Limited describing the lung imaging technology. The content is solely the responsibility of the authors and does not necessarily represent the official views of the National Institute of Allergy and Infectious Diseases or the National Institutes of Health.

#### Additional information

**Correspondence** and requests for materials should be addressed to R.P.M. or D.W.P.

**Reprints and permissions information** is available at [www.nature.com/reprints](http://www.nature.com/reprints).

**Publisher's note** Springer Nature remains neutral with regard to jurisdictional claims in published maps and institutional affiliations.



**Open Access** This article is licensed under a Creative Commons Attribution 4.0 International License, which permits use, sharing, adaptation, distribution and reproduction in any medium or format, as long as you give appropriate credit to the original author(s) and the source, provide a link to the Creative Commons license, and indicate if changes were made. The images or other third party material in this article are included in the article's Creative Commons license, unless indicated otherwise in a credit line to the material. If material is not included in the article's Creative Commons license and your intended use is not permitted by statutory regulation or exceeds the permitted use, you will need to obtain permission directly from the copyright holder. To view a copy of this license, visit <http://creativecommons.org/licenses/by/4.0/>.

© The Author(s) 2020



## C Substitution of figures in Chapter 2

The following figures were either substituted or removed from Chapter 2 (Literature Review) after examination of the thesis. The figure numbers are given as per the examined thesis, submitted on 12 February 2020.

1. Figure 2.1 from Patil & Sarasija (2012) has been replaced with a similar figure.
2. Figure 2.2 from West (2012) has been replaced with a similar figure.
3. Fig 2.3 from Marino (2014) has been replaced with a similar figure.
4. Fig 2.6 from Dreyfuss & Saumon (1992) has been removed.
5. Figure 2.7 from Schiller et al. (2001) has been replaced with a similar figure.



# Bibliography

Abrams, D. *et al.* Mechanical Ventilation for ARDS During Extracorporeal Life Support: Research and Practice. *American Journal of Respiratory and Critical Care Medicine* **In press** (2019).

Adrian, R. J. Twenty years of particle image velocimetry. *Experiments in Fluids* **39**, 159–169 (2005).

Agostoni, E. Mechanics of the pleural space. *Physiological Reviews* **52**, 57–128 (1972).

Allen, G. B., Suratt, B. T., Rinaldi, L., Petty, J. M. & Bates, J. H. T. Choosing the frequency of deep inflation in mice: balancing recruitment against ventilator-induced lung injury. *American Journal of Physiology-Lung Cellular and Molecular Physiology* **291**, L710–L717 (2006).

Altemeier, W. A., Matute-Bello, G., Frevert, C. W., Kawata, Y., Kajikawa, O., Martin, T. R. & Glenny, R. W. Mechanical ventilation with moderate tidal volumes synergistically increases lung cytokine response to systemic endotoxin. *American Journal of Physiology-Lung Cellular and Molecular Physiology* **287**, L533–L542 (2004).

Amato, M. B., Meade, M. O., Slutsky, A. S., Brochard, L., Costa, E. L. V., Schoenfeld, D. A., Stewart, T. E., Briel, M., Talmor, D., Mercat, A., Richard, J.-C. M., Carvalho, C. R. R. & Brower, R. G. Driving pressure and survival in the acute respiratory distress syndrome. *New England Journal of Medicine* **372**, 747–755 (2015).

Amini, R., Herrmann, J. & Kaczka, D. W. Intratidal Overdistention and Derecruitment in the Injured Lung: A Simulation Study. *IEEE Transactions on Biomedical Engineering* **64**, 681–689 (2017).

Ashbaugh, D. G., Bigelow, D. B., Petty, T. L. & Levine, B. E. Acute respiratory distress in adults. *The Lancet* **290**, 319–323 (1967).

Bachofen, H. Lung tissue resistance and pulmonary hysteresis. *Journal of Applied Physiology* **24**, 296–301 (1968).

Badea, C. T., Guo, X., Clark, D., Johnston, S. M., Marshall, C. D. & Piantadosi, C. A. Dual-energy micro-CT of the rodent lung. *American Journal of Physiology - Lung Cellular and Molecular Physiology* **302**, L1088–1097 (2012).

Badea, C. T., Johnston, S., Johnson, B., Lin, M., Hedlund, L. W. & Johnson, G. A. A dual micro-CT system for small animal imaging in *Proceedings of SPIE—the International Society for Optical Engineering* (2008), 691342.

Bates, J. H. T. *Lung Mechanics: An Inverse Modeling Approach* (Cambridge University Press, 2009).

Bates, J. H. T. & Irvin, C. G. Measuring lung function in mice: the phenotyping uncertainty principle. *Journal of Applied Physiology* **94**, 1297–1306 (2003).

Bayat, S., Porra, L., Broche, L., Albu, G., Malaspinas, I., Doras, C., Strengell, S., Petak, F. & Habre, W. Effect of surfactant on regional lung function in an experimental model of respiratory distress syndrome in rabbit. *Journal of Applied Physiology* **119**, 290–298 (2015).

Beitler, J. R., Malhotra, A. & Thompson, B. T. Ventilator-induced lung injury. *Clinics in Chest Medicine* **37**, 633–646 (2016).

Bellani, G., Laffey, J. G., Pham, T., Fan, E., Brochard, L., Esteban, A., Gattinoni, L., van Haren, F., Larsson, A., McAuley, D. F., Ranieri, M., Rubenfeld, G., Thompson, B. T., Wrigge, H., Slutsky, A. S. & Pesenti, A. Epidemiology, patterns of care, and mortality for patients with acute respiratory distress syndrome in intensive care units in 50 countries. *Journal of the American Medical Association* **315**, 788–800 (2016).

Betts, J. G., Young, K. A., Wise, J. A., Johnson, E., Poe, B., Kruse, D. H., Korol, O., Johnson, J. E., Womble, M. & DeSaix, P. *Anatomy and Physiology* (OpenStax, Rice University, 2013).

Borges, J. B. Why titrate PEEP in general anesthesia? *British Journal of Anaesthesia* **115** (2015).

Broccard, A. F., Hotchkiss, J. R., Kuwayama, N., Olson, D. A., Jamal, S., Wangenstein, D. O. & Marini, J. J. Consequences of Vascular Flow on Lung Injury Induced by Mechanical Ventilation. *American Journal of Respiratory and Critical Care Medicine* **157**, 1935–1942 (1998).

Brooks, F. J., Gunsten, S. P., Vasireddi, S. K., Brody, S. L. & Anastasio, M. A. Quantification of image texture in X-ray phase-contrast-enhanced projection images of in vivo mouse lungs observed at varied inflation pressures. *Physiological Reports* **7**, e14208 (2019).

Broseghini, C., Brandolese, R., Poggi, R., Bernasconi, M., Manzin, E. & Rossi, A. Respiratory resistance and intrinsic positive end expiratory pressure (PEEPi) in patients with the adult respiratory distress syndrome (ARDS). *The European Respiratory Journal* **1**, 726–731 (1988).

Brower, R. G., Lanken, P. N., MacIntyre, N., Matthay, M. A., Morris, A., Ancukiewicz, M., Schoenfeld, D. & Thompson, B. T. Higher versus lower positive end-expiratory pressures in patients with the acute respiratory distress syndrome. *New England Journal of Medicine* **351**, 327–336 (2004).

Brower, R. G., Matthay, M. A., Morris, A., Schoenfeld, D., Thompson, B. T. & Wheeler, A. Ventilation with lower tidal volumes as compared with traditional tidal volumes for acute lung injury and the acute respiratory distress syndrome. *New England Journal of Medicine* **342**, 1301–1308 (2000).

Caironi, P., Cressoni, M., Chiumello, D., Ranieri, M., Quintel, M., Russo, S. G., Cornejo, R., Bugedo, G., Carlesso, E., Russo, R., Caspani, L. & Gattinoni, L. Lung opening and closing during ventilation of acute respiratory distress syndrome. *American Journal of Respiratory and Critical Care Medicine* **181**, 578–586 (2010).

Campbell, R. S. & Davis, B. R. Pressure-controlled versus volume-controlled ventilation: does it matter? *Respiratory Care* **47**, 416–426 (2002).

Cannizzaro, V., Hantos, Z., Sly, P. D. & Zosky, G. R. Linking lung function and inflammatory responses in ventilator-induced lung injury. *American Journal of Physiology - Lung Cellular and Molecular Physiology* **300**, 112–120 (2011).

Cereda, M., Xin, Y., Hamedani, H., Bellani, G., Kadlecsek, S., Clapp, J., Guerra, L., Meeder, N., Rajaei, J., Tustison, N. J., Gee, J. C., Kavanagh, B. P. & Rizi, R. R. Tidal changes on CT and progression of ARDS. *Thorax* **72**, 981–989 (2017).

- Chen, L., Del Sorbo, L., Grieco, D. L., Shklar, O., Junhasavasdikul, D., Telias, I., Fan, E. & Brochard, L. Airway Closure in Acute Respiratory Distress Syndrome: An Underestimated and Misinterpreted Phenomenon. *American Journal of Respiratory and Critical Care Medicine* **197**, 132–136 (2018).
- Christley, S., Emr, B., Ghosh, A., Satalin, J., Gatto, L., Vodovotz, Y., Nieman, G. F. & An, G. Bayesian inference of the lung alveolar spatial model for the identification of alveolar mechanics associated with acute respiratory distress syndrome. *Physical Biology* **10**, 036008 (2013).
- Corrado, A. & Gorini, M. Negative-pressure ventilation: is there still a role? *European Respiratory Journal* **20**, 187–197 (2002).
- Cressoni, M., Cadringer, P., Chiurazzi, C., Amini, M., Gallazzi, E., Marino, A., Brioni, M., Carlesso, E., Chiumello, D., Quintel, M., Bugedo, G. & Gattinoni, L. Lung inhomogeneity in patients with acute respiratory distress syndrome. *American Journal of Respiratory and Critical Care Medicine* **189**, 149–158 (2013).
- D'Angelo, E., Pecchiari, M., Baraggia, P., Saetta, M., Balestro, E. & Milic-Emili, J. Low volume ventilation causes peripheral airway injury and increased airway resistance in normal rabbits. *Journal of Applied Physiology* **92**, 949–956 (2002).
- Dharmakumara, M., Prisk, G. K., Royce, S. G., Tawhai, M. & Thompson, B. R. The effect of gas exchange on multiple-breath nitrogen washout measures of ventilation inhomogeneity in the mouse. *Journal of Applied Physiology* **117**, 1049–1054 (2014).
- Donovan, C., Royce, S. G., Vlahos, R. & Bourke, J. E. Lipopolysaccharide does not alter small airway reactivity in mouse lung slices. *PLOS ONE* **10** (2015).
- Dreyfuss, D. & Saumon, G. Barotrauma is volutrauma, but which volume is the one responsible? *Intensive Care Medicine* **18**, 139–141 (1992).
- Dreyfuss, D. & Saumon, G. Role of tidal volume, FRC, and end-inspiratory volume in the development of pulmonary edema following mechanical ventilation. *The American Review of Respiratory Disease* **148**, 1194–1203 (1993).
- Drinker, P. & Shaw, L. The prolonged administration of artificial respiration. *Journal of the Franklin Institute* **213**, 355–372 (1932).
- Dubsky, S., Hooper, S. B., Siu, K. K. W. & Fouras, A. Synchrotron-based dynamic computed tomography of tissue motion for regional lung function measurement. *Journal of The Royal Society Interface* **9**, 2213–2224 (2012).
- Dubsky, S., Jamison, R. A., Irvine, S. C., Siu, K. K. W., Hourigan, K. & Fouras, A. Computed tomographic X-ray velocimetry. *Applied Physics Letters* **96**, 023702 (2010).
- Dubsky, S., Thurgood, J., Fouras, A., Thompson, B. R. & Sheard, G. J. Cardiogenic air-flow in the lung revealed using synchrotron-based dynamic lung imaging. *Scientific Reports* **8**, 4930 (2018).
- Dubsky, S., Zosky, G. R., Perks, K., Samarage, C. R., Henon, Y., Hooper, S. B. & Fouras, A. Assessment of airway response distribution and paradoxical airway dilation in mice during methacholine challenge. *Journal of Applied Physiology* **122**, 503–510 (2017).
- Evans, D. J., Schultz, A., Verheggen, M., Hall, G. L. & Simpson, S. J. Identifying pediatric lung disease: a comparison of forced oscillation technique outcomes. *Pediatric Pulmonology* **54**, 751–758 (2019).
- Faffe, D. S., Rocco, P. R. M., Negri, E. M. & Zin, W. A. Comparison of rat and mouse pulmonary tissue mechanical properties and histology. *Journal of Applied Physiology* **92**, 230–234 (2002).

- Faight, E. M., Verdelis, K., Zourelis, L., Chong, R., Benza, R. L. & Shields, K. J. Micro-CT analysis of vascular morphometry: a comparison of right lung lobes in the SUGEN/hypoxic rat model of pulmonary arterial hypertension. *Pulmonary Circulation* **7**, 522–530 (2017).
- Fan, E. *et al.* An Official American Thoracic Society/European Society of Intensive Care Medicine/Society of Critical Care Medicine Clinical Practice Guideline: Mechanical Ventilation in Adult Patients with Acute Respiratory Distress Syndrome. *American Journal of Respiratory and Critical Care Medicine* **195**, 1253–1263 (2017).
- Feldkamp, L. A., Davis, L. C. & Kress, J. W. Practical cone-beam algorithm. *Journal of the Optical Society of America* **1**, 612 (1984).
- Fouras, A., Allison, B. J., Kitchen, M. J., Dubsky, S., Nguyen, J., Hourigan, K., Siu, K. K. W., Lewis, R. A., Wallace, M. J. & Hooper, S. B. Altered lung motion is a sensitive indicator of regional lung disease. *Annals of Biomedical Engineering* **40**, 1160–9 (2012).
- Fouras, A., Kitchen, M. J., Dubsky, S., Lewis, R. A., Hooper, S. B. & Hourigan, K. The past, present, and future of x-ray technology for in vivo imaging of function and form. *Journal of Applied Physics* **105**, 102009 (2009).
- Fowler, S., Roush, R. & Wise, J. *Concepts of Biology* (OpenStax, Rice University, 2013).
- Frangi, A. F., Niessen, W. J., Vincken, K. L. & Viergever, M. A. Multiscale vessel enhancement filtering. *International Conference on Medical Image Computing and Computer-Assisted Intervention (MICCAI '98)*, 130–137 (1998).
- Frank, J. A., Pittet, J.-F., Wray, C. & Matthay, M. A. Protection from experimental ventilator-induced acute lung injury by IL-1 receptor blockade. *Thorax* **63**, 147–153 (2008).
- Fuld, M. K., Easley, R. B., Saba, O. I., Chon, D., Reinhardt, J. M., Hoffman, E. A. & Simon, B. A. CT-measured regional specific volume change reflects regional ventilation in supine sheep. *Journal of Applied Physiology* **104**, 1177–1184 (2008).
- Galetke, W., Feier, C., Muth, T., Ruehle, K.-H., Borsch-Galetke, E. & Randerath, W. Reference values for dynamic and static pulmonary compliance in men. *Respiratory Medicine* **101**, 1783–1789 (2007).
- Gattinoni, L., Caironi, P., Cressoni, M., Chiumello, D., Ranieri, V. M., Quintel, M., Russo, S., Patroniti, N., Cornejo, R. & Bugedo, G. Lung recruitment in patients with the acute respiratory distress syndrome. *New England Journal of Medicine* **354**, 1775–1786 (2006).
- Gattinoni, L., Caironi, P., Pelosi, P. & Goodman, L. R. What has computed tomography taught us about the acute respiratory distress syndrome? *American Journal of Respiratory and Critical Care Medicine* **164**, 1701–1711 (2001).
- Gattinoni, L., Marini, J. J., Collino, F., Maiolo, G., Rapetti, F., Tonetti, T., Vasques, F. & Quintel, M. The future of mechanical ventilation: lessons from the present and the past. *Critical Care* **21**, 183 (2017).
- Gattinoni, L. & Pesenti, A. The concept of "baby lung". *Intensive Care Medicine* **31**, 776–784 (2005).
- Gattinoni, L., Pesenti, A., Avalli, L., Rossi, F. & Bombino, M. Pressure-volume curve of total respiratory system in acute respiratory failure: computed tomographic scan study. *The American Review of Respiratory Disease* **136**, 730–736 (1987).
- Gattinoni, L., Quintel, M. & Marini, J. J. Volutrauma and atelectrauma: which is worse? *Critical Care* **22**, 264 (2018).

- Gattinoni, L., Tonetti, T., Cressoni, M., Cadringer, P., Herrmann, P., Moerer, O., Protti, A., Gotti, M., Chiurazzi, C., Carlesso, E., Chiumello, D. & Quintel, M. Ventilator-related causes of lung injury: the mechanical power. *Intensive Care Medicine* **42**, 1567–1575 (2016).
- Gerard, S. E., Herrmann, J., Kaczka, D. W., Musch, G., Fernandez-Bustamante, A. & Reinhardt, J. M. Multi-resolution convolutional neural networks for fully automated segmentation of acutely injured lungs in multiple species. *Medical Image Analysis* **60**, 101592 (2020).
- Gradl, R., Dierolf, M., Günther, B., Hehn, L., Möller, W., Kutschke, D., Yang, L., Donnelly, M., Murrie, R., Erl, A., Stoeger, T., Gleich, B., Achterhold, K., Schmid, O., Pfeiffer, F. & Morgan, K. S. In vivo Dynamic Phase-Contrast X-ray Imaging using a Compact Light Source. *Scientific Reports* **8**, 6788 (2018).
- Griffiths, M. J. D., McAuley, D. F., Perkins, G. D., Barrett, N., Blackwood, B., Boyle, A., Chee, N., Connolly, B., Dark, P., Finney, S., Salam, A., Silversides, J., Tarmey, N., Wise, M. P. & Baudouin, S. V. Guidelines on the management of acute respiratory distress syndrome. *BMJ Open Respiratory Research* **6**, e000420 (2019).
- Hamlington, K. L., Bates, J. H. T., Roy, G. S., Julianelle, A. J., Charlebois, C., Suki, B. & Smith, B. J. Alveolar leak develops by a rich-get-richer process in ventilator-induced lung injury. *PLOS ONE* **13**, e0193934 (2018).
- Harris, R. S. Pressure-volume curves of the respiratory system. *Respiratory Care* **50**, 78–98, discussion 98–99 (2005).
- Henderson, W. R., Chen, L., Amato, M. B. P. & Brochard, L. J. Fifty Years of Research in ARDS: Respiratory mechanics in acute respiratory distress syndrome. *American Journal of Respiratory and Critical Care Medicine* **196**, 822–833 (2017).
- Hernandez, L. A., Peevy, K. J., Moise, A. A. & Parker, J. C. Chest wall restriction limits high airway pressure-induced lung injury in young rabbits. *Journal of Applied Physiology* **66**, 2364–2368 (1989).
- Herrmann, J., Hoffman, E. A. & Kaczka, D. W. Frequency-Selective Computed Tomography: Applications During Periodic Thoracic Motion. *IEEE Transactions on Medical Imaging* **36**, 1722–1732 (2017).
- Herrmann, J., Lilitwat, W., Tawhai, M. H. & Kaczka, D. W. High-frequency oscillatory ventilation and ventilator-induced lung injury: size does matter. *Critical Care Medicine* **48** (2020).
- Hess, D. R. Respiratory mechanics in mechanically ventilated patients. *Respiratory Care* **59**, 1773–1794 (2014).
- Horsley, A. Lung clearance index in the assessment of airways disease. *Respiratory Medicine* **103**, 793–799 (2009).
- Hubmayr, R. D. Perspective on lung injury and recruitment. *American Journal of Respiratory and Critical Care Medicine* **165**, 1647–1653 (2002).
- Irvin, C. G. & Bates, J. H. T. Measuring the lung function in the mouse: the challenge of size. *Respiratory Research* **4**, 1 (2003).
- Jain, M. & Sznajder, J. I. Bench-to-bedside review: distal airways in acute respiratory distress syndrome. *Critical Care* **11**, 206 (2007).
- Janosi, T. Z., Adamicza, Á., Zosky, G. R., Asztalos, T., Sly, P. D. & Hantos, Z. Plethysmographic estimation of thoracic gas volume in apneic mice. *Journal of Applied Physiology* **101**, 454–459 (2006).

- Johnson, N. J., Luks, A. M. & Glenny, R. W. Gas exchange in the prone posture. *Respiratory Care* **62**, 1097–1110 (2017).
- Jones, H. D., Crother, T. R., Gonzalez-Villalobos, R. A., Jupelli, M., Chen, S., Davadorj, J., Arditi, M. & Shimada, K. The NLRP3 inflammasome is required for the development of hypoxemia in LPS/mechanical ventilation acute lung injury. *American Journal of Respiratory Cell and Molecular Biology* **50**, 270–280 (2014).
- Kaczka, D. W., Cao, K., Christensen, G. E., Bates, J. H. T. & Simon, B. A. Analysis of Regional Mechanics in Canine Lung Injury Using Forced Oscillations and 3D Image Registration. *Annals of Biomedical Engineering* **39**, 1112–1124 (2011).
- Kaczka, D. W. & Nieman, G. F. Designing protective mechanical ventilation for the injured lung: opportunities for the engineer. *Journal of Engineering and Science in Medical Diagnostics and Therapy* **2** (2019).
- Kalender, W. A. *Computed tomography: fundamentals, system technology, image quality, applications* 3rd edition (Wiley-VCH, 2011).
- Kalender, W. A., Durkee, B., Langner, O., Stepina, E. & Karolczak, M. Comparative evaluation: acceptance testing and constancy testing for micro-CT scanners. *Biomedizinische Technik* **50**, 1192–1193 (2005).
- Kim, E. H., Preissner, M., Carnibella, R. P., Samarage, C. R., Bennett, E., Fouras, A., Zosky, G. R. & Jones, H. D. Novel analysis of 4DCT imaging quantifies progressive increases in anatomic dead space during mechanical ventilation in mice. *Journal of Applied Physiology*, 578–584 (2017).
- Kitchen, M. J., Buckley, G. A., Gureyev, T. E., Wallace, M. J., Andres-Thio, N., Uesugi, K., Yagi, N. & Hooper, S. B. CT dose reduction factors in the thousands using X-ray phase contrast. *Scientific Reports* **7**, 15953 (2017).
- Kitchen, M. J., Habib, A., Fouras, A., Dubsky, S., Lewis, R. A., Wallace, M. J. & Hooper, S. B. A new design for high stability pressure-controlled ventilation for small animal lung imaging. *Journal of Instrumentation* **5** (2010).
- Kitchen, M. J., Lewis, R. A., Morgan, M. J., Wallace, M. J., Siew, M. L., Siu, K. K. W., Habib, A., Fouras, A., Yagi, N., Uesugi, K. & Hooper, S. B. Dynamic measures of regional lung air volume using phase contrast x-ray imaging. *Physics in Medicine and Biology* **53**, 6065–6077 (2008).
- Kuebler, W. M. Real-time imaging assessment of pulmonary vascular responses. *Proceedings of the American Thoracic Society* **8**, 458–465 (2011).
- Lam, M., Royce, S. G., Samuel, C. S. & Bourke, J. E. Serelaxin as a novel therapeutic opposing fibrosis and contraction in lung diseases. *Pharmacology and Therapeutics* **187**, 61–70 (2018).
- Larsson, D. H., Takman, P. A. C., Lundström, U., Burvall, A. & Hertz, H. M. A 24 keV liquid-metal-jet x-ray source for biomedical applications. *Review of Scientific Instruments* **82**, 123701 (2011).
- Larsson, D. H., Vagberg, W., Yaroshenko, A., Yildirim, A. O. & Hertz, H. M. High-resolution short-exposure small-animal laboratory x-ray phase-contrast tomography. *Scientific Reports* **6**, 39074 (2016).
- Lassen, H. C. A. A preliminary report on the 1952 epidemic of poliomyelitis in Copenhagen with special reference to the treatment of acute respiratory insufficiency. *The Lancet* **261**, 37–41 (1953).
- Lewis, J. F. & Jobe, A. H. Surfactant and the adult respiratory distress syndrome. *The American Review of Respiratory Disease* **147**, 218–233 (1993).

- Lex, D. & Uhlig, S. One-hit models of ventilator-induced lung injury - benign inflammation versus inflammation as a by-product. *Anesthesiology: The Journal of the American Society of Anesthesiologists* **126**, 909–922 (2017).
- Liu, Q., Gao, Y., Chen, R. & Cheng, Z. Noninvasive ventilation with helmet versus control strategy in patients with acute respiratory failure: a systematic review and meta-analysis of controlled studies. *Critical Care* **20**, 265 (2016).
- Lovric, G., Broche, L., Schleputz, C. M., Fardin, L., Schittny, J. C., Larsson, A. S. & Bayat, S. *Spatial distribution of ventilator induced lung injury at the um-scale: an in-vivo synchrotron phase-contrast microscopy study in BALB/c Mice in American Thoracic Society International Conference Abstracts: D105 Critical Care: Ventilator Induced Lung Injury and ARDS* (2018), A7526–A7526.
- Lovric, G., Mokso, R., Arcadu, F., Vogiatzis Oikonomidis, I., Schittny, J. C., Roth-Kleiner, M. & Stampanoni, M. Tomographic in vivo microscopy for the study of lung physiology at the alveolar level. *Scientific Reports* **7**, 12545 (2017).
- Lovric, G., Vogiatzis Oikonomidis, I., Mokso, R., Stampanoni, M., Roth-Kleiner, M. & Schittny, J. C. Automated computer-assisted quantitative analysis of intact murine lungs at the alveolar scale. *PLOS ONE* **12**, e0183979 (2017).
- Lu, Q. & Rouby, J.-J. Measurement of pressure-volume curves in patients on mechanical ventilation: methods and significance. *Critical Care* **4**, 91–100 (2000).
- MacIntyre, N. R. Current issues in mechanical ventilation for respiratory failure. *Chest* **128**, 561S–567S (2005).
- Marini, J. J. Dissipation of energy during the respiratory cycle: conditional importance of ergotrauma to structural lung damage. *Current Opinion in Critical Care* **24**, 16–22 (2018).
- Marino, P. L. *The ICU Book* 4th edition (Wolters Kluwer Health, 2014).
- Matute-Bello, G., Downey, G., Moore, B. B., Groshong, S. D., Matthay, M. A., Slutsky, A. S. & Kuebler, W. M. An official American thoracic society workshop report: Features and measurements of experimental acute lung injury in animals. *American Journal of Respiratory Cell and Molecular Biology* **44**, 725–38 (2011).
- Matute-Bello, G., Frevert, C. W. & Martin, T. R. Animal models of acute lung injury. *American Journal of Physiology - Lung Cellular and Molecular Physiology* **295**, L379–L399 (2008).
- Maunder, R. J., Shuman, W. P., McHugh, J. W., Marglin, S. I. & Butler, J. Preservation of normal lung regions in the adult respiratory distress syndrome: analysis by computed tomography. *Journal of the American Medical Association* **255**, 2463–2465 (1986).
- Mead, J., Takishima, T. & Leith, D. Stress distribution in lungs: a model of pulmonary elasticity. *Journal of Applied Physiology* **28**, 596–608 (1970).
- Milne, S., Jetmalani, K., Chapman, D. G., Duncan, J. M., Farah, C. S., Thamrin, C. & King, G. G. Respiratory system reactance reflects communicating lung volume in chronic obstructive pulmonary disease. *Journal of Applied Physiology* **126**, 1223–1231 (2019).
- Moloney, E. D. & Griffiths, M. J. D. Protective ventilation of patients with acute respiratory distress syndrome. *British Journal of Anaesthesia* **92**, 261–270 (2004).

- Motta-Ribeiro, G. C., Hashimoto, S., Winkler, T., Baron, R. M., Grogg, K., Paula, L. F. S. C., Santos, A., Zeng, C., Hibbert, K., Harris, R. S., Bajwa, E. & Vidal Melo, M. F. Deterioration of Regional Lung Strain and Inflammation during Early Lung Injury. *American Journal of Respiratory and Critical Care Medicine; New York* **198**, 891–902 (2018).
- Murrie, R. P., Morgan, K. S., Maksimenko, A., Fouras, A., Paganin, D. M., Hall, C., Siu, K. K. W., Parsons, D. W. & Donnelley, M. Live small-animal X-ray lung velocimetry and lung micro-tomography at the Australian Synchrotron Imaging and Medical Beamline. *Journal of Synchrotron Radiation* **22**, 1049–1055 (2015).
- Murrie, R. P., Paganin, D. M., Fouras, A. & Morgan, K. S. Phase contrast x-ray velocimetry of small animal lungs: optimising imaging rates. *Biomedical Optics Express* **7**, 79–92 (2016).
- Murrie, R. P., Werdiger, F., Donnelley, M., Lin, Y., Carnibella, R. P., Samarage, C. R., Pinar, I., Preissner, M., Wang, J., Li, J., Morgan, K. S., Parsons, D. W., Dubsky, S. & Fouras, A. Real-time in vivo imaging of regional lung function in a mouse model of cystic fibrosis on a laboratory X-ray source. *Scientific Reports* **10**, 447 (2020).
- Naeije, R. & Brimiouille, S. Physiology in medicine: importance of hypoxic pulmonary vasoconstriction in maintaining arterial oxygenation during acute respiratory failure. *Critical Care* **5**, 67–71 (2001).
- Needham, D. M., Colantuoni, E., Mendez-Tellez, P. A., Dinglas, V. D., Sevransky, J. E., Dennison Himmelfarb, C. R., Desai, S. V., Shanholtz, C., Brower, R. G. & Pronovost, P. J. Lung protective mechanical ventilation and two year survival in patients with acute lung injury: prospective cohort study. *British Medical Journal* **344**, e2124–e2124 (2012).
- Neudoerffer Kangelaris, K., Ware, L. B., Wang, C. Y., Janz, D. R., Hanjing, Z., Matthay, M. A. & Calfee, C. S. Timing of intubation and clinical outcomes in adults with ARDS. *Critical Care Medicine* **44**, 120–129 (2016).
- Ng, I., Paganin, D. M. & Fouras, A. Optimization of in-line phase contrast particle image velocimetry using a laboratory x-ray source. *Journal of Applied Physics* **112** (2012).
- Nichane, M., Javed, A., Sivakamasundari, V., Ganesan, M., Ang, L. T., Kraus, P., Lufkin, T., Loh, K. M. & Lim, B. Isolation and 3D expansion of multipotent Sox9+ mouse lung progenitors. *Nature Methods* **14**, 1205–1212 (2017).
- Nickles, H. T., Sumkauskaitė, M., Wang, X., Wegner, I., Puderbach, M. & Kuebler, W. M. Mechanical ventilation causes airway distension with proinflammatory sequelae in mice. *American Journal of Physiology - Lung Cellular and Molecular Physiology* **307**, L27–37 (2014).
- Nieman, G. F., Andrews, P., Satalin, J., Wilcox, K., Kollisch-Singule, M., Madden, M., Aiash, H., Blair, S. J., Gatto, L. A. & Habashi, N. M. Acute lung injury: how to stabilize a broken lung. *Critical Care* **22**, 136 (2018).
- Nilsen, K., Thien, F., Thamrin, C., Ellis, M. J., Prisk, G. K., King, G. G. & Thompson, B. R. Early onset of airway derecruitment assessed using the forced oscillation technique in subjects with asthma. *Journal of Applied Physiology* **126**, 1399–1408 (2019).
- Panta, R. K., Bell, S. T., Healy, J. L., Aamir, R., Bateman, C. J., Moghiseh, M., Butler, A. P. H. & Anderson, N. G. Element-specific spectral imaging of multiple contrast agents: a phantom study. *Journal of Instrumentation* **13** (2018).

- Papazian, L., Aubron, C., Brochard, L., Chiche, J.-D., Combes, A., Dreyfuss, D., Forel, J.-M., Guérin, C., Jaber, S., Mekontso-Dessap, A., Mercat, A., Richard, J.-C., Roux, D., Vieillard-Baron, A. & Faure, H. Formal guidelines: management of acute respiratory distress syndrome. *Annals of Intensive Care* **9**, 69 (2019).
- Parsons, D. W., Morgan, K., Donnelley, M., Fouras, A., Crosbie, J., Williams, I., Boucher, R. C., Uesugi, K., Yagi, N. & Siu, K. K. W. High-resolution visualization of airspace structures in intact mice via synchrotron phase-contrast X-ray imaging (PCXI). *Journal of Anatomy* **213**, 217–227 (2008).
- Paula, L. F. S. d. C., Wellman, T. J., Winkler, T., Spieth, P. M., Güldner, A., Venegas, J. G., Gama de Abreu, M., Carvalho, A. R. & Vidal Melo, M. F. Regional tidal lung strain in mechanically ventilated normal lungs. *Journal of Applied Physiology* **121**, 1335–1347 (2016).
- Peek, G. J., Mugford, M., Tiruvoipati, R., Wilson, A., Allen, E., Thalanany, M. M., Hibbert, C. L., Truesdale, A., Clemens, F., Cooper, N., Firmin, R. K. & Elbourne, D. Efficacy and economic assessment of conventional ventilatory support versus extracorporeal membrane oxygenation for severe adult respiratory failure (CESAR): a multicentre randomised controlled trial. *The Lancet* **374**, 1351–1363 (2009).
- Pelosi, P., Caironi, P. & Gattinoni, L. Pulmonary and extrapulmonary forms of acute respiratory distress syndrome. *Seminars in Respiratory and Critical Care Medicine* **22**, 259–268 (2001).
- Pelosi, P., D'Onofrio, D., Chiumello, D., Paolo, S., Chiara, G., Capelozzi, V. L., Barbas, C. S. V., Chiaranda, M. & Gattinoni, L. Pulmonary and extrapulmonary acute respiratory distress syndrome are different. *The European Respiratory Journal* **42**, 48s–56s (2003).
- Pelosi, P., Rocco, P. R. M. & Gama de Abreu, M. Close down the lungs and keep them resting to minimize ventilator-induced lung injury. *Critical Care* **22**, 72 (2018).
- Pelosi, P., Tubiolo, D., Mascheroni, D., Vicardi, P., Crotti, S., Valenza, F. & Gattinoni, L. Effects of the prone position on respiratory mechanics and gas exchange during acute lung injury. *American Journal of Respiratory and Critical Care Medicine* **157**, 387–393 (1998).
- Perchiazzi, G., Rylander, C., Derosa, S., Pellegrini, M., Pitagora, L., Polieri, D., Vena, A., Tannoia, A., Fiore, T. & Hedenstierna, G. Regional distribution of lung compliance by image analysis of computed tomograms. *Respiratory Physiology & Neurobiology* **201**, 60–70 (2014).
- Pesenti, A., Musch, G., Lichtenstein, D., Mojoli, F., Amato, M. B. P., Cinnella, G., Gattinoni, L. & Quintel, M. Imaging in acute respiratory distress syndrome. *Intensive Care Medicine* **42**, 686–698 (2016).
- Phua, J., Badia, J. R., Adhikari, N. K. J., Friedrich, J. O., Fowler, R. A., Singh, J. M., Scales, D. C., Stather, D. R., Li, A., Jones, A., Gattas, D. J., Hallett, D., Tomlinson, G., Stewart, T. E. & Ferguson, N. D. Has mortality from acute respiratory distress syndrome decreased over time? *American Journal of Respiratory and Critical Care Medicine* **179**, 220–227 (2009).
- Pinhu, L., Whitehead, T., Evans, T. & Griffiths, M. Ventilator-associated lung injury. *The Lancet* **361**, 332–340 (2003).
- Porra, L., Broche, L., Degrugilliers, L., Albu, G., Malaspinas, I., Doras, C., Wallin, M., Hallbaeck, M., Habre, W. & Bayat, S. Synchrotron imaging shows effect of ventilator settings on intrabreath cyclic changes in pulmonary blood volume. *American Journal of Respiratory Cell and Molecular Biology* **57**, 459–467 (2017).

- Porter, R. *MSD Manual Professional Version* (Merck Sharp & Dohme Corp., 2020).
- Preissner, M., Murrie, R. P., Bresee, C., Carnibella, R. P., Fouras, A., W., E. K., Dubsky, S., Pinar, I. P. & Jones, H. D. Application of a novel in vivo imaging approach to measure pulmonary vascular responses in mice. *Physiological Reports* **6**, e13875 (2018).
- Preissner, M., Murrie, R. P., Pinar, I., Werdiger, F., Carnibella, R. P., Zosky, G. R., Fouras, A. & Dubsky, S. High resolution propagation-based imaging system for in vivo dynamic computed tomography of lungs in small animals. *Physics in Medicine and Biology* **63**, 08NT03 (2018).
- Protti, A., Andreis, D. T., Milesi, M., Iapichino, G. E., Monti, M., Comini, B., Pugini, P., Melis, V., Santini, A., Dondossola, D., Gatti, S., Lombardi, L., Votta, E., Carlesso, E. & Gattinoni, L. Lung anatomy, energy load, and ventilator-induced lung injury. *Intensive Care Medicine Experimental* **3**, 34 (2015).
- Reiss, L. K., Kowallik, A. & Uhlig, S. Recurrent Recruitment Manoeuvres Improve Lung Mechanics and Minimize Lung Injury during Mechanical Ventilation of Healthy Mice. *PLoS ONE* **6**, e24527 (2011).
- Ritman, E. L. Micro-Computed Tomography of the lungs and pulmonary-vascular system. *Proceedings of the American Thoracic Society* **2**, 477–480 (2005).
- Robertson, H. T. & Buxton, R. B. Imaging for lung physiology: what do we wish we could measure? *Journal of Applied Physiology* **113**, 317–327 (2012).
- Romell, J., Häggmark, I., Twengström, W., Romell, M., Häggman, S., Ikram, S. & Hertz, H. M. *Virtual histology of dried and mummified biological samples by laboratory phase-contrast tomography in X-Ray Nanoimaging: Instruments and Methods IV, SPIE* (2019).
- Rubinfeld, G. D. & Herridge, M. S. Epidemiology and outcomes of acute lung injury. *Chest* **131**, 554–562 (2007).
- Ruiz Júnior, R. L., de Carvalho, L. R. & Cataneo, A. J. M. Compensatory lung growth: protein, DNA and RNA lung contents in undernourished trilobectomized rats. *Acta Cirurgica Brasileira* **20**, 219–224 (2005).
- Sahetya, S. K., Mancebo, J. & Brower, R. G. Fifty years of research in ARDS: tidal volume selection in acute respiratory distress syndrome. *American Journal of Respiratory and Critical Care Medicine* **196**, 1519–1525 (2017).
- Samarage, C. R., Carnibella, R., Preissner, M., Jones, H. D., Pearson, J. T., Fouras, A. & Dubsky, S. Technical Note: Contrast free angiography of the pulmonary vasculature in live mice using a laboratory x-ray source. *Medical Physics* **43**, 6017–6023 (2016).
- Scaramuzzo, G., Spadaro, S., Waldmann, A. D., Boehm, S. H., Ragazzi, R., Marangoni, E., Alvisi, V., Spinelli, E., Mauri, T. & Volta, C. A. Heterogeneity of regional inflection points from pressure-volume curves assessed by electrical impedance tomography. *Critical Care* **23**, 119 (2019).
- Schiller, H. J., McCann, U. G., Carney, D. E., Gatto, L. A., Steinberg, J. M. & Nieman, G. F. Altered alveolar mechanics in the acutely injured lung. *Critical Care Medicine* **29**, 1049–1055 (2001).
- Scholten, E. L., Prisk, G. K., Beitler, J. R. & Malhotra, A. Treatment of ARDS with prone positioning. *Chest* **151**, 215–224 (2017).
- Schuessler, T. F. & Bates, J. H. T. A computer-controlled research ventilator for small animals: design and evaluation. *IEEE Transactions on Biomedical Engineering* **42**, 860–866 (1995).

- Seah, A. S., Grant, K. A., Aliyeva, M., Allen, G. B. & Bates, J. H. T. Quantifying the roles of tidal volume and PEEP in the pathogenesis of ventilator-induced lung injury. *Annals of Biomedical Engineering* **39**, 1505–16 (2011).
- Seeger, W., Günther, A., Walmrath, H. D., Grimminger, F. & Lasch, H. G. Alveolar surfactant and adult respiratory distress syndrome. Pathogenetic role and therapeutic prospects. *The Clinical Investigator* **71**, 177–190 (1993).
- Sinclair, S. E., Molthen, R. C., Haworth, S. T., Dawson, C. A. & Waters, C. M. Airway strain during mechanical ventilation in an intact animal model. *American Journal of Respiratory and Critical Care Medicine* **176**, 786–794 (2007).
- Sluimer, I., Prokop, M. & van Ginneken, B. Toward automated segmentation of the pathological lung in CT. *IEEE Transactions on Medical Imaging* **24**, 1025–1038 (2005).
- Slutsky, A. S. History of mechanical ventilation: from Vesalius to ventilator-induced lung injury. *American Journal of Respiratory and Critical Care Medicine* **191**, 1106–1115 (2015).
- Slutsky, A. S. & Hudson, L. D. PEEP or no PEEP - Lung recruitment may be the solution. *New England Journal of Medicine* **354**, 1839–1841 (2006).
- Slutsky, A. S. & Ranieri, V. M. Ventilator-induced lung injury. *New England Journal of Medicine* **369**, 2126–2136 (2013).
- Sonobe, T., Schwenke, D. O., Pearson, J. T., Yoshimoto, M., Fujii, Y., Umetani, K. & Shirai, M. Imaging of the closed-chest mouse pulmonary circulation using synchrotron radiation microangiography. *Journal of Applied Physiology* **111**, 75–80 (2011).
- Spadaro, S., Park, M., Turrini, C., Tunstall, T., Thwaites, R., Mauri, T., Ragazzi, R., Ruggeri, P., Hansel, T. T., Caramori, G. & Volta, C. A. Biomarkers for Acute Respiratory Distress syndrome and prospects for personalised medicine. *Journal of Inflammation* **16**, 1 (2019).
- Stahr, C. S., Samarage, C. R., Donnelley, M., Farrow, N., Morgan, K. S., Zosky, G., Boucher, R. C., Siu, K. K. W., Mall, M. A., Parsons, D. W., Dubsky, S. & Fouras, A. Quantification of heterogeneity in lung disease with image-based pulmonary function testing. *Scientific Reports* **6**, 29438 (2016).
- Stampanoni, M., Wang, Z., Thuering, T., David, C., Roessl, E., Trippel, M., Kubik-Huch, R. A., Singer, G., Hohl, M. K. & Hauser, N. The first analysis and clinical evaluation of native breast tissue using differential phase-contrast mammography. *Investigative Radiology* **46**, 801–806 (2011).
- Suki, B. & Bates, J. H. T. Lung tissue mechanics as an emergent phenomenon. *Journal of Applied Physiology* **110**, 1111–1118 (2011).
- Suki, B., Stamenovic, D. & Hubmayr, R. Lung parenchymal mechanics. *Comprehensive Physiology* **1**, 1317–1351 (2011).
- Sylvester, J. T., Shimoda, L. A., Aaronson, P. I. & Ward, J. P. T. Hypoxic pulmonary vasoconstriction. *Physiological Reviews* **92**, 367–520 (2012).
- Tapfer, A., Bech, M., Velroyen, A., Meiser, J., Mohr, J., Walter, M., Schulz, J., Pauwels, B., Bruyndonckx, P., Liu, X., Sasov, A. & Pfeiffer, F. Experimental results from a pre-clinical X-ray phase-contrast CT scanner. *Proceedings of the National Academy of Sciences* **109**, 15691–15696 (2012).
- Terragni, P., Rosboch, G. L., Lisi, A., Viale, A. G. & Ranieri, V. M. How respiratory system mechanics may help in minimising ventilator-induced lung injury in ARDS patients. *The European Respiratory Journal* **42**, 15s–21s (2003).

- The ARDS Definition Task Force: Ranieri, V. M., Rubenfeld, G. D., Thompson, B. T., Ferguson, N. D., Caldwell, E., Fan, E., Camporota, L. & Slutsky, A. S. Acute respiratory distress syndrome: the Berlin definition. *Journal of the American Medical Association* **307**, 2526–2533 (2012).
- Tremblay, L. N. & Slutsky, A. S. Ventilator-induced injury: from barotrauma to bio-trauma. *Proceedings of the Association of American Physicians* **110**, 482–488 (1998).
- Uhlig, S. & Kuebler, W. M. 2017 Grover Conference Series: Difficulties in modelling ARDS. *Pulmonary Circulation* **8** (2018).
- Vande Velde, G., De Langhe, E., Poelmans, J., Bruyndonckx, P., d'Agostino, E., Verbeke, E., Bogaerts, R., Lories, R. & Himmelreich, U. Longitudinal in vivo microcomputed tomography of mouse lungs: no evidence for radiotoxicity. *American Journal of Physiology. Lung Cellular and Molecular Physiology* **309**, L271–279 (2015).
- Verbanck, S. Quantitative Computed Tomography in Asthma: For Good Measure. *American Journal of Respiratory and Critical Care Medicine* **In press** (2020).
- Vidal Melo, M. F. V., Layfield, D., Harris, R. S., O'Neill, K., Musch, G., Richter, T., Winkler, T., Fischman, A. J. & Venegas, J. G. Quantification of regional ventilation-perfusion ratios with PET. *Journal of Nuclear Medicine* **44**, 1982–1991 (2003).
- Vieillard-Baron, A., Matthay, M., Teboul, J. L., Bein, T., Schultz, M., Magder, S. & Marini, J. J. Experts opinion on management of hemodynamics in ARDS patients: focus on the effects of mechanical ventilation. *Intensive Care Medicine* **42**, 739–749 (2016).
- Vieira, S. R., Puybasset, L., Lu, Q., Richecoeur, J., Cluzel, P., Coriat, P. & Rouby, J.-J. A scanographic assessment of pulmonary morphology in acute lung injury: significance of the lower inflection point detected on the lung pressure-volume curve. *American Journal of Respiratory and Critical Care Medicine* **159**, 1612–1623 (1999).
- Von Neergaard, K. Neue Auffassungen über einen Grundbegriff der Atemmechanik: die Retraktionskraft der Lunge, abhängig von der Oberflächenspannung in den Alveolen. *Zeitschrift für die gesamte experimentelle Medizin* **66**, 373–394 (1929).
- Webb, H. H. & Tierney, D. F. Experimental pulmonary edema due to intermittent positive pressure ventilation with high inflation pressures: protection by positive end-expiratory pressure. *The American Review of Respiratory Disease* **110**, 556–565 (1974).
- Wellman, T. J., Winkler, T., Costa, E. L. V., Musch, G., Harris, R. S., Zheng, H., Venegas, J. G. & Vidal Melo, M. F. Effect of local tidal lung strain on inflammation in normal and lipopolysaccharide-exposed sheep. *Critical Care Medicine* **42**, e491–500 (2014).
- West, J. B. *Respiratory Physiology: The Essentials* 9th edition (Lippincott Williams & Wilkins, Wolters Kluwer, 2012).
- West, J. B. *Pulmonary Pathophysiology: The Essentials* 8th edition (Lippincott Williams & Wilkins, Wolters Kluwer, 2013).
- Wilkins, S. W., Gureyev, T. E., Gao, D., Pogany, A. & Stevenson, A. W. Phase-contrast imaging using polychromatic hard X-rays. *Nature* **384**, 335–338 (1996).
- Wolthuis, E. K., Vlaar, A. P. J., Choi, G., Roelofs, J. J. T. H., Juffermans, N. P. & Schultz, M. J. Mechanical ventilation using non-injurious ventilation settings causes lung injury in the absence of pre-existing lung injury in healthy mice. *Critical Care* **13**, R1 (2009).

- Wongviriyawong, C., Harris, R. S., Greenblatt, E., Winkler, T. & Venegas, J. G. Peripheral resistance: a link between global airflow obstruction and regional ventilation distribution. *Journal of Applied Physiology* **114**, 504–514 (2013).
- Xia, J., Sun, B., He, H., Zhang, H., Wang, C. & Zhan, Q. Effect of spontaneous breathing on ventilator-induced lung injury in mechanically ventilated healthy rabbits: a randomized, controlled, experimental study. *Critical Care* **15**, R244 (2011).
- Xin, Y., Cereda, M., Hamedani, H., Pourfathi, M., Siddiqui, S., Meeder, N., Kadlecsek, S., Duncan, I., Profka, H., Rajaei, J., Tustison, N. J., Gee, J. C., Kavanagh, B. P. & Rizi, R. R. Unstable inflation causing injury: insight from prone position and paired computed tomography scans. *American Journal of Respiratory and Critical Care Medicine* **198**, 197–207 (2018).
- Yamamoto, T., Kabus, S., von Berg, J., Lorenz, C. & Keall, P. J. Impact of 4DCT-derived pulmonary ventilation images on radiotherapy treatment planning for lung cancer. *International Journal of Radiation Oncology. Proceedings of the American Society for Radiation Oncology 51st Annual Meeting of the American Society for Radiation Oncology* **75**, S443 (2009).
- Yen, S., Preissner, M., Bennett, E., Dubsky, S., Carnibella, R., Murrie, R., Fouras, A., Dargaville, P. A. & Zosky, G. R. The association between regional lung volumes and gene expression during mechanical ventilation with endotoxaemia. *American Journal of Physiology - Lung Cellular and Molecular Physiology* **318**, L494–L499 (2020).
- Yen, S., Preissner, M., Bennett, E., Dubsky, S., Carnibella, R., OToole, R., Roddam, L., Jones, H., Dargaville, P. A., Fouras, A. & Zosky, G. R. The link between regional tidal stretch and lung injury during mechanical ventilation. *American Journal of Respiratory Cell and Molecular Biology* **60**, 569–577 (2019).
- Yin, Y., Hoffman, E. A. & Lin, C.-L. Mass preserving nonrigid registration of CT lung images using cubic B-spline. *Medical Physics* **36**, 4213–4222 (2009).
- Yoshida, T., Uchiyama, A., Matsuura, N., Mashimo, T. & Fujino, Y. Spontaneous breathing during lung-protective ventilation in an experimental acute lung injury model: high transpulmonary pressure associated with strong spontaneous breathing effort may worsen lung injury. *Critical Care Medicine* **40**, 1578–1585 (2012).
- Zosky, G. R., Cannizzaro, V., Hantos, Z. & Sly, P. D. Protective mechanical ventilation does not exacerbate lung function impairment or lung inflammation following influenza A infection. *Journal of Applied Physiology* **107**, 1472–1478 (2009).
- Zosky, G. R., Janosi, T. Z., Adamicza, A., Bozanich, E. M., Cannizzaro, V., Larcombe, A. N., Turner, D. J., Sly, P. D. & Hantos, Z. The bimodal quasi-static and dynamic elastance of the murine lung. *Journal of Applied Physiology* **105**, 685–692 (2008).